UNIVERSITÀ DEGLI STUDI DI PADOVA

Dipartimento di Fisica e Astronomia "Galileo Galilei"
Scuola di dottorato di ricerca in Astronomia
Ciclo XXV

PYRAMID WAVEFRONT SENSORS FOR ASTRONOMY AND FOR THE HUMAN EYE

Direttore della scuola: Ch.mo Prof. Giampaolo Piotto
Supervisori: Ch.mo Prof. Roberto Ragazzoni
Dott. Jacopo Farinato

Dottoranda: Maria Bergomi

Abstract

WaveFront Sensors (WFSs) may be defined as the heart of an adaptive optics system since they analyze the radiation coming from reference sources and allow to quantify the distortion of a wavefront.
Among the varieties of existing WFSs, my PhD research thesis focuses especially on innovative optical systems taking advantage of the peculiarities of the Pyramid WFS. In my PhD project I have designed, implemented, characterized or studied three different applications characterized by the fact that one or multiple pyramid WFSs play a major role. They extend from WATERFALL, an application for the human eye (8 mm), to a Very-Linear (and very sensitive) WFS (VL-WFS), part of a concept for a 40 meter telescope adaptive optics, passing through a very complex system featuring more than 100 degrees of freedom, to be mounted on 8.4 m×2 LBT telescope (Ground-layer WFS for LINC-NIRVANA).
WATERFALL concerns the design and successful realization of a prototype for opthalmologic application for industrial commercialization to measure dioptric power of Intra-Ocular Lenses. GWS for NIRVANA works includes the definition of tolerances to be met and the detailed description of its alignment, integration phase and successful verification, leading it toward its on-sky commissioning phase in the Pathfinder experiment. The VL-WFS is in its very early phase, concepts and new ideas (mostly coming from our group) have to be organized in order to make a real proposal of a Global MCAO instrument for the E-ELT.
The projects briefly presented are all based on the same optical concepts and if the ophthalmology application might at first sight look unrelated to astronomy, it is, in fact, representing a simple SCAO system applied to an optical system which is the eye, proving how the interaction between different research field can lead to successful results.

Riassunto

I sensori di fronte d'onda sono elementi chiave in un sistema di ottica adattiva, in quanto analizzano la radiazione proveniente da stelle guida e permettono di quantificare la deformazione di un fronte d'onda.
Nell'ambito delle diverse tipologie di sensori esistenti, il presente lavoro di tesi si concentra su sistemi ottici innovativi che sfruttano le peculiarità del sensore a piramide. Durante il periodo di dottorato ho partecipato all'ideazione, realizzazione, caratter-

izzazione e approfondito lo studio di tre diverse applicazioni accomunate dal ruolo dominante occupato da uno o più sensori a piramide. I suddetti progetti spaziano da WATERFALL, applicazione destinata all'occhio umano (8 mm), ad un sensore estremamente lineare e molto sensibile (VL-WFS), parte dello studio di un concetto per un sensore da 40 metri di diametro, passando per un sistema molto complesso che presenta più di 100 gradi di libertà (il sensore di turbolenza a terra GWS di LINC-NIRVANA), che dovrà essere montato ad LBT, caratterizzato da 8.4 m×2 di diametro.

Il progetto WATERFALL riguarda il disegno, la successiva realizzazione e test di un prototipo per un'applicazione oftalmologica atta a misurare il potere diottrico di lenti intra-oculari, con obiettivo una possibile commercializzazione del sistema.

Il lavoro svolto per il GWS di NIRVANA ha portato alla definizione di tolleranze da soddisfare ed in questo elaborato è contenuta la descrizione dettagliata delle varie procedure di allineamento e dei test svolti con successo, che hanno permesso il raggiungimento della fase di commissioning in cielo dello strumento nell'esperimento Pathfinder.

Il progetto VL-WFS si trova ancora in una fase embrionale, dove concetti ed idee, prevalentemente provenienti dal nostro gruppo di Padova, devono essere organizzate per raggiungere il livello di una reale proposta per la realizzazione di uno strumento di MCAO globale per l'E-ELT.

Tutti gli anzidetti progetti si basano sugli stessi concetti ottici e, anche se a prima vsita l'applicazione oftalmologica può essere vista come estranea all'astronomia, essa può essere in realtà qualificata come un semplice sistema SCAO applicato ad un sistema ottico che e' rappresentato dall'occhio umano, dimostrando come l'interazione tra diversi campi di ricerca possa portare a risultati di successo, anche in termini di applicazioni pratiche.

Contents

Introduction

The implementation on telescopes of an adaptive optics system, able to correct in real time deformations introduced on an incoming wavefront by the atmosphere, is getting everyday more important to exploit the increase of telescopes diameters (and the consequent better resolving power) and justify huge costs necessary to build them.
WaveFront Sensors (WFSs) may be defined as the heart of an adaptive optics system since they analyze the radiation coming from reference sources and allow to quantify the distortion of a wavefront.
Among the varieties of existing WFSs, my PhD research focuses especially on innovative optical systems taking advantage of the peculiarities of the pyramid WFS (Ragazzoni, 1996). In short, a pyramid WFS consists of two fundamental parts: a 4 square-based glass pyramid, whose vertex is placed at the nominal focal plane of the system, which divides the light in four beams, and an objective lens that re-images four pupils over a CCD detector. It is a 4-quadrant sensor, where the differential intensity of light on the same portion of each of the four pupils is proportional to the first derivative of the wavefront.
In my PhD project have been designed, implemented, characterized or studied three different applications characterized by the fact that one or multiple pyramid WFSs play a major role.

In the first chapter are described the atmospheric turbulence and the most commonly used adaptive optics concepts to overcome the wavefront distortion the latter causes. Most of the considered topics will be the theoretical basis of projects and studies described in the following chapters.

It is possible to extend the application of WFSs from astronomy to everyday life, specifically to the ophthalmology field. Technologies similar to the ones used to analyze wavefronts of objects of astronomical interest have been applied to the analysis of Intra-Ocular Lenses (IOLs). In the project WATERFALL, described in Chapter 2, a pyramid WFS is used to analyze the quality of several IOLs and to determine their dioptric power with a precision of $\pm$ 0.125 D.

The opto-mechanical design was devised and a prototype using commercial equipment was realized in Padova laboratory. During my PhD I characterized, tested and modified it in order to assure a good stability and improve precision and repeatability of measures. An IDL code to analyze 4-pupils images through decomposition in Zernike polynomials (mathematical functions which allow to recognize, describe and quantify the various WF aberrations) was implemented.

In the third chapter is described the integration, opto-mechanical alignment and test phase of the first of two Ground-Layer Wavefront Sensors (GWSs) of LINC-NIRVANA, an infrared camera working in a Fizeau interferometric layout which takes advantage of the multi-pyramid Layer Oriented MCAO MFoV technique to correct a 2' FoV using only Natural Guide Stars (NGSs). It is going to be installed at the Large Binocular Telescope and for each arm of the LBT telescope 2 WFSs optically conjugated, respectively at ground and high (7 km) layers, are used to search for NGSs. The two sensors look at different FoVs. The ground-layer one searches for up to 12 NGSs in an annular 2-6 arcmin FoV, while the high-layer one, limited by the pupils superposition, looks for up to 8 NGSs in the central 2 arcmin FoV.
I worked on the assembly and alignment of the subsystem (Star Enlargers (SEs), Pupil Re-Imager (PR-I)) and to their alignment to the whole GWS system, as well as to the characterization of its fast-frame detector. SEs are optical systems which allow the enlargement of the image of the star before reaching the pyramid vertex, which is positioned on the focal plane and PR-I is the objective which re-images the four pupils on the CCD, thanks to a parabolic mirror and an optical corrector.
Due to the complexity of this system, both for the high number of subsystems it is composed of, and for the need of a very high alignment precision to meet the requirements, it has been necessary to modify previously defined procedures, to overcome sudden problems or to be able to reach higher precisions in some alignment phases to compensate for a loss in precision encountered during other phases. Sometimes it has been necessary to implement or ask for modifications of mechanical details, to overcome interferences or to improve our alignment sensitivity.
In this chapter are also detailed the main tests performed in Padova and Heidelberg (MPIA) on the aligned GWS to verify that alignment was maintained and all requirements were fulfilled (considering both mechanical issues, optical quality and alignment tolerances), and maintained during time, rotation of the bearing, movements of the SEs to point for the reference stars and flexure of the system simulating the telescope pointing. It is finally sketched the pathfinder experiment, which aims to verify on-sky the GWS as seeing reducer, using the adaptive secondary mirror of LBT telescope with its 672 actuators, to which is optically conjugated.

In the project of the Extremely Large Telescope (ELT), the need for an adaptive

optics system is evident to exploit its 40-meter diameter, but extremely important is also to reduce the cost and to achieve a satisfactory level of correction on a large FoV (≈2'), with the advantage of looking for NGSs in a 10' FoV, meaning an area 25 larger than the one usable with 8-meter class telescopes.
In Chapter 4 is described a concept for an innovative system, which comes from an idea of the local Adaptive Optics group and is based on Global MCAO with a new WFS, which takes advantage of two different kind of WFSs, whose outputs are theoretically easy to combine thanks to a similar 4-pupils approach: the pyramid WFS, provided of a high sensibility, suitable to work in closed loop and the Yet Another Wavefront Sensor (YAW, Gendron et al, 2010), which presents a large linearity range, optimal to work in open loop. Central in the concept is also the idea of using virtual Deformable Mirrors (DM) to overcome the limitation that a large FoV would have reduced the thickness of the turbulence corrected by each DM , and the need of many real DMs, an impracticable hypothesis both for costs and for degradation of the incoming signal.
Is currently on-going study in collaboration with ESO to identify a track showing the feasibility of the Global MCAO concept. I participated to the development on this concept, which required as a starting point a better understanding on Pyramid wavefront sensor characteristics for a 40 m telescope, both in linearity, sensitivity, and gain in achievable limiting magnitude with respect to the well-known but less sensitive Shack-Hartmann wavefront sensor.

Chapter 1

Atmospheric turbulence and adaptive optics

The first part of this chapter describes the atmospheric turbulence which causes a decrease of angular resolution of astronomical data obtained by ground-based telescopes.

This limitation can be solved thanks to the use of systems able to compensate in real-time images distortions. In the second part of the chapter basic concepts of Adaptive Optics (AO) systems are introduced, explaining how it is possible to correct optical aberrations due to spatial and temporal variation of the incoming wave-front, working real-time on the telescope optics, using Deformable Mirrors (DMs). Further on, some typical limitations of classical AO systems are presented, and some techniques to solve them (as Multi-conjugated AO (MCAO), ground-layer AO (GLAO) and MOAO) are depicted. They are based on the evidence that atmospheric turbulence is not uniformly distributed at different altitudes and can be corrected thanks to one or more DMs conjugated at different altitudes.

1.1 Atmospheric turbulence

Atmosphere represents one of the main limitations for ground-based telescopes, both because it absorbs specific wavelength radiation and because it produces deformations in the wavefront.

The atmosphere imposes limitations to the possibility of observing celestial bodies into the electromagnetic spectrum in a discontinuous way, as shown in figure 1.1. At short wavelengths (between 100 and 300 nm) the terrestrial atmosphere is opaque and the radiation which reaches the ground is negligible. The opacity derives from the high absorption coefficient of O_2 and N_2 molecules between 100 and 200 nm,

and of the ozone (O_3) between 200 and 300 nm. Afterwards the first observability window is encountered, the optical one, extended between 300 nm and around 800 nm. Considering higher wavelength, in the IR domain, absorption is characterized by a series of narrow windows interrupted by a series of large bands of absorption due to oxygen and water vapor, which limit the IR window up to a few tenths of mm wavelength, after which the radio window starts. This last one extends from about 8 mm to about 15 m, where it is limited by the reflection caused from the high percentage of free electrons and ions in the ionosphere (above 100 km height).

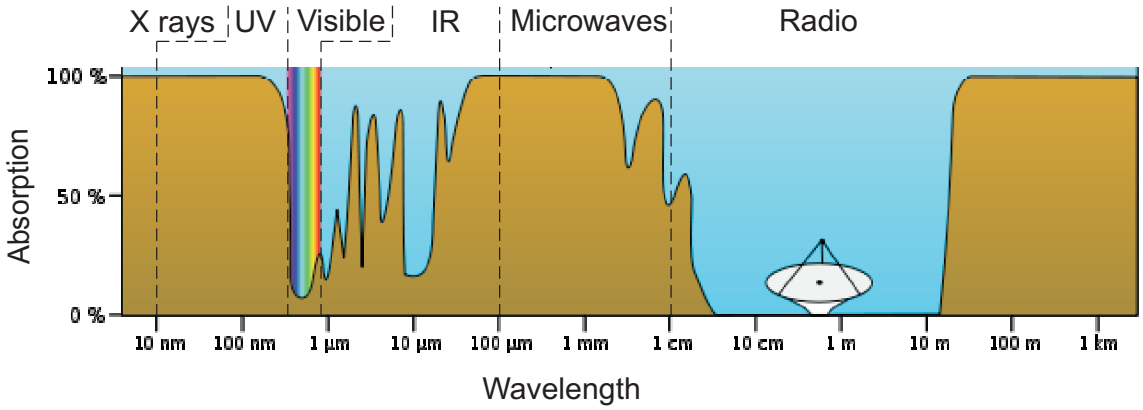

Figure 1.1: Terrestrial atmosphere transmissivity at different wavelength

In the region of our interest, which is the visible (380-800 nm) and the near IR (800 nm-2.5 μm), the atmosphere allows ground-based observations. However, it shows a layer distribution characterized by a turbulence regime with random variation of the refractive index n, between sea-level and about 25 km height (troposphere and the first part of stratosphere).
The atmosphere is not optically homogenous, since it is constituted by turbulence regions characterized by micro-variations, in time, of pressure, density and temperature and also of the refraction index: a flat wavefront passing through atmosphere is subject to deformations before reaching the telescope, since different sections composing it cover different optical paths. From the geometrical point of view, each ray which encounters a surface with a different refractive index, is subject to a deviation in the trajectory by a known angle, whose amplitude is given by *Snell's law*:

$$\frac{sin\theta_1}{sin\theta_2} = \frac{n_2}{n_1} \tag{1.1}$$

where n_1 and n_2 are absolute refractive index in the two media and θ_1 and θ_2 the angles between the ray propagation direction and the normal to the separating surface. The vacuum reflective index is is $n_{vacuum} = 1$ while the air one, in proximity of the earth surface layer, $n_{air} = 1.0003$.

An optical ray reaching the "superior limiting" surface of the atmosphere, is subject to a first refraction. Approximating the atmosphere to a series of layers, whose refractive index increasies getting closer to the ground, we can imagine that the refraction will happen layer after layer, so that the optical ray gets closer and closer to the normal of the earth surface. In this way the refractive index, even differing from the vacuum only from the 4th decimal number, produces an effect which is easily observable.

Unfortunately the atmosphere does not only curve the optical path of a ray, since the refractive index does not show only a vertical gradient, but, continuously varies in time and in space (also inside each single layer). This phenomenon produces as a consequence a continuous variation of rays direction and a wavefront perturbation. The atmospheric refractive index is related to the physical characteristics of the medium through the *Cauchy-Lorenz's law*:

$$n - 1 \approx \frac{77.6 \times 10^{-6}}{T} \left(1 + 7.52 \times 10^{-3} \lambda^{-2}\right) \left(P + 1810 \frac{P_{H_2O}}{T}\right) \tag{1.2}$$

where P (mbar) is the pressure, P_{H_2O} (mbar) the water vapor pressure, which is negligible, T (K) the temperature and λ (nm) the wavelength.
The approximate expression from equation 1.2 is called *Gladston's law*:

$$n - 1 \approx 77.6 \times 10^{-6} \frac{P}{T} \tag{1.3}$$

1.1.1 Kolmogorov's theory

Classical studies of turbulence are associated with the random velocity fluctuations of a viscous fluid such as the atmosphere. There are two distinct states of motion associated to the flow transmission's mechanisms: laminar and turbulent. The first one takes place when layers flow one over the other at different speeds with virtually no mixing between layers, while the second is characterized by irregular paths (no observable pattern) in the particles movement of the fluid and no definite layers. The latter is characterized by the presence of random vortexes, a large number of degrees of freedom and high dissipative and diffusive power.

The turbulence originates from instability of the laminar flow: when the *Reynolds' number*, Re, overcomes a critical value Re_{cr}, the transition from laminar to turbulent flow takes place. The Reynolds' number is defined by the dimensionless quantity:

$$Re(L) = \frac{L v_L}{\nu} \tag{1.4}$$

where L is the typical scale of the system, v_L (m/s) the typical velocity of the fluid at the scale L (m), dimension of the flow, and $\nu(m^2/s)$ the kinematic viscosity coefficient, which includes some properties of the fluid flow.

In general, laminar flow has a Reynolds' coefficient $1000 < Re < 2000$; incipient turbulence, where a small perturbation can easily lead to the turbulent flow, $2000 < Re < 10000$, and turbulent flow $Re > 10000$. This last Re value indicates the critical threshold Re_{cr}. For the air $\nu \approx 15 \times 10^{-6}\ m^2/s$ and for the atmosphere $L = L_0 > 15\ m$ e $v_{L_0} > 1 - 10\ m/s$, meaning that $Re(L_0) \approx 10^5 \gg Re_{cr}$, so we can state that all ground-based observations belong to a highly turbulent regime.
In astronomy the Kolmogorov (1941) model for the atmospheric turbulence is widely used. It is a conceptual framework for turbulence which applies to homogenous and isotropic turbulence for very high Reynolds number and describes how much energy is injected, transferred or lost in eddies. Kolmogorov was able to describe the pattern of the energy spectrum through some hypothesis over the statistic and physics nature of velocity fields. Considering the main characteristics of the atmosphere (pressure, density and temperature) Kolmogorov suggested to consider that when the wind speed is sufficiently high that the Reynolds' number is exceeded, large unstable air masses are created and energy is injected in the eddies (this happens at the outer scale L_0) and can feed velocity perturbations.

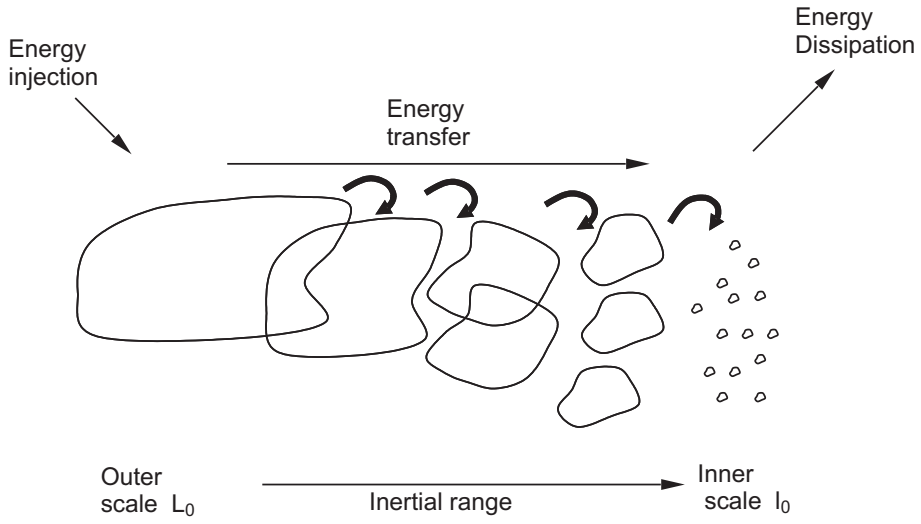

Figure 1.2: Schematic representation of the Kolmogorov energy cascade transfer.

The energy transition between different scales is due to non-linear processes which regulate a fluid flow. For each scale L, for which $Re(L)$ is higher than Re_{cr}, a similar process takes place, establishing a regime in which the energy for a unit of time and mass ϵ, introduced into the turbulent flow at scale L_0 is transferred without losses from scale to scale, increasing the turbulence at smaller scales. Unstable air masses under the influence of inertial forces break up into smaller eddies to form a continuum of eddy size for the transfer of energy from macro to micro scale. Once the l_0, called *inner scale*, is reached, so that $Re(l_0) \approx Re_{cr}$ ($l_0 \approx 1 - 10mm$), the kinetic energy is

converted into thermic energy for viscous friction the cascade transfer process arrests and we enter in the so called dissipation range. This cascade process is shown in figure 1.2. In the range $l_0 \ll L \ll L_0$, called *inertial regime*, the viscosity effect are negligible ($L \gg l_0$) and the turbulence can be considered to be isotropic and homogenous ($L \ll L_0$), so that turbulence structure is regulated only by ϵ which is transferred from scale to scale.
In this stationary regime, ϵ, which represents the energy dissipation per unit per mass, has to coincide with the kinetic energy loss from the fluid, meaning the dissipated energy due to viscous friction ϵ_0 at inner scale l_0. Dimensional considerations lead to

$$v(l) \propto \epsilon_0^{1/3} l^{1/3} \tag{1.5}$$

This means that velocity fluctuations at which turbulence vortexes vary depend only on the scale size and to the energy transmissivity rate. Since the kinetic energy depends on the squared velocity, then the energy fluctuations E_l in l scale perturbations will be:

$$E_l \; dl \propto \epsilon_0^{2/3} l^{2/3} \tag{1.6}$$

The turbulence power spectrum can be deduced from equation 1.6, integrating between l and $l + dl$, obtaining $E_l \propto l^{5/3}$. Once the wave-number for a vortex with scale size l is defined as $k = 2\pi/l$ and the vortex associated energy spectrum is E_k, then

$$E_k \propto k^{-5/3} \tag{1.7}$$

This relationship is defined one-dimension Kolmogorov frequency spectrum and is valid inside the inertial range. Integrating over the 3 spatial coordinates the relationship $E_k \propto k^{-11/3}$ is obtained.

In synthesis our relevant knowledge of the statistics of the atmospheric turbulence comes from the dimensional analysis and simple physical arguments, backed up by the fact that experimental measurements confirmed the statistical predictions.

Tatarski (1961) extended the Kolmogorov's statistics of turbulent velocity results to make them applicable to describe the distribution of the refractive index. In general, statistical homogeneity of the random velocity field implies that the mean value of the field varies statistically less than one radiant and that correlations between random fluctuations in the field from point to point are independent from the chosen observation points, depending only on their vector separation. The velocity structure function is defined as

$$D_V(\mathbf{r}_1, \mathbf{r}_2) = C_V^2 |\mathbf{r}_1 - \mathbf{r}_2|^{2/3} \tag{1.8}$$

for the points $\mathbf{r}_1$ and $\mathbf{r}_2$ separated by distance R and where the coefficient C_V^2 is the velocity structure constant.

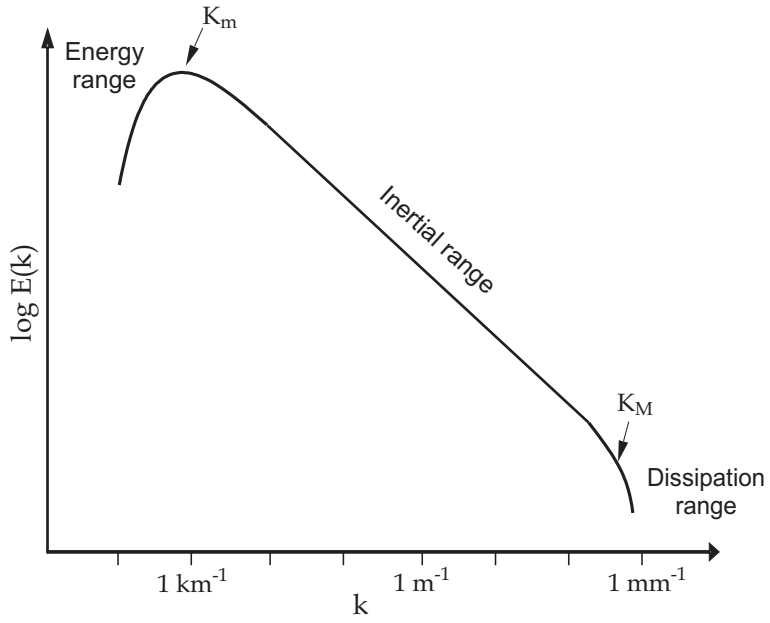

Figure 1.3: One dimensional power spectrum of the energy connected to vortexes in case of turbulence. In the graph:$K_m = 2\pi/L_0$ e $K_M = 2\pi/l_0$.

Velocity and its variations do not affect optical propagation, which is, instead affected by refractive index variations. The basic ideas of velocity fluctuations have also been applied to passive scalars and the temperature structure function defined as:

$$D_T(\mathbf{r}_1, \mathbf{r}_2) = C_T^2 |\mathbf{r}_1 - \mathbf{r}_2|^{2/3} \tag{1.9}$$

for the points $\mathbf{r}_1$ and $\mathbf{r}_2$ separated by distance R and with C_T^2 indicating the temperature structure constant.

Because there is essentially no pressure inducing atmospheric density variability within a local region, the atmospheric density can be considered to be inversely proportional to the absolute temperature. Since the refractive index deviation is proportional to density, and since the temperature variability induced by the turbulence is very small compared to the absolute temperature, it follows that the refractive index variations should also follow the same power-law of the temperature and velocity:

$$D_n(\mathbf{r}_1, \mathbf{r}_2) = C_n^2 |\mathbf{r}_1 - \mathbf{r}_2|^{2/3} \tag{1.10}$$

where the coefficient C_n^2 is called the refractive index (n) structure function constant. C_n^2 can be directly estimated through various instruments such as SCIDAR (SCIntillation Detection And Ranging) or, indirectly, measuring C_T^2 using aerostatic

balloons and then applying the following relationship:

$$C_n^2 = \frac{\partial n}{\partial T} C_T^2 \approx (7.8 \times 10^{-5} \frac{P}{T^2})^2 \; C_T^2$$

where P (mbar) is the pressure and T (K) the temperature. It is important to remember that this equation is valid only in the inertial range $l_0 \ll L \ll L_0$, meaning that C_n^2 can be considered constant in region of size smaller than L_0. The power spectral density from refractive index fluctuations over the inertial sub-range $l_0 \ll L \ll L_0$ is defined by:

$$\Phi_k = 0.033 C_n^2 k^{-11/3} \tag{1.11}$$

The vertical distribution of this parameter gives the perturbation entity which acts on the wavefront. In average, C_n^2 decreases moving away from the ground, but shows peaks in regions where two air masses in relative motion meet (*shearing*), in mechanical turbulence conditions and in regions where the vertical thermal gradient is high. Examples of this last condition can be found clearly at half troposphere($\approx$ 5000 m) and in correspondence of tropopause at 10000 m over sea-level, where thermal inversion takes place. The atmospheric region where C_n^2 varies in a distinguishable way, can be divided between 3 different layers: **superficial**, up to a few tenths of meters from the ground, where dome turbulence dominates; **Planetary Boundary Layer** up to 1000 m, subject to daily heat cycle; and **free atmosphere**, up to 20000 m, where the contribute is small because of the low gas density and is influenced only by the seasons cycle. Turbulence peak at about $\approx$ 10000 m is produced by strong winds of the tropopause. Above that C_n^2 decreases again and for $h > 25000$ m can be neglected. Observing figure 1.4 it is possible to notice how the strongest turbulent layer extends between ground and a few tens of meters. It is called ground-layer and is caused by the thermal exchange of atmosphere and earth surface, which, during night, gives back part of the heat stored during daylight.

1.1.2 Seeing parameters and turbulence effects on the focal plane

From the astronomical point of view it is important to find the connection between the atmospheric parameters previously shown and the image characteristics of a point source.

In astronomy the effects caused by atmospheric turbulence over the images are expressed through the **seeing** parameter. It is a quantity which measures the sky quality and refers to the angular dimension of a point source (i.e. a star) on the telescope focal plane. Technically it is the Full Width Half Maximum (FWHM) of the star's Point Spread Function (PSF). Seeing is the cumulative effect over the star light due to the fact it goes through a medium with a variable refractive index.

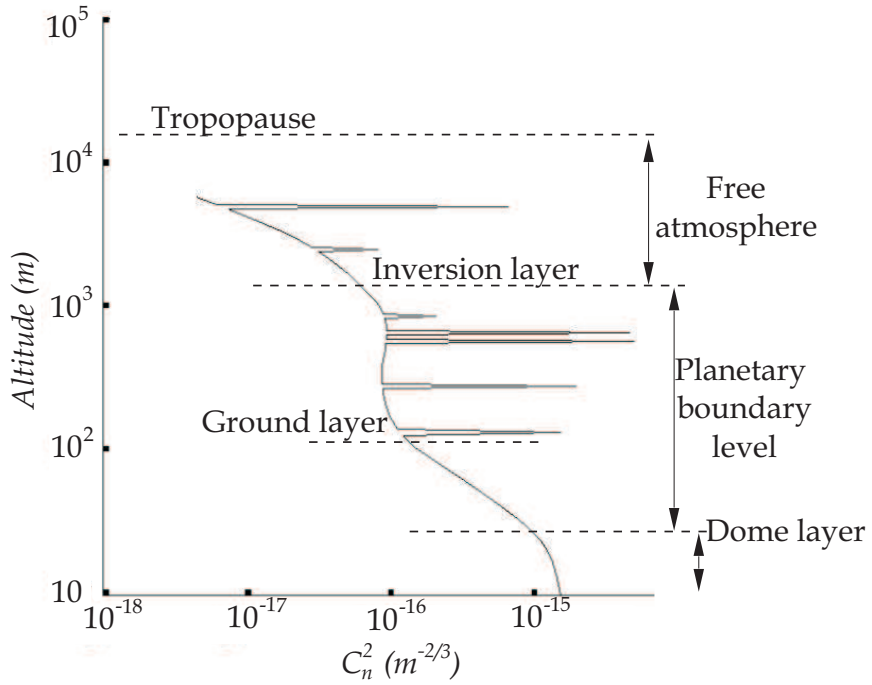

Figure 1.4: Schematic representation of atmospheric layers following a C_n^2 profile. Horizontal dashed lines represent the areas of maximum turbulence.

Despite of the telescope diameter increase, up to D=8-10 m, and the consequent increase in collecting photons, proportional to D^2, the resolving power does not follow the same pattern.

The theoretical resolution of a system (θ) is given by the angular dimension of Airy diffraction pattern

$\theta \approx \frac{\lambda}{D}$ whereas the actual one depends from the atmospheric seeing. This latter is characterized by 3 main parameters, which depend on the observing wavelength: Fried parameter r_0, isoplanatic patch, θ_0 and coherence time τ.

Fried radius is a mathematic parameter introduced by Fried (1966), which can be expressed as the average dimension of the unperturbed wavefront or as the average dimension of the turbulent bubble. Fried showed that inside the limitations of Kolmogorov's theory a turbulence typical linear scale exist, at the wavefront level, for which the wavefront varies statistically less than on phase radiant ($\lambda/2\pi$). This dimension is r_0 and can be expressed as a function of C_n^2 parameter:

$$r_0 = \left[0.424\pi^2/\lambda^2(cos\phi)^{-1}\int_0^\infty C_n^2(h)dz^{-3/5}\right]\ m \tag{1.12}$$

where h is the height over the ground, ϕ zenith angle (between earth surface's normal and observing direction angle), As it is possible to see, Fried's radius decreases with

the turbulence (expressed by C_n^2 integral), but grows almost linearly with the wavelength ($\lambda^{6/5}$). It is important to notice that in case of a laminar flow, the temperature structure coefficient is zero and the same is true for the integral of equation 1.12. Therefore, turbulence in the presence of a temperature gradient, produces seeing. Knowing the C_n^2 along the line of sight through those equation it is possible to determine the seeing. When a telescope has a diameter larger than the Fried's parameter size and is not provided of an adaptive optics system, its resolution is limited to:

$$\theta \approx \frac{\lambda}{r_0} \tag{1.13}$$

which, expressed in arcsec (multyplying by 206264.8 [”]), is the value given to the seeing. r_0 average values are about 10-20 cm in V-band and about 50-100 cm K-band, so the seeing measured at this second wavelength is slightly lower. Typical values of good seeing are about 0.4-0.5”. Local effects as instrumental seeing or dome seeing can significantly contribute to the seeing observed over images, meaning that the measured values need to be deconvolved for the local turbulence effects.

The **isoplanatic patch** θ_0 is the angle which subtends the field of view in which the wavefront phase varies statistically less than one radiant and inside which PSF can be considered constant.

$$\theta_0 = 0.31\frac{r_0}{H} \tag{1.14}$$

with H=turbulence average height, and is proportional to wavelength as $\lambda^{6/5}$.

The **coherence time** τ represents the time in which the PSF inside the isoplanatic patch is constant and is given by:

$$\tau = 0.36\frac{r_0}{v} \tag{1.15}$$

with v wind velocity and depending from wavelength as $\lambda^{6/5}$, as well. The coherence time, which is important to define the temporal variability level of the atmosphere over the incoming wavefront is, in general, of the order of a few millisecond and, as other previously cited parameters, depends on the observation site and the turbulence layer considered. τ inverse is called ***Greenwood frequency***, f_G.

Other parameters useful to characterize an optical system performance (not directly connected to the seeing), are the Strehl ratio and the Signal-to-Noise (S/N) ratio.

Strehl Ratio, SR or Strehl, is a parameter extremely useful to judge the quality of the distorted images. It is defined as the ratio between the peak of the observed PSF and the peak of the ideal one, ideally obtained with the same instrument. By definition it can vary between 0 and 1 and is 1 for an image not affected by seeing.

Finally, the **Signal to Noise Ratio** (SNR) indicates the signal quality on the detector and is a parameter which quantifies the image quality obtained with a given

instrument. Signal is called the radiation emitted by the source of interest, whereas the noise is the radiation flux external to the source plus the instrumental noise unavoidable for each measurement, which merges with the signal lowering the image (or spectrum) quality. The most commonly used detectors are CCDs (*Charge-Coupled Device*), which integrate photons and are based on the light conversion into electric charges on the silicon chip. Afterwards the charges are released through photoelectric effect and are accumulated for all the exposure time. Finally charges get read and translated into counts. The noise is given by the sum of many factors, among which the most relevant are read-out noise, Poisson noise and dark current noise. This last one is due to electrons generated thermally inside the CCD and can be reduced chilling the detector. The Poisson noise is due to the unpredictability of the photons arrival, integral to their statistical nature. It is important to see how, due to the achromaticity of the optical path perturbation, often, in the adaptive systems, the sensor is used in the visible, also to take advantage of the better characteristics in terms of noise with respect to infrared detectors.

The flat wavefront coming from an astronomical object, propagating through the atmosphere from an astronomical object through the vertical axis h, after passing through a turbulent layer, assumes a distorted shape W (x,y) (where (x,y) indicate the position in the optical aperture). The deformation introduced on the wavefront can be decomposed in two components, as shown in figure 1.5:

- the mean wavefront **tip-tilt**. Its effect on the focal plane is to generate a shift of the center of mass of the observed object. Integrating in time, this causes an enlargement of the object size and consequently worsens its resolution.
- the wavefront roughness characterized by the **higher orders** aberrations. The fluctuation of the refractive index translate into a phase difference between the various parts of r_0 size of the same wavefront, causing a differential delay in the wavefront phase. The consequence on the focal plane for integrations longer than the atmosphere variation time is the same generated by tip-tilt, meaning an enlargement on the focal plane of the mean dimension of the objects with a consequent loss in the definition of the image.

Moreover, atmosphere also causes scintillation, the apparent source intensity variation in time. This effects increases as the pupil size decreases and it is, in fact, clear in the human eye, because rays coming from the source reaches the retina either converging of diverging causing continuous light intensity variations.

Concluding, the wavefront deformations appears on the focal plane with scintillation, movements and deformations of the images, which, integrated in time, cause an enlargement of the point sources and subsequently a reduction of the telescope resolving power.

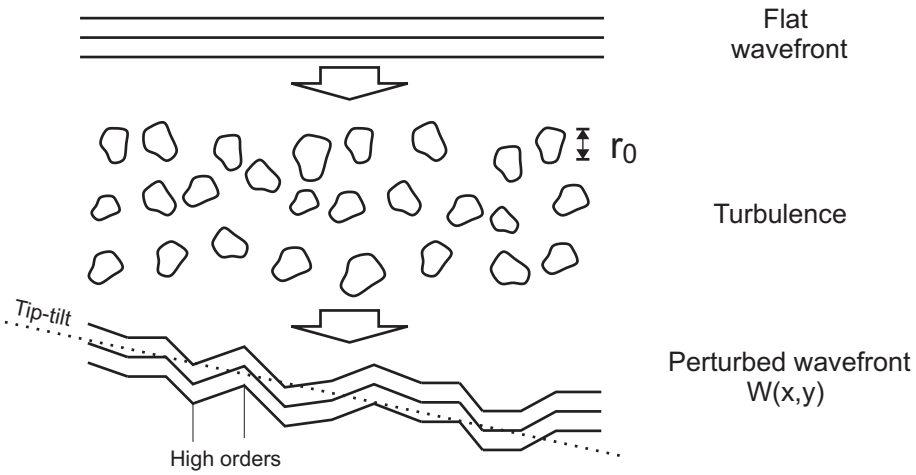

Figure 1.5: Schematic representation of the wavefront deformation caused by the atmospheric turbulence characterized by bubbles of mean size r_0. In the bottom part of the image, the dashed line indicates the mean wavefront tilt, while the full line the high orders effect.

1.2 Adaptive Optics

Babcock (1953), in "The Possibility of Compensating Astronomical Seeing", discussed about possible techniques to reduce atmospheric turbulence effect on the incoming wavefront. He affirmed that to solve casual shift of a star image, solutions were already existing, such as guiders instruments which centered a star on a pyramid or on the axis of rotation of a knife-edge, to divide the incoming beam. Those concepts are both based on Foucault principle used to determine lenses or mirrors aberrations. In this test a knife-edge was positioned in the focus of a convergent beam and wave-front perturbations are identified blocking the rays which were deviated from their ideal path by aberrations. Those systems were rotating and through the measurements of light intensities in different positions aberrations could be quantified. Babcock thought to use an instrument whose objective was the guide star seeing reduction caused by high order of atmospheric turbulence. This instrument had to measure continuous deviations of a guide-star to locally correct the shape of a deformable mirror in a way to compensate at the same time deviations due both to seeing and to optical imperfections. Since it would have not been possible to perform continuous correction on the primary mirror itself, he proposed to insert a corrector in a plane conjugated to the mirror. He immediately found the two main limitation of a similar system: the size-limited corrected FoV, due to higher layers turbulence and the dependency of the correction from the reference star magnitude. At tha time Babcock idea was hardly considered, both because many things still had to be discovered, even in seeing limited conditions and, of course, because of the

limitations in the technology needed to perform real-time corrections.

However, Babcock had a great intuition for the time in which it was suggested, which has been re-considered and implemented starting from the '80s under the name of Adaptive Optics. Adaptive optics is a technique to compensate in real-time the incoming wave-front deformations, introduced on its way through the atmosphere. The compensation is possible inserting in the optical path a device able to introduce a wavefront distortion equal but opposite to the one generated by the atmospheric turbulence. This correction has to be realized in a time which could allow the temporal evolution of turbulence itself (inverse of Greenwood frequency).

In figure 1.6 is shown the concept of an adaptive optics system. The beam coming from a distant object is distorted by atmospheric turbulence before reaching the telescope, then arrives on a device able to deform the wavefront, namely a **corrector**, which is generally a **deformable mirror** (DM). Than the beam is divided in two parts by a beam-splitter: one part is re-focused onto a **detector** for the image acquisition, while the other is sent to the **wave-front sensor**. It analyzes the radiation coming from a reference source to obtain information on the wavefront deformations on the pupil. Those information are then sent to a **reconstructor** which then determines the configuration needed for the corrector in order to compensate deformations. It is important to observe that, in this case, the sensor it's located after the corrector in the optical path. There are two different ways in which correction can be performed in adaptive optics: **open loop** and **closed loop**. In an open-loop the perturbed wave-front reaches the sensor before the DM. Extremely important becomes, then, the exact measurement of the wavefront and the knowledge on how the DM actually corrects it, to avoid a loss in the correction perfromance. There are ways of evaluating DM performance, namely referencing, and in case inserting the discrepancy between commanded and measured shape in the correction (which will be described in Chapter 4).

In the closed-loop system, instead, light reaches first the deformable mirror and the WFS measures the residual aberrations after the correction. Since the corrector needs to be faster than the wavefront variation, the perturbed wave-front finds a DM configuration similar to the one needed to flatten the wavefront. In this way the sensor will receive a wavefront whose deformations are given only by the residuals of the previous correction, increasing the adaptive optics system efficiency, reducing at each iteration the correction residuals.

1.2.1 The corrector

The corrector usually consists in a mirror whose reflective surface is very thin and can be deformed by actuators and, for this reason, is defined as deformable or adaptive mirror. The adapters number determines the spatial correction level,

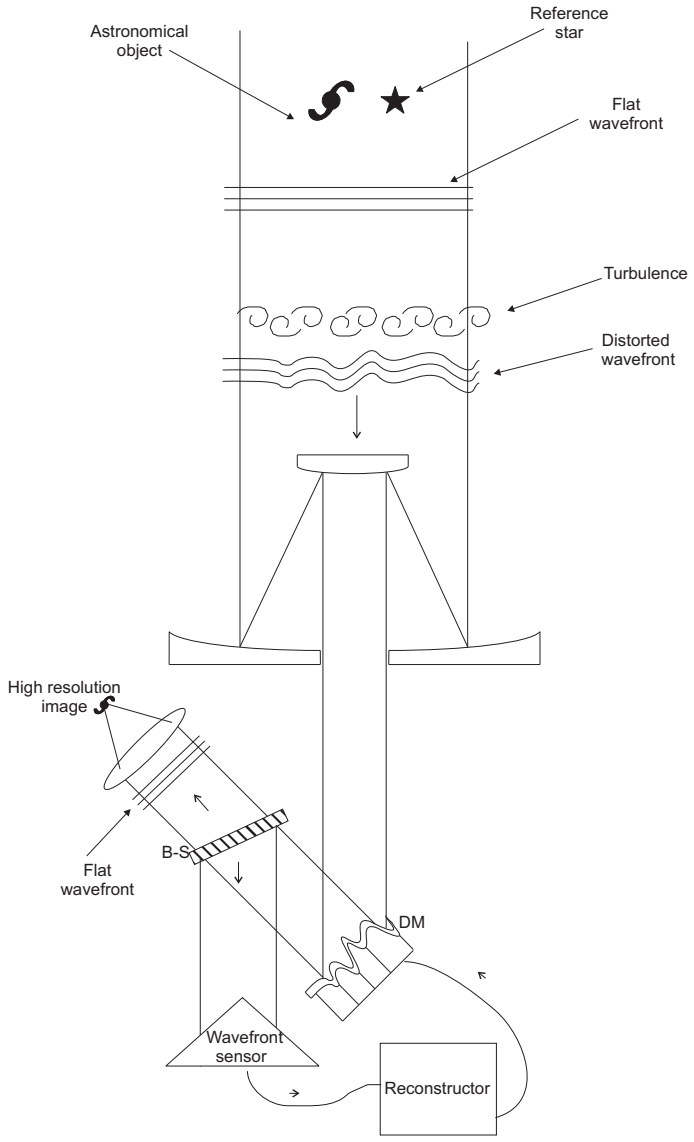

Figure 1.6: Layout of an adaptive optics system. A beam coming from a distant object is distorted by atmospheric turbulence. Main components are a corrector (DM), a wavefront sensor and a reconstructor. B-S is a beam splitter. (Note that the GS and the science object are represented one from the other a lot further than what happens in the reality).

which is possible to achieve. For an efficient correction, it is necessary that the whole adaptive optics system works at shorter times compared to the typical ones in which the perturbations evolve on the telescope pupil. For the best correction it is important that the actuators number and the sub-apertures number on the wavefront are coincident. In this case the sensor has $(D/r_e)^2$ active zones whose equivalent dimension in the pupil correspond to r_e (inter-actuator distance). In most

systems the DM is part of each telescope instrument and it is optically conjugated to the pupil. In this way pupil dimensions can be reduce with a proper optical design, and smaller mirrors can be used (making it easier to obtain a fast response in DM deformation). More recently, in particular at LBT (Large Binocular Telescope), MMT (Multi Mirror Telescope) and on VLT (Very Large Telescope) UT4 (as well as in the E-ELT design), the secondary mirror of the telescope is adaptive and designed to be conjugated to the ground-layer. In this way it is possible to provide to any telescope instrument an image with reduced seeing.

1.2.2 Wavefront sensor

A WaveFront Sensor (WFS) uses the radiation of a reference source in order to quantify wavefront distortion. Let us consider a wavefront W(x,y) which has already crossed a turbulent atmospheric layer and let us measure the intensity I in two subsequent layers z_1 e z_2 (corresponding at two different temporal moments). The variation intensity in a function of z is:

$$\frac{\partial I}{\partial z} = -(\nabla I \cdot \nabla W + I\nabla^2 W) \tag{1.16}$$

∇W is the slope and $\nabla^2 W$ the wavefront curvature. Some WFSs reconstruct a signal which is proportional to the first derivative of the wavefront from the light intensity variations (as Shack-Hartmann WFS and Pyramid WFS, both will be better described in the next sections), others, through second derivative $\nabla^2 W$ (curvature sensor, Roddier (1981)), others through interferometric techniques reconstruct directly the wavefront (such as Smartt interferometer). Generally, to identify high order aberrations, it is necessary to divide the wavefront in smaller parts. In other words, the main wavefront is divided in order to analyze wavefront aberrations on fractions of it, trying to reconstruct the tilt of each section of the retrieved wavefront. The used technique is to observe the light intensities differences or the center of mass shifts in subsequent moments. The wavefront shape is reconstructed integrating gradients in every sub-area over the entire aperture. It needs to be highlighted the fact that this is finally a spatial sampling of the wavefront, and a reconstruction is therefore better as the subareas number increases. It is necessary to consider two limitations to the sub-aperture numbers:

- the signal-to-noise (S/N) of each single sub-aperture, since it is obvious than as the number of sub-areas considered increases, the number of incident photons for each one of them will become lower;
- DM actuators density; it is of course impossible to achieve a higher correction than what it is allowed by actuator number

Therefore, the sub-apertures number to be considered in a wavefront is a compromise between what has already been said and, also, on the wavefront where the correction wants to be realized.

It is important to remember that r_0 increases with the considered wavelength requiring a lower sub-aperture number in the infrared compared to the visible to achieve the same correction quality.

4 quadrants sensors

To evaluate the tip-tilt of the incoming wavefront a quad-cell or four quadrant sensor can be used. The 4 quadrants center is the position where the center of mass of the image should lay in absence of tip-tilt. The sensor evaluates the light percentage which illuminates each of the quadrants and is able to determine the shift suffered by the image. Shift along x axis and y axis can be quantified through the signal S received in the 2 directions (sky background is not considered in the following):

$$S_x = \frac{(B+D)-(A+C)}{A+B+C+D} \qquad S_y = \frac{(A+B)-(C+D)}{A+B+C+D} \tag{1.17}$$

where A, B, C e D are the intensities of the relative portions of a spot shown in figure 1.7 and S_x and S_y are proportional to the wavefront first derivative, calculated along two orthogonal directions. The useful range to determine tip-tilt is the one in which S_x e S_y increase linearly, which is satisfied when the spot illuminates all four quadrants. Otherwise, saturation is reached. It is important to underline that the sensitivity of the sensor increases while the spot dimension decreases, because given the same amount of center of mass shift, the signal will vary in a higher percentage in the case of a smaller spot.

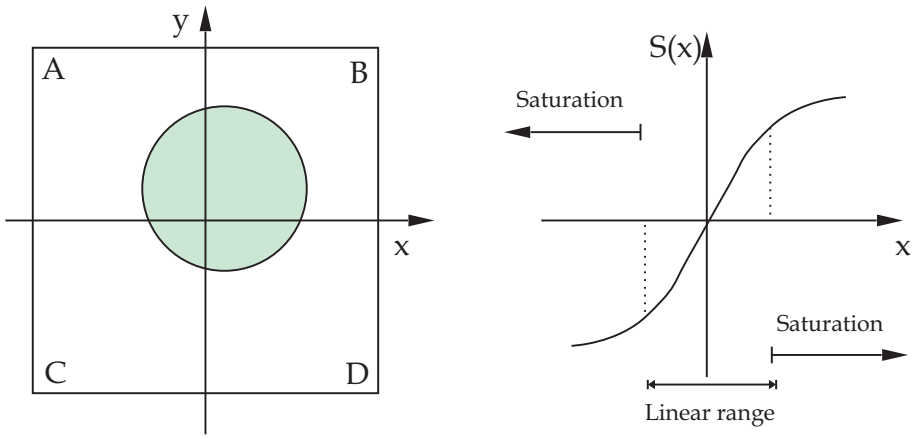

Figure 1.7: Left: layout of a 4 quadrants sensor. Right: S(x) signal function while shifting of the spot along z-axis.

Such a WFS can be realized in different ways, and the reevant ones for this thesis will be described in the following sections.

Shack-Hartmann sensor

The sensor is called Shack-Hartmann (SH), since it is based on the use of an array of lenses instead of the classical holes array of Hartmann test (1904). The telescope exit pupil image goes through a collimator and is projected on an array of identical small lenses (lenslets), located in a plane conjugated to the pupil one.

Lenses have the scope of dividing the wavefront and, to obtain the maximum efficiency, they need to be adjacent and cover the entire optical aperture. The lenses number will have to be chosen in a way to avoid oversampling of the wavefront, to prevent avoidable light losses. This is generally obtained dividing the telescope diameter for the r_0 value typical of observation site (for example for an 8 m telescope and $r_0 = 20\ cm$, a 40×40 sub-aperture array is needed). Being r_0 variable also from night to night, it is possible to select different arrays to vary the wavefront sampling. The light of a single reference source is then divided in more parts which are focused separately by each lens as shown in figure 1.8, producing an array of images on the focal plane. A detector, typically a CCD, records images in order to reconstruct the center of mass shift of each image, following the 4 quadrants concept.

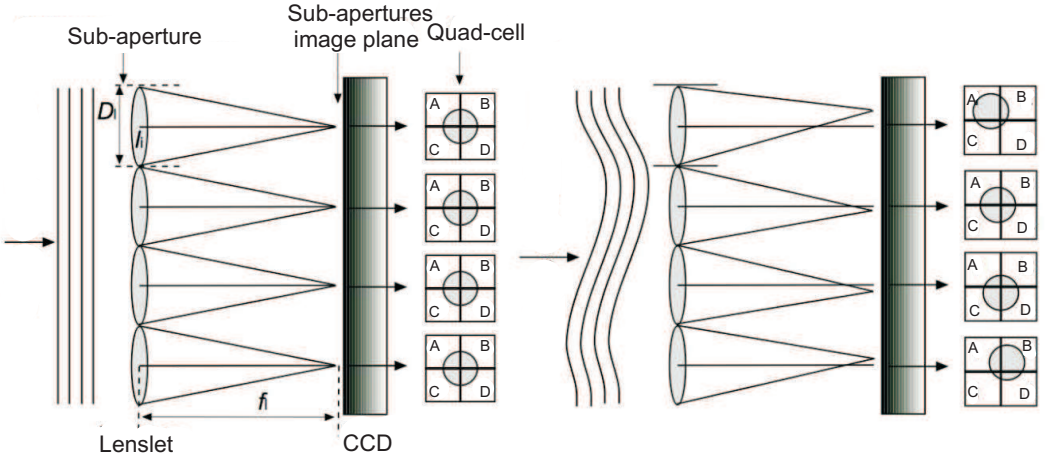

Figure 1.8: SH basic concept. On the left a flat wavefront generated images centered with respect to the quad-cell, while on the right the shift of the images due to aberrations is visible in each sub-aperture.

The dimension of the images produced on the detector is:

$$d = \lambda \frac{f_l}{D_l} \tag{1.18}$$

where f_l e D_l are respectively the focal length and the diameter of lenses. Without turbulence the image in each lens should fall in the center of the quad-cell, which is divided into 4 quadrants (A, B, C, D). As already said, perturbations produce small shifts $(\Delta x_B, \Delta y_B)$ of the center of mass of each image.

$$\Delta x_B \approx \frac{1}{2}\left(\frac{\lambda f_l}{D_l}\right)\frac{(B+D)-(A+C)}{A+B+C+D} \tag{1.19}$$

$$\Delta y_B \approx \frac{1}{2}\left(\frac{\lambda f_l}{D_l}\right)\frac{(A+B)-(C+D)}{A+B+C+D} \tag{1.20}$$

The derivatives $\partial W/\partial x$ e $\partial W/\partial y$ give the wavefront tilt with respect to the lens plane s that

$$(\Delta x_B, \Delta y_B) = \left(f_l\frac{\partial W}{\partial x}, f_l\frac{\partial W}{\partial y}\right) \tag{1.21}$$

Substituting the previous equation in equations 1.19 and 1.20 an estimate of aberration in each sub-aperture is obtained.

$$\frac{\partial W}{\partial x} \approx \frac{1}{2}\left(\frac{\lambda}{D_l}\right)\frac{(B+D)-(A+C)}{A+B+C+D} \tag{1.22}$$

$$\frac{\partial W}{\partial y} \approx \frac{1}{2}\left(\frac{\lambda}{D_l}\right)\frac{(A+B)-(C+D)}{A+B+C+D} \tag{1.23}$$

The computation seen here above are valid only if the image center of mass shift is a lot smaller with respect to its dimension; otherwise the linearity relation between W(x,y) first derivative and signals is lost.

Concluding, it is possible to obtain an estimate of the mean tip-tilt of the portion of wavefront which reaches each lens and the total deformation is reconstructed as a mosaic of tilt present in each sub-aperture in which the wavefront is subdivided.
SH sensor allows to correct high orders and to modify spatial sampling varying lenslet array.

Pyramid sensor

The concept of the pyramid WFS (PWFS) Ragazzoni (1996b) is based on the Foucault test, which allows to determine aberrations associated to an optical system, where a pyramid replaces the knife-edge (see also Riccardi (1996)). The image of a reference star, distorted by turbulence, reaches the pyramid whose vertex is placed on the telescope focal plane. The beam is then divided in 4 parts, each deflected in a different direction by the pyramid face that is tilted with respect to the focal plane. A lens then recreates on the pupil plane four images whose differential intensities are measured by a CCD. The separation and the enlargement of the four images are determined respectively by the pyramid angle and by the focal length of the lens.
If, instead, we want to sense also higher order aberrations, it is necessary to divide

the wavefront in smaller parts, similarly to what happens for the SH sensor. In the pyramid case, though, no other optical element is necessary since it is sufficient to modify the spatial sampling, binning groups of pixels while reading the CCD.

Referring to figure 1.9, to retrieve the wavefront tilt in the sub-aperture "A", it will be sufficient to combine the pixel light a', b', c', d' in an analogous way to the calculation of average tilt over all the aperture, which means $(a'+b')-(c'+d')/(a'+b'+c'+d')$ for x axis and $(c'+b')-(a'+d')/(a'+b'+c'+d')$ for y axis.
This characteristics unique to the PWFS determines a remarkable practical advantage because it allows to vary the wavefront sampling in a fast way, without other opto-mechanical implications and allows a higher adaptive capacity to r_0 values during observation.

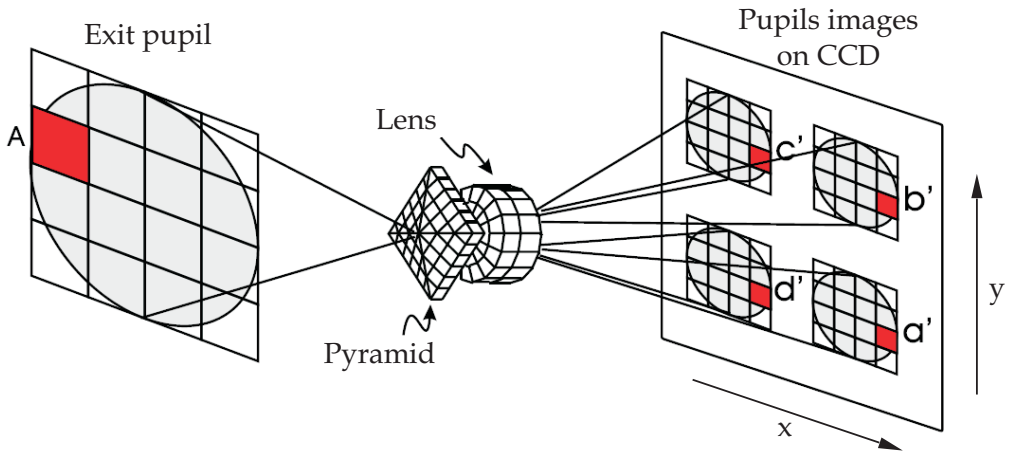

Figure 1.9: Pyramid sensor. Pyramid is positioned in the nominal focus of the reference source and the beam is divided in 4 parts, each reproducing a pupil image through an objective. To the sub-aperture "A" of the exit pupils corresponds to 4 sub-apertures on the CCD (named a',b',c',d').

To increase sensor linearity a few options were proposed: a circular modulation of the pyramid (Ragazzoni, 1996a)or a tip-tilt oscillation of a mirror conjugated to the telescope exit pupils (Esposito and Riccardi, 2001). This two techniques are optically equivalent and have the name of dynamic modulation, which determines the sensitivity and dynamic range of the PWFS.

To a small modulation corresponds an intense signal even with small aberrations, whereas to a big modulation corresponds a less sensitivity but aberrations of higher intensity can still be measured (the working range is therefore increased). In the first cycles of an open-loop a higher modulation can be used and then reduced to increase the sensitivity in closed-loop and subsequently the image quality.

Afterwards it has been devised that modulation is not necessary to have a PWFS

properly working (Costa et al., 2003). In fact, the atmospheric turbulence gives a "natural" modulation of PSF light on the pyramid pin. During first open-loop cycles atmospheric PSF size is of the order of λ/r_0, with results equivalent to those of a big modulation. When the open-loop is closing, lower orders which contain most of the turbulence (Noll, 1976) are corrected and the PSF size decreases, which is equivalent to say that the modulation decreases. In fact, improving the wavefront correction, r_0 in theory increases until reaching the telescope dimension in closed-loop (if the sensor is using the same wavelength as the one of the scientific instrument). It is therefore possible to start seeing speckles which have dimensions of the order of λ/D, randomly moving on the pyramid, producing a natural modulation.

Being the pin of the pyramid positioned in the focus, when the AO system is activated, the DM is guided by the electronics accordingly to the information retrieved by the WFS, up to the loop closing. At the same time the spot dimension on the pin of the pyramid, starting from the seeing-limited value of $\lambda/r0$, tends to its diffraction-limited λ/D. Because of this reason, the WFS sensitivity to the spot movements (i.e. the tilt, being it global or local) increases, allowing a wider dynamical range in the first AO iterations and a higher sensitivity when the loop is closed. Moreover, when the loop is closed, the SNR increases considerably (similarly to what happens for a curvature WFS but not for a SH WFS), consequently translating into a gain in the theoretical limiting magnitude of the WFS when compared to a SH WFS (Ragazzoni and Farinato, 1999), property which will be analyzed in section 4.4.2.
PWFS introduces in the adaptive optics system some parameters easy to modify (sensitivity and sub-aperture numbers) which allow adapting the system to the changes of the atmospheric turbulence, to the wavelength at which the observation is performed and to the luminosity of the available reference source. This is not straightforward for a SH WFS, where the spot size depends on the lenslet array number, which needs to be physically exchanged to obtain the required changes.

More details on recent studies concerning the pyramid WFS will be given in Chapter 4.

YAW sensor

The Yet Another Wavefront (YAW) has been proposed by Gendron et al. (2010). I will not dig into all sensors details, which can be found in the cited paper, I will just explain its main characteristics and basic layout. Optical differentiation wavefront sensors work by optically Fourier-filtering the pupil image, placing a varying amplitude transmission filter in the focal plane and transforming the phase gradient into intensity variations in the pupil plane. Instead of using a spatially varying

transmissive filter, in the YAW a spatially varying polarization-rotater is realized. The YAW exploits the properties of the Wollaston prisms, splitting the incoming beam from the star (not polarized light) into 2 linearly polarized beams, with orthogonal polarization axis. On both beams is placed an optically active material, with the property to rotate the polarization plane of an incident linearly-polarized wave by an angle α proportional to the crossed distance w (and highly dependent on the wavelength of the incoming beam). The shape of this material is realized as an assembly of two plates of a mono-crystal of quartz, one levo-rotatory and the second one dextro-rotatory (see figure 1.10). The width of the wedge (called w on the figure) corresponds to the zone into which the sensor will behave linearly. In this way depending on where the ray crosses the material a different polarization angle will appear.

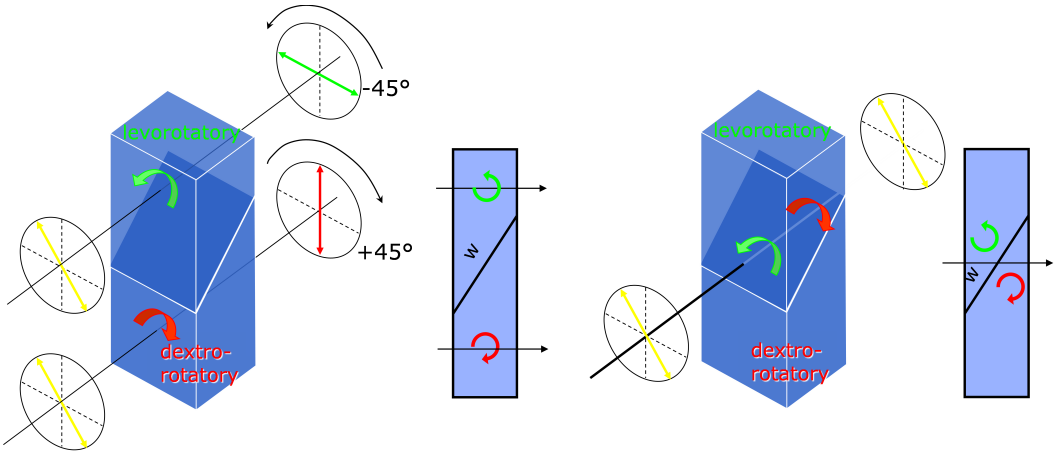

Figure 1.10: Variation of the rotation angle of the polarization versus position in the spatially variable rotatory plate. Two plates of a mono-crystal of quartz are assembled together. One is dextro-rotatory, the other levo-rotatory. The light propagates perpendicular to the plate. The optical axis is parallel to the light propagation. The polarization rotates proportionally to the height the ray went through the wedge, from -45$^c irc$ to +45$^c irc$.

Afterwards a second Wollaston prism acts as an analyzer, being its axis rotated by 45$^c irc$ with respect to the first one. On a non-aberrated beam, all the rays cross the center of the variable rotatory plate, and the polarization is rotated by 0$^c irc$ for any point of the pupil. Hence, the amplitude spreads equally on the axes of the second Wollaston prism, and the intensity is the same for the four pupil images. Instead, an aberrated ray will cross the focal plane at a particular location, characterized by a certain amount of polarization rotation. The second Wollaston prism will translate this rotation into a difference of intensity in the pupil planes. Being α proportional to the material thickness crossed, from the polarization of the beam the impact position of the ray in the focal plane is retrieved, which means to get the

phase gradient. The YAW layout is depicted in figure 1.11.

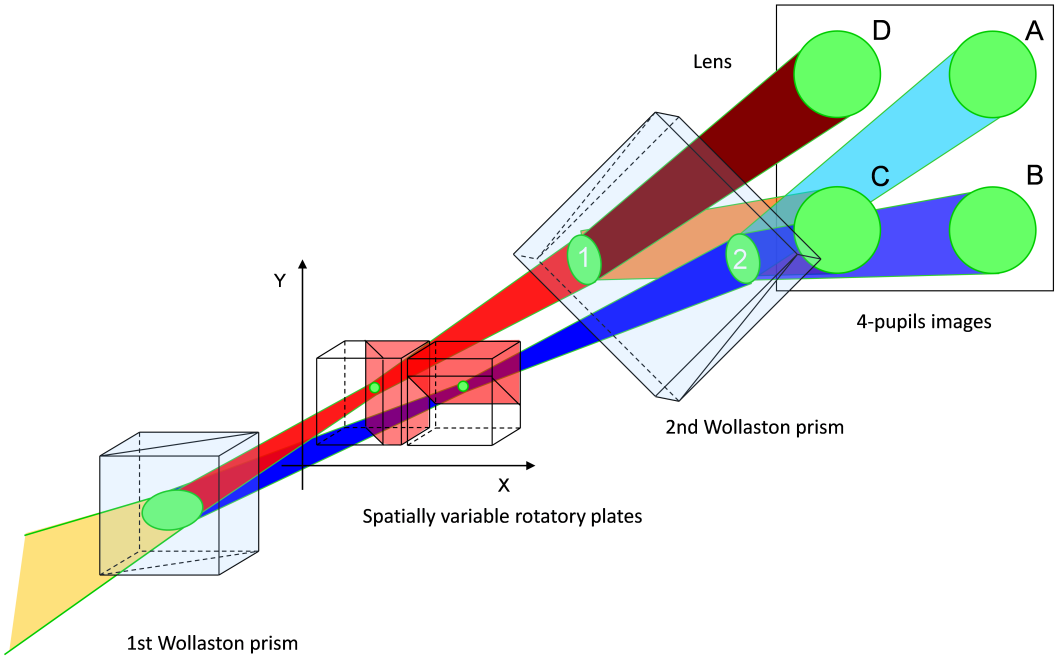

Figure 1.11: The concept of a YAW is depicted. A first Wollaston prism divides the star light into 2 orthogonally polarized beams which then reach 2 spatially variable rotatory plates. A second Wollaston prism is placed on the path and a lens allows to re-image pupils. Combining the signals of the pupils the rotation angle can be retrieved and therefore the direction of the incoming beam.

For a couple of the formed pupils, calling I_A and I_B the intensity at a pupil location, the rotation angle α can be retrieved as:

$$\alpha = \frac{1}{2} arcsin\left(\frac{I_A - I_B}{I_A + I_B}\right)$$

It should be noticed also that no particular edge of any material marks the "zero" of the wavefront sensor (in contrast with the pin of a PWFS). Thus, diffractive effects are minimized.
The sensor provides a higher noise level than quad-cell, but with the advantage of no centroid-gain problem. The balance between those two parameters is tuned by the only free parameter in the sensor design: the wedge size, w. A larger w provides increased gain stability and linearity with higher noise, while a small w reduces the range where gain stability and linearity are kept with better noise performance. A w = 0 reduces the sensor to a pure quad-cell or non-modulated pyramid.

The YAW has been conceived mainly in the use with Laser Guide Stars (see Section 1.4) for E-ELT system, working particularly well with monochromatic light and

being able to observe also elongated spots, being its sensitivity independent from the angular size and shape of the object (within a certain range corresponding to the size of the wedge of the sensor) to the detriment of the noise level. Moreover, it presents a very linear response versus the phase gradient, making it extremely interesting candidate for open-loop operations for MOAO. The outcome of the sensor are 4 pupils and combining the datas of the same areas (pixel) of the four pupils the phase can be retrieved. This outcome is essentially the same of a Pyramid one and in principle the two sensors outcomes could be combined. For all the above reasons it is also very suited for the Global MCAO concept described in Chapter 4.

1.2.3 The reconstructor

Since the WFS does not give directly the aberration function of wavefront W, it becomes necessary the use of a wavefront reconstructor to reconstruct the wavefront shape and send the commands to vary the DM shape. Two main categories of reconstruction exist: *zonal* or *modal*. The first one gives an estimate of ΔW in some of the pupil areas (typically in coincidence with DM actuators). The second one gives coefficients associated to the pupil function in which the aberration function W is decomposed (for instance Zernike's polynomials).

Depending on the WFS and the DM one of the two techniques can be used, for example for PWFS, the modal reconstruction is considered superior to the zonal one (Southwell, 1980), since it is less sensitive to propagation noise associated to ΔW estimates. On the contrary, in the case of a curvature WFS associated to a bimorph mirror, the zonal one is preferred because it is straightforward to apply the signal to the DM.

Zernike's polynomials

Noll (1976) showed that a suitable approximation to describe optical aberrations generated by a turbulence following Kolmogorov spectrum is represented by Zernike polynomials (Z_m^n). These polynomials Z_m^n constitute an orthogonal basis for the functions defined on a circle with unitary radius and are defined in polar coordinates:(ρ, θ).

The Zernike expansion describes separately known aberrations. Generic error of phase as $\phi = (\rho, \theta)$, defined over a circular pupil or radius R, is given from:

$$\phi(\rho,\theta) = \sum_{j=2}^{\infty} a_m^n Z_m^n(\rho,\theta) \tag{1.24}$$

$$Z_m^n(\rho,\theta) = \rho^n cos(m\theta) \tag{1.25}$$

where a_m^n are the coefficients of the linear combination and n and m are respectively the radial order and the angular frequency.

In figure 1.12 the main terms of the decomposition are shown and the most known aberrations are identified. The term of order $n = 0$ represents the *piston*, a rigid translation which changes the wavefront phase and which is extremely important for interferometry; with $n = 1$, are defined *tip* e *tilt*, gradients of light along two orthogonal axis, with $n = 2$ the *defocus* term ($m = 0$) and *astigmatism* (m=±2); with $n = 3$ *coma* aberrations ($m = \pm 1$) and, finally, polynomial Z_0^4 the *spherical* aberration.

Zernike polynomials are used in all codes throughout the thesis to analyze or simulate wavefront aberrations on pyramid pupils.

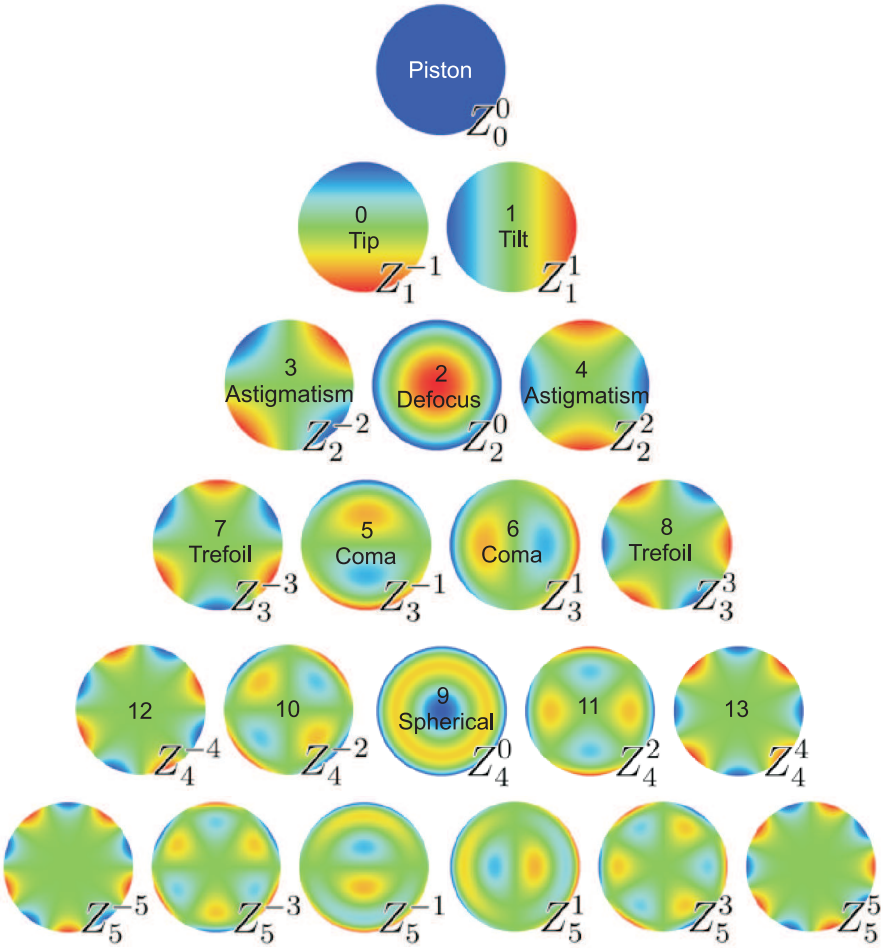

Figure 1.12: Zernike's polynomials. Each line represent a radial order, starting from 0. Main aberrations are identified. Small numbers at the center of each polynomial indicates the numbering which will be used in Chapter 2.

1.3 Adaptive optics limitations

Despite the improvement given to the imaging resolution, which allows to push the telescope resolving power to the theoretical limiting one, adaptive optics suffers some limitations. Hereafter we briefly describe the main ones, based on Hardy (1990).

Sampling errors

The optical wavefronts which passed through the atmosphere contain components on spatial scales range between a few millimiters and a few meters. The exact compensation of those wavefronts implies the use of very high spatial frequency, which in the real world is very difficult to obtain. We already mentioned that to decide in how many part to sample the wavefront is a matter of compromises between actuators of the deformable mirrors, the wavelength of correction and the photonic flux. Obviously this implies a residual error in the wavefront correction called sampling error. Its variance is given by:

$$\sigma_F^2 = \langle [W(x,y) - C(x,y)]^2 \rangle \tag{1.26}$$

where $W(x,y)$ is the turbulence wavefront and $C(x,y)$ the correlation function. For a starting turbulence with a Kolmogorov spectral distribution, the sampling error is (Beckers, 1993):

$$\sigma_F^2 \approx 0.34\,(r_e/r_0)^{5/3} \tag{1.27}$$

where r_e is the range in between the actuators.

Temporal errors

To obtain an efficient correlation, it is necessary to have the adaptive system work in real-time, in times shorter than the typical ones in which perturbations evolve on the telescope's pupil. The temporal fluctuations are caused mainly by the wind speed at different heights.

The delay between the measure and the correction of the turbulence causes an error in the correction of the order of:

$$\sigma_t^2 = \langle [W(x,t) - W(x,t+\Delta t)]^2 \rangle \tag{1.28}$$

where Δt is the time delay.

Limited isoplanatic angle

Classical adaptive optics, also defined as Single Conjugated Adaptive optics (SCAO) suffers some disadvantages which limit its applicability and its competitiveness. The whole adaptive optics system depends on the possibility to use the radiation of a reference source to quantify wavefront distortions. To obtain good results this source needs to be a point source and the measuring times need to be lower than the turbulence variation's frequency, which determines the inferior limit to the luminosity of the source, under which the low S/N ratio compromises the correction. In general, the scientific observed object is faint or extended, and for those reasons does not satisfy the conditions of reference sources and it is necessary to find a bright star in its neighborhood. However, the wavefront measured from a point-like source is similar to the one coming from the scientific object only if the two objects are angularly very close, meaning inside an isoplanatic angle (defined in section 1.1.2) from which the two objects are subject to the same phase perturbations, as shown in figure 1.13.

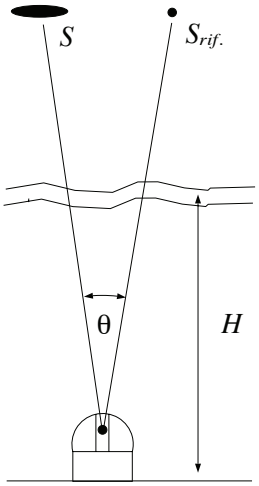

Figure 1.13: Figure shows how at the turbulence measured by the WFS on the reference source, S_{rif}, at a distance H from the ground, differs from the one of the studied object, S.

Remembering that for a single layer of turbulence the angle is $\theta_0 \approx 0.31\ r_0/H$, equation 1.14, if we consider $r_0 = 15\ cm$ at $\lambda = 0.55\ \mu m$ (visible light), and for a height $H = 10km$, we obtain an isoplanatic angle $\theta_0 \approx 3''$. Because the AO WFS can use only relatively bright stars (the limiting magnitude is of a range varying from 14 to 17 magnitudes in V-band), which are difficult to find in such a small field, this leads to a severe limitation of the *sky coverage*, meaning the sky region where it is possible to find suitable stars for the AO system, better described in the following section.

Sky coverage

The sky coverage is given by the simple counts of the possible Guide Stars (GSs), meaning those stars which can present a magnitude inferior to the one given as the limit, for a defined sky region, keeping into account the isoplanatic angle θ_0, to define the observable sky fraction. In fact, θ_0 is used to describe the degradation in the correction of an object as the distance from the GS increases. Obviously, the sky coverage will be different depending on the observability direction, since the probability of finding a star satisfying the requests changes depending on the considered galactic latitude. In particular, at the galactic poles the sky coverage will be the lowest (between 0,1% in V-band and between 0.5% in K-band), since the star number in the solid angle unit is lower than in the other directions, while it will be highest in correspondence of the galactic equator (1% V-band and 4% in K-band). This percentage, however, varies depending on many parameters, from the seeing to the telescope diameter, to θ_0, to the limiting magnitude of the WFS. In the visible the situation gets worst: in fact, not only the isoplanatic patch is smaller, but also the time in which the reference source can be integrated on the WFS detector.

These severe limitations lead on one side, to the idea of using a laser to create an artificial reference star in the direction of the observed object and, lately, to the idea of considering more reference stars and more DMs, to increase the FoV in which to find GSs, as it will be explained in the next sections.

1.4 Laser guide stars

A technologically innovative solution, has been proposed in the mid '80 (Foy and Labeyrie (1985), even though it was developed for US classified military projects US in the mid '60s), projecting on the side of a scientific object an artificial star, thanks to a laser positioned in proximity of the telescope itself or even coaxial to it, and called Laser Guide Star (LGS). At the moment two typologies are mostly used: sodium and Rayleigh LGSs. In the first case the laser ray, tuned on the Sodium doublet wavelength at λ=589 nm, covers the same atmospheric path covered by the light object, and then reaches the mesospheric sodium layer at about 90 km height and stimulates its fluorescence: in this way a monochromatic artificial source at a finite distance is created in the desired direction. In the second case the scattering of dust present at low atmospheric layers (around 20 km) is exploited. In both cases the sources re-emit light for fluorescence or for diffusion in all directions. Part of this light goes back to the telescope following the same path and is used as the reference source for the AO system. It is important to know that the LGS magnitude depends

on the laser power, which of course is proportional also to its cost. Moreover, the fact of having a source located at a finite height has some negative drawbacks:

- the turbulence on atmospheric layers above the LGS cannot be sensed;
- the wavefront of a star and of a LGS does not cross the same atmospheric turbulence. In fact, the wavefront coming from a LGS can be considered to be spherical and the region covered to reach the telescope will be therefore conical. A real star has, instead, a flat wavefront and its light covers a cylinder whose base is given by the telescope diameter. The difference between the two wavefronts generates an error on the correction called "cone effect" (Fried, 1995), and is shown in figure 1.14;
- does not allow to determine the tip-tilt because the beam in its travel forth and back from the laser source to the detector, passes through the same atmosphere portion, in a time range in which no significant variations of the mean tilt of the wavefront happen, having as a direct effect the nulling after the two paths. To solve this problem WFSs measuring tip-tilt coupled with NGSs needs to be used together with LGSs. This brings back to the original problem of NGS, the anisoplanatism;
- it has been verified Pfrommer et al. (2009) that sodium layer height varies seasonally and also during the same night, up to hundreds of meters or even kilometers, causing also a defocus problem, which needs as well to be sensed, adding the capability of sensing defocus for the NGSs WFSs. It has been recently pointed out that not only tip-tilt and defocus but orders up to Zernike mode 36 need should as well be sensed Diolaiti et al. (2012), transofrming the simple tip-tilt-defocus WFS into a more complex one;
- in the sodium case, another problem is due to the thickness of the atmospheric sodium which is crossed (about 10 km), meaning that the artificial reference is not point-like but rather a segment (problem known as "spot elongation", shown in figure 1.14. Of course this problem will be even more evident for a 40 m telescope.

In the last years many experiments on LGSs took place and the major problems are connected to the light intensity of the artificial star, the technological challenges and the reliability of high power laser systems, other than the high cost of the realization of those systems.

The use of LGSs can lead to an improvement on the sky coverage, but this happens to the detriment of the corrections, which can reduce up to 70 % unless a very high number of them is used and dedicated WFSs to sense low order modes

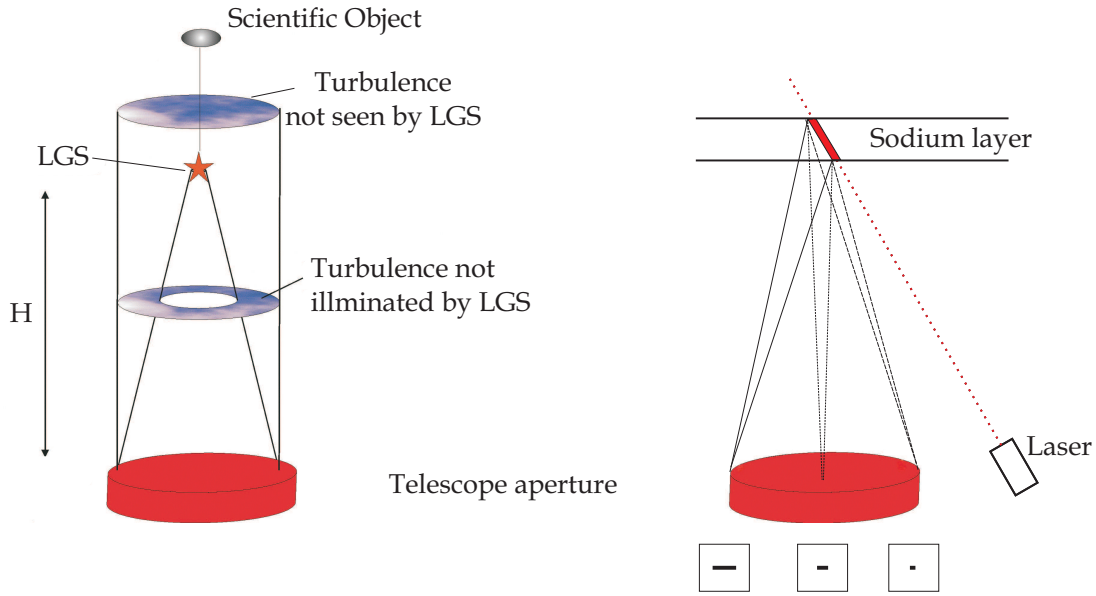

Figure 1.14: Schematic representation of the cone effect (left) and of spot elongation (right), typical of LGSs.

on NGSs are added aside. Moreover the problem of the limited FoV on which the correction can be applied is not solved by LGSs and if we want to resolve for example an extended objects, another solution is needed.

1.5 Multi-conjugated Adaptive Optics

To reduce anisoplanatism effects typical of classical AO, which do not allow wavefront correction for FoV larger than a few arcsec (about 30" in IR, a few arcsecs in the visible), Beckers (1989) introduced Multi Conjugated Adaptive Optics (MCAO). MCAO tries to reconstruct tri-dimensional turbulence shape, in order to compensate atmospheric turbulence using several DMs conjugated to different heights in order to correct the most turbulent layers. In this way, not only the conjugated layers are corrected, but also, a few others, even if the correction efficiency degrades (lower frequencies will be corrected) as the distance from the conjugated DM increases. The DM conjugation height depends on the position which allows to minimize the residual correction and does not necessarily coincide with the most turbulent layer. This technique foresees the use of more GSs to analyze the atmospheric turbulence on a larger FoV and directly on a larger atmosphere volume. In this way the PSF variation along the FoV is reduced: the observation of a single GS allows the correction of a column of atmosphere, while, using more reference objects, it is possible to measure the turbulence on a tridimensional volume. A WFS properly conjugated,

allows to reconstruct turbulence in the desired atmospheric layers. For example, a DM conjugated to the telescope entrance pupil, removes only the turbulence introduced in its proximity, corresponding to the ground layer, but not the one which originates far from the telescope.

The atmospheric distribution has been historically identified with 5 to 10 stronger layers, depending on the site, one of which is certainly the ground-layer. The number and the height of DMs depend on the observing site (in relation to C_n^2 profile) and of the correction level which needs to be reached.

The superposition of the telescope pupils projection on the high layers in the direction of the GSs is called meta-pupil and varies with respect to the conjugation height, as shown in figure 1.15.

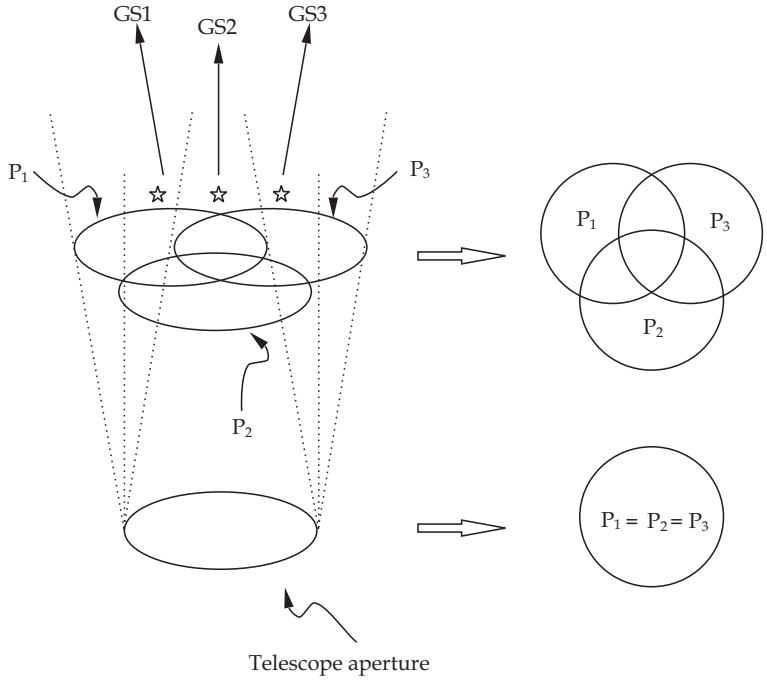

Figure 1.15: Meta-pupil representation given from the superimposition of the projection of the telescope pupil conjugated layer for 3 GSs on top, while on the bottom is shown how at the ground-layer all pupils are superimposed.

Referring to figure 1.16, if we consider a real example, LBT telescope (8.2 meter diameter) and a layer at 7 km (see chapter 2) with a FoV of 2', the meta-pupil will have a diameter of about 12.3 m. With 3 GS, assuming they are in a triangle shape, good sky coverage is shown. If we wanted to consider higher layers, more stars would be needed to cover almost completely the FoV. Of course, in the latter case, it is difficult to find 9 bright enough stars. Moreover, in reality, the distribution of NGSs is not uniform and this translates in some areas of the meta-pupil not covered. Added to the differential magnitudes between stars, this translates into a correction quality

and a Strehl ratio variable along the scientific FoV and dependent from the observed direction.

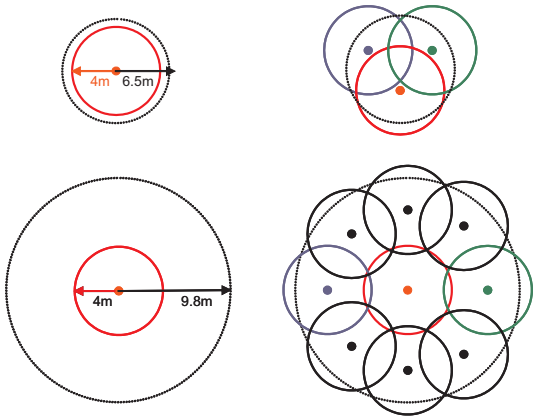

Figure 1.16: Schematic representation of the meta-pupil concept. Red line shows the telescope aperture, 8 m, the black dashed line the meta-pupil for 2 different cases: top: 10 km height and 1 ' FoV, bottom: 20 km height and 2 ' FoV. On the left is shown the GS number necessary to cover the two different FoVs, 3 GSs for the first case and 9 GSs for the latter.

Tallon and Foy (1990) introduced the tomography concept in order to divide numerically and in open-loop the turbulence at different heights, through independent measure over a defined number of stars, using classical WFSs, as SH and curvature sensors. This concept was revised as modal *tomography* (Ragazzoni et al., 1999) and experimented on sky almost immediately, even though in a preliminary way (Ragazzoni et al., 2000c). Referring to figure 1.17, two different layers are analyzed, one very close to the ground and one at high atitudes. Observing three stars at different distances from the telescope line of sight, three different wavefront deformations are retrieved. None of those could be used alone to correct distortion along the optical axis of the system, whereas the tomographic reconstruction of the perturbation, divided in layers allows to estimate the perturbed wavefront in a direction were no GSs is present. The wavefront distortion coming from the three directions is the same for the ground-layer and highly depends on the stars geometry for the higher layers.

MCAO refers essentially to the way in which DMs are introduced in the optical path, but a key role is represented, of course, by the way in which the WFSs operate and the DMs are controlled. Two possible main approaches proposed in the last years are: Star-Oriented (SO) e Layer-Oriented (LO), described in the following sections.

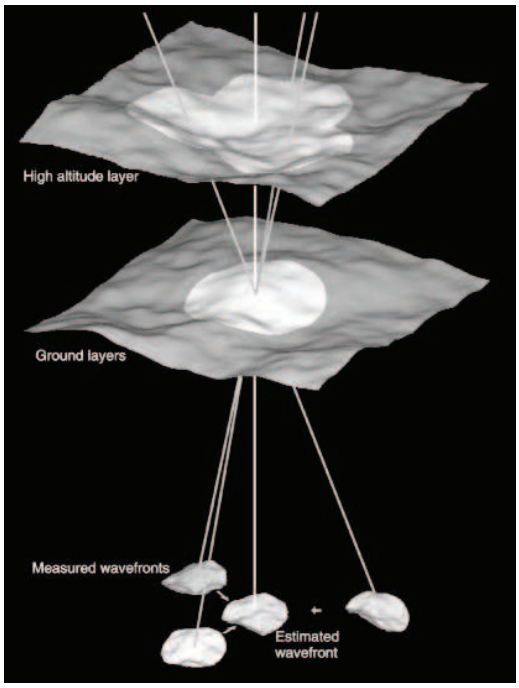

Figure 1.17: Tomographic measurement of the WFSs of 3 GS (full lines), for 2 atmospheric layers , allows estimating the wavefront for a specific direction (dashed line) where there are no GS.

1.5.1 Star Oriented

The Star Oriented technique uses a WFS for each reference star, as shown in figure 1.18. Each sensor retrieves the wavefront perturbation of each single object and analyzes the atmosphere cylinder selected by the telescope entrance pupil projection in the GS direction.

The complexity of the system is proportional to the GSs and DMs number, since the signals coming from all sensors are combined together to calculate the atmospheric turbulence correction over the entire meta-pupil. This technique is called **Global reconstruction** and has one of its bigger limitation in the complexity from a computational point of view.
Moreover, the limiting magnitude depends on each sensor and therefore the sky coverage advantage is limited to the FoV dimension.

1.5.2 Layer Oriented

In the *Layer Oriented* (Ragazzoni et al., 2000a) approach, WFSs are optically conjugated to a specific height and guide a DM conjugated to the same altitude. Each sensor takes advantage of the light coming from all the stars: in fact, through

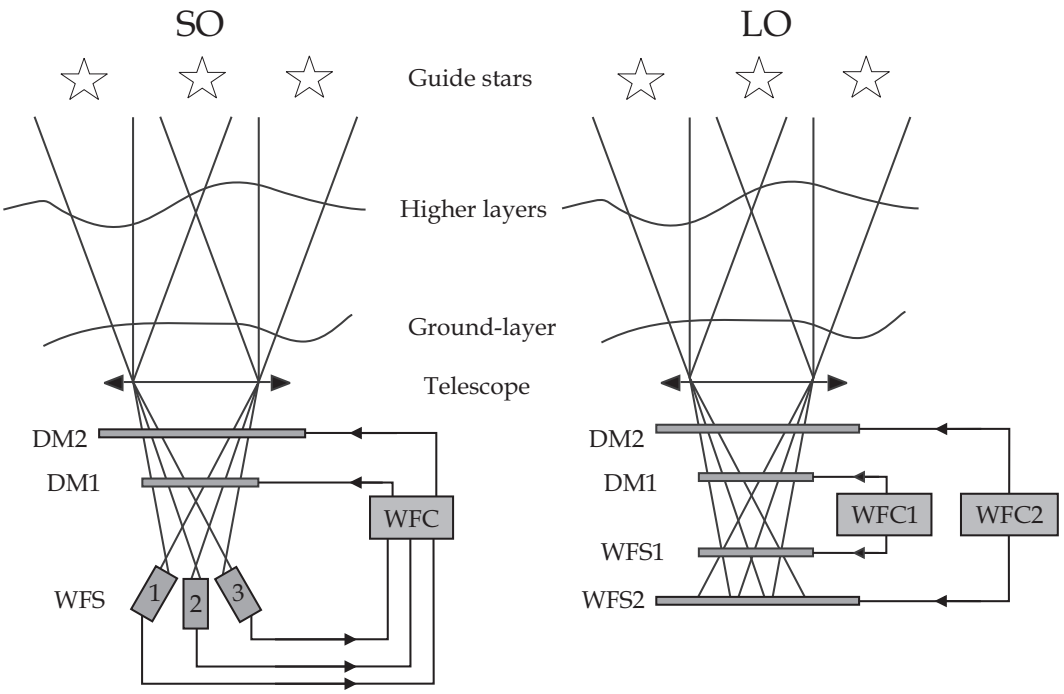

Figure 1.18: In the SO concept, one WFS is associated to each GS and a computer in real-time sends commands to DMs, taking into account all the retrieved measurements. In the LO concept, instead the WFS is conjugated to a specific height associated to a DM.

an objective, the optical superimposition of the signals is obtained. An objective projects the pupil image on a CCD which is conveniently positioned along the optical axis, in order to obtain the same pupil superimposition which takes place in the atmosphere at the conjugated layer altitude. The LO MCAO system reconstructs the phase delay introduced by the conjugated layer in an independent manner for each single layer, to which the DM is conjugated,and the correction applied to DMs is calculated using entirely signals of the corresponding sensor. This technique is called **Local Reconstruction**.

The LO method allows to implement in parallel correction cycles of different atmospheric layers and it is possible, then, to vary the spatial and temporal sampling which optimizes the correction for each sensor, depending on r_0 and τ_0 estimated at each altitude (r_0 is usually higher for the higher layers while the wind speeds is lower in the lower ones, allowing a longer integration time for the latter).

The superimposition of light in LO is optical and not numerical, with the advantage of increasing the limiting magnitude on the single GS. In fact, the limiting magnitude is given by the integral of the reference star magnitudes (integrated magnitude). In this way even stars that are dimmer than the ones usable in SCAO systems can be used.

Another important characteristic is the fact that LO technique allows in its configuration an easy use of pupil sensors, and, in particular, of the PWFS, which determines a gain in magnitude with respect to other sensors as already said. A small disadvantage of this method is that to be able to detect all 4 pupils on the detector, the CCD size, especially for higher layers, needs to be bigger than the one which could be used for a WFS SO. Furthermore, it is necessary to split the light between sensors conjugated at different altitudes. This can be done easily using a beam-splitter. It is clear, though, that this solution has a direct negative consequence: the need of using lower magnitude or a higher number of stars. A smart solution is the Multiple FoV concept described in the next section.

1.5.3 Multiple Field of View concept

Multiple Field of View (MFoV) Layer Oriented concept (Ragazzoni et al., 2002) is an extension of the previously described technique LO, but every sensor looks at a different FoV. In particular, a larger FoV will be used for the ground-layer conjugated WFS.
This concept is based on the fact that the telescope entrance pupil superimposition on the WFS decreases as the FoV increases and as the altitude increases. When the FoV tends to infinity, an angle is defined $\theta_\gamma = D/h$ (with D telescope diameter and h conjugation height), which indicates the limit above which the meta-pupil superimposition is so poor that no advantage to the photonic density is given.
For a height h close to zero (ground-layer) the angle θ_γ does not have theoretical limits, the pupils superposition is total and even stars angularly far from the scientific objects can be used to increase photons density. For the higher layers it is important to choose stars angularly close to the scientific object, in order to have good sky coverage of the meta-pupil. The higher layers, therefore, determine the sky coverage. In this case, though, r_0 is bigger for the ground layers and since the photonic gain is $\propto r_0^3$, this technique allows taking advantage of the independence of the sensors in the closed-loop in the spatial-temporal sampling to increase the S/N and subsequently the integrated magnitude.

Let us consider the specific case of LINC-NIRVANA. For a telescope of diameter size about 8 m, an inner 2' FoV is chosen to look for NGSs for the higher layers (around 7 km), thanks to the Mid-High Wavefront Sensor (MHWS) and an annular FoV (with internal diameter of 2' and external of 6') for the ground-layer, thanks to the Ground-layer Wavefront Sensor (GWS). In this way it is not necessary to separate the light of single stars on the two sensors and when comparing to the classical LO, a gain in terms of photons of a factor 2 is obtained. The atmosphere corrected thickness in the GWS case is lower than in the MHWS case because the FoV

in the first case is bigger. This means that the planes conjugated to the turbulent layers, even if very close, appear very defocused and are therefore observed with difficulties. In the MHWS the situation reverts because the FoV is smaller, while the corrected thickness is bigger. This new technique allows increasing the sky coverage using solely NGSs, reaching about 20% at galactic poles and more than 90% at the equator (Arcidiacono et al., 2004), and to be competitive with LGSs also in terms of sky coverage.

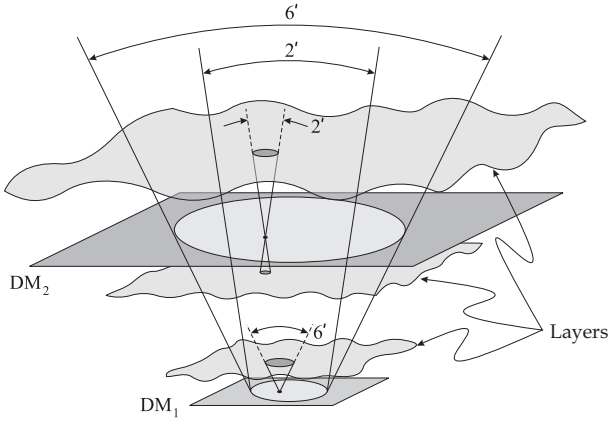

Figure 1.19: Multiple FoV LO MCAO concept. 2 DMs are shown, one conjugated to the ground-layer, which has a FoV in an annulus of 2-6' in diameter, and one conjugated to higher layers, where FoV is 2'.

1.6 Ground-layer Adaptive Optics

Ground-layer correction was first suggested by Rigaut (2002), to compensate wavefront distortion in a FoV up to 10 arcmin. This AO concept, named Ground-Layer Adaptive Optics (GLAO), does not aim to diffraction-limited correction, but, rather, to a seeing improvement on a large FoV. Being the existence of a very turbulent layer very close to the ground known, even in the sites considered to have the best seeing, Rigaut proposed to implement tomography in a concept very similar to MCAO, but using only one DM conjugated to the ground. The area uniformly corrected turns out to be very wide, since the layer close to the telescope distorts in the same way wavefronts coming from different directions and we could ideally correct an infinite FoV, removing completely this layer and virtually increasing r_0. With an infinite FoV, though, the corrected FoV would reduce to an infinitesimal layer and layers even very close to the conjugated one, would not be corrected. It is therefore important to find a compromise between the dimension of the FoV to be corrected and the correction we aim to reach, considering that the highest turbulence layer is located between a few tenths and a few hundreds of meters, depending on

the observing site.
The approximation of a single atmospheric layer is given from $2r_0/\theta$, where θ is the FoV diameter. If we consider a 6 arcmin FoV, as the GWs of NIRVANA, and a good seeing, of around 0.5" in the visible (and $r_0 \approx 20$ cm in the visible and $r_0 \approx$90 cm in K-band), the useful correction will be obtained in the visible for a layer of about 200 m and in K-band for about 1000 m.

In the last few years, various studies in various astronomical sites demonstrated that the strongest contribution to the atmospheric turbulence comes from the lower layers. Studies in Paranal with MASS and DIMM instruments on the C_n^2 profile, showed that the lower layers contribute at least for the 60% of total turbulence and that 40% of it is located in the first 200 m, confirming the potential of GLAO in the improvement of the image quality.

From a Mauna Kea (Hawaii) campaign (Chun et al., 2009), we can see that the optical turbulence is limited inside a thin layer (up to about 80 m) and that, instead, the turbulence between 80 m and 650 m is generally very low.

The site showing without any doubts the greater advantages for GLAO is Antarctica (Travouillon et al., 2004). This website shows a 1.78" seeing, which is very high if compared to the other sites previously described, where it usually varies form 0.4" to 0.9". However, the 96 % of its turbulence is located in the first 220 m, therefore it is possible to have an almost total correction thanks to GLAO.
In figure 1.20 it is possible to observe that ground-layer seeing contribution is higher than the higher layers contribution.

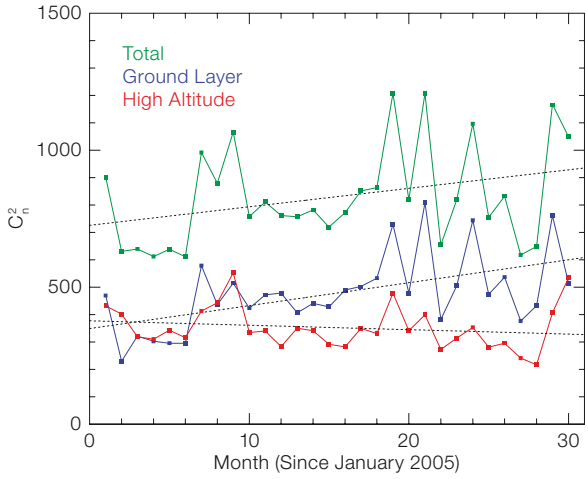

Figure 1.20: This figure shows ground-layer seeing contribution (blue), the higher layers one (red) and the total seeing (green).

Many simulations demonstrate how important is GLAO correction in seeing improvement. As we infer from Hubin et al. (2005), generally, the gain using a GLAO

system is higher in the case of a worst seeing, because in this condition ground-layer turbulence is higher. From these results it was inferred that a GLAO system is not only a seeing reducer, but also a seeing stabilizer, meaning that it increases the probability of having a good seeing and, therefore, guarantees a better PSF stability for observations made in different moments.
Andersen et al. (2006) from simulations in R, J, H, K bands for various atmosphere models, underline how the correction gets better as the ground-layer increases. This means that the best seeing conditions (which in the absence of an AO system will spontaneously take place 20% of the time), with GLAO will happen for 60-80% of the time. Moreover, they simulated a perfect GLAO system, obtaining a 0.28" seeing in J-band, to be compared with the 0.56" measured in the absence of AO.

In Rigaut (2002) the medium FWHM, obtained using GLAO is 0.2" in K, translating into a gain of about a factor 2 with respect to FWHM defined by seeing. This translates in a gain of a factor 4 in the light concentration and therefore on the exposure time of background-limited images. Moreover, it would make possible to gain 0.75 magnitudes in sensitivity, corresponding to the magnitude reached with a telescope with a diameter doubled, for a constant seeing.

From studies by Le Louarn and Hubin (2006), looking at figure 1.21, we can observe how the FWHM of the PF is improved using GLAO by a factor of about 2 in K-band (2.2 μm), going from 0.44" to 0.25", and of about 1.5 in Y-band (1 μm), going from 0.6" to 0.46", and is about constant getting further of some arcmins from the FoV center.

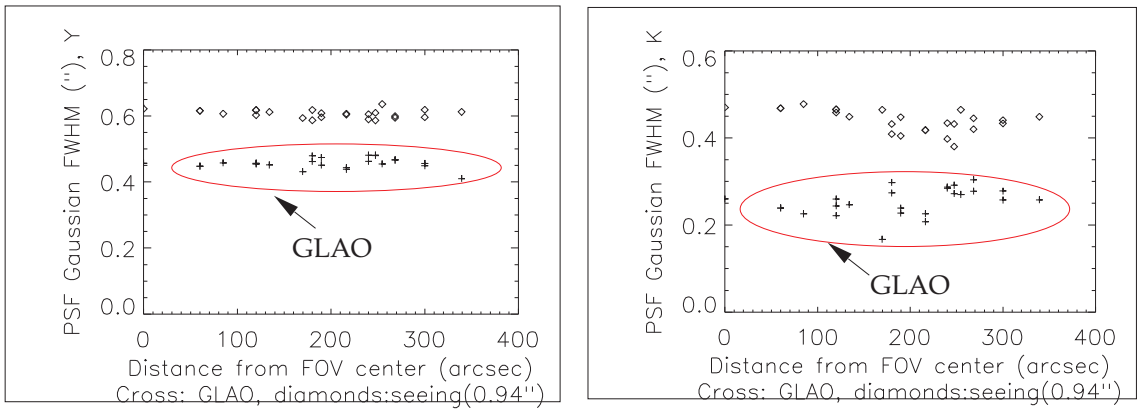

Figure 1.21: Comparison of PSF's FWHM with and without GLAO correction. In Y-band (left), seeing is reduced from 0.6" to 0.46", and in K-band (right), from 0.44" to 0.25" .(Le Louarn and Hubin, 2006)

For what concerns the choice between LGSs and NGSs, the first ones have been preferred for most of the projects, because the cone effect at the considered heights, is negligible and they allow larger sky coverage at every galactic latitude. Another

characteristic of GLAO systems is to angularly separate the scientific corrected FoV from the one necessary for AO, operation easily obtained positioning LGSs wherever it is more useful for observations. However, we remind that NGSs introduce less dishomogeneities to the PSF in the region where they are located and that with GLAO there is the possibility to exploit a much larger FoV in which it is possible to look for the brightest NGSs. This is particularly important for observations at high galactic latitudes where the sky coverage is very low. Moreover, thanks to pyramid WFS in LO mode with optical co-add of the light, , it is possible to exploit also dimmer stars to increase SNR.

From simulations by Andersen et al. (2006) it is possible to deduce that GLAO performances depend on a high number of factors, as the corrected FoV, the density actuators on the DM, the conjugation height of DM, the type and geometry of LGSs. For example, increasing the FoV, the correction decreases because we consider a thinner layer and, therefore, in reality, turbulence of the higher layers degrades the image. Anyhow, it is a modest decrease, of about 18% for an increase of the FoV of about 6 times.

Moreover, from studies realized on the conjugation height for GEMINI, by Andersen et al. (2006), it was obtained that the best conjugation height for all atmospheric models was ≈100 m, but that a conjugation height differing of ≈200 m would lead to a low decrease, of about 5% of the FWHM.
Finally, GLAO is complementary to all others AO techniques and can improve the image quality in the visible even in conditions of bad seeing, in which most of the AO systems become unusable. Most of GLAO system in study or in project phase, foresee the use of an adaptive secondary mirror which would allow to extend the AO correction, even partial, to all instruments of the telescope.

In the GWS of LINC-NIRVANA, an annular 2-6' FoV will be available to find up to 12 NGSs, whose light will be optically co-added through LO technique. This concept, other than being simulated it was tested through a lab experiment (Egner et al., 2007) using four NGSs in closed-loop. Furthermore, it was proved on-sky thanks to the Multi-Conjugate Adaptive Optics Demonstrator (MAD) on VLT, with a FoV of 2' (Arcidiacono, 2007). Observing the globular cluster 47-Tucanae, with 4 NGSs distributed along the FoV, an improvement on the FWHM in IR was obtained, going from 0.43" in open-loop to 0.26" in closed-loop, as shown in 1.22. Just to have a comparison, in the observation of the same cluster in the same conditions with MCAO, the gain is of a factor 2.5, going from 0.4" in open loop to about 0.16" in closed loop.

The science case for GLAO is very broad and general. To a first approximation all observations that are presently made in natural seeing will benefit from GLAO as it produces "improved" seeing, particularly at red and infrared wavelengths. As stated

by McCarthy (2010) some science programs are naturally better suited to GLAO. Applications that target objects with sizes near 200 mas and high sky densities potentially gain the most from GLAO, as do science questions that require large statistical samples where the multiplexing potential on 10 arcminute scales is high. Proposed scientific applications range from studies of the formation and evolution of galaxies, stellar populations in the Milky Way and nearby galaxies, proper motion studies in the local group, star formation studies and time critical observations of transient targets, stellar populations in crowded regions, IFU observations of galaxies at intermediate redshifts and multi-object spectroscopic surveys of galaxies at z 2 and at the epoch of reionization.

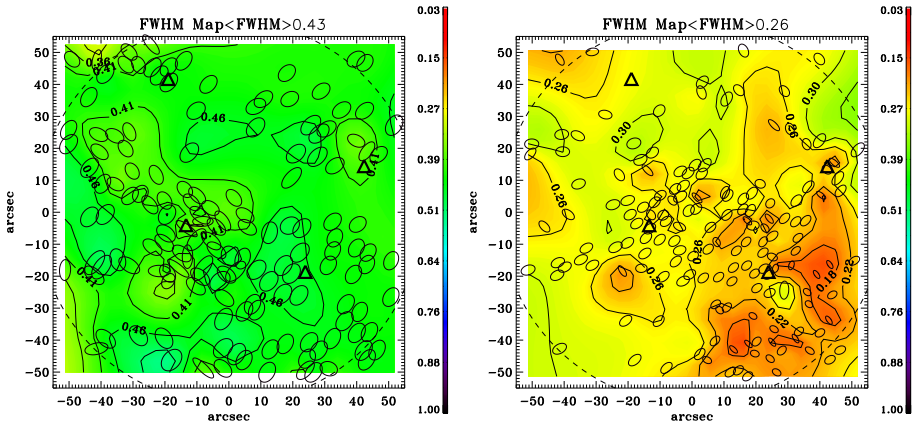

Figure 1.22: Variation of FWHM in open-loop 0.46"(left) and in *closed-loop* 0.23" (right). The four triangles indicate the NGSs. The correction was done in narrow band, Bracket Gamma (2.166μm) (Arcidiacono, 2007).

1.7 Comparison between SCAO, GLAO and MCAO

In this section we want to briefly compare the three AO typologies described so far, evaluating mainly the PSF behavior as a consequence of the applied corrections. The image of a point source produced by a circular aperture, is made of two main components: a central peak and a halo. In a diffraction-limited image, the central peak has a FWHM of 1.22 λ/D, as already seen in section 1.1.2, which contains about 84% of light, and which is surrounded by diffraction rings. On the other side, an image obtained without any compensation, presents a number of speckles of about $(D/r_0)^2$, quickly moving around. For exposure times higher than a fraction of second, the speckles become a unique luminous spot and no more central peak will be observed.

When turbulence is compensated by AO correction, part of the energy is transferred from halo to peak, varying depending on the correction type. For GLAO a larger

halo and a less definite peak, while for SCAO a higher concentration in the peak, as can be observed in figure 1.23. The total correction in SCAO becomes difficult. We remind that, for sources further than an isoplanatic angle from the GS, the image degrades quickly. This is the main reason why MCAO is used to try to have a good resolution up to 1-2 arcmin FoV on a 8 meter telescope while GLAO to obtain a partial correction but on a 3-10 arcmin FoV.

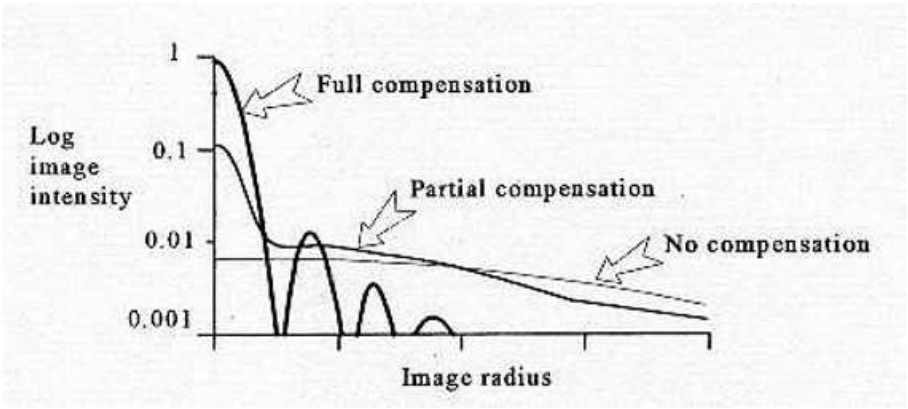

Figure 1.23: Effects on the partial and total compensation on the PSF (Hardy, 1998).

In figure 1.24 is shown a comparison between SCAO, GLAO and MCAO obtained with MAD at VLT observing globular cluster Omega Centauri in K-band (Marchetti et al., 2007), with an initial non-corrected seeing of 0.7". This cluster offers many bright NGSs. 3 NGSs with magnitude in V-band of about 12.5 and distributed on a circle of about 100" in diameter have been selected. In this way it is possible to map the correction obtained along the FoV in order to obtain a map of the correction along the scientific camera FoV, corresponding to 2'. In SCAO mode it is possible to observe a high Strehl value (40%), but a corrected field of about 20". For MCAO an optimal correction is achieved inside the polygon defined by NGSs, higher on the NGSs (Strehl 40%), uniform enough in the center and rapidly decreasing on the edges: therefore the corrected FoV is of the order of 2', corresponding to the scientific FoV. For GLAO, instead, the correction is opposite, the maximum is present in the FoV center and the correction is lower than for MCAO, even if it is more uniform along the entire FoV. The average Strehl obtained during different observations, varies from 15 and 20%.
Finally, the different angular resolution of the 3 systems deserves a comparison. The first one allows obtaining a resolution comparable with the telescope resolution, which, for a telescope of 8 m as VLT, in K-band is about 0.05". The resolution obtained with MCAO, with the configuration previously described, is about 0.1", while GLAO is about 0.3" (Marchetti et al., 2007).

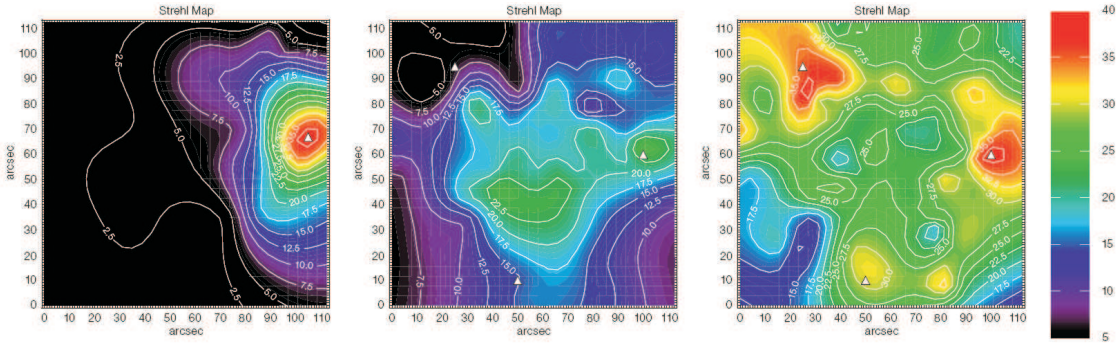

Figure 1.24: A typical example of correction for a FoV of 2'in K-band. Strehl maps going from left to right are related to 3 different corrections: SCAO, GLAO, and MCAO. In the first case the corrected field is 20". For GLAO SR reaches the maximum in the center and is low but uniform. For MCAO Strehl is greater, with peaks of the guide stars (Marchetti et al., 2007).

1.8 Multi-Object Adaptive Optics

The AO techniques seen so far allow obtaining excellent resolution on small FoVs (a few tenths arcsec) with SCAO, or uniform good correction on a larger FoVs (about 2') with MCAO, or modest correction but on a very large FoV with GLAO (about 6'). However many times astronomers need to look at many small objects (a few arcsecs) simultaneously with improved resolution, and to select them over a wide field of view (larger than 5'). It is required for example for key surveys of the first stars, and to determine the assembly mechanism of galaxies. It can also be used for detailed studies of more recent stellar populations in external galaxies and to other surveys investigation.

Multi-Conjugated Adaptive Optics has been proposed for the first time by Hammer et al. (2002) and aims to correct locally only small areas of interest distributed on a large FoV. The whole turbulent volume above the telescope is determined and individual lines of sight toward astronomical targets are projected through this volume by the control system, and the resulting corrections fed to an independent SCAO system (which includes a small DMs), for each scientific target. As remarked by Myers (2010), differently than for the most used AO techniques, the correction for these mirrors must be applied in an open-loop fashion, meaning that the DMs correct only a small region, and the WFS sees the non-corrected turbulence, needing therefore a WFS with high dynamic range. In fact, it is not possible to relay the light from the guide stars to each correction channel without each relay being of excessive size due to the very large field of view required.

A closed-loop system has the advantage that errors in the achieved DM positions, and some other static and dynamic errors in the optical system, are sensed by the

wavefront sensor and automatically corrected. In open-loop, instead, there is always the potential for non-common path aberrations which must be pre-calibrated and kept as much constant as possible. In the case of open-loop control the control requirements on the DM therefore become more stringent and there are additional requirements for general opto-mechanical stability and/or auxiliary sensing. The implications of open-loop control extend to the area of control system calibrations. Most conventional closed loop AO systems achieve this calibration by observing the wavefront sensor response to DM commands. This provides a DM-WFS interaction matrix, which may then be pseudo-inverted, with some refinement, to produce a control matrix. This is not possible in an open-loop system, where the WFS does not see the DM. A partially-related problem is the calibration of the tomographic reconstruction system, in which WFS information from various points in the field of view must be combined to produce a vertically resolved measurement of the turbulence above the telescope. Projections through this volume are then made along the scientific lines of sight and applied to the DMs. The potential advantages of open-loop control include the elimination of the feedback control system and its corresponding reduction in gain and hence dynamic response. The narrow fields of MOAO also permit the use of much smaller DMs with compact relays as described above. All he above discussed issues on open-loop, discussed also by Basden et al. (2012) andRousset et al. (2010) apply to the concept of Global MCAO which is presented in Chapter 4.

Because of the novelty of MOAO in terms of open loop control, high accuracy tomography and calibration required, several laboratory and on-sky demonstrator projects have been implemented. Between those I spend a few words on the CANARY demonstrator (Gendron et al., 2011), an on-sky LGS MOAO pathfinder for the EAGLE MOAO for the E-ELT (Cuby et al., 2010) instrument, installed at the William Herschel Telescope, which is going to investigate the LGS tomography and calibration problems. The first, NGSs only, variant of CANARY has been successfully demonstrated on-sky demonstrator, using in open loop three WFSs on three widely off-axis NGSs to compute by tomography the atmospheric turbulence real-time compensation delivered in open loop by the DM to the on-axis target. In figure 1.25 are shown the SR measure by a SCAO a GLAO and a MOAO system. The next steps in MOAO development will include the validation of proposed technical improvements, such as combining laser guide star information from different altitudes to enhance correction at shorter wavelengths.

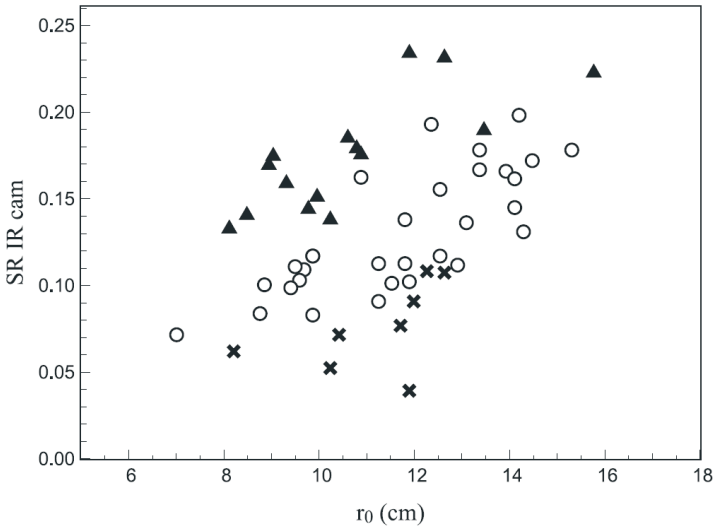

Figure 1.25: Strehl ratios in H-band vs. $r_0(0.5\ \mu\text{m})$ measured by the off-axis WFSs simultaneously with the IR images. SCAO = Δ, MOAO = $\circ$, GLAO= $\times$ (Gendron et al., 2011).

Chapter 2

WATERFALL Wavefront Sensor for human eye applications

The WATERFALL project was developed in the framework of a collaboration between research institutes and industry, for a technological and knowledge transfer, supported by the Italian Ministry of University and Research (MIUR). This projects connects two different realities, the astronomical world represented by the Astronomical Observatory of Padova (INAF) and an opthalmology company, SIFI S.r.L. It aims to transfer AO knowledge coming from astronomy to the vision science. In this specific case the pyramid wavefront sensors, generally used to analyze the aberrated wavefronts coming from reference objects in the sky, will be used to performed the analysis of Intra-Ocular Lenses (IOLs) which are used during cataract surgery operations to replace an opaque crystalline lens.
The first aim of this project is the definition of a prototype for an instrument to determine IOLs dioptric power with a precision of ± 0.125 diopters (inverse of focal length) and to analyze their wavefront up to the first few Zernike modes with a best effort requirement. This prototype has to be developed considering its future use in industries and therefore be compact, economic, made with off-the shelf component and requiring the less possible human interaction, trying to devise an as much as possible automatized procedure around it for a fast and cheap high quality tests of intra-ocular lenses.
The design, characterization and tests on this prototype are described in this chapter.

2.1 Adaptive optics for vision science

From the mid 90s scientists working on vision science have taken advantage of the AO technology developed for astronomy for a more accurate study of the human visual system (Liang et al., 1994). In fact, the eye is an optical system and even it

works greatly to allow us to look outside (thanks to the brain that convert light into electro-chemical impulses), its aberrations make it difficult to observe from outside in, reducing contrast and resolution, for example to look at the retina and try to observe retinal diseases for an early diagnosis. With the use of AO it is now routinely possible to compensate for these ocular aberrations and image cellular level structures with adequate resolution. In figure 2.1 is shown an AO system to observe retinal images. Essentially it is provided with the same components of an astronomical AO system. Even similarly to the LGSs, a laser (with a specific wavelength not to procure damages to the eye) is shined into the eye and the reflected light is analyzed to correct for wavefront distortion caused by the eye.

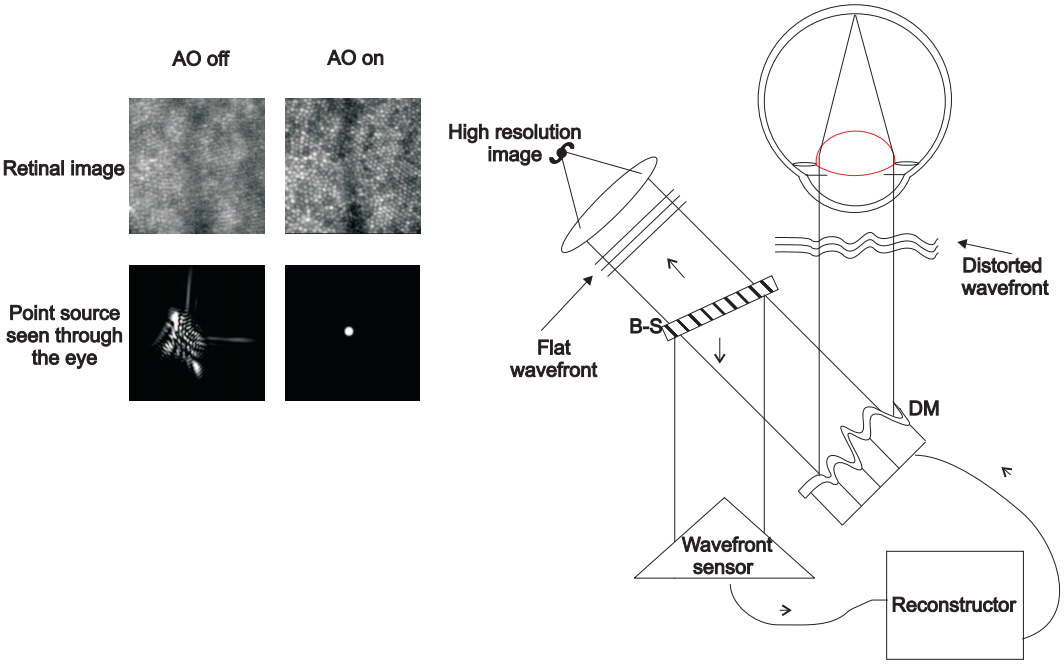

Figure 2.1: AO vision science works essentially in the same manner of astronomical AO. It is used to achieve high resolution to observe diseases. In the picture is shown how the retinal image looks with and without AO and how a point source is aberrated by the eye.)

The eye main optical contributions come from the cornea and the crystalline, highlighted in figure 2.2. This last one is naturally adapts to see far or close objects, but with age this property is reduced and furthermore the crystalline lens becomes opaque due to a disease named cataract. To restore satisfactory visual ability, starting from Dr. Harold Ridley in 1947, operations to replace the crystalline lens with an artificial one (called Intra-Ocular Lenses) have been performed. Nowadays they are considered routine operations since they can be performed in few minutes. Once in place, this lens remains fixed within the eye with no need to be cleaned or replaced.

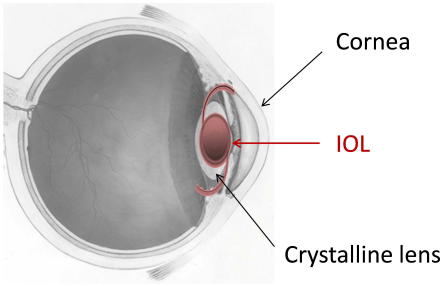

Figure 2.2: The eye with its main optical component, the cornea and the crystalline lens. The latter during cataract surgical operation i replaced by an IOL (the red color is just for illustrative purpose but the IOL real color is transparent.)

Lenses are chosen through a pre-operative examination providing only indications regarding size and dioptric power, and disregarding the physical and functional characteristics of the crystalline lens, which differ from individual to individual. In this operations eye problems could resolved with a proper eye characterization, but to perform this operation it would be important to distinguish the contribution between cornea and crystalline. And this could be done in a similar way to MCAO. However, this is not the purpose of the prototype which will be discussed in this chapter, but eventually a step further on. In fact if it is possible to know with high accuracy which lens we want to insert in the patient eye, we need firstof all to measure with the same accuracy the lens we want to surgically implant.

2.2 Prototype Concept

The objective of the prototype which has been designed realized, aligned and tested in daptive Optics laboratory of the Astronomical Observatory of Padova is to measure the dioptric power of the IOL with an accuracy of the order $\pm$ 0.125 diopters and to analyze the low order aberrations (up to 13 Zernike polynomials). The accuracy needed to measure this other aberrations had not been specified, it is considered a best effort one.
This prototype study has to be done in the view of a commercialization of the proposed instrument, therefore important characteristics are the use of off-the shelf components, a reasonable price, compactness, devise an automatized procedure, reducing at most an operator intervention and making it a user-friendly instrument. The key component of this prototype is a pyramid WFS. The basic concept behind the prototype is essentially to illuminate the IOL with a white-light collimated beam and to analyze the transmitted wavefront with a pyramid WFS.

2.3 Prototype Design

The real design of the prototype was driven by the necessity to minimize time and cost of the prototype realization (in the view of the future industrial commercialization of the instrument) and, therefore, commercial off-the-shelf optical components have been used. Various factors, some of which were discovered during the setup characterization, forced us to change components or to modify the design.
Technical constraints were driven by the fact that IOLs need to be always conserved in a physiological saline solution to maintain their optical properties, mainly related to their elasticity. One of the immediate consequences was the realization of a proper holder for the IOL itself, which could be filled with liquid and would introduce minimum aberrations. To avoid the distortion of the wavefront, the surfaces of the holder are flat (not to introduce any optical power) and have a good optical quality. The holder is positioned in a horizontal configuration. In this way, thanks to the gravity, the IOL always lays on the bottom window internal surface and therefore a reference plane is defined.
Unlike a regular lens, it is not possible to position the IOL with enough accuracy inside its holder and so, for a precise characterization, the WFS needs to be aligned to the IOL. For this reason it was mouted on a 3-axis very precise motorized linear stage, to minimize the relative de-centering between IOL and WFS and to allow a proper focus positioning, which is obviously connected to the IOL focal length. The motorized stages allow also a future automatization of the system. Finally, the available pyramid vertex angle imposed the introduction of a Star Enlarger system (see section 3.3.xx) between the IOL and the WFS, to increase the spot diameter on the pin of the pyramid in order to decrease the pupils dimension on the detector (to avoid the pupils overlapping on the CCD) for the complete range of IOLs diopters.

2.4 Setup

The whole lab setup for the experiment, shown in 2.3 and 2.4 is composed of:

- a HeNe laser used as a tool for relative alignment of the optical components, in terms of centering and tip-tilt;
- the source S (positioned after the laser) the laser an optical fiber fed with white light, mounted on a kinematic magnetic base-plate, to be easily removable and accurately repositionable, whenever an alignment check with the laser beam is required;
- a lens, named L1, collimating the optical beam coming from the source, before illuminating the IOL;

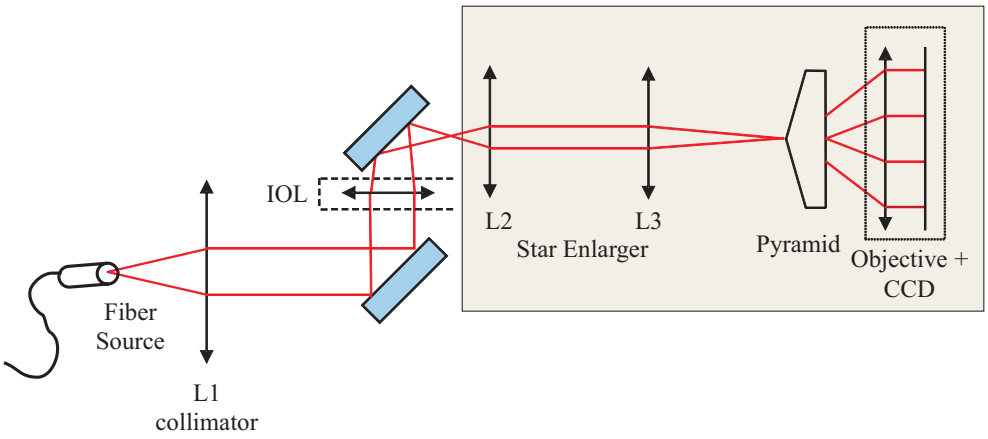

Figure 2.3: Optical setup used for IOLs tests. A fiber source is collimated by lens L1 and is focused by the IOL on the pyramid vertex (the beam is previously enlarged by a system named Star Enlarger) and the four beams are re-imaged on a CCD thanks to an objective. To have a reliable reference plane, the IOL is positioned horizontally inside its holder (for this reason two folding flat mirrors are inserted in the path). All components represented inside the grey area are mounted on a x-y-z motorized linear stage, which allows the relative centering and focusing between the pyramid vertex and the IOL focal plane.

- the IOL, inserted in its holder and immersed into the physiological solution to maintain its flexibility, positioned horizontally in an area in which the optical axis is vertically folded by a flat mirror (during tests glass lenses can be positioned in the path instead of the IOL);

- the pyramid WFS, whose position is remotely adjustable in order to have the IOL focal plane on the vertex of the pyramid. A Star Enlarger, positioned in front of it (composed by lenses L2 and L3), increases the spot dimension on the pin of the pyramid.

- a commercial photographic objective (moving integrally with the pyramis) re-images the four beams coming from the pyramid onto the detector (CCD), which is the last component of the prototype.

In table 2.1 are summarized the main optical characteristics of the commercial components used to realize the optical setup, shown in 2.4.

The realized IOL holder, shown in figure 2.5, is composed of two $\lambda/4$ quality optical windows (2mm thickness), separated by a rigid rubber shim, which at the same time keeps them at a fixed relative distance of 2 mm and avoids any liquid leakage. On one side of the rubber shim the two surfaces are glued with a silicon glue to avoid liquid spillage, while on the other side, open to the air, it is possible to fill the holder with the physiological solution and insert the IOL. The surface tension

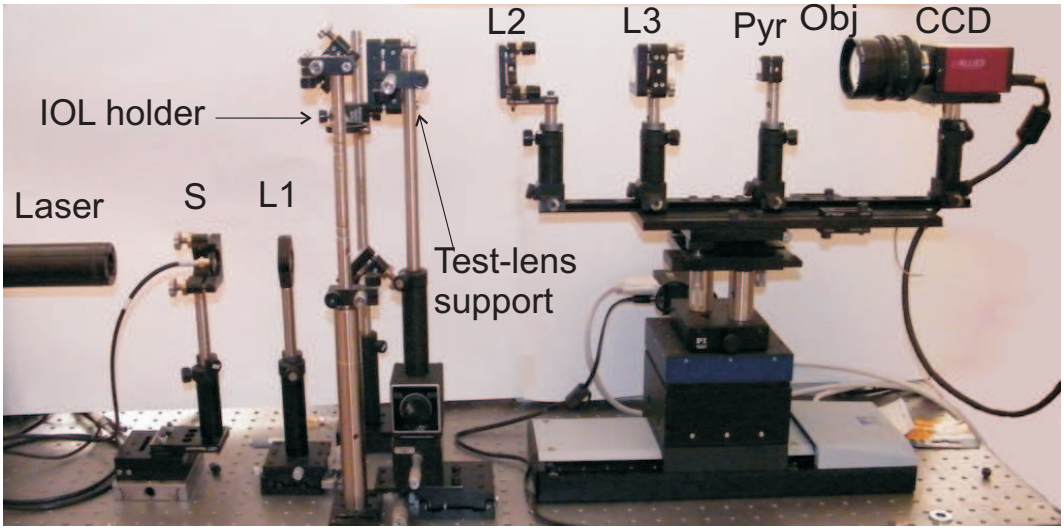

Figure 2.4: Prototype optical setup used alternatively for IOLs and laboratory lenses.

	Component	Characteristics
S	Source: optical fiber	core = 200 μm
L1	Collimating lens	f_{L1}= 76 mm
IOL	Intra-Ocular Lens	$f_{IOL} = 30 - 200mm$
L2	SE lens 1	f_{L2}= 9 mm
L3	SE lens 2	f_{L3}=125 mm
Pyramid	Refractive pyramid	Vertex angle $\alpha \approx 1°$
Obj	Objective	f_{obj}= 75mm
CCD	CCD AVT Pike F-145B	1388x1038 pixels, pixelsize = 6.45 μm

Table 2.1: Main characteristics of the commercial components used for the prototype optical setup.

on this side is enough to keep the liquid inside the holder when it is positioned horizontally.

Enlargement

The spot diameter on the pin of the pyramid ($S_{pyramid}$), once the parameters in table 2.2 are fixed, depends on the focal length of the IOL to be tested and is obtained from the following equation:

$$S_{pyramid} = S \cdot \frac{f_{IOL}}{f_{L1}} \cdot \frac{f_{L3}}{f_{L2}}$$

where $\frac{f_{L3}}{f_{L2}}$ is the SE enlarging factor and is equal to 13.9.

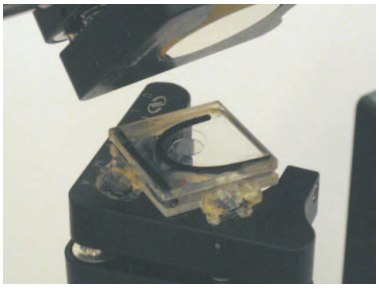

Figure 2.5: IOL holder (composed of two $\lambda/4$ optical windows), which allows to conserve the IOL in a saline physiological solution.

	MIN	**MAX**
f_{IOL}	30 mm (33 diopters)	200 mm (5 diopters)
$S_{pyramid}$	1.10 mm	7.32 mm

Table 2.2: IOL focal range and related spot enlargement on the pyramid vertex.

Mothorized linear stages

In table 2.3 are listed the main characteristics of the *Physics Instrument* motorized linear stages used to align the WFS to the IOL. Each stage has an internal reference (defined by Hall effect) corresponding to the zero value of the encoder. While the stages resolution is given by design, the positioning repeatability has been estimated through a statistic analysis based on 10 determinations for each stage (it is reported in the last column of table 2.3. The z stage has a range shorter than the total range of focal to be tested (102 vs 170 mm). It has been integrated in the system in an intermediate position, to allow analyzing and comparing IOLs with focal lengths between 48 and 150 mm.

Axis	**Linear stage**	**Travel range (mm)**	**Design resolution (μm/step)**	**Positioning precision**
z	M-511DG	102	0.033	1.15 mm
y	M-501DG	12.5	0.0056	2.33 mm
x	M-126.PD1	25	0.125	3.62 mm

Table 2.3: WFS *Physics Instrument* motorized linear steges main characteristics.

2.5 Prototype Characterization

The main steps of the demonstrator characterization are:

- analysis of the sensor linearity ranges in tip, tilt and defocus;

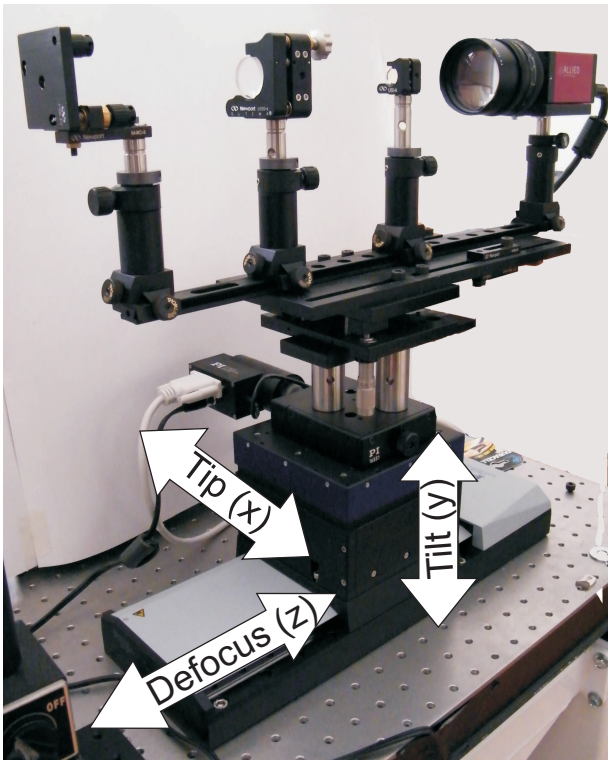

Figure 2.6: WFS mounted on a mechanic mount which allows the movement in the depicted x,y,z direction thanks to 3 motorized linear stages.

- optimization of the phase concerning the alignment of the pyramid with respect to the lens, whose position in the x-y plane is extremely variable, since it is immersed in a liquid. Decentering and defocus of the pyramid with respect to the lens have to be measured and minimized;

- accurate measurement of the static aberrations introduced by the setup: once they have been characterized, it is possible to infer whether they can be ignored or they have a consistent impact on the wavefront analysis and it is therefore needed to subtract them. IOL's holder has been also studied;

- wavefront repeatability measures.

In various phases of the system characterization, laboratory BK7 achromatic doublets with a diameter of 50.8 mm (hereafter defined *lab lenses*) have been used. They were needed both to verify the functionality of the system for the case of a traditional lens (avoiding initially possible unknown issues) and to have a complete set of focal lengths in the range allowed by the z stage.

2.6 Tip, tilt and focus WFS linearity range

2.6.1 Relationship between Zernike defocus coefficient and diopters

We remind that the first target of this prototype is to measure the dioptric power of the lens under test.
The first test we performed is aimed to retrieve the IOL focal plane position measuring its defocus term through the Zernike polynomial decomposition (described in section 1.2.3). The IOL focal plane position f_{IOL} is expressed in mm as the distance from a reference position of the focusing stage. Defining z_{WFS} the position of the linear focusing stage along the z axis and $c_{defocus}$ the retrieved Zernike defocus coefficient, the main steps for the procedure (for each IOL or *lab lens* are:

- take a set of measurements of z_{WFS}, varying the WFS position along the optical axis z, in order to map the aberration caustic;
- plot $c_{defocus}$ versus z_{WFS} and compute a linear interpolation to retrieve the best fit, defining for each focal length an empiric law that will be used to link the two parameter:

$$z_{WFS} = c_{defocus} \cdot m(f_{IOL}) + q(f_{IOL})$$

- once the best fit is retrieved, the position of the WFS that minimizes the defocus coefficient can be computed, and the WFS is moved to reach such a position;
- the defocus coefficient is measured again in this new position; in an ideal situation the measured defocus coefficient should be null, but the real measurement can be useful to quantify the related error in the WFS position $\delta z_{WFS} = \delta c_{defocus} \cdot m(f_{IOL})$.

Remembering that

$$d = \frac{1}{f}$$

and

$$\pm\Delta d = \frac{1}{f^2} \cdot \Delta f$$

where f and Δf are respectively the focal length and its indetermination, expressed in m, and d and Δd are the dioptric power and its indetermination, due to the error of the WFS positioning with respect to the lens focal plane. The previous expression can be easily inverted to obtain the indetermination on the focal length:

$$\pm\Delta f = \Delta d \cdot f^2$$

Substituting $\Delta d_{max} = 0.125$ the maximum acceptable error in the focal length, Δf_{max} can be then retrieved (the obtained values are reported in table 2.4).

2.6.2 Defocus measurements linearity and sensitivity

Taking advantage of the empiric law retrieved in the previous section, the whole procedure has been repeated with test lenses (both IOL and commercial glass lenses) with different focal lengths in order to retrieve angular coefficients m reported in last column of table 2.4 and shown in figure 2.7 as a function of the lens dioptric power.

Focal length (mm)	**Dioptric power**	$\mathbf{\Delta f_{max}}$	**m (mm)**
49*	20.4	0.30	0.004
61*	16.4	0.47	0.006
76.2	13.1	0.73	0.008
82.5*	12.4	0.86	0.014
95.2*	10.5	1.15	0.020
100*	10	1.25	0.023
125*	8	1.98	0.054
150*	6.7	2.81	0.113

Table 2.4: In the first two column are shown the focal length and the corresponding dioptric power of the tested lenses (asterisks identify IOLs, while the other are *lab lenses*). In the third column are computed the maximum acceptable error in the focal length, corresponding to $\pm$ 0.125 diopters. In the last column the angular coefficients m (relating a defocus coefficient with a WFS movement in z).

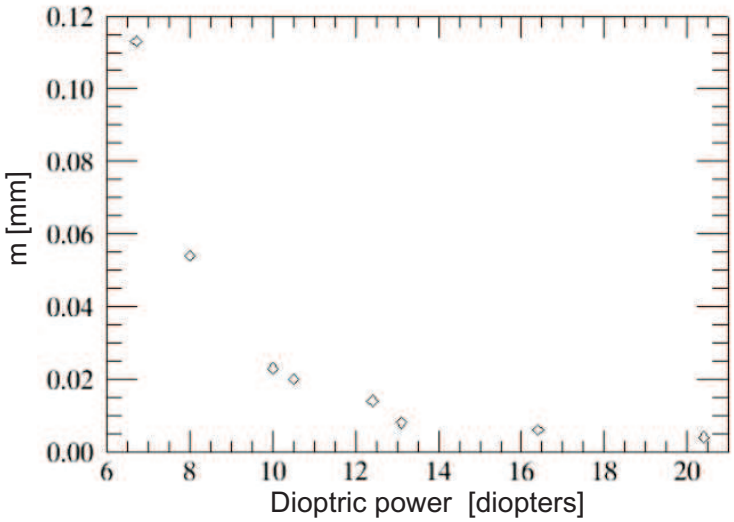

Figure 2.7: Angular coefficient m plotted as a function of the dioptric power of the lenses.

Furthermore we want to verify the ability of the described procedure to define the position which minimizes defocus coefficient ($\delta c_{defocus}$) even when the WFS starting position δz_{WFS} is very far from the IOL focal plane (where $\delta z_{WFS} = 0$). From this

point of view, the maximum distance from the actual focal plane in which the WFS is properly working represents the linearity range of the sensor itself and depends upon the focal length of the lens to be tested. In Figure 2.8, $\delta c_{defocus}$ is plotted as a function of the WFS position along the optical axis (0 represents the focal plane position), for a lens with a focal length of 100 mm. The retrieved plot deviates from linearity when the WFS distance from the best focus (δz_{WFS}) is higher than 6 mm (meaning that the defocus linearity range fort this 100 mm lens is about 12 mm). Before starting our measurements it is important to define a parameter that guarantees that the WFS is inside the linearity range.

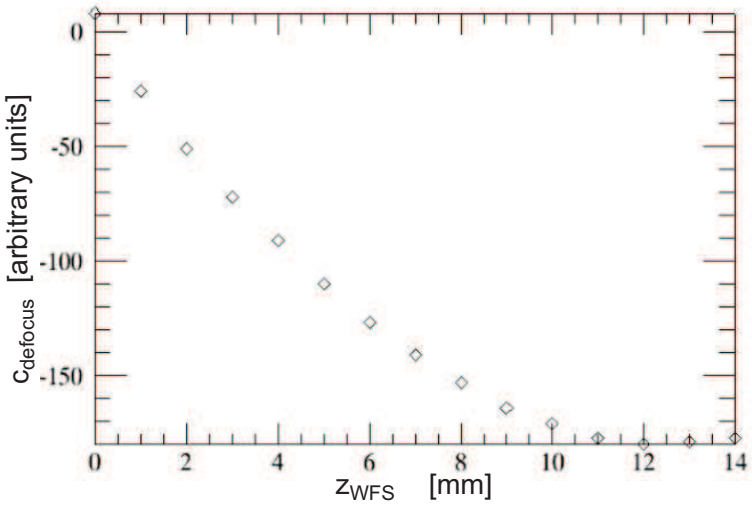

Figure 2.8: Defocus coefficients for a 100 mm focal length lens as a function of the distance of the WFS from the best focus position (in mm). The total range is of course symmetric, but the graph shows only the WFS movement in one direction. The linear behavior of the WFS is maintained up to a 6 mm distance from the best focus position, while for bigger distances the WFS the saturation of the signal is reached.

2.6.3 Tip and tilt measurements sensitivity and linearity

The WFS centering with respect to the optical axis defined by the IOL is realized minimizing the tip and tilt coefficients retrieved by the WFS in the Zernike polynomials analysis. The centering procedure is analogous to the focusing one, described in section 2.6.2. The aim of this test is the characterization of the linearity range and the sensitivity of the WFS concerning the tip-tilt measurements. Table 2.5 shows the linearity ranges computed in geometric approximation for each considered focal length. These values have to be compared with the corresponding values obtained experimentally.

Focal length (mm)	Dioptric power	Tip-tilt linearity range (mm)
49	20.4	0.13
61	16.4	0.16
76.2	13.1	0.20
82.5	12.4	0.22
95.2	10.5	0.25
100	10	0.26
125	8	0.33
150	6.7	0.40

Table 2.5: Results from the geometric computation of the WFS linearity range for lenses with different focal lengths (the one we use for the characterization). The obtained values depend from the 200 μm fiber-core, the L1 collimating lens focal length and the tested lens.

Laboratory lens

To obtain a sensitivity estimation, we used two *lab lenses*, considering only their central area, in order to minimize the errors due to the aberrations introduced by the lens itself. The focal lengths of the lenses are 150 mm and 100 mm, respectively. A procedure analogous to the test performed on the defocus coefficients has been used. First of all, a set of measurements of the tip and tilt coefficients, varying the WFS respectively along x and y positions, has been taken for each of the two test lenses; then the best linear fit has been computed on the values of the positions of the WFS along the x and y axis plotted versus the tip and tilt coefficients, respectively, to retrieve the empiric law describing the relation between WFS position and measured Zernike coefficient. The angular coefficients of the best linear fit for each lens are expected to be the same in the two directions. The result, compatible with the latter is shown in table 2.6.

Focal length (mm)	$\mathbf{m_{tip}}$ (mm)	$\mathbf{m_{tilt}}$ (mm)
150	0.00107	0.00101
100	0.00047	0.00045

Table 2.6: Angular coefficients m (relating a tilt or tilt coefficient with a WFS movement in x or y) for 100 and 150 mm focal length *lab lenses*. As expected, for the same lens, x and y results are similar.

As an example, figure 2.9 shows the trend of the retrieved tip coefficient c_{tip}, for the 150 mm focal length lens, as a function of the x_WFS position. It has been verified, and it is visible in figure 2.9, that the WFS behavior is linear in approximately a 0.3 mm wide range, centered around the minimum tip position of the WFS, where the four pupils are equally illuminated, range compatible with the estimate given in 2.5.

If the WFS at the beginning of the measurements is already inside its linearity range, it can adjust its position automatically, simply minimizing the tip and tilt coefficients. If, on the contrary, the WFS is outside the linearity range, two of the pupils are not illuminated at all, but the acquisition range can be increased determining which of the pupils are illuminated and moving the WFS in the correct direction in order to enter inside the linearity range.

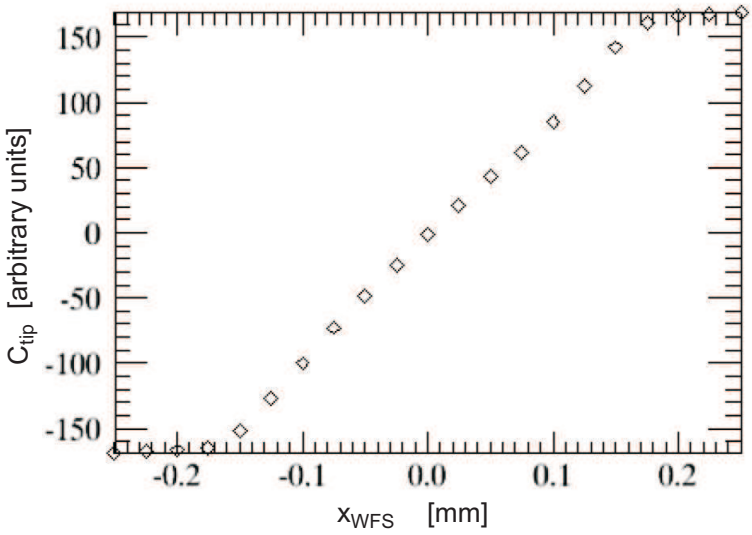

Figure 2.9: Tip coefficients as a function of WFS movement along x axis. The linearity range is around 0.3 mm.

IOL

The same linearity test was performed also for an IOL, to validate the procedure. The linearity ranges have been measured for an IOL with focal length equal to 95.2 mm, in the three axes. The results are shown in figure 2.10 and the obtained linearity ranges are about 5 mm for the defocus and 0.2 mm for the tip and tilt. The retrieved tip-tilt ranges are compatible with the computations reported in table 2.5 and are wider than the minimum ranges required to perform our measurements (as will be explained in section 2.8.1).

2.7 Wavefront computation and aberrations conversions in nanometers

We compute the aberrations retrieved by the WFS as the linear combination of a set of Zernike polynomials (see section1.2.3), whose coefficients vary according to

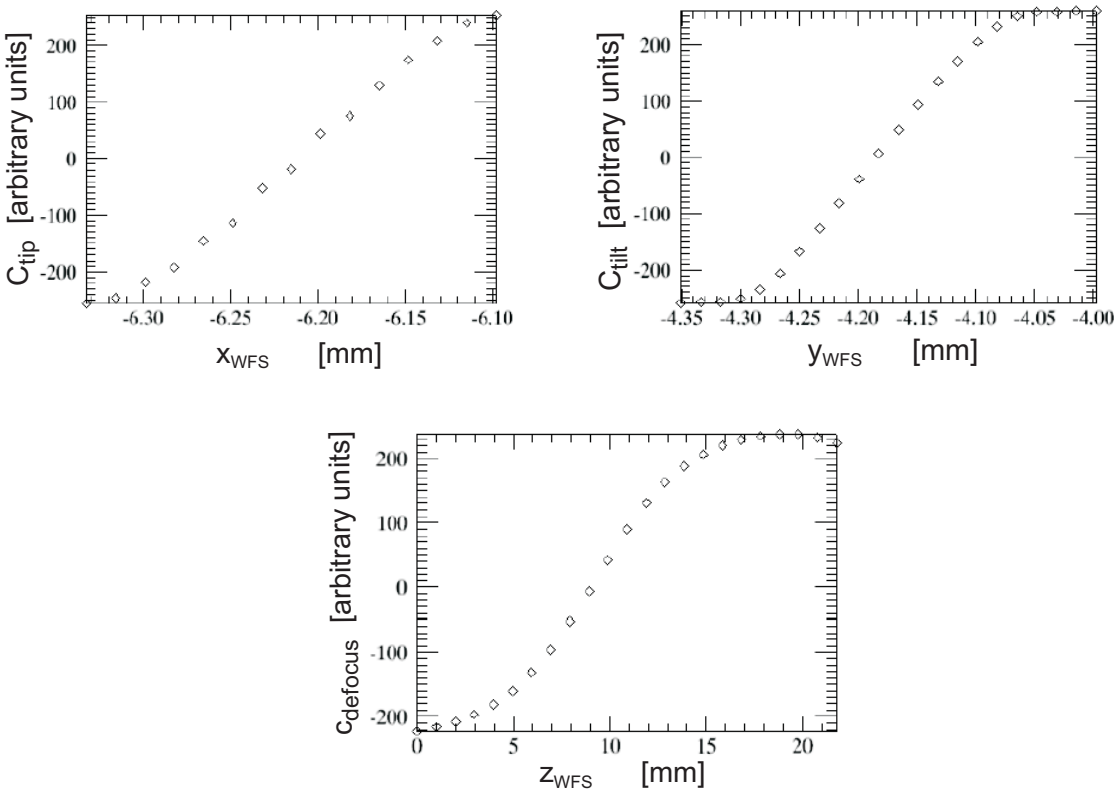

Figure 2.10: Tip, tilt and defocus coefficients as a function of WFS position along respectively x, y, z axis for a 95.2 mm IOL focal length. Linearity range is around 5 mm for defocus and 0.2 for tip and tilt, compatible with the theoretical value computed in table 2.5.

the entity of the of aberration and are normalized according to Noll (1976), to always have a standard deviation equal to 1. We decided to reconstruct each wavefront up to 14 Zernike polynomials, corresponding to the 4th radial order.

Before each measurement we decenter and focus the WFS with respect to the lens minimizing the retrieved tip, tilt and defocus coefficients with the procedure described in section 2.6. The residual tip, tilt and defocus terms are subtracted from the final retrieved wavefront by software.

Since the coefficients in the wavefront computation are not expressed in physical units, it is necessary to gauge them in order to translate the coefficients aberrations in arbitrary units into nanometers.

A spatial range along the z axis, centered on the best focus position is defined and the defocus coefficient is measured for both the extreme intra-focal and extra-focal positions (which are symmetric with respect to the best focus). The converting factor

($conv$) can be retrieved as follows:

$$conv = \frac{1}{8 \cdot 2\sqrt{3}} \frac{D^2}{f^2} \frac{\Delta z}{\Delta c}$$

where D is the IOL diameter (6 mm or of the diaphragm diameter if we are using a *lab lens*), f (mm) is the lens focal length, Δz is the considered range along z and Δc the difference between the measured defocus coefficients in the intra and extra-focal positions. The factor $2\sqrt{3}$ allows to convert from RMS to PtV values.
To increase the robustness of the conversion factor, instead of using only two determinations, several position inside the chosen range were used and Δc was retrieved from the best linear fit of the experimental data. All the measurements have been repeated for each of the lens in the sample, and the results are reported in table 2.7.

Focal length (mm)	**Dioptric power**	**conv (nm)**
49*	20.4	2.2
61*	16.4	2.0
76.2	13.1	1.9
82.5*	12.4	2.7
95.2*	10.5	2.9
100	10	3.2
125*	8	4.5
150	6.7	6.5

Table 2.7: Conversion coefficients to translate coefficients arbitrary units into nm and properly quantify aberrations for the set of available lenses.

2.8 Calibration lines determination

As explained in section 2.6.1, two defocus measurements, in intra and extra-focal positions, can be used to retrieve the position which minimizes defocus. Afterwards, two other measurements, taken around the position of the first iteration, allow obtaining higher precisions.

2.8.1 Minimum distance between measurements for the correct computation of m and conv

The pair of measurements used to determine the calibration line shall not be taken too close one to the other (Δz should not be too short), since errors in the defocus coefficients ($C_{defocus}$) computation translate into an indetermination in the calibration line angular coefficient which is increasing while the intra and extra-focal

positions distance decreases. On the other hand, this distance shall not exceed the linearity range, discussed in section 2.6.2. An error in the calibration line angular coefficient propagates into the determination of the test lens focal plane position and, consequently, into the dioptric power measurement. We want to define the minimum and the maximum Δz to properly determine the test lens focal plane position (2.6.2). Moreover, we want to define the range and the number of images, which are suitable for a reliable computation of the conversion coefficient described in section 2.7. Since the conversion coefficient is directly proportional to the calibration line angular coefficient, the indetermination in the latter propagates into the former. Tests have been performed using two *lab lenses*, (100 mm and 150 mm focal legth respectively), and an IOL in the same focal range (95.2 mm focal length), to verify if the obtained results were compatible.

Lab lenses

Table 2.8 shows a set of measurements of the calibration line slope and of the conversion coefficient, taken for different ΔZ, for both the *lab lenses* considered. The reference represents a reliable focal plane position measurement. For the 100 mm *lab lens*, it has been chosen to use the mean value of 13 determinations, obtained with a set of 13 images taken in a ΔZ=1.2 mm with a 0.1 mm step.
All ranges chosen for the test are centered in such a reliable focus position, and the reported Δz and δd represent, respectively, the difference between the position of the retrieved focal plane and the dioptric power, with respect to the reference. A check on the reliability of the measurements has been performed re-computing both the coefficients using 10 different couples of images, with a fixed ΔZ. The obtained coefficients are very stable, presenting totally negligible fluctuations. Figures 2.12 and 2.11 show the variation of the conversion coefficients (conv) and the residual dioptric power (error) measured considering different ranges (ΔZ), respectively for 100 and 150 mm cases. The required precision for the prototype in the measurement of the dioptric power is 0.125 diopters, translating, for the considered100 mm and 150 mm focal legth *lab lenses*, into a 1.27 mm and 2.81 mm precision in the definition of the test lens focal plane position. We can notice that all the retrieved measurements are inside such a requirement. However, we arbitrarily decided to limit the acquisition range, in a way that the indetermination on the retrieved coefficients is lower than the $\pm$5%. This leads to a range between 0.1 mm and 4 mm for the 100 mm focal legth lens and between 0.07 mm and 0.25 mm for the 150 mm focal length one.
Finally, we checked the stability of the obtained conversion coefficient measuring it in different days and daytimes (meaning also different environmental conditions) for the lens with f = 100 mm. For a complete set of measurements, the coefficients varies between 2.9 nm and 3.3 nm. Considering that the mean value of the static aberration due to the setup (see next sections) is about 100 nm, this indetermination, translating

into an error of about 13 nm, still allows a WF reconstruction with a precision better than $\lambda/50$.

Focal length 100 mm

Δz (mm)	**m**	$\delta z(\mu$**m**$)$	**δd (diopters)**	**conv (nm)**
0.025	-33.83	-5.51	-1.39 $\cdot 10^{-4}$	3.84
0.05	-37.21	-1.19	-3.00 $\cdot 10^{-5}$	3.49
0.1	-40.05	0.33	8.33 $\cdot 10^{-6}$	3.24
0.2	-39.77	0.26	6.67 $\cdot 10^{-6}$	3.27
0.4	-39.53	-0.40	-1.00 $\cdot 10^{-5}$	3.29
0.6	-39.35	-0.76	-1.92 $\cdot 10^{-5}$	3.30
0.8	-39.49	1.16	2.92 $\cdot 10^{-5}$	3.29
1	-39.46	0.33	8.33 $\cdot 10^{-6}$	3.29
1.2	-39.73	4.92	1.24 $\cdot 10^{-4}$	3.27
2	-39.42	-1.72	-4.33 $\cdot 10^{-5}$	3.30
4	-39.05	5.35	1.35 $\cdot 10^{-4}$	3.33
6	-37.31	0.83	2.08 $\cdot 10^{-5}$	3.48
8	-35.22	-13.99	-3.53 $\cdot 10^{-4}$	3.69
Ref	-39.60	0.00	0	3.28

Lens focal length 150 mm

Δz (mm)	**m**	$\delta z(\mu$**m**$)$	**δd (diopters)**	**conv (nm)**
0.07	-9.77	-5.94	-9.0 $\cdot 10^{-4}$	5.91
0.13	-9.42	-2.11	-3.2 $\cdot 10^{-4}$	6.12
0.26	-9.47	-0.26	-4.0 $\cdot 10^{-5}$	6.10
0.53	-8.16	-181.53	-2.8 $\cdot 10^{-2}$	7.07
1	-8.34	-162.69	-2.5 $\cdot 10^{-2}$	6.92
2	-8.21	-142.79	-2.2 $\cdot 10^{-2}$	7.02
Ref	-8.87	0.00	0	6.51

Table 2.8: Calibration line angular coefficients (m), measured with different Δz ranges, centered on the reference focal position. The reported δ z and δ d represent, respectively, the residual shift of the focal plane and the dioptric power error, with respect to the reference. In the last column are listed the retrieved conversion coefficients.

IOL

Analogous tests have been performed on a IOL in the same focal range of the *lab lenses* used to verify the best acquisition ranges. In table 2.9 the results of this test

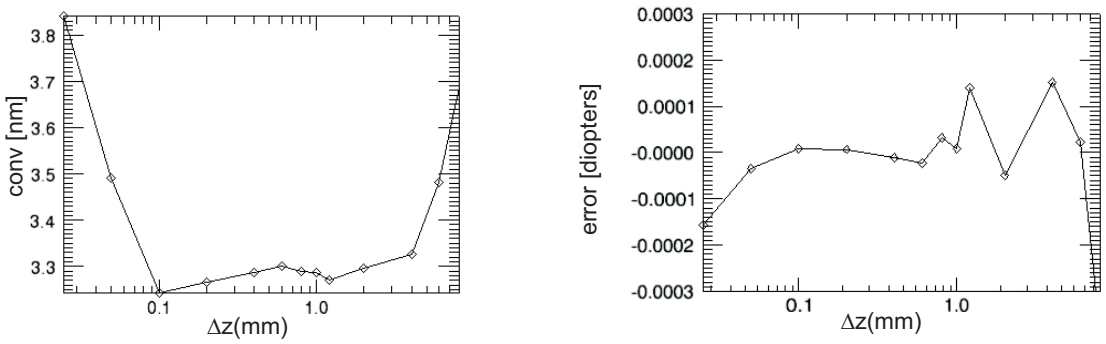

Figure 2.11: Conversion coefficient (left) and dioptric power error (right) measurements resulting for different ranges Δz for a 100 mm lab lens. The x axis is logarithmic.

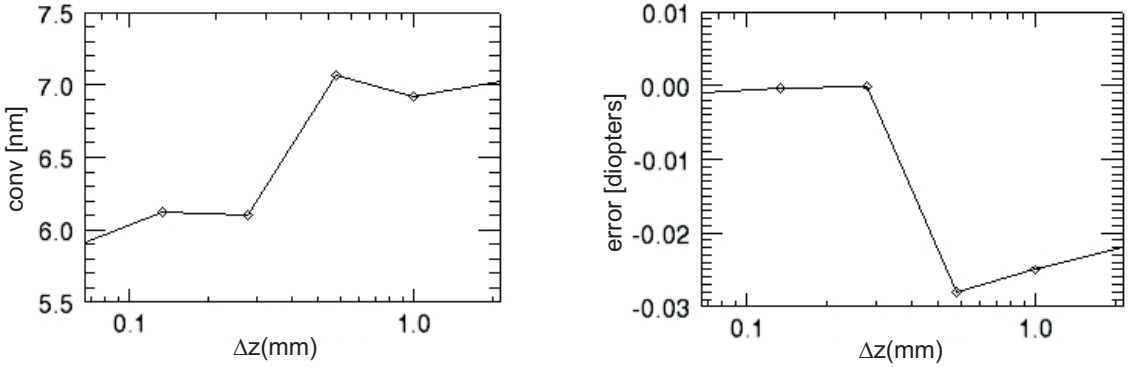

Figure 2.12: Conversion coefficient (left) and dioptric power error (right) measurements resulting for different ranges Δz for a 150 mm lab lens. The x axis is logarithmic.

are listed, with the same definitions used in the previous paragraph. As obtained for the 100 mm lab lens, the minimum distance between the couple of images, to compute the focal plane position, is 0.1 mm. Concerning the conversion coefficient stability, however, the 5% indetermination is exceeded if $\Delta z \leq$0.2 mm.

2.9 Wavefront analysis

After the characterization of the procedure for the WFS alignment with respect to the IOL, and the conversion of Zernike coefficients into nanometers, the first IOL wavefronts can be retrieved. These measurements, however, will include also the aberrations introduced by the setup. Because of this reason, these static aberrations have to be quantified, to determine if they are negligible, if they can be subtracted or if they do not allow a proper wavefront measurement.

IOL focal length 95.2 mm

Δz (mm)	m	$\delta z(\mu m)$	δd (diopters)	conv (nm)
0.025	-46.35	11.96	$2.63 \cdot 10^{-4}$	3.09
0.05	-46.77	88.23	$1.94 \cdot 10^{-3}$	3.06
0.1	-47.83	13.17	$2.90 \cdot 10^{-4}$	3.00
0.2	-48.52	-1.28	$-2.81 \cdot 10^{-5}$	2.96
0.4	-48.50	0.69	$1.52 \cdot 10^{-5}$	2.94
0.6	-48.76	-0.04	$-8.34 \cdot 10^{-7}$	2.94
0.8	-48.74	-2.00	$-4.39 \cdot 10^{-5}$	2.95
1	-48.67	-1.62	$-3.55 \cdot 10^{-5}$	2.94
1.2	-48.79	10.94	$2.41 \cdot 10^{-4}$	2.93
2	-48.93	7.83	$1.72 \cdot 10^{-4}$	2.95
4	-48.67	11.64	$2.56 \cdot 10^{-4}$	2.94
6	-48.74	1.19	$2.62 \cdot 10^{-5}$	2.95
8	-48.66	-2.70	$-5.94 \cdot 10^{-5}$	2.94
Ref	-48.74	0.00	0	3.28

Table 2.9: Calibration line angular coefficients (m), measured with different Δz ranges, centered on the reference focal position. The reported δz and δd represent, respectively, the residual shift of the focal plane and the dioptric power, with respect to the reference. In the last column are listed the retrieved conversion coefficients.

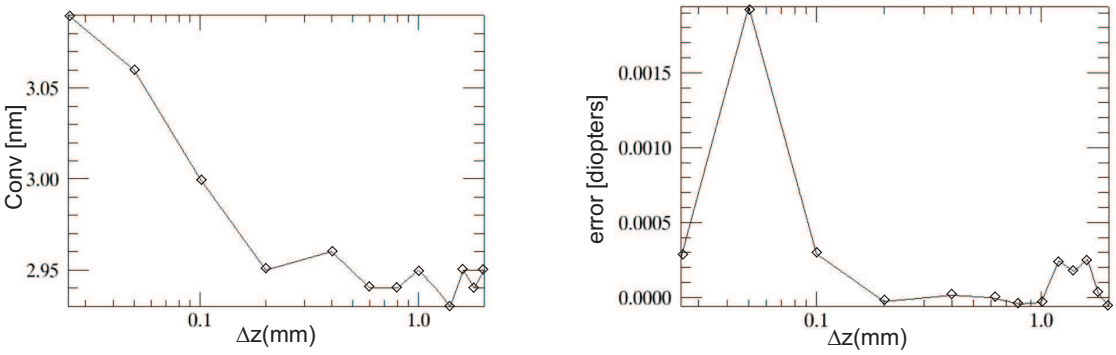

Figure 2.13: Conversion coefficient (left) and dioptric power residual (right) measurements resulting for different ranges Δ z for a 95.2 mm IOL. The x axis is logarithmic.

2.9.1 Static aberrations characterization

To measure the IOLs optical quality with our demonstrator, the first step was to characterize the static aberrations introduced by the setup itself.
Since the optical elements to be analyzed by the prototype have a non-negligible optical power, we could not simply measure the aberrations of the setup, retrieved removing the IOL from the optical path, since in such a configuration the light would

not focus on the pin of the pyramid WFS. So, to characterize the setup static aberration we had to replace the IOL with another focusing optical element.
Calibrated achromatic doublets have been selected to perform this analysis. They have 50.8 mm diameter, and only the inner part (6 mm, corresponding to the IOL size) was selected by a diaphragm in order to work in quasi-paraxial conditions, reducing as much as possible aberrations introduced by the lens.

There are several possible sources of error in determining the static aberration introduced by the setup. First of all we want to be sure that this aberration is actually static, that is to say that we do not accidentally change it during operations on the setup. During the test on the IOL, in fact, some setup components are sometimes removed to check the alignment of the setup or to disentangle one component from another.
The setup alignment is regularly checked with the laser beam, and during this operation the optical fiber can be removed either removing the magnetic base plate on which it is fixed or simply disconneting the fiber from its holder. In both cases, the effect should not be the introduction of aberrations on the setup, since the only aberrations directly depending upon the optical fiber position are the tip-tilt, which is automatically subtracted, and the defocus, always minimized before each measurement. In case the fiber does not deliver a uniform and spherical wavefront, however, the repositioning of the fiber itself could change the static aberration of the setup. The positioning of the test lens could, in principle, be another source of error. Its position could vary in x-y directions, again acting on the tip-tilt coefficients, or along the optical axis, slightly changing the focus position. But, again, these are contributes which are subtracted or minimized. However, if the lens itself is not center-symmetric or the 6 mm area selected by the diaphragm is changing, some unknown aberrations could be introduced. Moreover, also the environmental conditions should be taken into account, since different temperature-pressure on the setup could can produce variations in the performances and the static aberration itself. Finally, also the choice of the test lens could introduce some systematic errors on the static aberration measurement. More than one lens should be used, therefore, for a proper haracterization. The result of this discussion is that what we are calling static aberration is, in fact, non-static at all. What we want to verify, though, is whether it is static enough to be simply subtracted by the measured IOL wavefronts or, better, if we could simply consider it as negligible, or none of them.

In Table 2.10 are summarized the Zernike coefficients (tip (0), tilt (1) and defocus (2) modes are subtracted) and the overall Peak-to-Valley (PtV) aberrations, obtained in various configurations, to possibly disentangle aberrations which could be introduced during any operation on the setup.

The different performed tests are the following (the first nine tests are obtained using a 100 mm focal length lab lens, while the last two using a 150 mm lab lens):

1. the WFS is centered and focused with respect to the lens;
2. same as test 1, to verify they are not introducing an unexpectedly variable aberration;
3. same as test 1, but repeated in other conditions (a different day and daytime) to verify stability in different environmental conditions;
4. again, same as test 1, but repeated in other conditions (a different day and daytime);
5. the optical fiber is taken off and re-inserted on its holder;
6. same as test 5, to check the repeatability;
7. the optical fiber mount is removed and then repositioned (we remind it is mounted on a kinematic repositionable mount);
8. the lens is axially rotated of 90 °;
9. the lens is flipped (reversed with respect to the optical axis);
10. same as test 1, with the 150 mm focal length lens replacing the 100 mm focal length one;
11. same as test 10, to check the repeatability.

The first thing to be noticed about the results reported in table 2.10 and figure 2.14 is that, even if the Zernike coefficients vary, the system introduces a PtV aberration which is always of the same order of magnitude. The rotation of the test lens (test 8 and 9), for example, does not change the measured WF aberrations more the previous tests, except for the test 9 the spherical aberration coefficient which increase correctly due to the different curvature of the lens. The repositioning of the optical fiber, in particular, seems not the change the results at all.
Overall, the most powerful Zernike polynomial turned to be the spherical one (Zernike mode 9). However, this does not mean that the demonstrator is introducing a high spherical aberration, since such a term is decreasing when using the 150 mm focal length lens instead of the 100 mm one, because of the lower curvature of the lens surfaces. However, this underlines the low dependency of such a parameter from the prototype setup, being more related to the test lens itself. Let's try now to quantify the static aberration.

For all the performed test, the PtV aberration appears to be smaller than 90 nm, that is to say lower than $\lambda/6$ (considering the white light peak at about 550 nm). We can, then, conclude that the static aberration effect is negligible and it is possible to retrieve the IOL dioptric power with the required precision, even without subtracting its contribution.
Moreover, a variance of $\lambda/4$ in the wavefront delivered by the IOL can also be measured.

	$C_i(nm)$											
Test #	**3**	**4**	**5**	**6**	**7**	**8**	**9**	**10**	**11**	**12**	**13**	**PtV**
1	11	2	10	17	2	4	49	29	2	7	12	**83**
2	30	3	32	2	7	13	38	6	6	7	13	**74**
3	22	3	34	3	13	9	40	7	5	9	15	**71**
4	17	0	35	3	16	11	40	6	4	8	15	**74**
5	19	1	32	11	18	10	31	17	4	8	14	**71**
6	18	5	29	10	17	8	30	20	5	13	15	**69**
7	13	30	21	10	16	9	59	0	1	6	11	**84**
8	11	23	17	3	17	25	54	1	4	6	8	**73**
9	3	41	15	2	14	23	44	9	1	5	7	**69**
10	48	8	15	10	13	2	14	15	10	1	6	**89**
11	4	49	19	13	14	13	10	3	20	1	3	**85**

Table 2.10: Zernike coefficients C_i for Zernike modes up to 13 measured in different setup conditions in order to quantify the static aberrations introduced by the optical setup and to verify their stability.

2.9.2 IOL holder aberrations

With the test described in the previous section, the prototype static aberration has been quantified for the complete setup except for the IOL holder, composed of two flat optical windows with a nominal $\lambda/4$ optical quality. Then we performed tests to verify if the aberrations introduced by such a holder are not negligible consists of introducing the holder itself, filled with the physiological saline solution, in the collimated beam before the 100 mm lab lens, whose wavefront is already known. Then, the measured wavefront is subtracted from the one measured with the holder inside the optical path, before computing the polynomial fit with the Zernike terms. In figure 2.15 are reported the 3D shapes of the following wavefronts: static aberration without the IOL holder, static aberration with the holder and the residual of the subtraction between the two. Table 2.11 summarizes the measured aberration coefficients, reported also in figure 2.16. The result of such a test is that we estimate the IOL holder to introduce about 50 nm of astigmatism (Zernike modes 3 and 4),

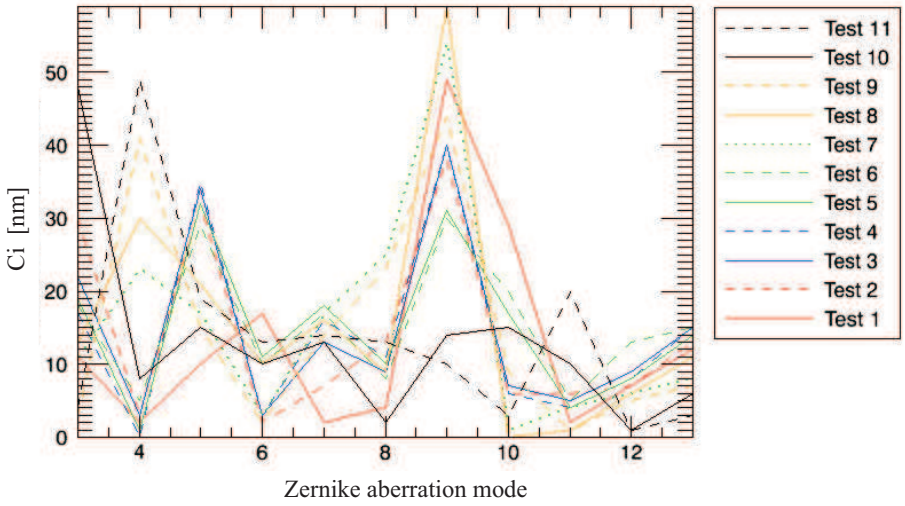

Figure 2.14: Zernike coefficients C_i for Zernike modes up to 13, reported in table 2.10, measured in different setup conditions in order to quantify the static aberrations introduced by the optical setup and verify their stability.

probably due to a small curvature of one of the windows. This aberration, however, is negligible, since it is of the same order of magnitude of the static aberrations.

	$C_i(nm)$											
	3	**4**	**5**	**6**	**7**	**8**	**9**	**10**	**11**	**12**	**13**	**PtV**
Static	29	9	30	9	11	3	44	6	6	6	15	**92**
Static + IOL holder	68	46	37	3	3	0	44	12	8	4	10	**116**
IOL holder	38	37	8	6	13	4	1	7	14	3	5	**87**

Table 2.11: Zernike coefficients C_i for Zernike modes up to 13 measured with and without IOL holder (filled with physiological saline solution), to quantify aberrations the latter introduces.

2.10 IOL wavefront computation and repeatability tests

The IOL selected for the test has a nominal focal length 95.2 mm, corresponding to 10.5 diopters. For this test the wavefront measurements are repeated 10 times, re-positioning the IOL each time, in order to verify the measurements repeatability. Before each measurement, the WFS is aligned to the IOL, minimizing the tip-tilt and defocus terms. The IOL holder is equipped with a tip-tilt mount, which is adjusted in order to be orthogonal to the beam with a precision of 0.3° and to mantain the lens in a horizontal position. For each wavefront measurement (WF), the focal plane position is retrieved, as explained in section 2.6.2. The resulting residual

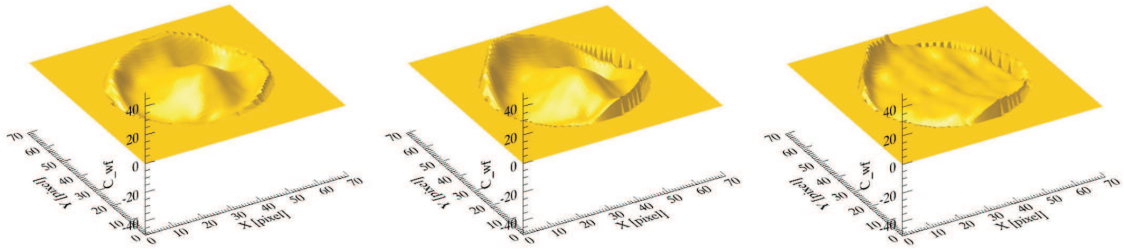

Figure 2.15: Wavefront 3d representations of respectively the static aberration without the IOL holder (left), the static aberration with the IOL holder (center) and an estimate of the holder contribution (right), obtained from the subtraction between the left and center image. The wavefront coefficients are expressed in arbitrary units.

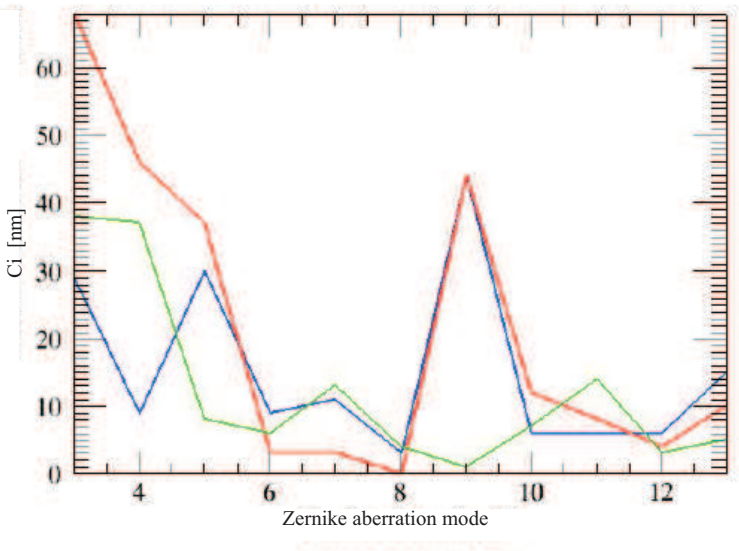

Figure 2.16: C_i for Zernike modes up to 13, reported in table 2.11 with and without IOL holder (filled with physiological saline solution), to quantify aberrations it introduces. The blue and red lines represent the static aberrations measured without and with the IOL holder, respectively. The green line shows the residuals of the subtraction between the two measured wavefronts

displacements from the 10 WFs mean value, taken as a reference, are reported in table 2.12. The requirement for the precision of the dioptric power determination is 0.125 diopters, that is to say 1.15 mm indetermination in the measurement of the focal plane position, for the considered test IOL. The retrieved measurements of the focal legth are inside a 255 μm range, which is inside the requirement. To verify the WF repeatability, since the IOL is immersed in a liquid and can rotate around the optical axis, it is advisable to rotate the retrieved WFs before comparing them.

The rotation angle is computed maximizing the correlation factor of two WFs, as a function of the rotation angle of one of them. We used the first retrieved WF as a reference and optimized the rotation of the other WFs. Figure 2.13 and table 2.17 show, respectively, the obtained WFs and the correlation factors between each WF (tip,tilt and defocus terms already removed) and the mean of the ten WFs. In figure 2.18 the Zernike polynomials coefficients of the 10 already rotated WFs fits are shown.

In figure 2.19 the conversion factor in nanometers is shown as a function of the nominal focal length of the lenses. An error of 5mm on the focal length of the IOL translates in an indetermination on the conversion factor of about $0.3 \cdot 10^{-6}$nm, which corresponds to a PtV variation on the WF measurement of about 20nm (from 170 to 190nm).

	Wavefront measurements #									
	Wf1	Wf2	Wf3	Wf4	Wf5	Wf6	Wf7	Wf8	Wf9	Wf10
δz (μm)	2	27	-17	171	-65	-84	24	-9	-51	-14

Table 2.12: Focal plane residual shifts from a defined reference. All measurements are inside a range of 255 μm, giving us a precision of almost a factor 10 with respect to the $\pm$0.125 allowed error.

Figure 2.17: Wavefronts retrieved for then different measurements.

	Wavefront measurements #									
	Wf1	Wf2	Wf3	Wf4	Wf5	Wf6	Wf7	Wf8	Wf9	Wf10
Correlation factor	0.98	0.99	0.99	0.94	0.97	0.96	0.99	0.97	0.98	0.98

Table 2.13: Correlation factors between each WF and the average WF (obtained from the 10 WFs).

2.11 IOL dioptric power measurement

In table 2.14 are reported the main characteristics of the IOLs we received from SIFI Srl company to validate our prototype. It is possible to notice how the nominal dioptric power P declared to the public and the effective power P_{eff} measured by the

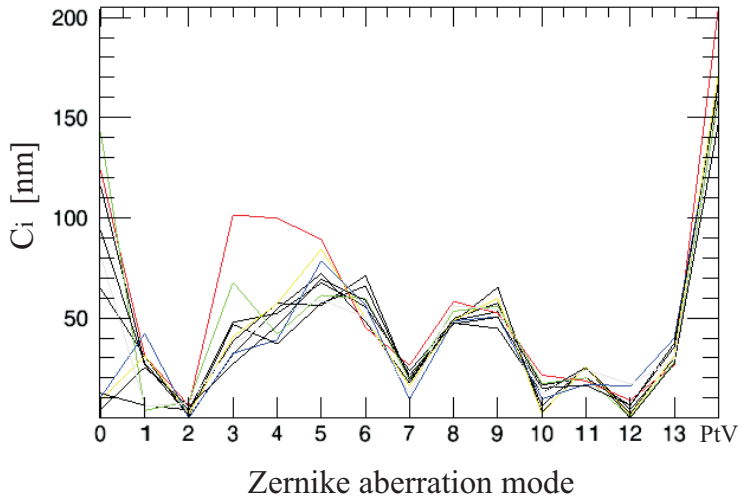

Figure 2.18: Zernike coefficients retrieved for 10 different wavefront measures of the same IOL.

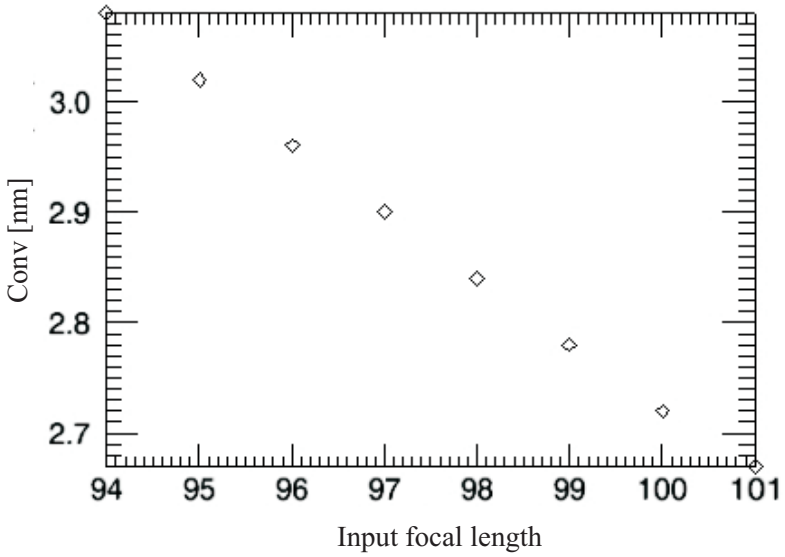

Figure 2.19: Conversion factor is shown as a function of the input focal length used for the computation.

company for this calibrated set, are very different. We remind that the goal of our test was to measure the IOLs focal length (and subsequently their dioptric power) with a maximum error of $\pm$ 0.125 diopters from the calibrated range given by the company.

Sample #	Serial number	Refractive index	P_{nom} (diopters)	P_{eff} (diopters)	Curvature radius (mm)	Center thickness (mm)
1	1204028000	1.4603	20.00	20.40±0.06	12.44 ± 0.01	0.95 ± 0.02
2	1204028005	1.4603	20.00	20.40±0.06	12.44 ± 0.01	0.95 ± 0.02
3	1011008485	1.4602	16.00	16.09±0.09	15.69 ± 0.01	0.81 ± 0.02
4	1106018502	1.4603	16.00	16.39±0.07	12.55 ± 0.01	0.81 ± 0.02
5	1109023005	1.4603	12.00	12.12±0.12	20.76 ± 0.02	0.67 ± 0.02
6	1109023006	1.4603	12.00	12.12±0.12	20.76 ± 0.02	0.67 ± 0.02
7	1012009783	1.4602	08.00	8.22±0.05	31.49 ± 0.04	0.53 ± 0.02
8	1012009412	1.4602	08.00	8.20±0.09	31.49 ± 0.04	0.53 ± 0.02

Table 2.14: Relevant characteristics of SIFI IOLs. P_{nom} and P_{eff} are, respectively, the nominal power of the lens and the effective power measured with a different WFS. All the lenses are biconvex and the surfaces radius and central thickness are reported in the last two columns of the table, respectively.

In table 2.15 are shown again the P_{eff} values given by the company and their translation into focal length. In the last column are listed the retrieved measurement of WFS position (directly related to the IOL focal length) with respect to an arbitrary reference since the company did not provide us a IOL calibrated with a small indetermination to be set as the zero point of our system and therefore we could only estimate the focal length difference between the given lenses but not an absolute value.

Since the IOLs in the sample had different indetermination associated to their nominal focal lengths f_{eff}, all IOLs have been used as calibration lenses for the system, and the final reference position has been retrieved as an average between all the retrieved reference positions, weighted according to the inverse of each lens focal length indetermination. The resulting reference position is then 86.87 mm.

Figure 2.20 shows the resulting dioptric power measurement for each IOL, already calibrated according to the defined reference position, to which the nominal power P_{eff} has been subtracted. The yellow area in the plot represents the indetermination in the dioptric power nominal value, claimed by the IOLs providing company. The error bars, associated to each power measurement represent the maximum acceptable error to fulfill our precision requirement (± 0.125 diopters). All the bars are entering the yellow area, therefore we have no evidence that any of our measurements is out of specifications, considering the indetermination in the calibration nominal focal lengths given from the providing company.

Sample #	P_{eff} **(diopters)**	f_{eff} **(mm)**	z_{wfs} **(mm)**
1	20.40±0.06	49.02±0.14	38.09
2	20.40±0.06	49.02±0.14	38.28
3	16.09±0.09	62.15±0.35	25.52
4	16.39±0.07	61.01±0.26	24.99
5	12.12±0.12	82.54±0.81	4.36
6	12.12±0.12	82.54±0.81	4.69
7	8.22±0.05	121.65±0.74	-37.14
8	8.20±0.09	121.95±1.32	-36.84

Table 2.15: In the first column is reported the dioptric power value given by the company, in the second column the latter is translated into focal lengths and in the third column are reported the values obtained by our measure with respect to an arbitrary reference position.

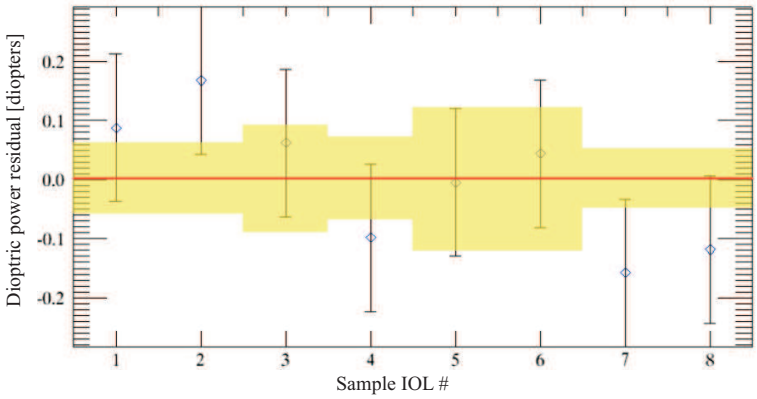

Figure 2.20: For each IOL sample is shown the difference between the dioptric power measured by the sensor and the dioptric power claimed by the company. Each retrieved measure has associated an error bar of ±0.125 diopters, the precision requirement for our measure. The yellow area represents the indetermination in P_{eff} given by the company. Our measurement goal is fulfilled.

2.12 Conclusions

WATERFALL, the prototype of a wavefront sensor for the analysis of the optical quality of Intra-Ocular lenses and the accurate measurements of the IOL dioptric power, was designed aligned and tested in Padova Adaptive Optics laboratory.
The conditions behind the project were that the overall layout of the prototype had to be realized with cheap and compact (as much as possible not to compromise the quality of the results) off-the-shelf components, in the view of a future comercialization of the instrument.

The WFS is mounted on a 3-axis very precise linear stage and, analyzing the Zernike polynomials for 3 couples of images, taken in 2 different positions of the WFS along each axis, we obtained the WFS position needed to minimize tip and tilt (to reduce de-centering) and defocus (to get the real position of the lens from a fixed reference point).

Test to characterize our setup were the study of WFS sensitivity and linear range for tip-tilt and defocus. One characteristic of pyramid WFSs and 4-quadrant sensors in general, is that linearity is inversely proportional to sensitivity, which means that a smaller spot hitting the pyramid has a smaller linear range (when all 4 pupils are illuminated), but a higher sensibility, because even a small movement of the spot can be appreciated, while the opposite will happen for a bigger spot. In this setup the dimension of the spot on the pupil is directly proportional to the IOL's FL and, with the final chosen fiber core dimension (200 μm), it could vary from $\approx$1 mm (for a 30 mm IOL's FL) to $\approx$7 mm (200 mm IOL's FL). Afterwards we analyzed the aberrations of the optical window that contains the IOL (which has to be conserved in a physiologic solution) and the static aberrations of the setup, due to minor misalignments and fiber re-positioning, concluding they were negligible. We proceeded on to determine the repeatability of optical power and for the wavefront measures and we obtained a reliable system that measures optical power of IOLs with an error lower than 0.125 diopters for the foreseen diopters range. It also provides IOLs wavefront analysis (low order aberrations: astigmatism, trefoil and coma) to determine their optical quality.

Further improvements are still possible, such as implementing an optical trap to remove the spurious light coming from the collimated beam and not passing through the IOL, in order to increase the collimated beam diameter and further reduce the precision required to position the IOL inside its holder. Moreover, a more favorable pyramid vertex angle could be chosen, so that a star enlarger would not be needed anymore and the system would be lighter and more compact, very important parameters for a commercial use. Finally, the whole system could be remotely controlled and a procedure implemented so that an operator, or even a robot, would only have to position the lens inside its holder and no specific alignment knowledge would be needed to obtain the desired measures.

Chapter 3

Ground-layer Wavefront Sensor for LINC-NIRVANA for the LBT

In the first part of this chapter will be given an overview of the Large Binocular Telescope (LBT), LINC-NIRVANA instrument, a Fizeau interferometer for imaging, and, finally, on the Ground-layer Wavefront Sensor (GWS), aimed to sense perturbations introduced on the wavefront by the ground-layer turbulence. In the second part of this chapter will be described the alignment, integration and verification performed on the first GWS sensor at the Adaptive Optics Laboratories of Padova first and at MPIA of Heidelberg afetrwards. Finally, the future steps, including the pathfinder experiment to validate on sky ground-layer correction, through the conjugated secondary adaptive mirror, will be outlined.

3.1 LBT

The Large Binocular Telescope (LBT, Hill and Salinari, 2003), located on Mount Graham in Arizona (3191 m), is one of the largest existent telescope. It is composed of two primary mirrors of 8.4 m of diameter each, mounted on a monolithic structure, in order to let both mirrors have identical altazimutal movements.
LBT is the result of an international collaboration between the University of Arizona, INAF (Istituto Nazionale di Astrofisica), LBTB (LBT Beteiligungsgesellschaft, Germany), the Ohio State University and Research Corporation (USA).

Each of the two LBT arms (telescopes hereafter) has a Gregorian configuration, allowing to have a real focus before the secondary mirror and to exploit adaptive optics. In fact, the plane conjugated to the secondary mirrors (adaptive, as it will be explained later) is located at about 100 m where a very strong component of the atmospheric turbulence is present (see chapter 1).

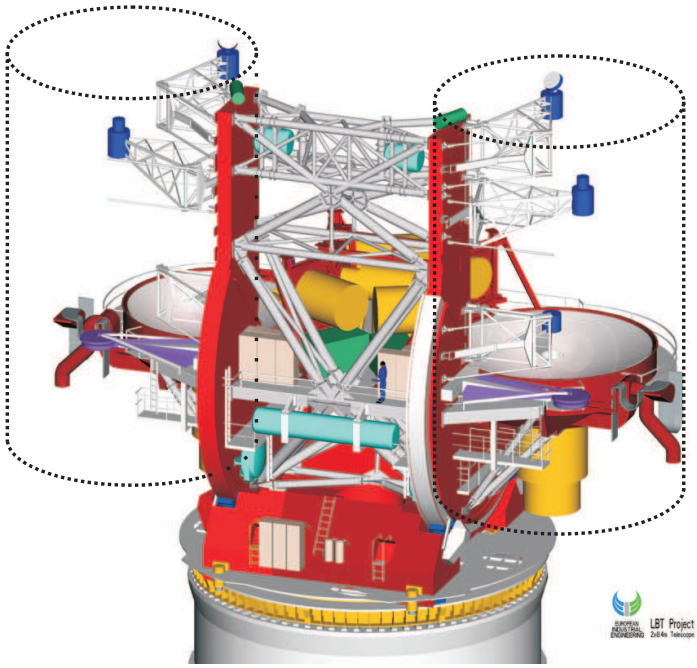

Figure 3.1: Large Binocular Telescope: the two LBT arms (telescopes) are highlighted.

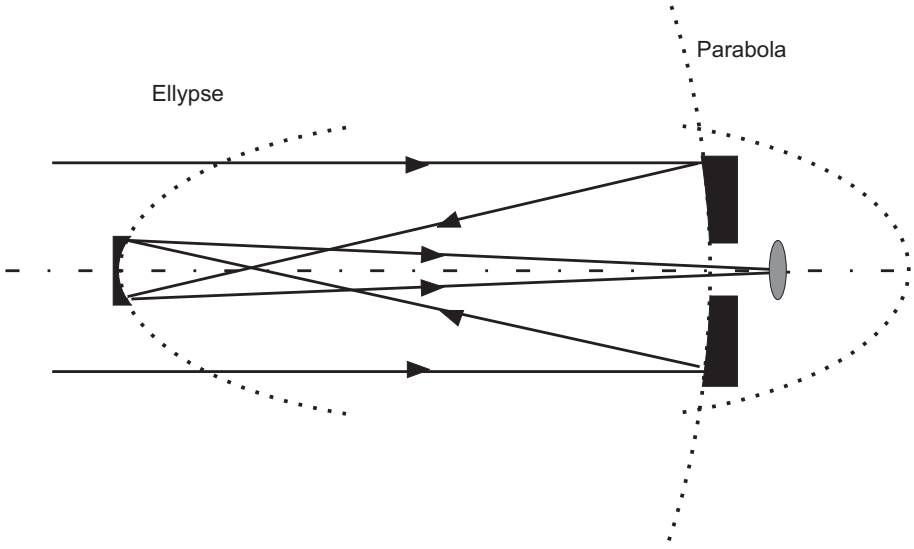

Figure 3.2: Optical scheme of a Gregorian telescope. Primary mirror is parabolic and has a central obstruction to allow a focal plane underneath; secondary mirror is elliptic and positioned after the primary mirror focus.

LBT can operate in 3 different ways (Herbst and Hinz, 2004):

- two telescopes independently, each with its own focal plane and instruments;

- pointing the same field, to obtain a collecting area equal to the one of a single telescope with a circular aperture of 11.8 m and angular resolution corresponding, instead, to a 8.4 m telescope. In this case the light is combined incoherently on the focal plane;
- interferometrically, where the beams coming from the two telescopes are coherently combined, allowing to reach a diffraction-limited angular resolution of a 23.8 m telescope (this size, larger than any telescope built so far, corresponds to the distance between the outer edges of the two mirrors and is called baseline). This is the way in which LINC-NIRVANA will be operated.

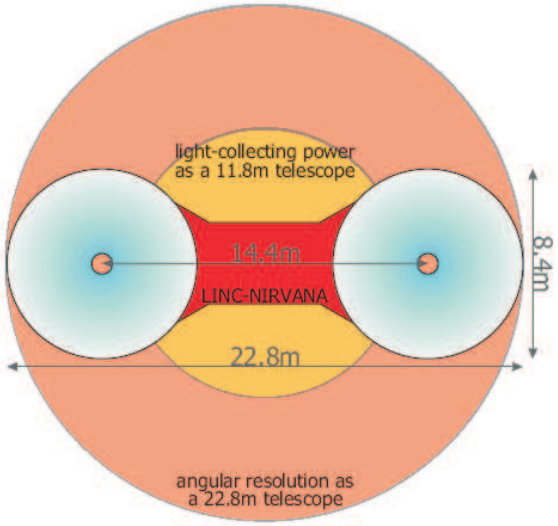

5

Figure 3.3: LBT different possible combinations and angular resolutions.

The light path of an astronomical object inside the telescope is depicted in figure 3.4. The light reaches its primary monolithic mirror, covered by a very thin layer of aluminum and provided with active optics, realized through 164 actuators. Afterwards it is reflected and captured either by the Large Binocular Cameras (LBCs), prime focus cameras (located at about 10 m distance from the primary mirror) or reaches the secondary mirrors and it is sent to other instruments. The secondary mirrors are adaptive mirrors, provided with 672 piezo-electric actuators and fold the light toward the tertiary mirror tilted of $\approx 45°$ (and located at about 2.25 m distance from the primary mirror), which can direct the light toward three different gregorian focal stations in an area located between the two primary mirrors. At one of this stations will be located the LINC-NIRVANA system.

Active and adaptive optics have always been fundamental in LBT project, fundamental to increase the telescope performances in the visible and near-IR bands and

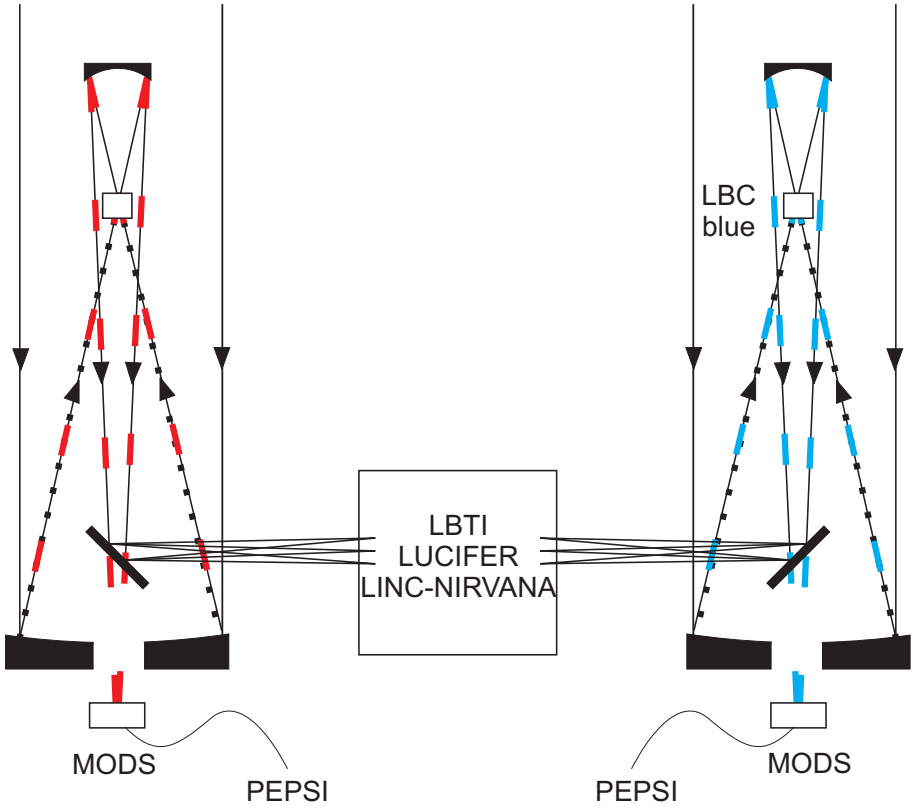

Figure 3.4: Representation of the light path coming from a star and reaching all instruments. The dotted line reaches the prime focus, where LBC is located, the dashed line the Gregorian focus and the full line the combined Gregorian focal stations, different instruments can be reached tilting the tertiary mirror.

fully justify its realization. One of the biggest innovation, followed in the last few years by other telescopes (MMT, where it has been tested for the first time and VLT UT4) is the use of an adaptive secondary mirror, which allows to extend the AO correction to all the telescope instruments (obviously LBCs excluded). Each of them is composed of a thin aluminized glass surface (1.6 mm) and a 0.91 m diameter mirror, to which are glued 672 magnets. The 672 corresponding electromagnets actuators are located in the support part of the mirror (realized of glass), which guarantees the necessary rigidity. The secondary mirrors are under dimensioned in order to act as diaphragms of the system and minimize the thermic background (very high in the IR). Therefore, the effective diameter of the primary mirror is reduced from 8.4 to 8.2 m.
The main characteristics of the telescope are summarized in table 3.1.

Weight: 700 tons
Telescope height: 25 m
Dome height: 40 m
Mount: alt-azimuthal
Max allowed wind velocity while operating telescope: 80 km/h
Optical scheme: 2 Gregorian telescopes with interferometric combination
Primary mirrors (2)
Diameter : 8.4 m
Focal/#: F/1.14
Central obstruction diameter: 0.89 m
Conic: parabola
Weight: 16 tons
Secondary mirrors (2)
Diameter: 0.91 m
Thickness: 1.6 mm
Conic: ellipse
AO Actuators: 672
Tertiary mirrors(2)
Diameter: 0.50 m $\times$ 0.64 m
Distance from primary mirror: 2.25 m
Conic: flat
Telescope Focal/#: F/15
Telescope magnification factor: 13.16
Focal stations and instruments
Prime focus: 2 LBC
Gregorian focus: 4, 2 direct(MODS), 2 through fibers (PEPSI)
Combined focus: 3, LBTI, LUCIFER, LINC-NIRVANA

Table 3.1: LBT main characteristics.

Interferometry As already mentioned, thanks to the mechanical mount of LBT, allowing to move simultaneously the two telescope, and therefore reducing the difficulties in co-phasing and other factors, the light coming from each mirror can be combined using interferometry, obtaining great advantages in terms of sensitivity and angular resolution. This technique has been used in astronomy for years in the radio wavelength but just in the last 10 years has started to be used also in the visible and IR domains. Some telescopes of the class 8-10 meters (such as VLT and Keck) use Michelson interferometry, while LBT is a Fizeau type interferometer.

A Michelson interferometer combines the beams coming from two apertures on the pupil plane. Considering a point source, the image produced on the focal plane

gives an interference figure with intensity modulation of the signal due to the Optical Path Difference (OPD) of the rays coming from the different apertures. Michelson interferometry does not impose any limitation to the baseline, which can be orders of magnitude larger than the apertures and allows to retrieve, high theoretical resolutions, however it provides a limited FoV, lower than 1" Herbst et al. (2001), due to the fact that OPD needs to be lower than the coherence length.

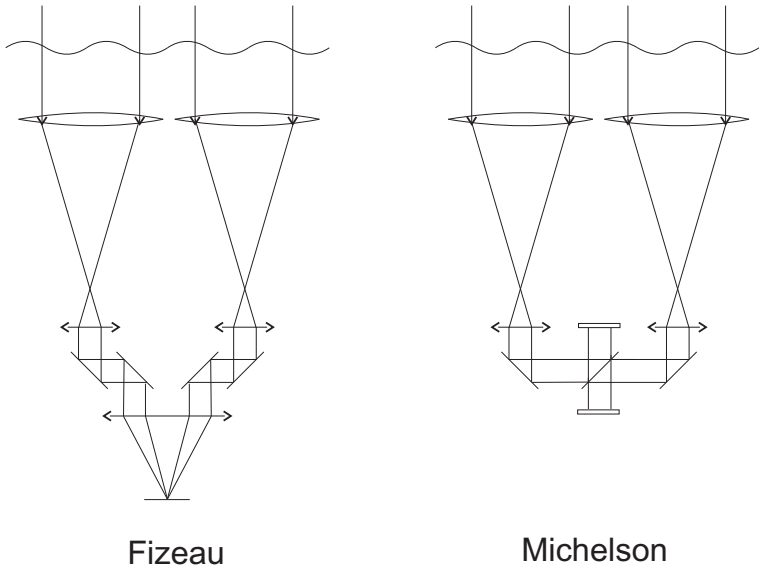

Figure 3.5: A comparison between a Fizeau and a Michelson interferometer.

In a Fizeau interferometer, instead, the wavefronts of a source located at infinite, interfere on the focal plane. The main advantage of Fizeau interferometry in the Visible and Infrared bands is the larger FoV which can be achieved (limited only by atmospheric parameters).

Because of these considerations, the LBT beams are combined in a Fizeau interferometric configuration, since the telescope structure optimizes such a concept, having a baseline comparable to the single apertures and holding both apertures on a common mount. The FoV is of the order of 10"x10". The theoretical resolution of such a system corresponds to a 22.8 m telescope's one ($\approx$0.02" in K-band, 2.2 μm). These unique characteristics hereabove described allow to improve studies in several different research fields.

3.2 LINC-NIRVANA

LINC-NIRVANA (LN, Herbst et al., 2003; Bizenberger et al., 2006), acronym for LBT INterferometric Camera and Near-InfraRed/Visible Adaptive iNterferometer for Astronomy, is a near-infrared imager which exploits Fizeau-type beam combination and multi-conjugated adaptive optics (MCAO) to achieve the spatial resolution of a 23-meter telescope. It is one of the most technologically advanced instruments for LBT and is being realized by a consortium of four institutes: Max-Planck-Institut für Astronomie (MPIA) in Heidelberg, INAF in Italy (including the observatories of Padova, Bologna, Arcetri and Rome), Universität zu Köln and Max-Planck-Institut für Radioastronomie (MPIfR) in Bonn.

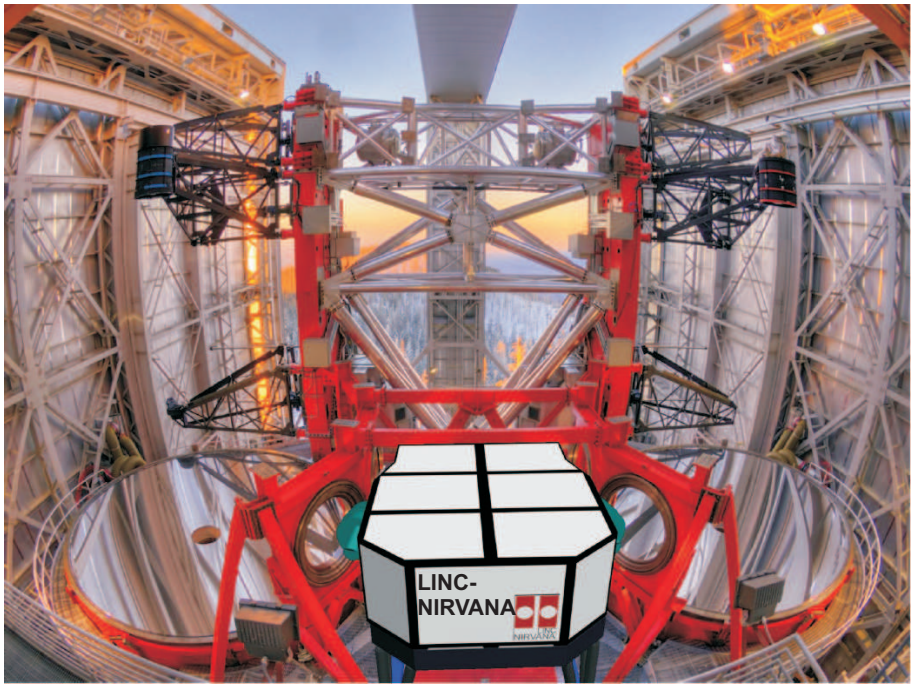

Figure 3.6: LINC-NIRVANA in its future location at gregorian bent focal station at LBT.

In LINC-NIRVANA case, the highest priority is to be able to search for NGSs in a large FoV, in order to achieve a good correction of the turbulence at every galactic latitude and in between the many approaches to implement MCAO, explained in section 1.5, the layer-oriented one has been selected. NIRVANA MCAO is based on multi-pyramid WFS, working in the visible (Ragazzoni et al., 2003).
To reconstruct the deformations introduced on the wavefront by atmospheric turbulence, each telescope arm is equipped with a pair of WFSs: a Ground-layer Wavefront Sensor (GWS), for the correction of ground-based turbulence and a Mid-High Wavefront Sensor (MWHS) for the correction of high atmospheric layers. As foreseen in

the MFoV concept (section 1.5.3), the first sensor can look up to 12 NGSs in an annuar FoV of 2-6' diameter and is conjugated to the secondary adaptive mirror; the second can look up to 8 NGSs in a circular FoV of 2' (corresponding to the "hole" of the previous field), and is conjugated to a DM which in principle can be conjugated between 7 and 15 km height. Each star light is optically summed so that also dimmer stars can contribute to the increase of signal-to-noise, since what really is important is the integrated limiting magnitude.

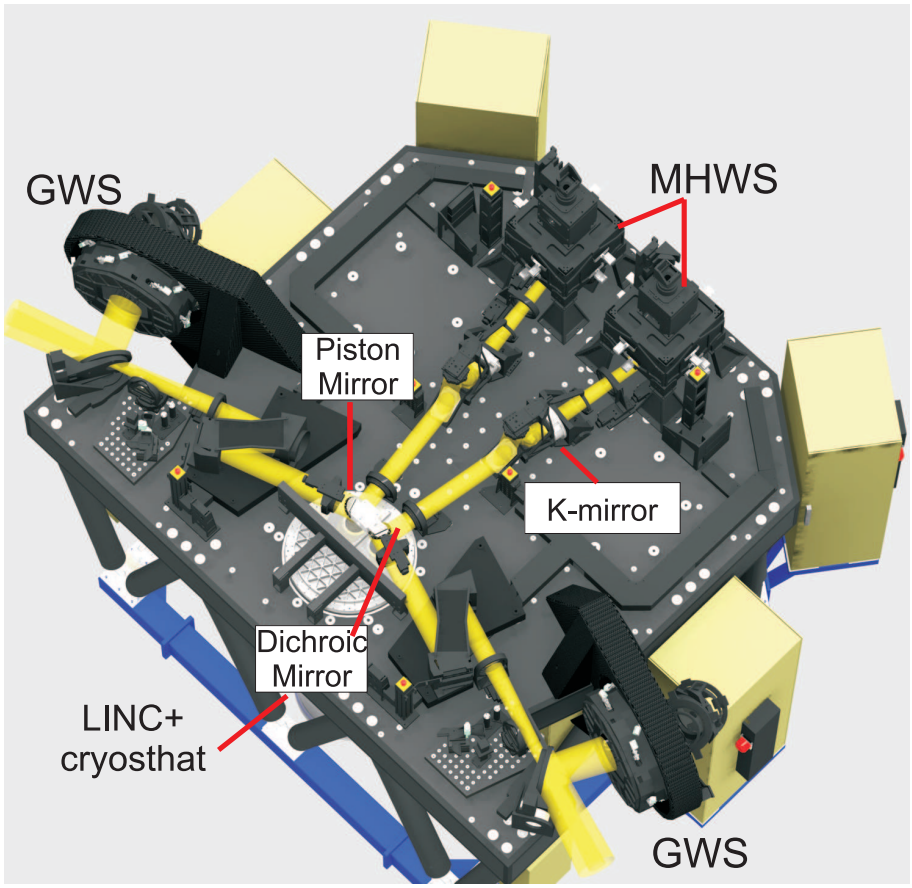

Figure 3.7: LINC-NIRVANA optical carbon fiber bench (6 × 4 × 3.40 m) fully populated: the two GWSs and the 2 MHWSs are highlighted. It is possible to see the beam path inside the bench, in particular the incoming beam, divided in two parts by the annular mirror (tilted of 45 ○): the central 2' are transmitted toward MHWS and science camera, while the annular between 2' and 6' is reflected toward the GWS

The light path, shown in figure 3.7 and summarized in the flow diagram (figure 3.10), will be briefly described. All the optical components are mounted on a carbon fiber optical bench, which ensures mechanical rigidity and the minimization of temperature variations. The F/15 beam coming from each telescope arm, is separated in

two areas. The 2-6' outer annular region is folded by a properly dimensioned annular mirror toward the Ground-layer Wavefront Sensor (GWS), where the distortion due to ground-layer turbulence is retrieved and sent to the adaptive secondary mirror. The central 2' are collimated before reaching a DM. In principle the conjugation height of the annular mirror can be easily adjusted to the night conditions (not requiring a large space thanks to the Z-configuration (see figure 3.7)). Anyhow for the first light of the system the conjugation height is fixed at 7 km height. The beams coming from the two sides of LBT are cophased using a Beam Combiner, able to compensate the OPD introduced by the different regions of atmosphere encountered or to system flexures. This compensation is obtained moving along the axis which links the two telescopes, a pair of mirrors tilted by 45° with respect to incoming beams (Piston Mirror). The two beams, now parallel, are then sent to a dichroic, located close to the image plane, which allows the IR light to be folded to the IR detector (HAWAII-2, 2048 x 2048 pixel, 0.005 arcsec/pixel, with a 10"x 10" scientific field), located in a cryostat below the optical bench to minimize thermal background. The visible band (between 0,6 and 1 μm) is, instead, focused by a F/20 objective and sent toward Mid-High Wavefront Sensor(MHWS), which reconstructs the wavefront distortion at the DM conjugation height. Because of the alt-azimutal mount of LBT optical derotators named K-mirrors are inserted in the path toward MHWS, while the GWS is mounted on a rotating unit.

LINC-NIRVANA main parameters are listed in table 3.2.

LINC-NIRVANA characteristics

Instrument type	NIR Fizeau interferometer for imaging
Wavelength	Science, fringe tracking: 1.0-2.4 μm (J,H,K)
	Adaptive optics: 0.6-1 μm
FoV	Science: 10" x 10"
	Fringe tracker: 1' x 1.5'
	MHWS: 2' diameter circular
	GWS: 2'-6' diameter annular
Diffraction limit	J-band: λ/B=0.01" λ/D=0.03"
	K-band: λ/B=0.02" λ/D=0.07"

Table 3.2: LINC-NIRVANA main characteristics

LINC-NIRVANA interferometer should allow to realize photometry (and potentially spectrocopy) on a 10"×10" FoV, with a resolution equivalent to the diffraction limit of a 22.8 m: 0.02" in K-band. It is therefore an imaging instrument valid for a different variety of astrophysical cases requiring a high sensitivity and high angular resolution in the near IR. Due to the binocular nature of the telescope, the PSF of each observed object will be described as the Airy figure of the diffraction limit of

an 8.4 m telescope, crossed by Young fringes due to the interference between the two apertures, characterized by a 22.8 m baseline. As shown in figure 3.8, the angular resolution along one axis is given by λ/D (where D is one aperture diameter), while the resolution along the ortogonal axis coincides with the width λ/B of the central interference fringe (where B is the baseline). For this reason the angular resolution is anisotrope. To be able to obtain an image with an isotrope image with a 23 m telescope resolution, the same scientific object needs to be observed at different orientations, taking advantage of the Earth rotation which varies the baseline orientation. Afterwards the images are combined through a data deconvolution process and an image with 22.8 m angular resolution is retrieved.

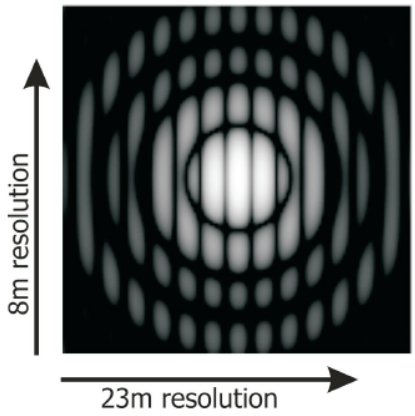

Figure 3.8: LBT pupil geometric and typical PSF.

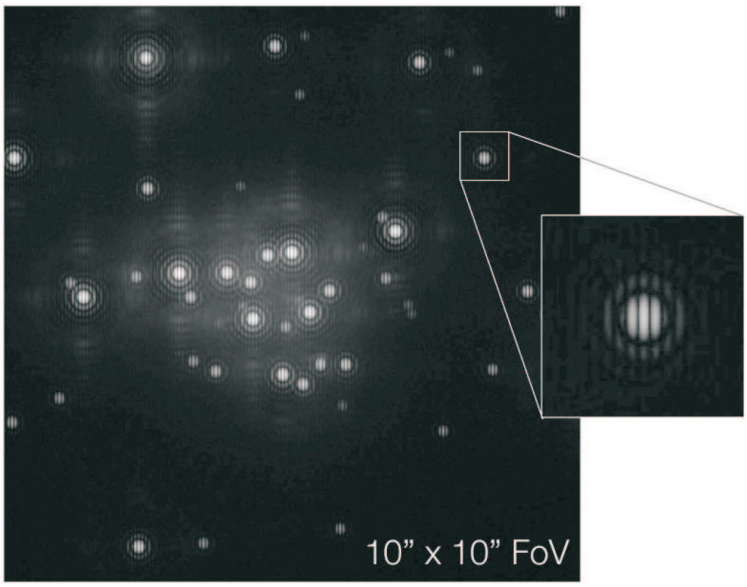

Figure 3.9: Globular cluster simulated image. All the objects in the FoV show the typical PSF.

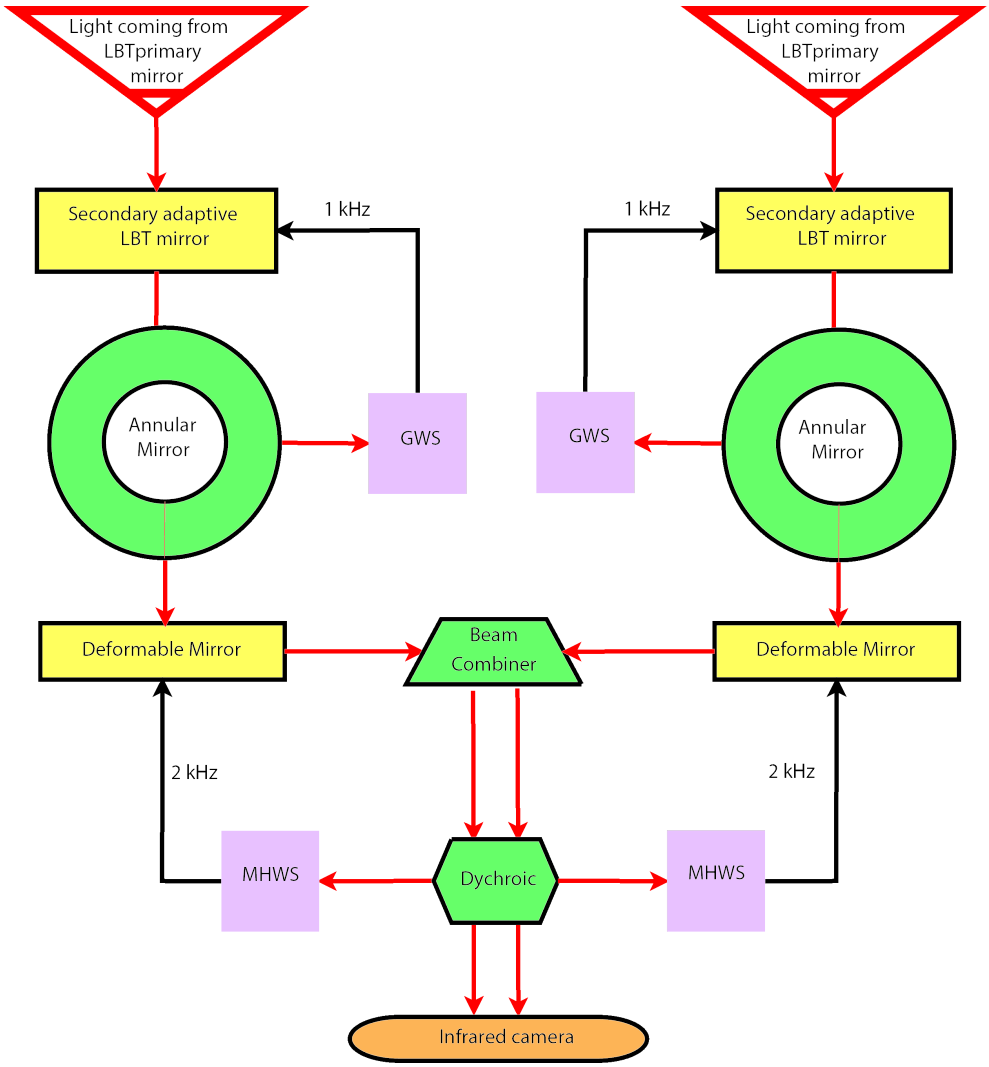

Figure 3.10: Flow chart of LINC-NIRVANA: WFSs (purple),deformable mirrors (yellow) and auxiliary optical elements (green) are highighted. Red arrows show the light optical path, black ones the information sent between system components.

3.3 The Ground-layer Wavefront Sensor Alignment, Integration and Verification phase

The Ground layer Wavefront Sensors (GWS) consist of two identical units (one for each LBT arm) optically conjugated at a 100 m altitude that is to say just above the entrance pupil of the telescope and has as a corresponding DM is the Adaptive Secondary Mirrors, in order to sense the effects caused to the wavefront by the lower layers of the turbulence. For a better comprehension, we will discuss from now on just one of the two units. The whole unit is mounted on a bearing in order to compensate for the field rotation during observations and is attached to one side of LN optical bench thanks to a carbon fiber supporting arm.
Part of the telescope incoming beam is folded by an annular mirror (2'-6' annular FoV, see figure 3.11) to the GWS.

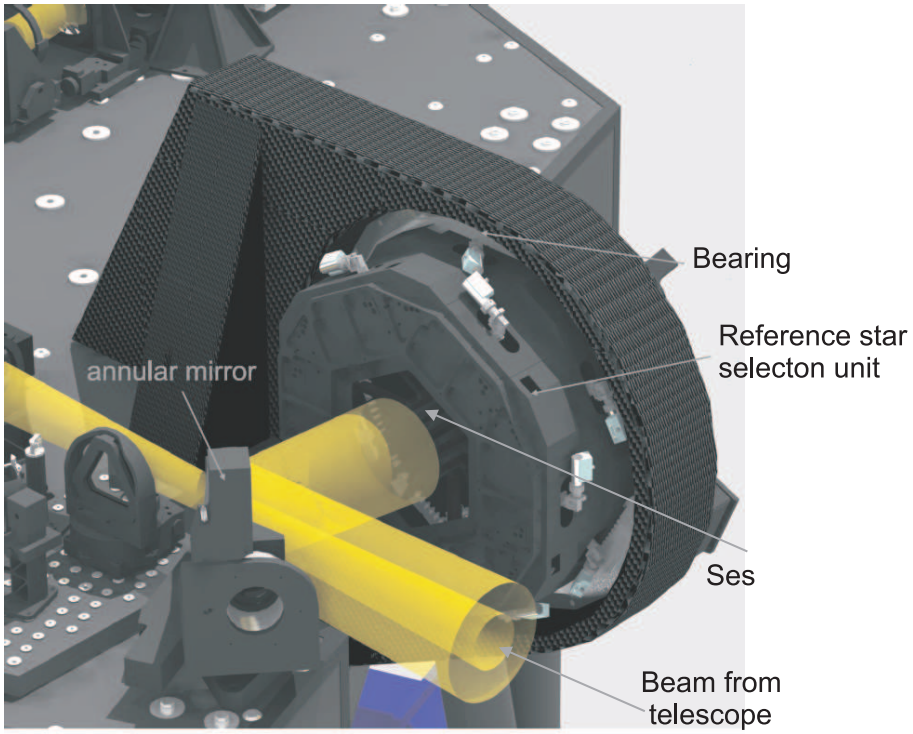

Figure 3.11: GWS CAD drawing showing the beam coming from the telescope deflected by an annular mirror toward the entrance of the GWS. Very close to the focal plane are positioned the Star Enlargers. All system is mounted on a rotating bearing which allows to compensate for field rotation.

Very close to the entrance focal plane (characterized by an F/15 focal ratio), 24 motorized remotely-controlled stages (in an x-y configuration) can position up to 12 Star Enlargers (SE, optical devices described in section 3.3.1) inside the FoV, in

order to select the NGSs to be used for the wavefront sensing. Each SE increases the F/# of the light coming from a reference star, enlarging the stars dimension but not their reciprocal distances, and focuses it on the pin of a refractive pyramid, after which four beams are produced.
The Pupil Re-Imager (PR-I), a Schmidt-folded camera composed by a flat folding mirror, a parabolic mirror and a 4-lenses corrector, collects the beams produced by each pyramid and superimposes them producing four common images of the entrance pupil of the telescope on the CCD (a Scimeasure CCD50 with 128 × 128 pixels with pixel-size 24 μm). The differential intensity distribution of the light between the pupils allows the reconstruction of the incoming wavefront, according to the Pyramid WFS concept.
The GWS main components just outlined can be seen in figure 3.12 and their main characteristics are reported in table 3.3.

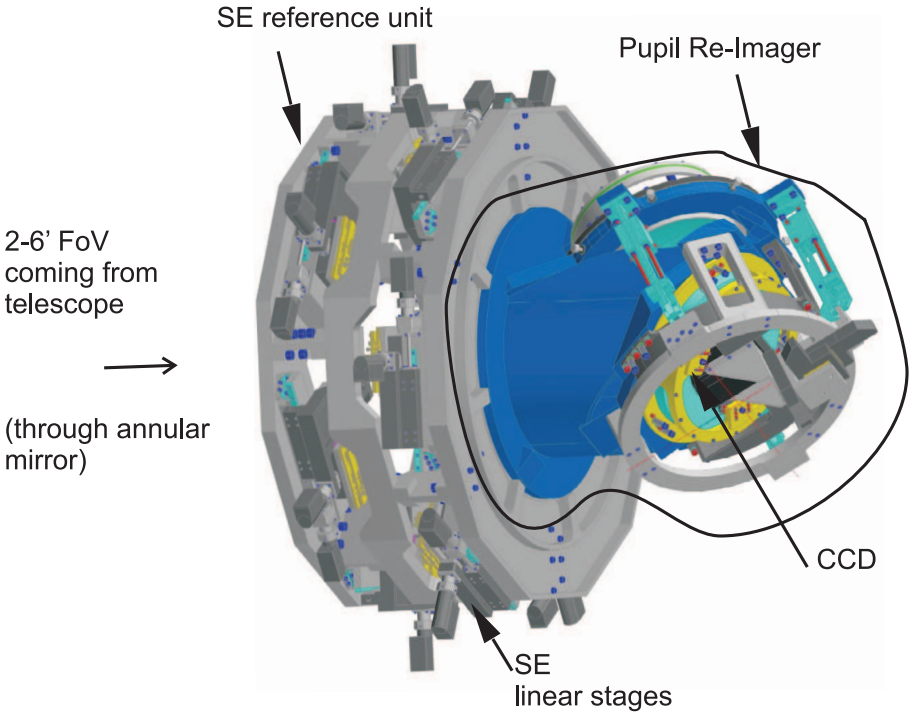

Figure 3.12: GWS CAD drawing. The flanges to which SE stages are connected can be observed, as well as PR-I and CCD.

One of the main challenges realizing the optical LO approach (see section 1.5.2) is the optical co-addition of the light from the reference stars on the same detector. In fact, the achievement of an accurate pupil superposition at the level of the detector requires a great number of opto-mechanical constraints and tolerances, making the Alignment, Integration and Verification (AIV) of the system very challenging.

Theoretical incoming beam F/#: F/15
Incoming FoV: 2'-6' annular
SE (12)
d_1: 5 mm
d_2: 14.7 mm
f_1: 13 mm
f_2: 162.5mm
k: 12.5
F'=F/187.5
FoV: $>$ 1"
Minimum NGS distance: 30"
Pyramids β: 0.566°
PR-I
f_{PR-I}: 220 mm
d_{PR-I}: 245 mm
F_{PR-I}: F/0.9
CCD
Pixels: 128×128
Pixel dimension: 24 μm

Table 3.3: Main optical parameters of GWS components.

In section 3.3.2 are described the main tolerances taken into account during the alignment of the system, in order to obtain and to maintain in all conditions (thermal variations, gravity...) the requested level of pupil superposition.
Afterwards, in sections 3.3.1, 3.3.3), a brief description of the main opto-mechanical components (SEs, PR-I) and their alignment procedures are depicted, as well as the characterization tests performed on the fast frame-rate CCD (section 3.3.4).
Then, in section 3.3.5 is described the procedure devised and followed for the overall integration, alignment and verification tests performed on the first GWS (GWS DX) in the adaptive optics laboratory of the Astronomical Observatory of Padova.
In section 3.3.7 are thoroughly discussed the results of flexures tests, performed at the Max Planck Institute für Astronomie in Heidelberg, taking advantage of their facilities and testing the complete system on the LN optical bench. Finally, in section 3.4 the results of the performed worked are discussed and future steps, in particular concerning the GWS pathfinder experiment at LBT, are also described.

3.3.1 Star Enlargers and pyramids

One of the practical difficulties in the implementation of the layer-oriented approach is the large size of the re-imaged pupils formed by the pyramids, which would impose the use of large and with very fast focal ratio optics, including CCDs, impractical in AO because of the need of fast frame-rates and low read-out noise, generally granted by smaller CCDs.
The Star Enlarger (SE) is an optical system used to enlarge the guide star image on the pin of the pyramid, enlarging the focal ratio of each reference star individually. In this way the re-imaged pupil size, inversely proportional to the focal ratio, can be arbitrarily reduced to fit in the detector, while the reciprocal distances among the stars in the focal plane are left unchanged (Ragazzoni et al., 2005). Moreover, this optical system reduces the requirement tolerances on the pyramid pin, increasing the spot size reaching it.
The entrance telescope focal plane is characterized by a focal ratio F/15. Each NGS beam, assumed to be telecentric, is collimated by a first small achromatic doublet (SE1, $f_1 = 13$ mm, $d_1 = 5$ mm). A second achromatic doublet (SE2, $f_2 = 162.5$ mm, $d_2 = 14.7$ mm), positioned at a distance of $f_1 + f_2$ from the intermediate pupil image, returns an enlarged star size , with a focal ratio of F'=kF, where k, the enlarging factor is $k = f_2/f_1 = 12.5$ and therefore F'=F/187.5. At a distance of f_2 from the SE2 is positioned the vertex of the refractive pyramid. The optical scheme of a SE is shown in figure 3.13. The pyramids, realized in BK7 glass, are fundamental

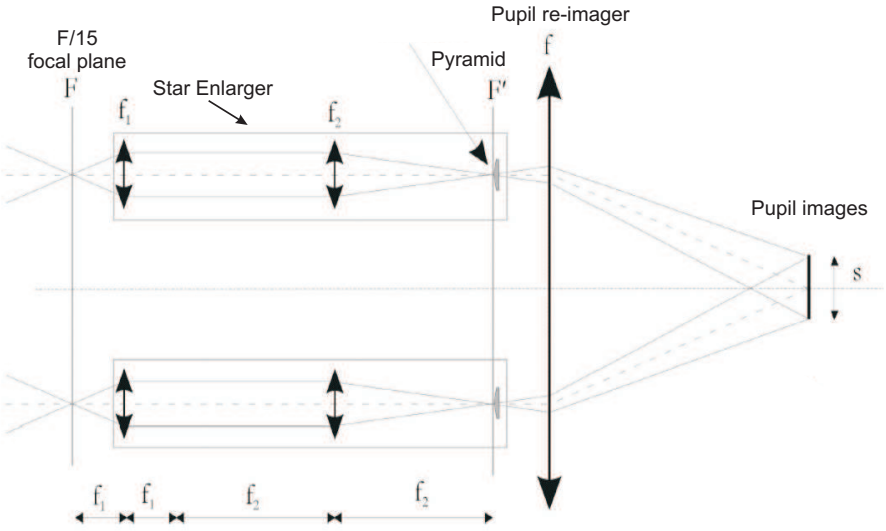

Figure 3.13: Optical scheme of the GWS. The incoming beam focal ratio $F = F/15$ is resized to a $F' = F/187.5$ beam by the SE. A lens with a focal length f recreates pupils of dimension $s = f/F'$ on the CCD. The two achromatic doublets in the SEs have focal length of f_1=13 mm and f_2=162.5 mm.

elements inside the GWS. It is very important that the diverging angle of the four beams coming from the pyramids are kept inside the requirement $\beta = 0.566° \pm 0.008°$ to reduce the pupil blur, due to the superimposition of the pupils coming from the 12 SEs, down to 5 μm. This has been verified as reported in Farinato et al. (2008). Moreover each pyramid face is a prism and introduces a chromatic effect on the pupil image, estimated with Zemax computations, resulting in a pupil blur of 6 μm.
From the mechanical point of view, each Star Enlarger lenses and pyramid are mounted on three different aluminum barrels, mounted on a common mechanical support, realized in order to minimize the vignetting and to allow focus, centering and tilt adjustment of the three optical components (see figure 3.14).

Figure 3.14: The mechanical structure of one SE, supporting the 2 lenses and the pyramid. The T-shaped support is needed to connect the SESs to the GWSs stages.

The SE alignment has been completely realized in the Observatory of Padova laboratories, and the performed verification test results are inside the tolerances set before the alignment (concerning relative distances and decentering between optical components), to fulfill the requirements listed in section 3.3.2, in terms of diffraction, introduced aberration and enlarging factor repeatability. In particular, concerning k, the magnification factor of the star enlarger, the mean resulting value is k = 12.51 and the measured RMS repeatability is 1/605, far lower than the 1/240 requirement, leading to a 5 μm pupil blur. The FoV size was checked to be 1.3". This size is determined by SE2 lens and its holder which act as a stop surface. I will not enter in the details of this alignment, just an image of the alignment setup is shown in figure 3.15. The 12 aligned SEs for the first GWS are shown in figure 3.16.

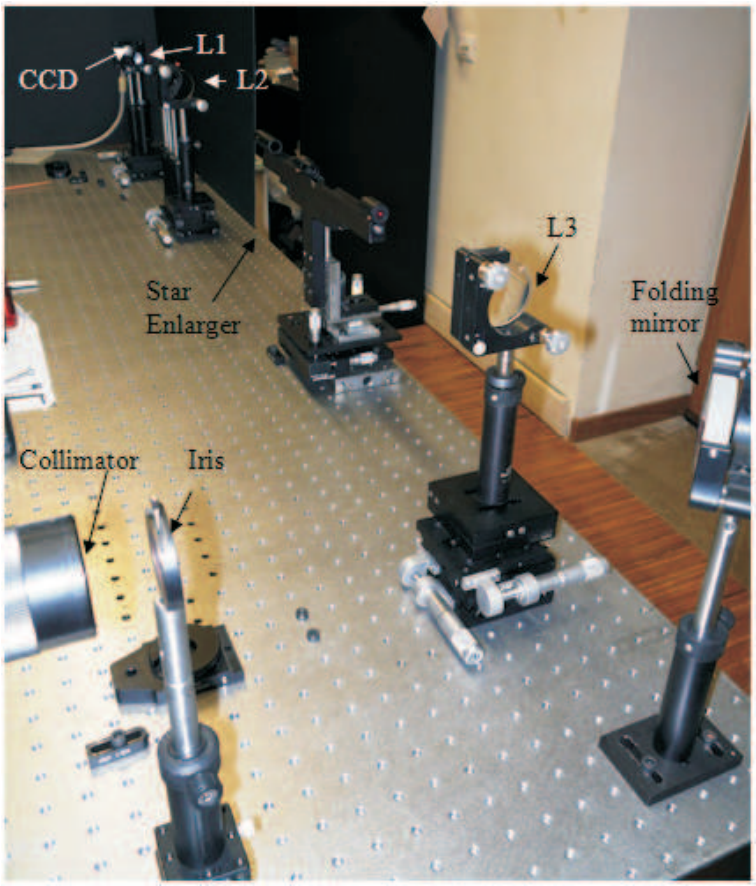

Figure 3.15: Setup for the internal alignment of the SEs.

Figure 3.16: 12 aligned SEs for the GWS.

3.3.2 Error budget

An error budget is an essential tool for evaluating and tracking the various factors in a project design that may degrade performance and, as a consequence, confirm that project requirements can be and are being met. It typically includes terms associated with subsystems designed by different teams of engineers and fabricated by different vendors and it is a useful tool at all levels of design since it provides a mean to negotiate design trades in the broadest possible context. Error budgeting is in many ways fundamental to the mission of systems engineering and of course to the overall project success.
What we are interested in is to infer the estimate WaveFront Error (WFE) and, thanks to the Marechal law, derive the Strehl achievable on sky for our system. The upper limit is given by the requirement to obtain a Strehl Ratio of 0.85 in K-band and 0.60 in J-band.

The large number of opto-mechanical elements (12 star enlargers, each with 3 optical components in a wide annular FoV and sending the light to a common pupil re-imager) which compose the GWS, and consequently the large number of potentially introduced errors, due both to components and to uncertainties related to their alignment, together with the request to obtain a really good pupils superposition onto the detector, translates into a great number of requirements and tolerances to be met in order to not excessively decrease the performance of the system. Evaluating the performances is crucial to define specifications of components, to be asked to the providing companies.
The rotation of the entire WFS to compensate for the sky movement, moreover, introduces a further difficulty in ensuring the required pupil superposition stability. Those error sources and their consequent effect as blur on the four re-imaged pupils and the related requirement will be depicted. A blur on the pupil translates into relative shifts of the sub-apertures in which the pupils are divided, causing a “cross-talk" between adjacent sub-apertures for pupils produced by different SEs (i.e. in a certain sub-aperture there will be some undesired light coming from the adjacent ones), altering the signal analysis to reconstruct the wavefront. Of course, this shift should be much smaller than the sub-aperture size in order to minimize the undesired cross-talk. The sub-apertures considered have a dimension of 48×48 μm (assuming a 2×2 binning), and correspond to the sampling of the pupil in 24×24 sub-apertures. Initially, tolerances had been set to achieve a total pupil blur of the order of one tenth of sub-aperture (meaning about 5 μm). However, some mechanical components could not be provided with the needed requirements (i.e linear stages in x-y configuration with pitch and roll below 25 microradians). For this reason an investigation on how SR performance would have decreased while scaling the specs to about a half of sub-aperture have started. The results still gave reasonable SR (of about 0.60 in J-band). Due also to the fact that the tolerances were too tight also on

other components and the alignment size, this has been set as the new requirement to be met, in worst conditions. Therefore, the maximum contribution from each item of the error budget is supposed to give a pupil shift lower than 1/10th of a sub-aperture. The expected performances are generally tested, as well as the alignment precision, to check their compliance with the specifications and, in case of better or worst results, relax or tighten the tolerances for other error budget items. The detail of the described components and the verification of their estimated performance, , will be found in next sections.

GWS components

- **SE diffraction**: it is due to the SE optical design, and it is estimated with Zemax computation as a **7** μ**m** blur on the pupil;

- **Pyramid chromatism**: pyramids are dispersive elements, and they are working with polychromatic light. The chromatism introduced, estimated with Zemax computations, results in a pupil blur of **6**μ**m**;

- **Pyramid vertex angle**: the constraint is on the repeatability of the pyramid vertex angle of the 12 SEs. The requirement is $\pm$17" repeatability, which leads to a blur on the pupil of **5** μ**m**;

- **Pyramid faces orthogonality**: pyramid faces orthogonality requirement asked to the providing company ($\pm$5') can be translated into a maximum pupil blur of 5μm. However, the providing company test certificate reports a pyramid face orthogonality better than 50" for all the delivered pyramids, translating into a pupil blur lower than **1**μ**m**;

- **Linear stages wobble**: The effect on the detector plane both of pitch and roll of the linear stage which move a SE is a shift of the 4 pupils generated by the pyramid held by that star enlarger. The pupils shift due to a SE tilt α can be computed as

$$s = (\frac{1}{k} + 1) \cdot \alpha \cdot f_{PR-I}$$

  where k is the SE enlarging factor and f_{PR-I} the PR-I equivalent focal length. The specification is a shift of the order of 1/10 of the dimension of the sub-aperture itself, meaning a 25μrad requirement for the linear stages pitch and roll. The real values measured on the SE positioning stages delivered by the providing company, translate in a SE 5" RMS global tilt (25μrad). This wobble translates into a pupil blur of about **5**μ**m**;

GWS internal alignment

- **Enlarging factor k**: is the requirement on the repeatability of k value, since SEs with different k produce pupils of different sizes. Reminding that the chosen value is k = 12.50, the specification is a repeatability of k better than 1/240, leading to a pupil blur of **5μm**;
- **SE relative tilt**: as for the linear stages wobble, the effect of a tilt of a SE with respect to the PR-I optical axis is a shift of the 4 pupils generated by the pyramid. A tenth of a sub-aperture corresponds to a maximum SE relative tilt of 5", which translates in a pupil blur of 5 **μm**.
- **Pyramid orientation**: a different orientation of one pyramid with respect to the others leads to an incorrect superposition. The tolerance for the pyramids differential orientation is 10'. The tenth of a sub-aperture, considered on the pupil edges (1.68 mm away from the rotation center) corresponds to a pupil blur of **5 μm**.
- **Pupil Re-Imager optical quality**: PR-I optical quality in terms of blur onto the pupil image can be directly verified on the PR-I itself once it is aligned, considering it as a stand alone camera and measuring the RMS spot radius of the spots in its FoV ($\pm$0.44°). Initial computations on the alignment precision gave a maximum Root Mean Square (RMS) spot radius in the edges of the FoV of 25 μm. However, from laboratory measurements, obtained feeding the PR-I with a wide collimated beam, we retrieved a value of **13μm**, which allowed us to relax other tolerances.

Thermal effects LN and, consequently, the GWS are required to work in a temperature range from -15° to +20°(ΔT = 35°C). However, the detector can be refocused in order to compensate for temperature variations, so for ΔT > 5°C we plan to build a look-up table with a 5°C increment. Only the PR-I optical quality degrades for a variation of less than 5°, resulting in a pupil blur of **7μm**, whereas in this same range, we can consider negligible the influence on the SE lenses misalignments and on the wobble of linear stages.

SEs defocus issue Because of the LBT focal plane being curve, there is a difference in the focal plane position along the optical axis which depends on the distance between the center and the edge of the FoV. A check on the LBT optical design has been performed with Zemax, resulting in the focal plane positions summarized in table 3.4 and represented in figure 3.17.

The PtV of the curved focal plane in the GWS on board LINC-NIRVANA is 4.94 mm, between the focal position at 2' and at 6' radius. Because the pyramids will

FoV radius [arcmin]	FP offset [mm]	Defocus RMS [nm]
1	0.66	102
2	2.65	410
3	5.97	922

Table 3.4: Offset of the focal position along the FoV of LBT with respect to the 0° FoV focus. The resulting defocus signals measured by the WFS are listed too.

not be modulated, it is important to check if in the best seeing conditions (assumed to be 0.25") the seeing effect on the pyramid WFS exceeds or not the one caused by defocus. In case the defocus will dominate, the defocus term will saturate the pyramid WFS causing the impossibility to retrieve higher order aberrations. As the GLAO correction leads to a gain in terms of equivalent seeing by a factor two (to be conservative), the above mentioned condition translates into the one that half of the seeing must exceed the size of the defocused spot, in angular terms. A Δz SE displacement with respect to the LBT F/15 focal plane leads to an angular spot enlargement by:

$$\theta = \frac{206265'' \cdot \Delta z}{D \cdot F^2}$$

Using mm as unit of measure and considering the factor 2 correction operated by GLAO, we get θ= 0.11Δz and considering the PtV of 4.94 mm this translates into the condition that the seeing should be worse than 0.54", while the considered very good seeing limit for estimation is 0.25". For this reason it has been devised the solution of dividing the GWS annular FoV into two equivalent areas. The computed best offset to divide the two areas is 3.31 mm, corresponding to 2.24 arcmin radius in the FoV. In such a configuration the inner 12.57 arcmin^2 are in intra-focal position, while the outer 12.57 arcmin^2 are in extra-focal position. The effective defocus signal retrieved by the WFS is depending on the asterism of the NGSs, and, since it is not used in the AO loop, it's only affecting the WFS capability to retrieve higher order aberrations. It has been decided to split the SEs into two groups, odd SEs and even SEs. The first group spans the 1'-2.2' radius area while the second one the 2.2'-3' radius area. For each SEs group it has been identified an offset to which align it in a way to both divide their regions into two equivalent areas, which will respectively be in intra-focal and extra-focal position, and to have a similar residual defocus WFE in the edges. The odd SEs are aligned and focused to a radius of 1.71' and their offset is 1.93 mm from the 0° FoV focus, while the even SEs are aligned to a radius of 2.63', with an offset of 4.5 mm. The residual maximum defocus for both groups is 2.65 mm, so, applying the formula derived above, the seeing should be better of 0.29" to become an issue, that is to say a rather unlikely case. This will be the limit of the correction which can be reached with the ground-layer loop, meaning that in case of good seeing (lower than 0.30"), the GWS will not be sensitive to the atmospheric

aberration. Of course this will only be an extremely conservative limit, that would be effective only in the case of an asterism in which all the NGSs were placed on the outer 6' diameter rings of the FoV. If a slightly better case, in which all the stars are placed in a 5.8' ring, is considered, such a seeing limit would decrease to 0.23". In any case the effect of even a huge defocus is **negligible** in terms of pupil blur on the detector and only results in a defocus signal detected by the WFS, which can be subtracted as a static aberration, during the calibration procedures.

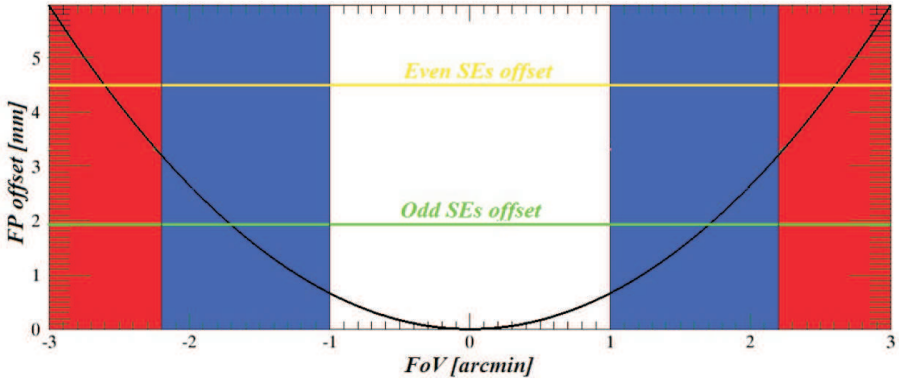

Figure 3.17: Curvature of the LBT focal plane for a 6' FoV. The coloured areas highlight 2'-6' annular FoV which is re-imaged at theGWS entrance focal plane. The blue area is the FoV covered by the odd-SEs, focused on an offset represented by the green line. The red area is the FoV covered by the even-SEs, focused on an offset represented by the yellow line. The two offsets are been chosen in order to minimize the residual defocus WFE on their respective regions.

Bearing contribution

- Bearing wobble: it produces a global tilt of the entire GWS and a consequent pupil shift, according to:

$$\Delta s = \alpha \frac{f_{PR-I}}{k_{SE}}$$

  varying with time and so resulting in an additional pupil blur. The measured bearing wobble is lower than 12 arcsec, producing a pupil shift of about **1** μ**m**.

Flexures A Finite Element Analysis (FEA) concerning the GWS structure flexures has been carried out by the mechanics providing company, resulting in an estimated deformation of about 0.07 mm, but a lack of detailed information clearly appears. Let's us, therefore, do some preliminary considerations:

- a deformation which occurs along the optical axis, would entirely translate in a defocus signal, not introducing relevant blur onto the pupil (as already discussed for SE defocus);

- a deformation which occurs in a direction orthogonal to the optical axis, has an effect which obviously depends upon the point on which we apply it. If we consider this deformation as a 0.07 mm rigid shift of the whole GWS with respect to its optical axis (of course this is a very conservative hypothesis), the overall effect is a GWS decentering, translating into a SE displacement during an exposure. Moreover, if we consider a SE remote re-centering every minute, the maximum not-corrected SE displacement translates into a residual 10 μm SEs shift. As the GWS global decenter, however, this effect would not increase the pupil blur, but would only introduce a tip-tilt signal.

- A rigid tilt of the whole GWS with respect to the bearing, in the most conservative case would introduce a tilt of the GWS of about 24" which would translate into a 2 μm pupil shift. Since this shift would be the same for the pupil images produced by all the SEs, this effect would not introduce any pupil blur.

The only misalignment induced by flexures which translates into an actual pupil blur is a differential tilt of the Star Enlargers, which cannot be estimated only knowing the maximum shift of a point in the whole system. With our *a priori* informations, then, a real estimation of the effect of GWS flexures on the pupil blur cannot be done. The actual effect of the flexures onto the pupils position has been quantified, however, after the system delivery at the MPIA in Heidelberg, where the GWS installation on the final LN optical bench, mounted on a tilt platform, allowed the direct measurement of such an effect. The estimated effect of GWS flexures will be discussed at the end of this chapter.

- **SE tilt due to support flexures**: SE support flexures cause 40μrad tilt for 90° rotation. Maximum rotation angle during observation is 60°and the SE tilt becomes approximately 2/3 of 40μrad, translating into a **6μm** blur at the level of the pupil.

- **SE tilt due to ring flexures**: 6 SE experience no tilt due to ring flexures, while the other 6 have a 60μrad tilt in a common direction. Differential effect is 30μrad. At 60° rotation, the estimated tilt is approximately 20μrad, corresponding to a **4μm** blur onto the pupil.

- **SE tilt due to stage flexures**: the flexures of the linear and tip-tilt stages coupled together for different orientations with respect to the gravity vector

have been measured by the MPIA team in Heidelberg. The highest differential tilt, retrieved for different orientations of the tip-tilt and the linear stage with respect to the inclination axis, is 24" for a complete 60° range of inclination. This reduces to about 4" of tilt if the maximum differential inclination which the system can experience during one exposure is considered. The effect of such a differential tilt of the SEs, during an exposure, translates into a pupil blur of $\mathbf{4\mu m}$.

Error budget conclusions Table 3.18, which summarizes all the error budget items described above, will be presented at the end of this chapter with the updated values coming from the verification tests. The conversion from pupil blur to WaveFront Error (WFE) has been accomplished according to the relation shown in figure 3.18, which has been computed by an end-to-end simulation (seeing FWHM = 0.7" in R band, turbulence equally divided between ground and high altitude layer).

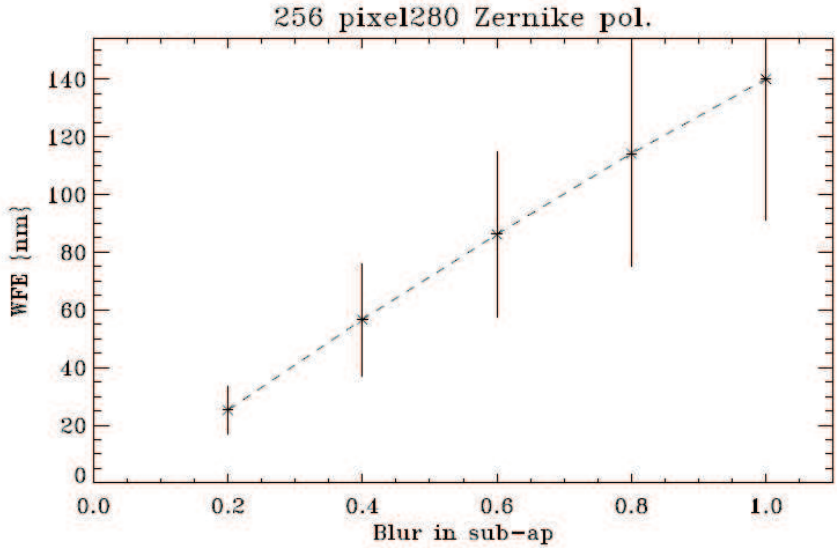

Figure 3.18: Relation between blur in sub-apertures and WFE devised through an end-to-end simulation.

The sum of all these contributions, converted in WaveFront Error (WFE), thanks to the Marechal's law

$$SR(\lambda) = e^{-(2\cdot\pi\cdot WFE/\lambda)^2}$$

is used to determine the total Strehl Ratio of the GWS.

One can notice that some of the considered items are not introducing any applicable blur onto the pupil, in most of the cases because they are acting on the WFS linearity side, in the sense that such sources of error do not affect the pupil

resolution, but introduce a low order signal (tip, tilt defocus) onto the WFS, which can be either calibrated and subtracted or simply neglected, since the GWS is not asked to retrieve the very low order aberrations. These sources of error, however, have to be kept under control because they could exceed the linearity range of the WFS.

3.3.3 Pupil re-imager

The GWS pupil re-imager, realized using a combination of lenses and mirrors in a Folded-Schmidt camera configuration, optically co-adds the light coming from the 12 SE, forming four pupil images on a 128 $\times$ 128 pixels detector, which will be described in section 3.3.4.
It is composed of a flat annular mirror folding the beam toward a parabolic mirror (245 mm) which focuses the light toward an optical corrector (located inside the flat mirror hole and composed of 4 achromatic doublets). The latter acts as an objective lens and projects the images of the four pupils on the CCD (see figure 3.19 for the optical design). It delivers a very fast focal ratio F/0.9, being its focal length f=220 mm and its aperture d=245 mm.

The two mirrors are mounted on custom mounts equipped with different degrees of freedom to perform its alignment. The flat mirror has tip-tilt capabilities, being fixed to the main structure with three points at a relative distance of 120 °. The parabolic mirror mount is equipped with centering capabilities, which, combined with the tip-tilt mechanism of the objective, allow for the proper relative alignment of the PR-I optics. The tilt of the parabolic mirror can be performed thanks to three screws, positioned at a relative distance of 120° on the back of the mirror mount, which allow also the shift of the mirror on a plane perpendicular to the optical axis. The CCD is mounted on three x-y-z linear motorized stages which allow centering and focusing.

Pupil re-imager internal alignment

The goal of the PR-I alignment procedure is to make the parabolic mirror optical axis match the Prime focus corrector optical axis, within the requirements of 0.02 ° in tilt and 0.1 mm in de-center. Moreover, the distance between the parabolic mirror and the 4-lenses group has to be the nominal one, within a tolerance of 0.5 mm, to meet the requirement of having the RMS spot radius lower than 25 μm. Beams with a focal ratio F/187.5, coming from the SE, recreate the 4 pupils on the CCD plane, independently from which part of the parabolic mirror reflects them. Since the pupil re-imager and the SEs are integral (and connected to the same bearing), the positions of the 4 pupils on the CCD theoretically do not vary during the rotation of the bearing. It is not fundamental that the pupil re-imager optical axis matches

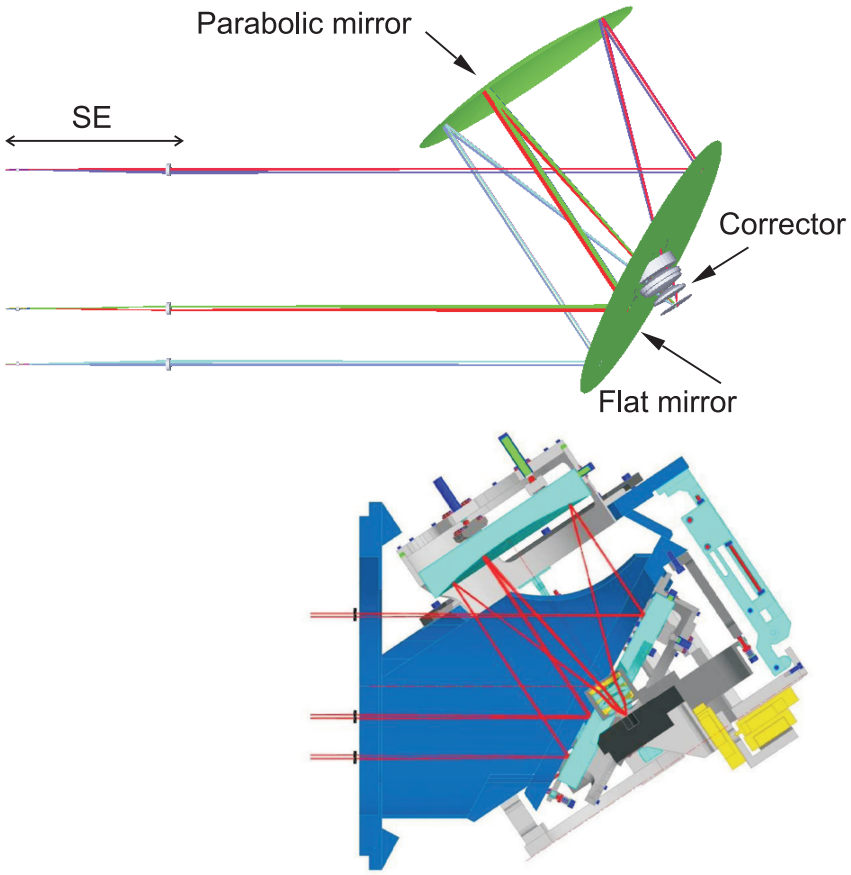

Figure 3.19: Optical layout of the Pupil Re-Imager (top) and CAD drawing of the optics and mechanics (bottom).

the bearing rotation axis, but they are required to be parallel, operation which can be performed in a second time adjusting the PR-I folding mirror in tip-tilt.
To simplify its internal alignment phases the PR-I has been positioned onto an optical bench rotated by 90° counterclock-wise with respect to its working position depicted in figure 3.19. Of course flexure variations between this and final position will have to be evaluated. It is necessary to explore a wide area of the parabolic mirror to leave the area of the osculating sphere (the area in which the parabola can be approximated with a sphere) to be able to correctly identify the optical axis. Therefore, the overall idea is to illuminate the PR-I with a wide collimated beam and to align the Parabola to the Objective (the small Optical Corrector or Prime Focus) checking the amount of coma on a defocused image of the reference spot on

axis and the optical quality over the entire PR-I FoV (0.88° diameter). To fold upward the collimated beam into the mirror an alignment setup flat mirror (330 mm) is positioned underneath the PR-I (it will be referred as setup mirror). The PR-I in this procedure is not oriented as it will be when mounted inside the GWS meaning that the gravity vector direction is different from the PR-I working one. However, the PR-I at the telescope will work in several gravity conditions, since it will rotate around its optical axis to de-rotate the FoV and it will be tilted together with the overall bench to follow the source in the sky. Moreover, the working conditions will be, from the flexures point of view, worse than the one adopted for the internal alignment. Because of this, the effect of the gravity on the mirrors and the test CCD, in this particular configuration, is not expected to introduce additional errors on the PR-I alignment.

The alignment procedure has been divided in six phases which will be hereafter described and the achieved results shown.

PHASE 1: On axis reference definition on the test camera This phase has the purpose to define the objective optical axis projection (PHASE 1A) and to align and center a test camera to the latter (PHASE 1B), materialized by a laser beam positioned on an optical breadboard (as shown in figure 3.20), with a precision of 27 μm in centering and 29" in tilt.

A. A small laser is mounted on a breadboard on the side of the removed PR-I parabola and provided with centering and tip-tilt capabilities (centering micrometers sensitivity: 0.01 mm , tip-tilt micrometer sensibility: 0.05 mm = 0.029").
Observing the back-reflected spots the objective optical axis is materialized. In order to minimize the alignment error, the alignment has been performed several times and the mean values of centering and tip-tilt positions are considered. The values obtained for this phase lead to a resulting movement of the spot on the CCD of $\pm$ 5 μm.

B. The test camera (2.2 μm pixel-size) is mounted on a magnetic baseplate (figure 3.21), which needs to be repositionable with a precision of $\pm$ 0.55 mm. Due to the limited space in that area and to the short focal extraction of the objective of the PR-I, it has been chosen a camera with no housing.
It is centered with respect to the objective optical axis, materialized by the laser, and properly focused; afterwards the position of the spot on the CCD is recorded.
To properly determine the total indetermination of the optical axis definition, further tests were performed, in particular:

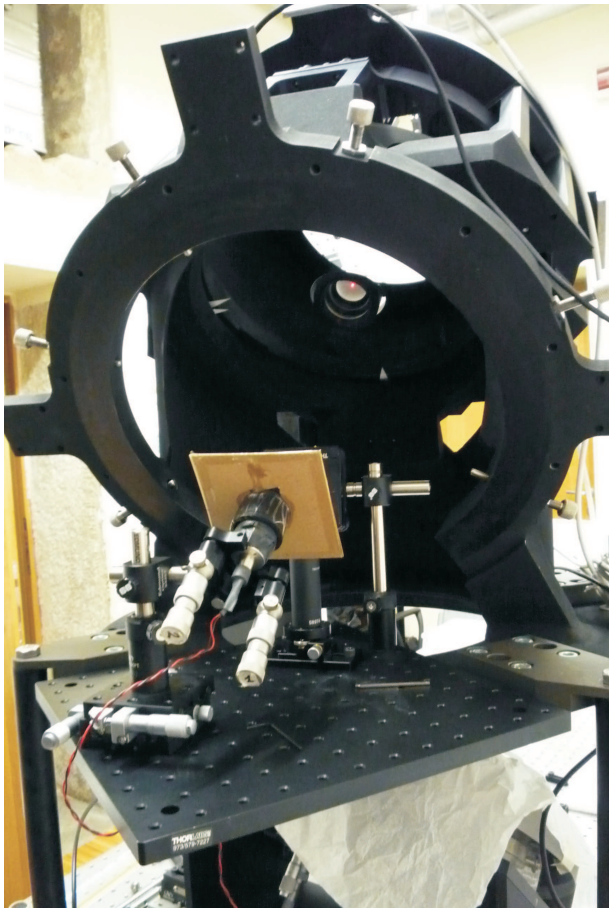

Figure 3.20: The laser source materializing the Prime focus corrector optical axis for phase 1A. It is positioned in the place of the PR-I parabola.

- Tests on repositionability of the test camera on its magnetic base plate. With the laser beam illuminating the test camera, the latter was removed and re-positioned 10 times and the spot centroid position was computed. The spot centroid moved in a range of 3.26 pixels in the camera x direction and 5.43 pixels in the y-direction, corresponding respectively to a 7.2 μm and a 11.9 μm ranges.

- Tests on the movement of the spot due to motorized stages repositioning. As previously described, the test camera is mounted on 3 motorized linear stages in x-y-z configuration. During the test, each of the three stages is re-initialized and sent to a specific position 10 times. Each time the position of the spot on the test camera is retrieved. Considering all the three contributions in their worst possible combination, the spot centroid is expected to move in a range of less than 4.4 μm (2 pixels) in the camera

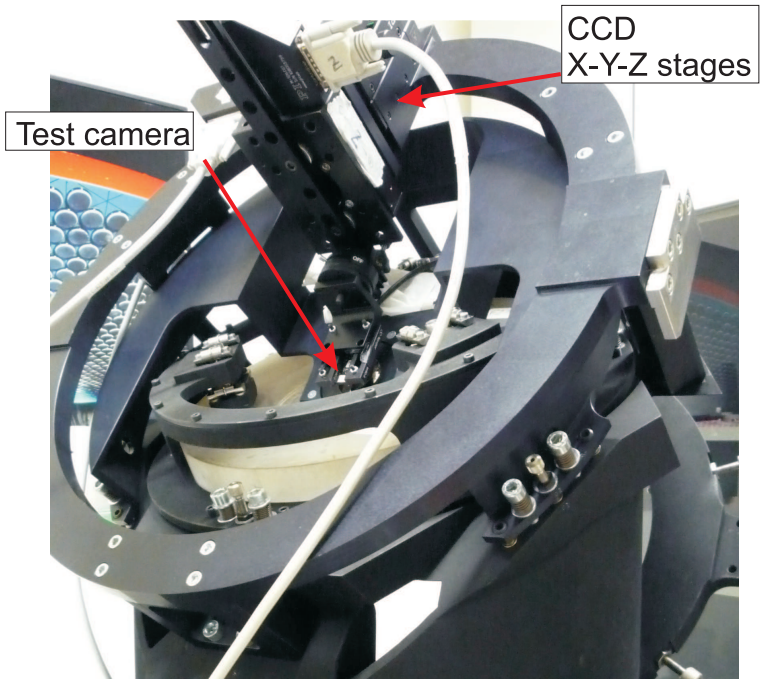

Figure 3.21: The test camera mounted on a repositionable magnetic baseplate and movable with the x-y-z linear motorized stages of the final CCD detector (PHASE 1B).

x-direction and 6.6 μm (3 pixels) in the y-direction.

- Characterization of the angle between the Prime Focus Corrector optical axis and the z-stage movement axis. This test provides the movement of the spot on the test camera while the latter is shifted along the direction of movement of the z-stage (resembling the objective optical axis) for 8.825 mm, in order to characterize the angle between the true movement of the stage and the Prime Focus Corrector optical axis itself. The considered range is far larger than what expected as necessary for the following procedure phases (focusing of the test camera). The movements of the spot between the starting position (x =1316.39, y=1239.38) and the end position (x =1330.84, y =1223.52) are 15.15 pixels in the x-direction and 16.24 in the y-direction, corresponding respectively to a 33.3 μm and a 35.7 μm ranges. These values are still far inside the required precision in the camera positioning, even if the 8.825 mm considered range is really wide.

The total indetermination on the optical axis definition on the CCD for Phase 1, considering a quadratic sum of all the described contributions is $\pm 71\mu$m, corresponding to 13% of the repositioning required precision, which is ± 0.55 mm.

PHASE 2: Alignment on axis between the objective and the parabola
This phase has the purpose of realizing a rough pre-alignment of the Parabola to the Objective, in order to accomplish, during Phase 3, the alignment of 2 flat mirrors (PRI and setup). At this stage, having only one observable (described hereafter) it is impossible to distinguish between the decenter and the tilt of the Parabola.

A. The parabolic mirror is mounted on the PR-I main structure (see figure 3.23 left) and positioned at its nominal focal place, with a mechanical precision which should fulfill the tolerance of 0.5 mm in focus. The nominal distances given by mechanical drawings of the parabola and the flat mirror of the PR-I inside their mount cells are depicted in figure 3.22. The test camera is temporarily dismounted.

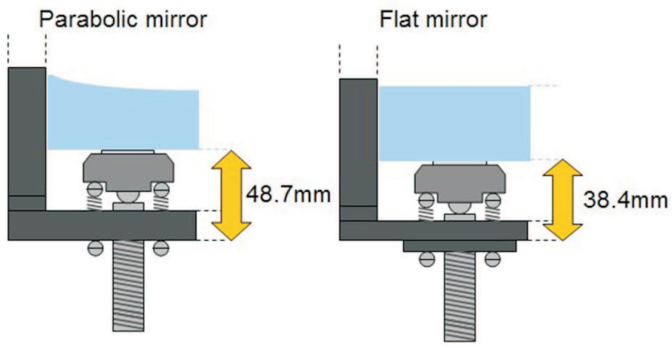

Figure 3.22: Nominal positions in focus for the parabolic and flat mirrors inside their mount cells (PHASE 2A).

Afterwards, the parabola is temporarily masked with a black screen. A small laser source (positioned on the same side of the test camera), equipped with centering and tip-tilt adjustment capabilities is shined toward the Objective and aligned to its optical axis observing the back reflected spots (see figure 3.23 right). This operation which aims to materialize the optical axis of the Objective is achieved with a precision of ± 120 μm in center and ± 60 arcsec in tilt.

B. The black screen from the parabola is removed and the parabola is aligned with the laser materializing the objective optical axis. Of course, shining a laser on the central area of the Parabola, we can only align the parabola surface normal with the incoming laser beam, since there will always be a tilt compensating a certain amount of decenter (and vice versa). This operation has to be achieved with a precision of 0.6 mm in centering and 0.06° in tilt.

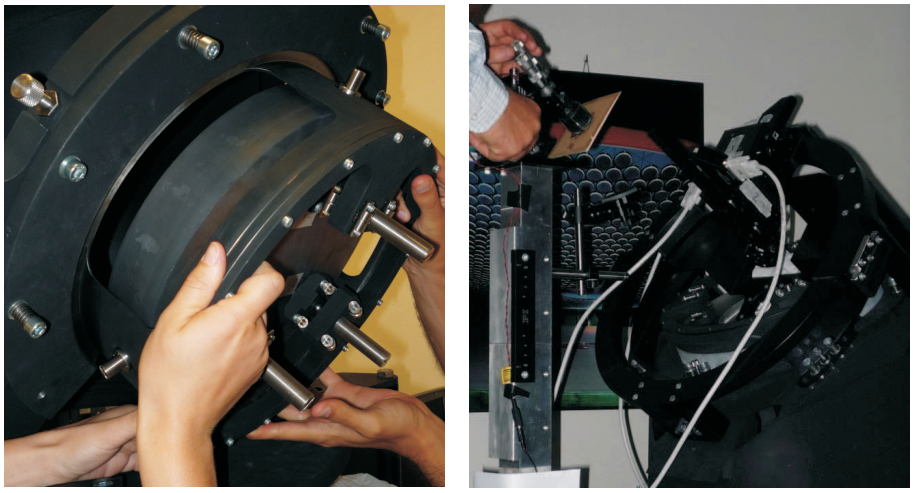

Figure 3.23: Left: the GWS parabolic mirror is mounted and first of all aligned with mechanical precision. **Right**:alignment of the laser source to materialize the PrimeFocus Corrector optical axis (PHASE 2A).

The total indetermination of the alignment of the Parabola surface in order to be normal with respect to the Objective optical axis is the sum of the errors in aligning the Parabola (0.6 mm and 0.06°) and the propagation of the errors, computed in Zemax, depending from the indetermination in the materialization of the Objective optical axis with the laser beam (120μm and 60 arcsec). They give a total error (in the conservative case of a simple sum of the two contributions) of 1.75 mm in centering and 0.15° in tilt.

PHASE 3: Alignment of the two flat mirrors This Phase has the purpose to illuminate the PR-I with an extended collimated beam. When the beam reaches the Parabola, it has to be parallel to the Objective optical axis. Once this configuration is reached, there will be only one way to align the Parabola minimizing the coma effect and keeping the spot fixed on the recorded position on the CCD (Phase 4 and Phase 5). This optical setup is shown in figure 3.24 and is composed of:

- a 100 μm optical fiber (mounted on a X-Y-Z stage for alignment purposes) used as reference light for the alignment (it can be fed both with laser or visible light);
- an Off-Axis Parabolic mirror (OAP), mounted on a custom-made tip-tilt mount, to collimate the beam coming from the optical fiber, directing it toward the PR-I;
- an additional flat folding mirror, positioned below the PR-I, to send the collimated beam up toward the PR-I itself; this folding mirror has tip-tilt ad-

justments (performed using actuators with differential micrometers, with a resolution of 1 μm, corresponding to 1.16 arcsec), in order to tilt the reference created by the fiber over the whole PR-I field of view;

- the test camera (used in the previous phases), with a very high spatial sampling (2.2μm of pixel size) in order to have the highest possible resolution for the evaluation of the images affected by the coma during the alignment procedure.

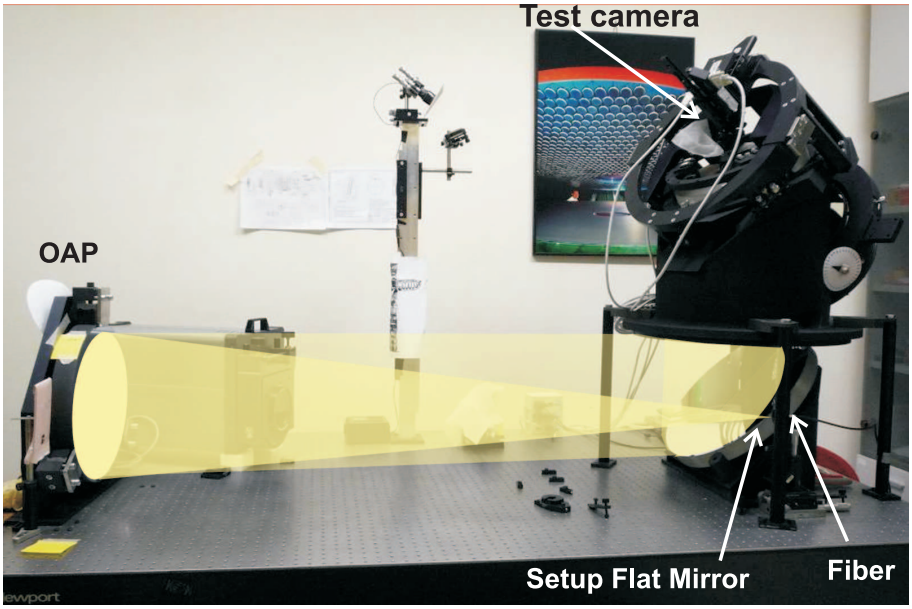

Figure 3.24: The optical setup used to align the Pupil Re-Imager. The main components are highlighted, the fiber, the OAP, the large flat mirror used to fold the light and the CCD camera (PHASE 3).

OAP Alignment The setup OAP alignment consists of a relative orientation and centering of the optical fiber and the OAP itself. Namely, the optical fiber has to be placed on the focal point of the OAP, along the optical axis of its parent parabola. The required precision in the positioning of the fiber on the focal plane of the OAP is $\pm$ 3 mm in de-center. In this way an eventual coma effect introduced on the spot on Phase 4 and Phase 5 by the OAP would be smaller than the minimum coma we aim to detect on the CCD. The focusing precision is not defined since the beam will not be used for focusing purposes. The alignment procedure can be summarized as follows:

1. a collimated beam (100 mm diameter) is reflected by the OAP and focused on a CCD camera. The relative orientation of the incoming beam and the OAP is modified in the three rotation axes in order to minimize the dimension of

the spot on the camera, reducing the coma effect, within a certain error (40 arcsec for the inclination of the incoming beam with respect to the OAP parent parabola optical axis).

2. in such a way, the position of the focused spot defined the focal point of the OAP within a certain error, which is ± 0.3 mm in the two directions.

3. the optical fiber has then been placed in order to be coincident with the focused spot, with an indetermination lower than ± 0.5 mm in the two directions. The total indetermination in the fiber positioning on the OAP focal plane is then lower than ± 0.8 mm in both directions, which is far inside our requirements.

4. the focal position of the optical fiber has been checked with an auto-collimation procedure, resulting in an indetermination of the fiber position along the optical axis lower than ± 2.5 mm (the long focal distance of the OAP is 1503 mm).

The last step of Phase 3 is to tip-tilt the flat folding mirror below the PR-I in a way to superimpose the spot to the reference, recorded on the CCD during Phase 1, within an accuracy of 0.001° (corresponding to a shift of the spot on the CCD of 7μm, that is to say about 3 pixels).

PHASE 4: Alignment of the PR-I At this point of the procedure the PR-I is fed with a wide collimated beam corresponding to the on-axis beam of the PR-I FoV, within the already described indetermination.

There will be only one way to align the Parabola minimizing the coma effect and keeping the spot fixed on the recorded position on the CCD, which is the preliminary "center of the field", used as a reference for the alignment phase. The camera is then defocused in the intra-focal direction of 0.22 mm. The resulting image shows a central dark "hole" due to the central obscuration of the PR-I. To measure the coma, the position of the central obstruction with respect to the whole defocused reference image is determined. Using an IDL procedure interpolating the contours of the outer and inner ellipses (shown in figure 3.25), the relative de-centering between the two ellipses is computed and then translated in a coma measurement. They are not exactly circles, because of an astigmatism effect, discussed later.

The goal is to iteratively adjust tip-tilt and centering of the parabolic mirror, in order to minimize the de-centering between the two ellipses without changing the position of the focused spot on the CCD camera. According to the error budget of the PR-I internal alignment, the misalignment accepted in this phase between the Parabolic mirror and the Objective smaller than 0.2 mm in de-centering (and 0.01° of tilt).

The Parabolic mirror - Objective de-centering is required to be smaller than 0.2 mm, which translates in a de-centering between the ellipses has to be smaller than

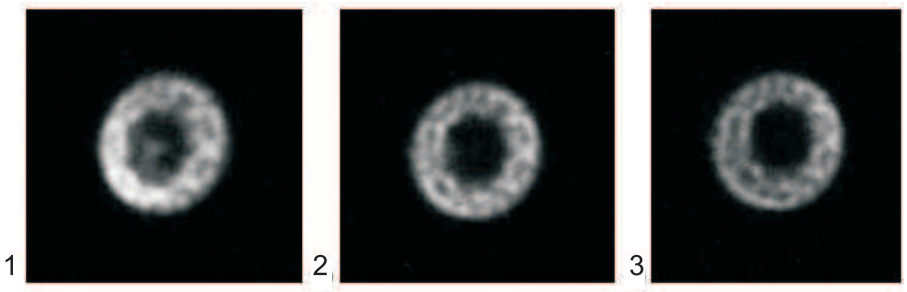

Figure 3.25: Defocused images of the spot (0.22 mm intra-focal direction). Image 1 and 3 show a de-centering between the inner and outer ellipses of 3 pixels (in opposite directions), while image 2) shows a de-centering of less than 0.5 pixels (PHASE 4).

1 pixel of the test camera, that is to say 2.2 μm. The reached value for the de-centering of the two ellipses after the iterative procedure is 0.25$\pm$0.25 pixels ($<$ 1 pixel), corresponding to 0.69$\pm$0.69 arcsec of coma.
Astigmatism contribution The images obtained in Phase 4 show an astigmatism component, which could, in principle, either depend on the PR-I optics (Prime focus corrector internal misalignments, each optical component manufacturing, etc.) or on the test setup. Measuring the outer ellipses eccentricity, the resulting astigmatism component is 5.5 arcsec. To check the effect of such an aberration on the PR-I optical quality, the whole amount of astigmatism is considered as introduced by the PR-I (in particular by the Parabolic mirror surface) and the resulting RMS blur is computed. The resulting RMS spot radii are 8.0 μm, 9.4 μm and 10.8 μm in the center of the FoV, at 0.44° and at 0.55° from the center, respectively (see table 3.5).

PHASE 5: Final Focus Adjustment of the PR-I A manually operated measurement arm that measures the surface of real physical objects, tracing the exact coordinates of space, is used to check the distance between the parabolic mirror and the Prime focus corrector. The reference planes are the rear of the Parabolic mirror and the flange holding the Prime Focus Corrector (see figure 3.26). The nominal distance (considering Zemax and CAD drawings) is 353.68 mm. The measured distance is 353.62 mm.
The focal positioning requirement (0.5 mm) is then fulfilled, giving a focal error lower than 0.1 mm.

In table 3.5 is shown the expected spot enlargement due to the various contributions in the alignment procedure, which has to be verified in Phase 6.

PHASE 6: final PR-I optical quality check Tilting the additional flat folding mirror located below the PR-I, the off-axis optical quality is checked. The limit of

Contributions to the spot enlargement	On axis	±0.44° FoV	±0.55° FoV
RMS nominal spot radius	5.6 μm	7.4 μm	8.9 μm
Maximum de-focus contribution (0.1 mm)	6.2 μm	7.7 μm	9.2 μm
Maximum off-axis alignment contribution - due to the source (0.3°)	7.0 μm	11.9 μm	15.6 μm
Alignment (0.025 mm decenter, 0.005° tilt)	5.9 μm	7.8 μm	9.3 μm
Measured astigmatism effect (5.5 arcsec)	8.0 μm	9.4 μm	10.8 μm
Total RMS spot radius	**9.6 μm**	**13.6 μm**	**17.1 μm**

Table 3.5: Error budget summarizing the various contributions to the total RMS blur, measured as the RMS spot radius, obtained optimizing the focus position of the CCD over the full FoV with polychromatic light.

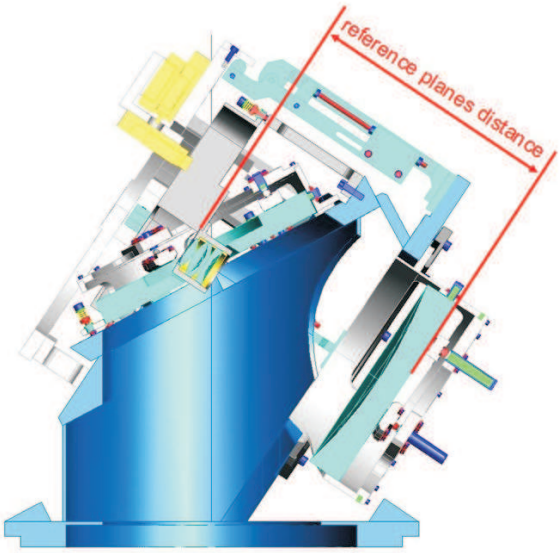

Figure 3.26: The reference planes for the mechanical measurement of the distance between the optics inside the PR-I are shown (PHASE 5).

the PR-I FoV ($\pm 0.44°$) is reached tilting the Flat mirror of $0.22°$ in several directions. The flat folding setup mirror is tilted using three manual actuators, positioned on the rear of the mirror, with $120°$ of relative separation. A $0.22°$ tilt corresponds to a 0.7 mm travel of one of the actuators. First of all, the test camera is precisely positioned on the focal plane, minimizing the spot radius of the image at the center of the FoV, both considered as the width of the Gaussian curve fitting the spot bi-dimensional profile and the RMS spot radius (see figure 3.27).
The camera is fixed at the focal plane position, and a set measurements of the RMS spot radius all over the FoV (see figure 3.28) of the PR-I, is taken. The RMS spot radius is computed on each image, considering only the pixel values over a threshold of 5% of the peak intensity of the spot at the center of the FoV.

As estimated in table 3.5, the expected RMS blur due to the alignment procedure described above is well under the required optical quality of 25μm over the whole FoV, therefore the alignment satisfies the requirements. Since at the end of the alignment we had achieved a higher precision than what was foreseen, a new value of 13 μm RMS radius has been introduced as a PR-I optical quality measurement in the Error Budget (section 3.3.2) to relax other tolerances.

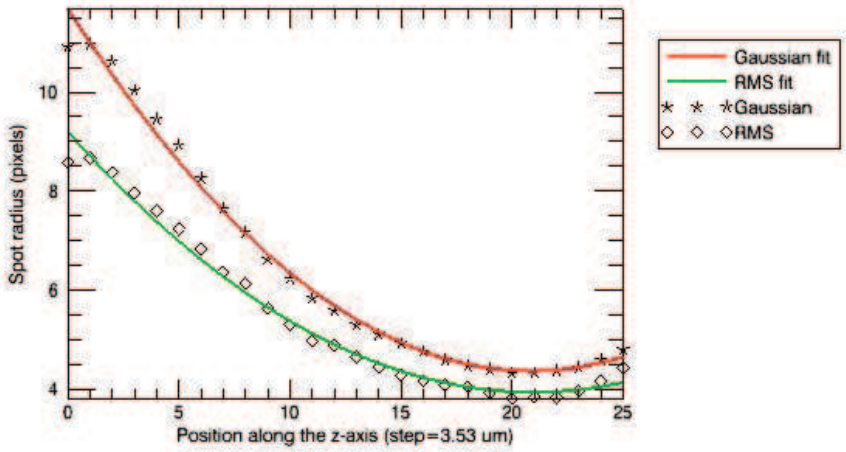

Figure 3.27: Through focus values of the spot radius to define the focal plane position(PHASE 6).

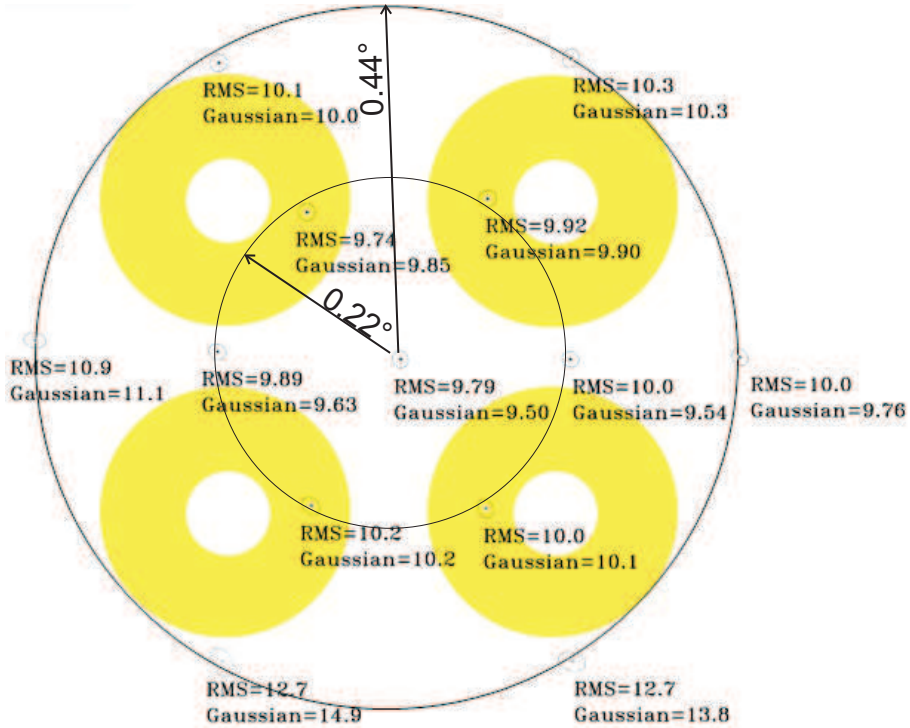

Figure 3.28: Spot images and relative RMS spot radius on the test CCD in sample positions at the center, at a radius of 0.22 ° and at the outer radius of 0.44°(all measurements are in μm). Underneath are depicted the 4 pupils on the final CCD50 to simplify the concept (PHASE 6).

3.3.4 CCD50 Detector

Both GWS are equipped with SciMeasure Analytical Systems Inc. detectors with Little Joe readout electronics that mount Marconi CCD50 sensors, split frame-transfer detectors, 14 bits, with an image area of 128 x 128 pixels (24 μm) and 16 parallel output amplifiers, 8 for each side (see figure 3.29 left).
This sensor has been particularly designed for high framerate operations, especially for wavefront sensing in adaptive optics applications. Frame rates of close to 1 kHz, with readout noise lower than 5 e- rms is achieved from this backside thinned CCD. Each CCD is mounted on x-y-z motorized linear stages for the remote positioning in center and focus, see 3.30. A heat-exchanger structure, through which it is connected to the stages, allows for the cooling of the detector. The theoretical diameter chosen of each pupil is 48 pixels in diameter (see figure 3.29 right), corresponding to 24 sub-apertures for 2×2 binning.

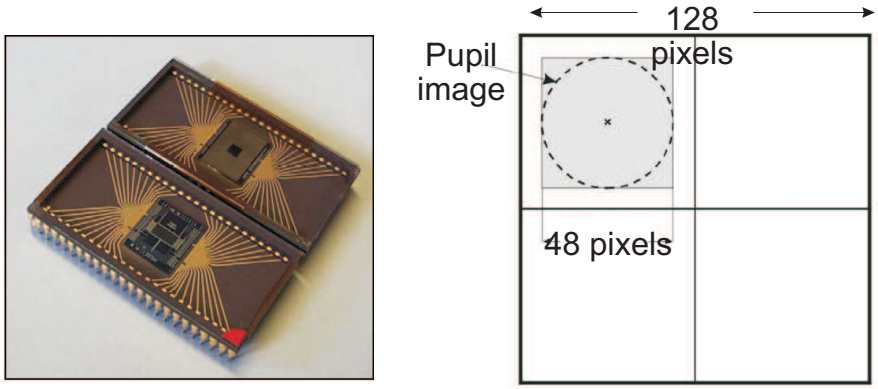

Figure 3.29: Left: CCD50 chip. Right:Schematic representation of one pupil on the CCD.

In table 3.6 are shown the 8 possible combinations of frame-rate and binning available on the CCD electronics, in order to face different atmospheric parameters during different observations. Since each of the 16 amplifiers reads simultaneously the image (starting from the outer pixel lines), the pixel-rate has to be calculated on one/sixteenth of CCD size. Moreover, for each one of the programs there are 4 possible gain values (see table 3.7), for a total of 32 combinations, called programs hereafter. Many parameters (such as the bias-level, integration time, ...) can be set independently.

Another characteristic, which has to be underlined, is that the exposure time of each readout mode is defined by its frame rate, since no shutter is implemented, and to a certain extent it can be incremented deciding to read the frame only after a certain number of repetition of the chosen readout mode (reaching around 0.4 s in the best case, maximum exposure time on lowest frame-rate). In figure 3.31 is shown the amplifier numbering as seen through Little Joe electronics, for the different

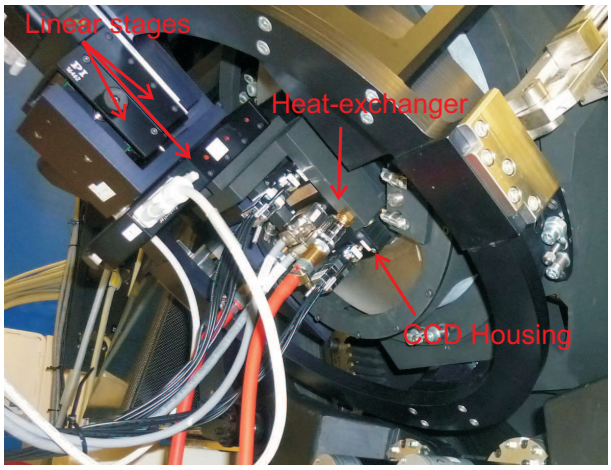

Figure 3.30: CCD50 mounted on the 3 linear motorized stages on the PRI structure. The orange hoses are attached to the heat-exchanger structure which allows cooling of the detector.

channels (corresponding to the 16 amplifiers). Each channel, of size 16 × 64 pixels, is analyzed individually.

0	2	4	6	8	10	12	14
1	3	5	7	9	11	13	15

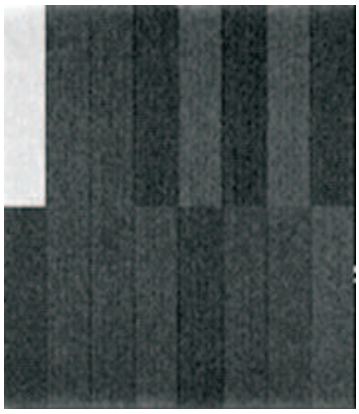

Figure 3.31: Left: channel numbers as defined on the electronics grouped 4 for each quadrant.**Right:** an example of bias, where it is possible to observe the 16 channels in which the CCD is divided and the difference of bias value vefor their adjustment .

CCD50 Characterization

All the following tests were performed connecting a liquid re-circulator to the CCD, which allowed us to test the CCD about 1-2 degrees above ambient temperature, meaning in average at 25°C, thanks to its Peltier-cooling system, supposed to

Program #				**Frame-size**	**Frame-rate**	**Theoretical**	**Actual**
Gain0	*Gain1*	*Gain2*	*Gain3*	(pixel) [Binning]	**(Hz)**	**pixel-rate (kHz)**	**pixel-rate (kHz)**
0	8	16	24	128 x 128 [1x1]	77.4	80	79
1	9	17	25	128 x 128 [1x1]	237.8	250	244
2	10	18	26	128 x 128 [1x1]	1245.5	1500	1276
3	11	19	27	64 x 64 [2x2]	301.6	80	77
4	12	20	28	64 x 64 [2x2]	884	250	226
5	13	21	29	64 x 64 [2x2]	1023.5	350	262
6	14	22	30	64 x 64 [2x2]	3594.5	1500	921
7	15	23	31	32 x 32 [4x4]	475.9	80	30

Table 3.6: Summary of the parameters of the 32 programs, combination of different gain value, binning and frame-rates (plus corresponding pixel-rates, both theoretical and actual), implemented for the camera, to face different atmospheric conditions.

Gain	**Value (dB)**
0	30
1	10
2	3
3	1

Table 3.7: Actual gain values corresponding to Gain 0...3 of table 3.6.

cool down the temperature of about 40°C, it was internally reaching -15°C, whereas its best performance are reached at -20°C . In preliminary tests without cooling the CCD head temperature had, in fact, increased about 15°C above ambient temperature in less than 2 hours. To start read-out noise and gain tests are performed for each program, for a total of 32 different situations.

Bias-level and read-out noise To measure both bias-level and Read-Out-Noise (RON), the window is completely obscured, covered with black tape and the camera placed in a dark room. First of all offset levels (black level) are re-assessed to minimize bias-value difference between channels, due to an exchange of the provided short cables with longer cables to be used for the final instrument. For programs with gain 0, the values have been set to obtain an average value of 630 Analog to digital units (ADU), while for gain 1, 2, 3 the value was 430 ADU, for conformity of the values retrieved with shorter cables. About 15 minutes after the CCD had been turned on, 100 images for each program are recorded. As previously explained, the exposure time cannot be set to 0 s, and the minimum possible exposure time (which was of course set for this test) varies depending on the frame-rate associated to each program, so they are actually dark frames and some Poisson noise of dark current is present. Through dedicated routines written in IDL, the images were divided in the 16 channels composing the CCD and each one analyzed separately, to retrieve RON and bias value. For each pixel we computed its average value over the 100 images and its standard deviation. The standard deviation of the previously obtained standard deviation was computed and represents the RON value in ADUs, while the average pixel value over the 100 images is the bias.

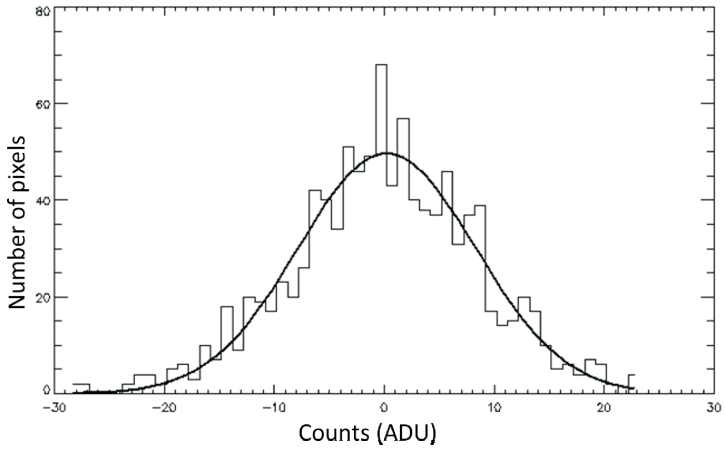

Figure 3.32: Histogram showing an example of the distribution of pixel intensities (ADU) for 100 averaged images along one CCD channel. It is possible to see how it follows the theoretical Gaussian shape (black line).

Program #	Gain	Theoretical Pixel-rate (Hz)	Measured RON (e-)
0-3-7	0	80	3.39 ± 0.24
8-11-15	1	80	3.61 ± 0.26
6-19-23	2	80	4.11 ± 0.30
24-27-31	3	80	9.62 ± 0.69
1-4-5	0	250-350	3.90 ± 0.28
9-12-13	1	250-350	3.96 ± 0.28
17-20-21	2	250-350	4.39 ± 0.32
25-28-29	3	250-350	9.25 ± 0.70
2-6	0	1500	7.88 ± 0.57
10-14	1	1500	7.92 ± 0.57
18-22	2	1500	8.05 ± 0.58
26-31	3	1500	11.09 ± 0.88

Table 3.8: Measured RON combined for programs with the same theoretical gain, but divided for different frame-rate values.

In table 3.8, average values over the whole CCD for programs with similar theoretical pixel-rate are reported. ADU have been converted into electrons (e-) with the measured conversion factor (see table 3.10). The associated error is the average of the standard deviation of all channels for all the considered programs. In table 3.9 are detailed the RON values for all programs and for the Gain0 case can be compared to the values given by SciMeasure.

Analysis of the RON showed the retrieved values to be fairly similar (always a little higher) to the RON provided by the manufacturer and, as expected, depends on used pixel-clock rate. The RON (in electrons) also depends on the used gain factor, it slightly increases with the gain-factor (for a gain setting of 0, 1, 2). Only for a gain setting of 3, the RON is much larger than for the other settings of the same pixel-rate. Since these values have been converted with the system gain values (as measured in the next paragraph), they should be independent of the gain-factor. Since this is not the case, we suspect that by changing the electronics for the higher gain settings, something influences the gain computation. The same problem was encounteres during CCD39 (equipped with the same electronics of CCD50) characterization tests, but no problems during its use arose. The bias-level showed slight variations with time, but those are the same for all channels, so they should not introduce additional signal in the pyramid measurements. Bias-value in different channels varies of a few ADUs, it is important to subtract a bias image before analyzing images.

Binning	Theoretical Pixel-rate (kHz)	Gain 0	Theoretical RON	Gain 1	Gain 2	Gain 3
1x1	80	3.56±0.26	3	3.74±0.27	4.13±0.32	9.74±0.70
1x1	250	3.83±0.27	3.5	3.89±0.28	4.36±0.32	9.24±0.69
1x1	1500	7.81±0.56	7.7	7.83±0.56	8.01±0.59	12.60±1.02
2x2	80	3.23±0.23	3	3.50±0.25	4.07±0.29	9.58±0.67
2x2	250	3.88±0.27	3.7	3.93±0.28	4.43±0.31	9.29±0.66
2x2	350	3.98±0.28	3.9	4.04±0.29	4.38±0.33	9.24±0.74
2x2	1500	7.95±0.58	7.5	8.06±0.58	8.22±0.60	12.63±1.04
4x4	80	3.40±0.24	3.4	3.59±0.26	4.15±0.29	9.58±0.67

Table 3.9: Measured RON for each program is shown. Gain 0 given by Scimeasure is reported for comparison in the 4th column.

Gain In order to determine the gain factor, a uniform illumination with a white lamp and a diffusing element is produced and sets of 100 images at seven different light intensities are taken. To determine the gain factor we take advantage of the fact that the measured intensity in ADU depends directly on the system gain factor, while the measured variance of the images is independent from the gain (mean-variance method). Thus, when plotting the measured mean signal against the calculated variance of the signal (the so-called photon-transfer curve), for each channel, the slope of the linear part of this curve is directly the gain-factor. We considered only a limited number of pixels around the center of the channel (25, 16 and 9 disposed in a square respectively for binning 1×1,2×2 and 4×4), and the plotted the mean and variance of each pixel throughout all the 100 images, for each different intensity (see figure 3.33). Linear interpolation was computed and the inverse of the angular coefficient of the slope is the gain factor (e-/ADU) and is reported in table 3.10, where it is also reported the value given. We can infer that the retrieved values are compliant with the given ones.

Linearity Linearity has been verified just for program 0 with a uniform white light source put in front of the camera and increasing exposure time, up to 25000 "repetitions" with steps of 1000, reaching up to about 13500 ADU. For each setting, 10 images were taken and the average pixel-value for each channel was determined and then plotted versus the repetition number, as shown in figure 3.34. Linearity fit was found to be above 99.9% for all CCD50 channels.

Flat field We did not have an integrating sphere and therefore we could not carefully analyze the flat-field. What can be stated anyhow is that structures appear different changing program. For readout programs with the higher pixel-rates, sen-

Program #	Gain Gain	Theoretical Pixel-rate (Hz)	Measured Gain (e-/ADU)	Given Gain (e-/ADU)
0-3-7	0	80	0.4	0.37
1-4-5	0	250-350	0.39	0.37
2-6	0	1500	0.41	0.37
10-14	1	1500	1.48	1.4
8-11-15	1	80	1.42	1.4
9-12-13	1	250-350	1.38	1.4
17-20-21	2	250-350	2.59	2.6
18-22	2	1500	2.69	2.6
6-19-23	2	80	2.61	2.6
25-28-29	3	250-350	9.42	10
26-30	3	1500	9.48	10
24-27-31	3	80	9.56	10

Table 3.10: Measured gain values. They looks independent from pixel-rate as expected. Values retrieved are fairly similar to the theoretical one.

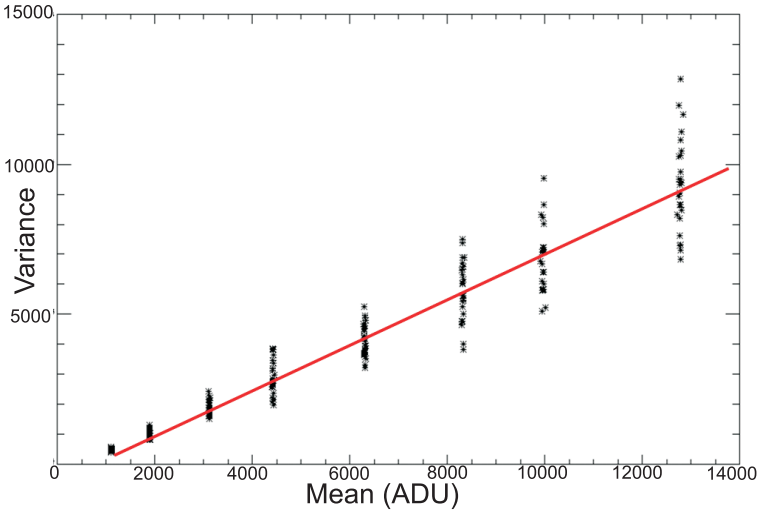

Figure 3.33: An image showing the mean versus variance curve for 25 pixels (of the same channel), throughout 7 sets (each one of 100 images) taken with different flux intensity.

sitivity variation between pixels shows up as an apparent lack of light in the first column of each readout amplifier (an example of this can be seen in figure 3.35). Anyhow this problem seems to be solved by removing a flat-field image taken in similar light conditions and using the same program setting. In some programs the first pixel on each column looks insensitive to light (is black), due to the fact that the first pixel on each amplifier has been replaced with a frame counter by SciMeasure

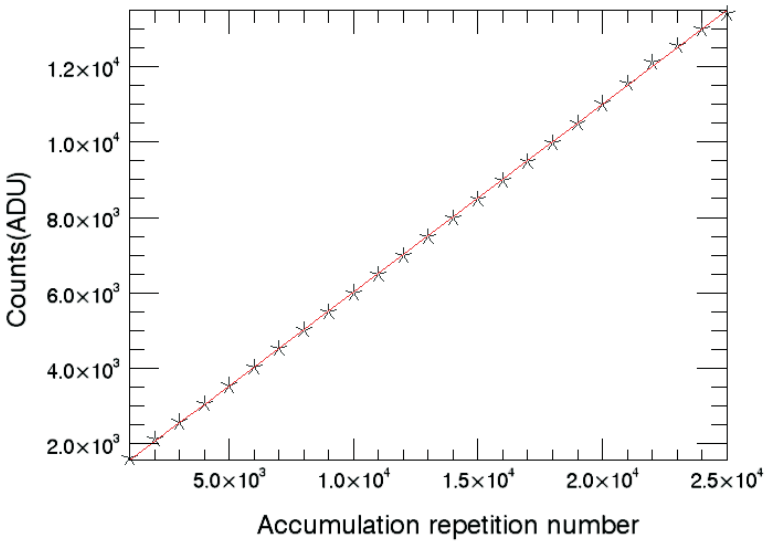

Figure 3.34: Plot of accumulation repetition number (exposure time) versus average pixel value for one channel (in ADU).

controller for error diagnosis. Some of these strange features behaviors are discussed by the manufacturer and the main features on the CCD seem to be due to the aggressive clocking chosen for this camera to increase the overall frame-rate. For this reason the adopted solution was to record and use precise flat-fields maps. We have also seen a somehow strange behavior observed when the CCD was illuminated with a flux that was above the saturation level (which of course depended on the selected gain value): if the flux is increased, starting from outer pixels a constant 0 ADU value. In any case, the manufacturer affirms that is not uncommon for analogue signal chains to initially saturate and then give an apparent zero level when signal increases further.

Conclusions All images were analyzed through IDL codes and the obtained results are consistent with the construction specifications. Before acquiring images, however, due to the presence of structures, the solution of recording bias and precise flat-field images is adopted.

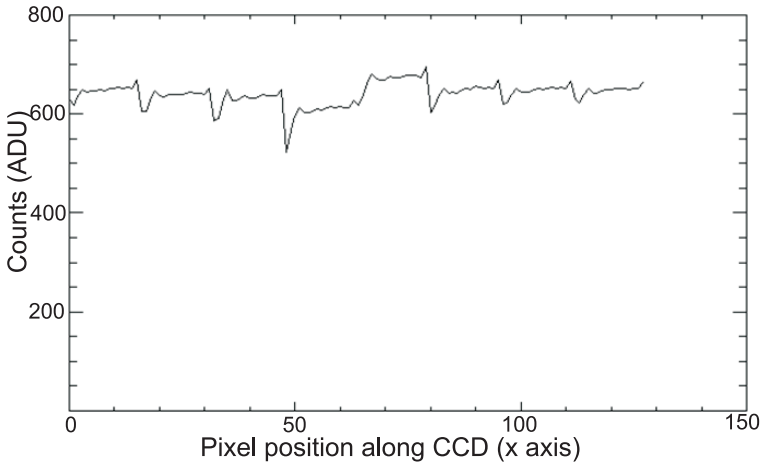

Figure 3.35: A plot which showing an example of a program with high pixel-rate where it is visible the lack of sensitivity of first pixel-column of each amplifier (x axis represents the pixel position along CCD, while y-axis the counts in ADU for each of the pixel of axis x).

3.3.5 GWS alignment

The GWS system is mounted on a rotation unit, defined hereafter as bearing, which allows the derotation of the system to follow the apparent rotation of the sky. Its full range is $\pm 60°$.This bearing is mounted on a mount structure used to connect the GWS to the bench.
The SE support structure, to which we refer as SE reference unit (or lower part), is composed of two flanges, to each of which of them are fixed 6 motorized linear stages, allowing the positioning of the SEs in the field (visible in figure 3.36 top left). On each linear stage is fixed a tip-tilt stage, used to align all the SEs optical axis parallel, in order to avoid differential shifts of the pupils on the detector that cause pupils blur. It is the first part to be connected to the bearing, operation which was performed at Tomelleri S.r.l. premises.
Because of the GWS weight and size, a mechanical handling has been realized in order to perform the integration of the other components in Padova and hold the system during the internal alignment procedure. The handling is equipped with shelves and chains to keep a standard optical bench integral with the handling itself (see figure 3.37), to avoid differential movements, due both to temperature variations and movements, during the alignment.
The GWS internal alignment consists in the relative alignment of the SEs in tilt and pyramid rotation, to avoid a wrong pupil superposition on the detector, the alignment of the PR-I optical axis to the bearing rotation axis, performed with the flat folding mirror at the entrance of the PR-I itself, and the proper positioning of the SEs entrance focal plane with respect to a mechanical reference representing

the nominal position of the LBT focal plane. All these alignment steps have to be followed by a verification of the performance, in order to be sure that all the Error Budget requirements are met.

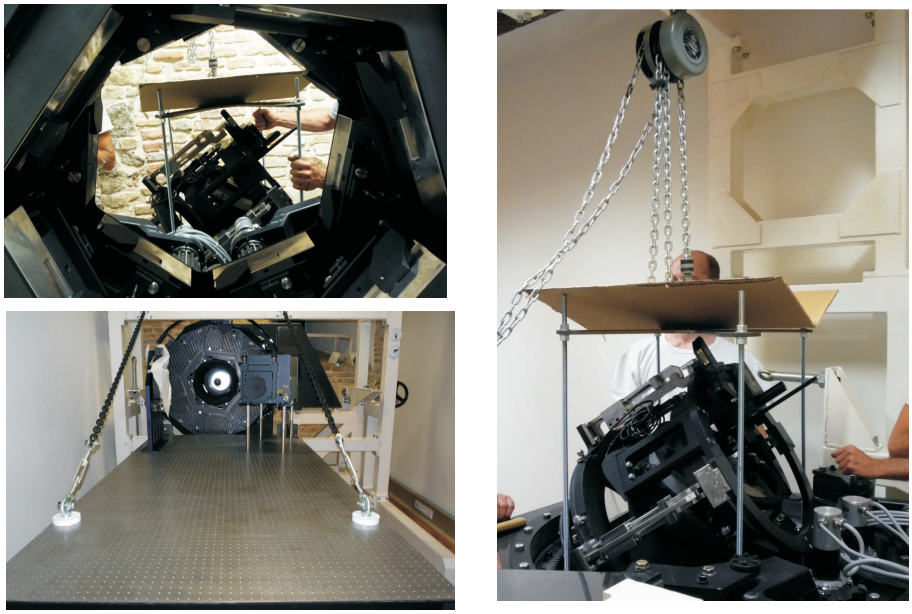

Figure 3.36: Pictures of different moments of the integration.**Top-left**: SE reference unit (SE stages are visible) has been connected to the bearing and PR-I in the background is going to be integrated. **Right**: PR-I integration performed. **Bottom-left**: the optical bench is attached to the handling in order to minimize differential variation between the alignment setup and the GWS during alignment.

PR-I flat mirror alignment

As a first step the PR-I, previously internally aligned 3.3.3, is attached to the bearing (see figure 3.36 right). To adjust the tip-tilt position of the PR-I flat mirror, in order to make the GWS rotation axis parallel to the center of the PR-I field of view, defined during the PR-I alignment, a collimated beam (materializing the rotation axis direction) is required. The used source is an Off-Axis Parabolic mirror (same as the one used in the PR-I alignment), illuminated with an optical fiber (100 μm core), which provides a 330 mm diameter collimated beam. It has been verified in Zemax that the OAP introduces an aberration on the GWS re-imaged spot, which is negligible with respect to the spot aberrations produced by the PR-I.
The collimated beam produced with the parabolic mirror has been folded with a setup flat mirror toward the GWS entrance. The inclination of such a setup mirror has then been adjusted in order to minimize the spot movement on the test CCD

Figure 3.37: GWS assembled on its handling in Padova laboratories.

for a complete ±60° GWS rotation.
To align the internal flat mirror of the PR-I, the GWS rotation axis has to be parallel to the beam defining the center of the field inside the PR-I ±0.44 ° FoV. Operatively, the flat mirror inclination has to be adjusted in order to achieve a field (rotating the GWS) in which the optical quality is center-symmetric. The center of the field corresponds to the GWS rotation axis.

The results obtained are shown in figure 3.38, where the values refer to the Gaussian fit width in test camera pixels unit of the dimension of the focused spot of a collimated incoming beam, mapping the whole FoV. The measurements have been repeated in three configurations, corresponding to 0°, +60° and -60° rotation angle of the bearing. These results translates into an optical quality, expressed in RMS value, which confirms the results obtained from the PR-I alignment, and is lower than 13 μm in the whole PR-I FoV.

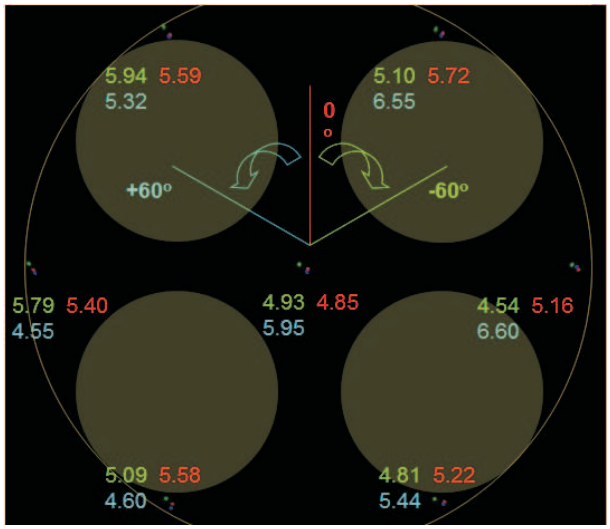

Figure 3.38: PR-I quality along its FoV, measured as the dimension of the focused spot of a collimated incoming beam, mapping the whole FoV. The red, blue and green configurations correspond, respectively, to 0° , +60° and -60° rotation of the bearing.

SE-to-GWS alignment

The last sub-systems to be assembled and aligned to the GWS are the 12 SEs, mounted on T-shaped supports. Two headless screws, pushing the SE in two opposite directions along the rail on which the SE is coupled with its T-arm, are used to change the position of the SE along the optical axis (see figure 3.14). A copper stripe is mounted around the SEs as visible in figure 3.39 in order to block the system in case of a collision between two SEs. Finally, the SEs are inserted inside the GWS lower part and fixed to the tip-tilt stages (figure 3.39).

To align the SEs to the GWS mechanics, the setup shown in figure 3.40 can be used. The idea is to take advantage of a wide collimated laser beam (150 mm), coming from a commercial interferometer (FISBA), as a reference, aligned to the GWS to be parallel to the GWS optical and rotation axis (which were made coincident in the previous alignment phase). A commercial f = 700 mm, 2 inches diameter lens is used to focus part of the wide beam in the nominal focal plane, defined by the mechanics of the GWS itself, and a physical stop, properly dimensioned, positioned at the proper distance from the focusing lens (according to the entrance pupil position at LBT: 14 m) defines an F/15 beam. The focused beam (the green beam in figure 3.40), once passed through a SE, produces four images of the pupil stop on the CCD. Since the precision required for the SE alignment cannot be achieved with the CCD50, it shall be still used a test detector allowing better sampling (2.2μm pixel size). The part of the beam which is not focused by the lens reaches the GWS optics still collimated (the red beams in figure 3.40). If this collimated beam passes through a SE, on

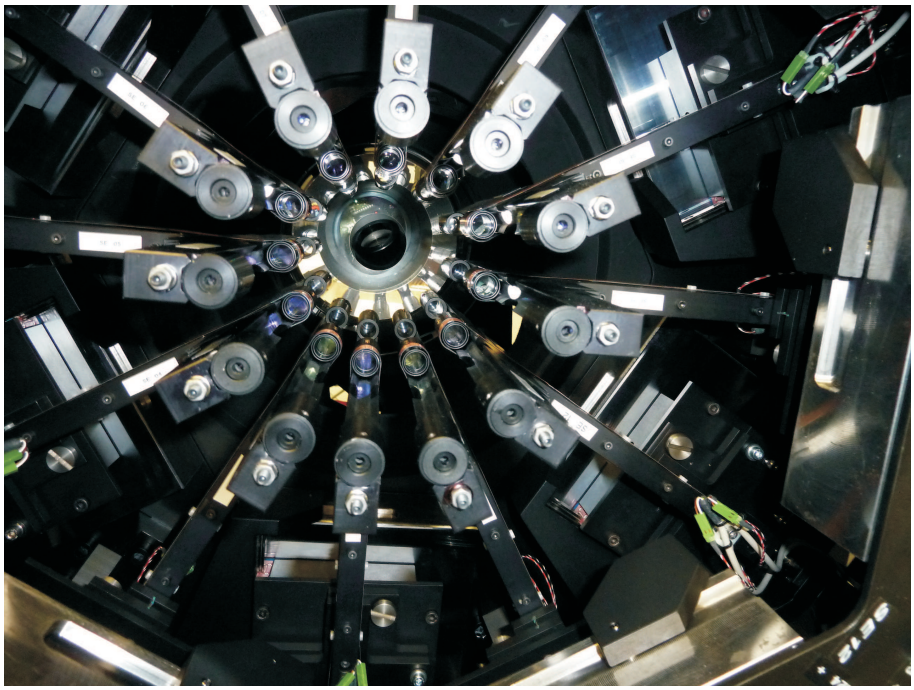

Figure 3.39: SEs mounted inside the GWS on top of tip-tilt and linear stages. The copper collision control stripes are clearly visible.

the test CCD, 4 spots will be produced and their barycenters define the positions of the 4 pupils re-imaged when the same SE is reached by the beam focused at its entrance focal plane. The part of the collimated beam entering the GWS where no SEs is present, instead, focuses on the center of the PR-I FoV. This operation was first of all performed in Padova and afterwards was repeated after shipping the system in Heidelberg. I'm reporting results from this second alignment. Just as a note, since the tolerances of this alignment are very tight, is probable that this same re-alignment will have to be repeated also after the shipping to the telescope, due to vibrations which can occur even with the system highly protected in a damped double-box.

Materialization of bearing mechanical axis Using a dedicated flange, a flat mirror (equipped with a tip-tilt mount) is attached to the GWS on the SEs side. The mirror is aligned perpendicular to the bearing mechanical axis (which acts in this case as the reference for the alignment) looking at the interferometer back-reflected beam passing through a lens and minimizing its movement on the CCD camera; the angle of the beam (in radians) is given by the movement on the camera divided by the lens focal length, and this number has to be again divided by 2 because of the mirror reflection. A lower limit to this movement is of course given by the bearing wobble,

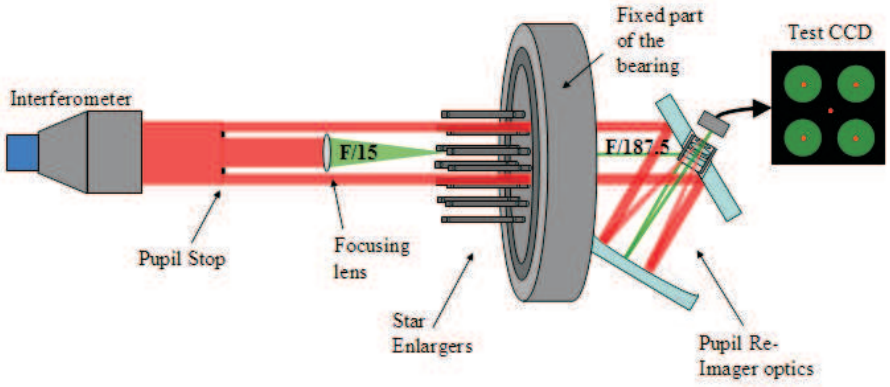

Figure 3.40: A wide collimated beam, materializing the GWS rotation axis, is used to align the SEs to the GWS mechanics. Part of this beam is focused in the nominal mechanical focal plane, producing an F/15 beam which will be used to focus the SEs, looking at the differential light intensities of the four pupils re-imaged on the test CCD (green beam). The beams which enter the GWS still collimated will produce a spot centered on the center of the field. When part this beam goes through a SE, on the test CCD are produced 4 spots, which will be used to align the rotation angle of the pyramid and the SE tip-tilt (red beam).

which is of the order of 20". At this point the beam is centered with respect to the GWS center (a few mm precision is sufficient) and the interferometer (equipped with tip-tilt capabilities) is tilted till seeing the fringes on the interferometer and minimizing their number. The precision of this operation is given by

$$\frac{Number\ of\ fringes \cdot \lambda \cdot 206265}{Beam\ diameter}(arcsec)$$

. Being the mirror size 100 mm and the number of observed fringe 3, we obtained a precision of about 4 arcsec. In this way we have a collimated beam (which will be used for the latter SE alignment) perpendicular to this mirror (and thus parallel to the bearing axis) with an erro lower than 20". Finally the flat mirror is removed and the CCD is centered with respect to the collimated beam acting on the CCD XY motorized stages. Performing a sweep in focus (acting on the z-stage) to define the position at which the spot size is smaller, the CCD is also aligned in focus. Considering only the PR-I without SEs, the pupil conjugation (the exit pupil of LBT is placed at a 14 m distance from LBT focal plane) can be achieved moving the detector away from the focal plane by a certain amount (3.51 mm, remembering the PR-I equivalent focal length=220 mm) away from the PR-I objective. This amount, however, is reduced by a factor k=12.5 (SE enlarging factor) because of the SEs insertion in the optical path translating into a shift of the CCD50 detector from the PR-I focal plane of 0.28 mm.

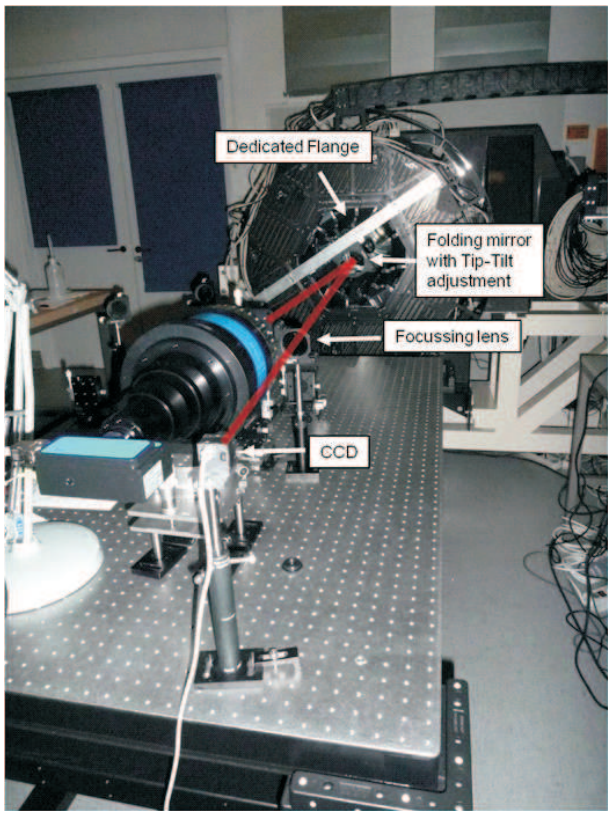

Figure 3.41: The setup to tune the position of the flat mirror connected to the GWS. The flat mirror, inserted in a mount with Tip-Tilt capabilities, and mounted through a dedicated flange, is attached to the SE side of the GWS.

F/15 beam realization A 2-inches diameter lens with a 700 mm focal length is used to focus an F/15 beam at the entrance of the GWS, to reproduce the LBT entrance focal ratio, in order to properly align the SEs in focus. This lens is aligned in auto-collimation, placing a reference mirror in the GWS nominal mechanical entrance focal plane, with a 100μm accuracy. Figure 3.42 shows the auto-collimation setup used to focus the F/15 lens: the collimated beam coming from the interferometer is divided by a beam splitter into two separated beams, one reflected by a mirror toward a setup lens focused on a test camera (yellow beam in figure 3.40) and the other passing through the F/15 focusing lens, being reflected by the reference mirror in the GWS focal plane and back on the beam splitter (red beam in figure 3.40), which reflects it toward the same test camera collecting the spot coming from the first beam. The setup lens focusing onto the test camera is moved along its optical axis to minimize the first beam spot size of the first beam on the test camera, through a sweep in focus, moving the linear stage on which the lens is mounted. The used range and steps to perform this operation are $\pm$1 mm and 100 μm respectively).

To perform this operation, the back-reflected beam coming from the reference flat connected on the GWS is masked. Once the focusing lens is properly positioned, the second beam is considered. The lens focusing the F/15 beam at the entrance of GWS is moved along the focus axis in order to find the position minimizing the size of the spot focused onto the test camera, in auto-collimation. A sweep in focus is performed also in this case. The obtained measurements give a precision of less than 50 μm. Following the described procedure, the F/15 beam which will be used as a reference for the SEs alignment is focused at the nominal mechanical entrance focal plane of the GWS, with a precision which can be estimated combining the indetermination in the reference mirror mechanical positioning and in the best focus position of the F/15 focusing lens: $\sqrt{100^2 + 50^2} = 112\mu m$. An error of such an amount in the GWS focal plane positioning would introduce about 18 nm WFE defocus signal onto the GWS, which is still far from bringing the WFS out of its linear regime.

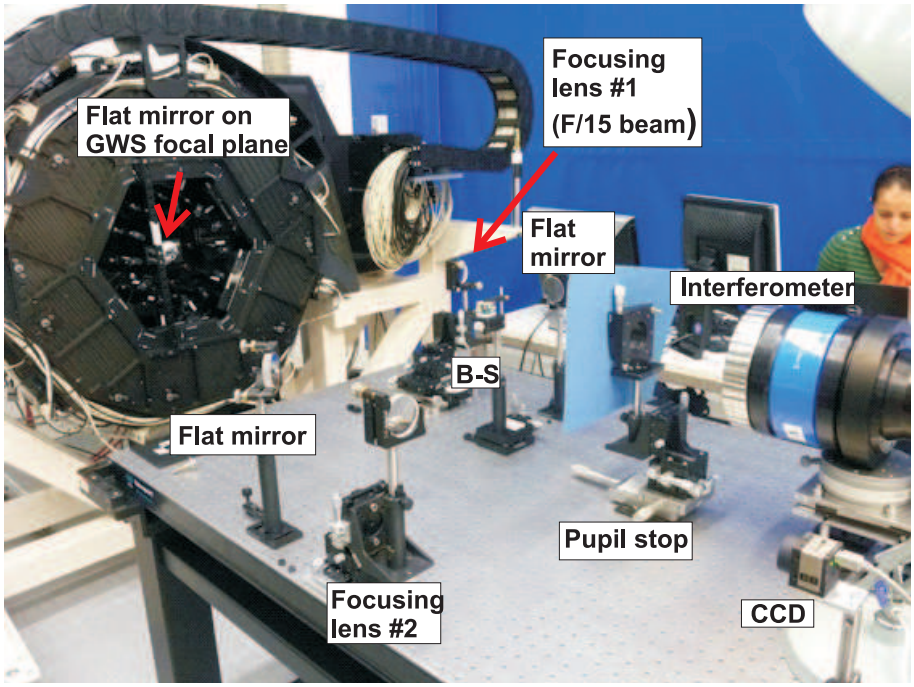

Figure 3.42: The setup used to properly position the F/15 lens in front of the GWS, with the main components outlined.

The SEs have to be aligned in order to realize a superimposition of the four pupils, created by each SE, as good as possible on the detector, when conjugated to the telescope pupil. To achieve this, the SEs shall have the Pyramids all oriented in the same way, they have to be properly focused and they need to have a relative tilt which is as small as possible, in order to reduce the blur created on the detector. Due to the high precision requested, the alignment is performed replacing the CCD50

with a test camera with 2.2 μm pixel-size, allowing a much better spatial sampling of the pupil can be achieved and the required alignment precision can be accomplished.

The SEs alignment inside the GWS is described in the following:

- **Defocus alignment**: to position the SEs in the optical path along the optical axis, the defocus signal retrieved by the wavefront sensor has to be minimized. The F/15 beam passing through one SE is then re-collimated by the pupil re-imager and produces 4 images of the pupil onto the test CCD. The wavefront shape is retrieved comparing the intensities of the four pupils using the quad-cell equations. To convert the retrieved Zernike coefficients into metric values, a converting factor has been retrieved using the following procedure: a spatial range along the optical axis, centered on the best focus position, is defined and the defocus coefficient is measured for both the extreme intra-focal and extra-focal positions (which are symmetric with respect to the best focus). The converting factor can be retrieved as explained in section 2.6.3. The retrieved converting factor for the SEs, illuminated with the light coming from the interferometer (λ= 633 nm), is 0.074 nm. This factor is then multiplied to the retrieved Zernike defocus coefficients in order to obtain the residual defocus WaveFront Error (WFE) in nanometers. The original required precision for this operation is a defocus lower than 20nm, corresponding to a defocus RMS equal to $\lambda/28$ for the considered wavelength. However, as explained in section 3.3.2the SEs have been focused on two different levels , at a relative distance along the optical axis of 2.57mm, with SESs positioned at R_1 and R_2 depicted in figure 3.43. Because of this choice, the SEs operative areas are reduced. The residual maximum defocus with respect to the LBT focal surface is 1.37 mm and the tolerances could be in principle relaxed. To rech this two focal positions the setup F/15 lens was shifted of the proper quantity from the alignment reference position.

- **Tip-tilt adjustment**: when a collimated beam goes through the SE, four spots appear on the test CCD. The relative distances between the spots depends upon the pyramid vertex angle and faces orthogonality, but the position of the overall barycenter can be used as a measurement of the tilt of the SE with respect to the incoming beam. Before measuring this tilt, the collimated beam, used as reference, has to be adjusted in tip-tilt in order to focus on the center of the field, previously defined on the camera, and corresponding also to the GWS rotation axis projection. This adjustment has to be done with a precision which is far better than the required GWS global tilt, since such a beam will act as a reference for all the SEs alignment. The usual goal of a tenth of a sub-aperture shift of the pupils is reached with a tilt of the SE lower than 5 arcsec. The SEs alignment in tip-tilt has been reached in their mid-range

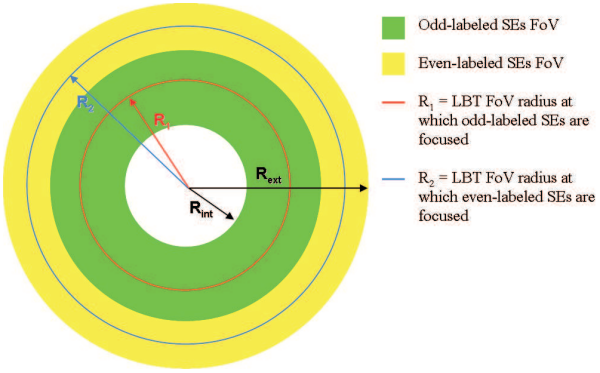

Figure 3.43: GWS FoV areas in which the SEs are expected to move. Odd-labeled SEs have been focused to the LBT F/15 beam at a radius R1 = 62.7 mm and will be positioned only in the green area (corresponding to a 2.2 arcmin maximum radius). Even-labeled SEs have been focused to the LBT F/15 beam at a radius R2 = 95.7 mm and will be positioned only in the yellow area.

Figure 3.44: Effect of different defocus signals on the four pupils on the test CCD. This effect is amplified because, for alignment purposes, a monochromatic red laser light is used, producing a very small spot on the pin of the pyramid.

position along the radial axis, as for the defocus, which is to say at a radius R_1 for the odd-labeled SEs and R_2 for the even-labeled SEs.

- Alignment of the**rotation angle of the pyramid**: the goal for the precision in the pyramid rotation alignment is 10', leading to a displacement of the sub-apertures, which are at the outer edges of the pupils, in the direction of the CCD corners, of 1/10 of sub-aperture. To measure the residual rotation after the alignment, the barycenter positions of the four spots obtained illuminating the SEs with the collimated beam are considered. Because of small defects in the pyramids faces orthogonality, the rotation angle of each pyramid is measured considering the diagonals connecting each pupil center to a common barycenter defined considering the 12 SEs, and their mean deviation from the 45° is taken as a rotation measurement.

Alignments goals are summarized in table 3.11

Item	Measured Effect	Goal max value	Effect on Error Budget
Pyramid rotation	Four spots rotation	10 arcmin	1/10 sub-aperture
SE tip-tilt	Four spots shift wrt goal position	9.6 micron	1/5 sub-aperture
SE defocus	Defocus signal	20 nm WFE	Negligible

Table 3.11: Summary of the goals for the SE alignment.

Results Comparing the measured values listed in table 3.12 with the requirements listed in table 3.11, the alignment result inside tolerances for all the considered items.

SE #	SE tip-tilt [μm]	Pyramid rotation [arcmin]	SE defocus [nm WFE]
SE01	2.1	-5.0	-19.0
SE02	4.5	8.0	-3.3
SE03	1.3	2.1	-7.6
SE04	0.7	6.7	-9.6
SE05	1.7	-3.3	4.1
SE06	1.8	-1.3	5.7
SE07	1.1	2.5	-4.8
SE08	0.5	1.9	10.4
SE09	2.3	-2.4	13.9
SE10	2.1	-5.8	-6.2
SE11	2.0	1.0	4.4
SE12	2.0	-4.6	-6.1

Table 3.12: SE alignment values. If compared with the goals of table 3.11 all requirements are fulfilled.

3.3.6 GWS rotation test

After the GWS system internal alignment, in which each sub-system has been separately aligned and tested and the GWS has been completely assembled and internally aligned in a static configuration, with the bearing oriented at 0° (center of its range) some tests on the system performance as a whole have been carried out, to measure the different SEs pupils superposition stability during the bearing rotation. The aim of this verification is to measure the RMS blur, measured as the RMS differential shift of the spots produced by the 12 SEs illuminated with red beam. The goal is to find an RMS shift of the spots, representing the centers of the pupils,

compatible with what expected considering the following blur sources (discussed in the overall error budget):

- Pyramid vertex angle;
- Pyramid faces orthogonality;
- SE relative tilt;
- Pyramid orientation;
- PR-I optical quality (a small fraction, here neglected);
- SE tilt due to support flexures (a fraction. Here considered 1/sqrt(2));
- SE tilt due to ring flexures (a fraction. Here considered 1/sqrt(2));
- SE tilt due to stage flexures (a fraction. Here considered 1/sqrt(2)).

The root sum square of the listed items is 10.5 μm. The test has been carried out in a way that the SEs orientation with respect to the gravity vector changed only around a single axis (the bearing rotation one) while in the true life of LINC-NIRVANA also the elevation of the telescope will play a role. Details of how these flexures splits into these two components are beyond the limit of this test and it is here assumed that the two effects are similar and incoherently added, leading to the factor 1/sqrt(2) used for the test.

To perform the test, after the SEs alignment, the bearing has been rotated and graphs showing the relative movements of the SEs spots barycenter for a 120° rotation have been produced (figure 3.45). Essentially due to flexures of the various mechanical components of the GWS (SEs arms, T-T stages, positioning stages, GWS mechanics, CCD group), when rotating the bearing and observing the behavior of each set of pupils coming from the different SEs, there are common and differential movements:

- The common movement of the pupils on the detector is coming from flexures of everything which is after the SEs, i.e. mostly the pupil re-imager and the detector group. This movement, being common to all the SEs, can in principle be compensated by the moving the motorized stages of the CCD. Therefore, we computed it by software and is shown in figure 3.46 (black line).
- The differential movement is essentially due to the differential flexures of each SE, i.e. local differential deformations of the GWS structure, of the XY SE stages, of the tip-tilt adjusting systems and of the SE mechanical structure itself. It is shown in figure 3.46 after the subtraction of the common mode.

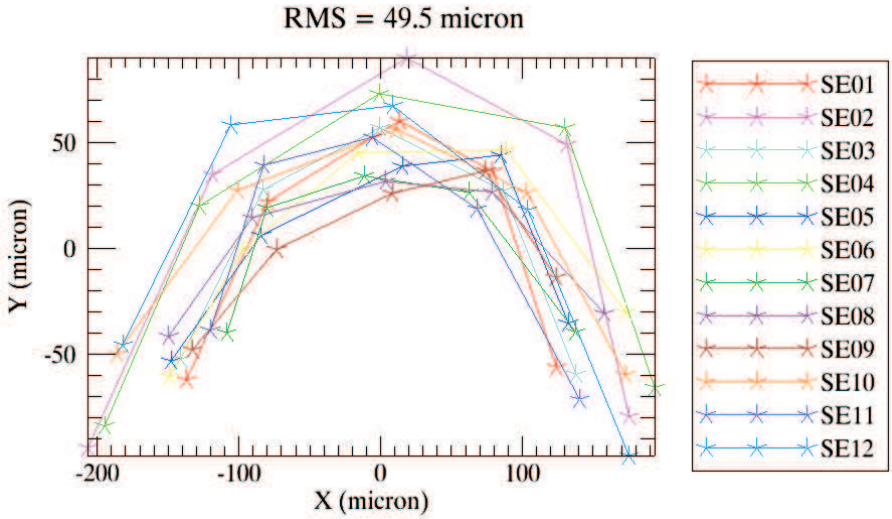

Figure 3.45: Pupils movements on the CCD50 for a complete 120° rotation of the GWS. Test CCD X and Y axis reproduce a vertical orientation of the gravity vector when the bearing is in the 0 ° position.

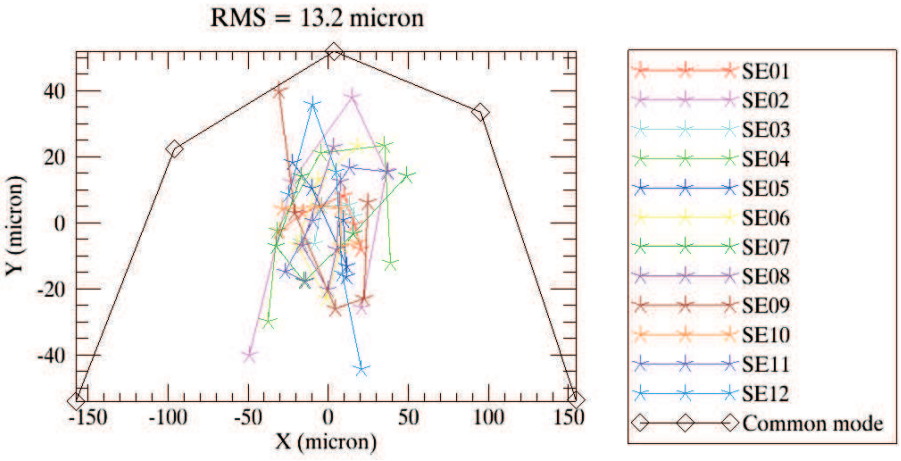

Figure 3.46: Pupils movements on the CCD50 for a 120° rotation of the GWS, after the software subtraction of the common mode, which can be compensated moving the CCD.

Since the value obtained after the subtraction of the common mode, was higher than expected, we repeated the SEs alignment in tip-tilt following this procedure:

a) Using the collimated beam setup, we coarsely aligned all the SE in tip-tilt with the bearing position set at 0° in a way that each set of four spot was roughly superimposed;

b) Using the F/15 setup, we aligned each SE in focus;

c) Using the collimated beam setup and for one SE at a time, we recorded the movement of the four spot when rotating the bearing in its full range, with steps of 30° (thus, we recorded 5 positions being the total travel 120°). This operation has been done for all the SEs and rotating the bearing both clock-wise and counter clock-wise;

d) We computed numerically the theoretical position of the four spot created from each SE which is minimizing the RMS of the movement of the four spots themselves over a rotation of 60°, around the zero position of the bearing. The choice of optimizing the spots position over only 60° is due to the fact that the bearing will be operated at maximum in a range of 60°. This numerical operation is giving as an output, for each set of four spot coming from a certain SE, the position where that SE shall be aligned to (figure 3.47);

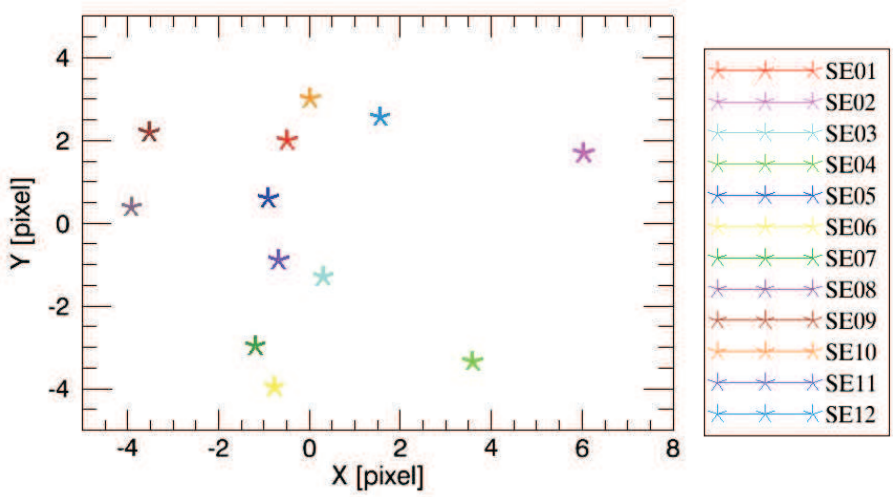

Figure 3.47: Retrieved SEs alignment position in tip-tilt to minimize the rotation effect on the pupil blur.

e) Using the collimated beam setup, we aligned each SE in tip-tilt to the positions previously identified;

f) Using the F/15 setup, we checked the focus alignment of each SE and, if necessary, we adjusted it;

g) We checked the quality of the performed alignment: using the collimated beam setup and for one SE at a time, we recorded the movement of the four spot when rotating the bearing in its full range, with steps of 30° (thus, we recorded 5 positions being the total travel 120°). This operation has been done for all the SEs and rotating the bearing both clock-wise and counter clock-wise;

h) We compared the obtained RMS results with the theoretical ones previously numerically computed, both in the range [-60 °,60 °] and in the range [-30 °,30 °]. In the last operation we are removing the "common mode" movement, supposing that the CCD XY adjustments will compensate the common flexures during a scientific exposure, either by actively checking the pupils common movement on the detector and compensating it or based on a look-up table which is characterizing the pupils motion at each bearing rotation angle and at each telescope observation altitude.

Because of the expanded Fisba beam diameter (150 mm), the odd-labeled SEs could be positioned exactly in the positions inside the FoV used during the alignment, while the even-labeled SEs had to be disposed in a smaller radius (23.1 mm closer to the center), in order to be illuminated by the collimated beam. Figure 3.48 shows the resulting spots shifts for all the SEs, whose RMS value is 14.3 μm, which is still larger than what we would expect. However, we have to remember that only the odd-labeled SEs performance are measured in the proper position, while it is clear that the spots produced by the even-labeled SEs are slightly shifted with respect to the median position of the spots, and that is due to the fact that the wobble of the stages and the pupil re-imager optical quality are playing a role (they should not, in this verification test. In fact they are not part of the listed blur sources), since the SEs are not exactly in the positions in which they have been aligned. Figure 3.49 shows the results obtained only with the odd-labeled SEs in the field. The RMS relative shift turns to 9.4 μm (below the expectations), and we have no reason to expect something different from the even-labeled SEs, if they are performance would be verified in the proper field positions, since they have been aligned with the same precision than the odd-labeled ones.

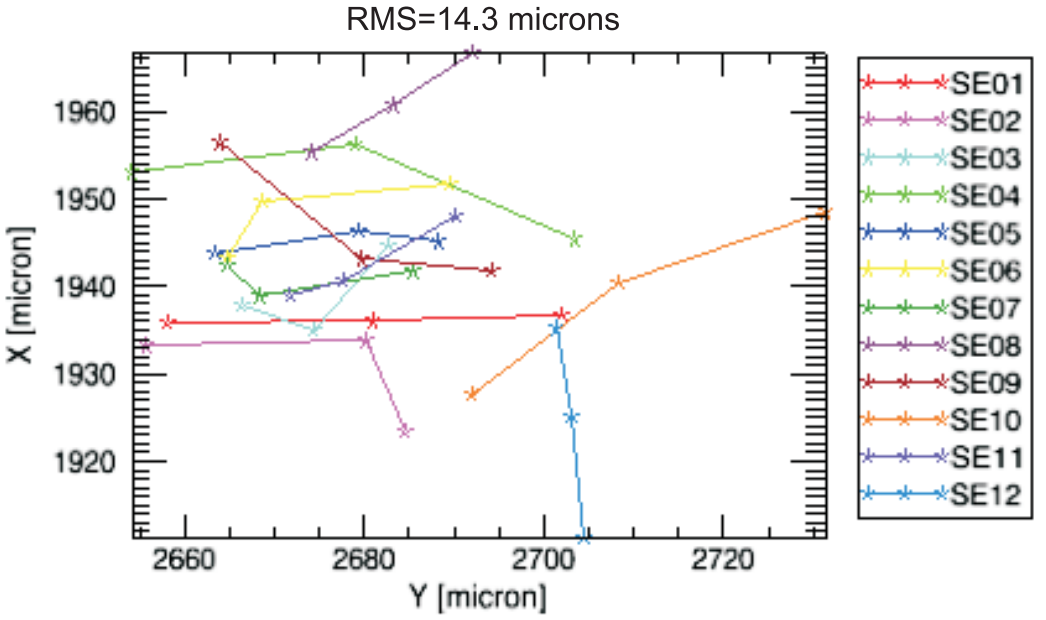

Figure 3.48: All the SEs together in the field for a 60° rotation of the bearing. The RMS relative shift is 14.3 μm, but that the spots produced by the even-labeled SEs are slightly shifted with respect to the median position of the spots, since the SEs are not exactly in the positions in which they have been aligned.

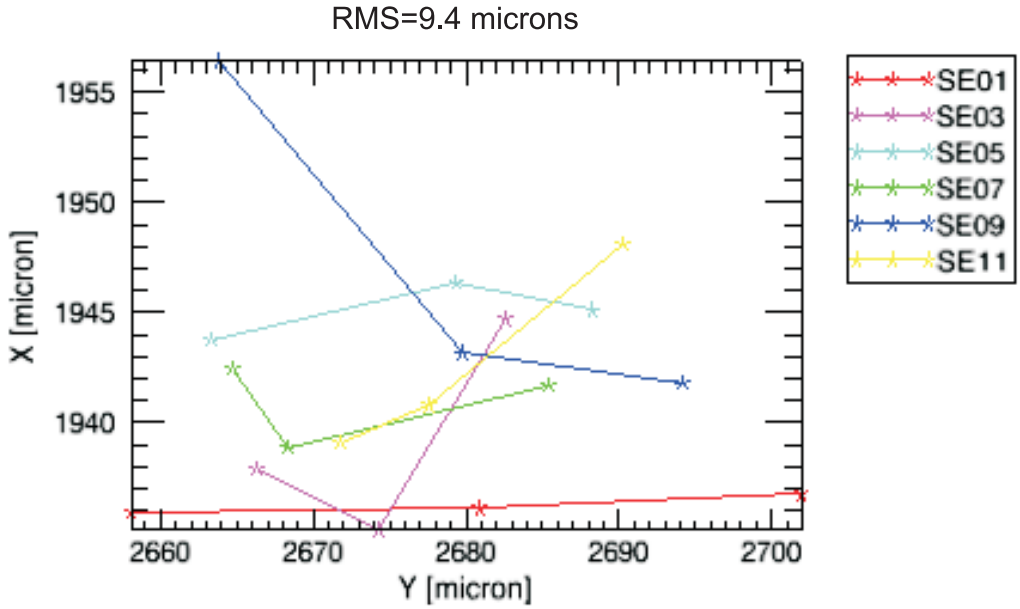

Figure 3.49: Only the odd-labeled SEs in the field for a 60° rotation of the bearing. The RMS relative shift is 9.4 μm. These SEs have been aligned in the same position in which the rotation test has been performed.

3.3.7 Flexure tests

The main purpose of the flexures tests is to measure the flexure effects and to possibly devise calibration procedures based on look-up tables to be used during final operation of the system. Flexures occur when the GWS orientation with respect to gravity changes, due to altazimutal telescope pointing, which causes the LN bench to tilt up to 60°. The tests were performed at MPIA of Heidelberg, where the GWS was mounted on the final LN bench, which is equipped with a system allowing it tilt in a fast and precise way (0.1°). We were interested in testing the whole range and therefore we decided to consider flexures every 15° of bench tilt, as will be better explained along this section. We want to focus first of all on the main effects which could be produced by flexures of different opto-mechanical components:

A. Pupil image shift (lateral and axial), which may be due to different reasons:

1. **shift of the CCD camera**. A lateral shift of the camera of a distance r corresponds to the shift of the pupil lateral image. Since the PR-I works at a focal ratio close to F/1, the axial shift of the pupil, meaning a defocus of the CCD (or the PR-I), translates into a lateral pupil blur of the same amount. This blur should be compared to the sub-aperture size both for lateral and axial shift;
2. **SE tilt.** A SE tilt by an angle α produces an angular tilt of the exit pupil by an angle α (1+1/k), where k=12.5 is the SE magnification factor. This angular shift of the pupil may be translated into a pupil image lateral shift on the CCD camera simply multiplying the angle by the Pupil Re-Imager focal length (f = 220 mm):

$$r = \alpha\ (1+1/k)\ f$$

3. **overall structure tilt**. A tilt of the overall structure (i.e. a flange flexure) by an angle β produces a pupil image lateral shift that is given by the tilt angle reduced by a factor k=12.5 (due to the star enlarger effect) multiplied by the pupil re-imaging objective focal length f:

$$r = \beta/k\ f$$

It should be noticed that, in the absence of the SE, the same tilt angle β produces a pupil image lateral shift that is magnified by a factor k.

B. Star Enlarger shift (lateral and axial). The SE lateral and axial shifts are detected by the pyramid wavefront sensor respectively as a wavefront tilt and defocus. The SE lateral shift may be compared to the diffraction limited spot FWHM. At F/15 and wavelength λ=0.633 μm, the diffraction limit width is w = 9.5 μm. The SE axial shift may be compared to the depth of focus. At F/15

and wavelength λ=0.633 μm, the depth of focus is d = 140 μm and corresponds to a wavefront defocus of approximately 20 nm RMS. However, we remind the decision of accepting a maximum defocus of 1.37 mm.

Different operation CCD modes of the GWS are foreseen, translating into different sub-aperture sizes. The test results presented in this section are given in pixels (24 μm) or μm units. Flexure effects can be compensated by the available degrees of freedom:

- the pupil displacement, provided it is the same for all the SEs, can be corrected by centering and/or refocusing the CCD camera by means of the motorized linear stages specifically foreseen for this purpose;
- the tilt signal due to a SE lateral shift can be corrected by centering the SE on the respective reference star;
- the defocus signal can be compensated by refocusing the annular mirror in front of the GWS entrance, provided the defocus is the same for all SE.

F/15 sources: description and calibration

To test GWS for flexures four F/15 sources, simulating the F/15 telescope beam, are used. Each source consists of an optical fiber re-imaged by a lens; a telecentric aperture stop is placed between the source and the lens, in order to obtain the proper F/# and obtaining on the CCD50 camera four pupil images of approximate diameter Ø48 pixels. A 200 μm core multimode optical fiber is used, the core size was chosen in order to have a linear response of the pyramid wavefront sensor under the expected flexure effects. An incoherent white light source is used to feed the fiber. Since the white light source can introduce too much chromatism (i.e. chromatic focal shift of the F/15 source lens): for the defocus measurements a narrow band-pass filter centered at λ = 0.630 μm (0.62-0.64 μm) is inserted in the source emulator in order to cancel chromatic effects. The characteristics of the source light are described in table 3.13 Before proceedings to the test on LN bench, the response of the system to the

Component	**Characteristic**	**Value**
Lens	Focal length	19 mm
Stop	Diameter	1.3 mm
Optical fiber	Size	200 micron
Narrow band filter	Light Wavelength	620-640 nm

Table 3.13: F/15 source components.

light sources has been calibrated, to understand if the linear range was consistent with

what expected and to be able to convert the tip-tilt and defocus coefficients retrieved during flexures tests into physical units. First of all the F/15 beam produced by one of the reference sources is collected by one of the Star Enlargers and aligned in tip-tilt, looking at the pupils positions onto the CCD50, and in defocus, minimizing the defocus term in the signal retrieved by the wavefront sensor. Afterwards two calibrations are done:

A. the Star Enlarger is moved along the focal plane and the tip-tilt signal is retrieved.

We found the calibration curve of the SE lateral shift with respect to the F/15 source vs. the tilt signal detected by the pyramid wavefront sensor (see figure 3.50). This curve depends on the source features (i.e. fiber core).
The tip-tilt calibration has been performed moving the SE01 along its x axis (corresponding also to the CCD50 camera axis) for a complete range of 10000 counts, with 1000 counts steps (the linear stage resolution is 29.5 counts/μm). A preliminary set of measurements has been taken to verify the repeatability of the signals measurement. The retrieved Standard Deviation, for a set of 10 measurements, is 0.3 arbitrary units. The images were combined and a tilt signal calculation routine similar to the one applied in Chapter 2 was applied to calculate the differential tilt signal of the PWFS with respect to reference image taken at zero shift. The retrieved conversion factor (for the linear range,

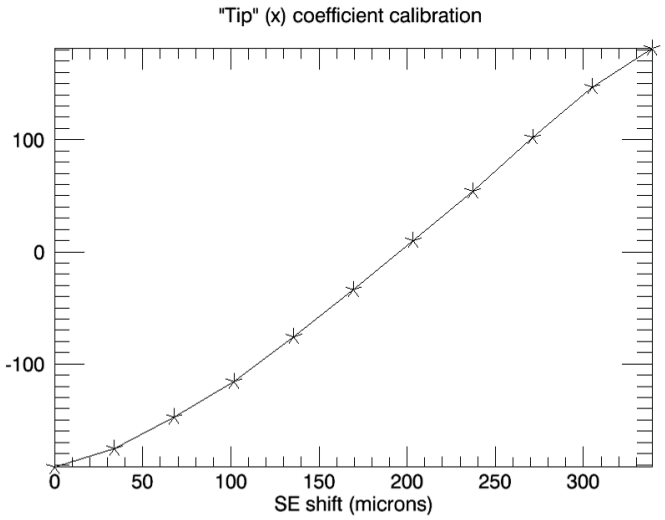

Figure 3.50: The Tip-tilt signal calibration measurements. The Y axis reports the first Zernike coefficient variation.

which is about 200 microns wide) is: C = **1.3 arb. units/μm**;

B. the F/15 source is moved along the optical axis and the defocus signal is retrieved
We found the calibration curve of the SE defocus with respect to the F/15 source vs. the defocus signal detected by the pyramid wavefront sensor (see figure 3.51). This curve depends on the source features (i.e. fiber core).
The Defocus calibration has been performed moving an F/15 source along the optical axis (corresponding also to the GWS rotation axis) for a total travel of 5 mm, with 0.5 mm steps. A preliminary set of measurements has been taken to verify the repeatability of the signals measurement. The retrieved Standard Deviation, for a set of 10 measurements, is 0.04 arbitrary units. The images were combined and a defocus signal calculation routine similar to the one applied in Chapter 2 was applied to calculate the defocus signal of the pyramid wavefront sensor. The retrieved conversion factor is: K= **30**

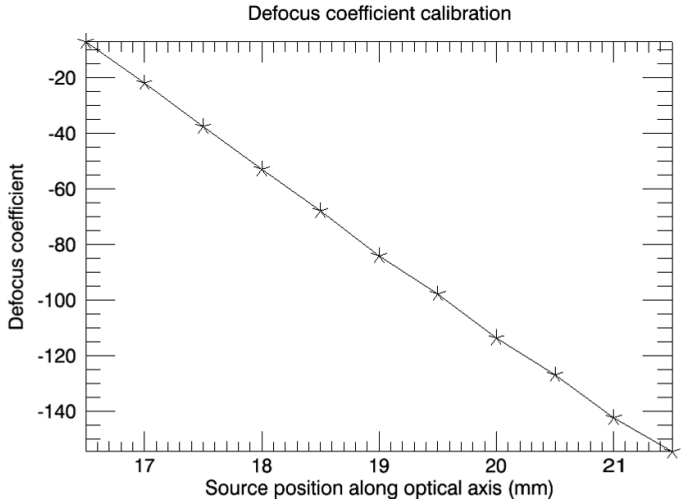

Figure 3.51: The Defocus signal calibration measurements. The Y axis reports the third Zernike coefficient variation (without piston).

arb.units/mm.

Experimental setup

To perform the flexures tests the GWS was mounted on the LN bench, as can be seen in figure 3.52.

As a first thing, the CCD needs to be properly positioned in focus and center. To check this is still happening after the lifting of the GWS onto the bench, a wide collimated laser beam, coming from a commercial Fisba interferometer is used as a reference and it is aligned to the GWS in order to be parallel to the GWS optical and rotation axis and focus the CCD50 minimizing the re-imaged spot diameter.

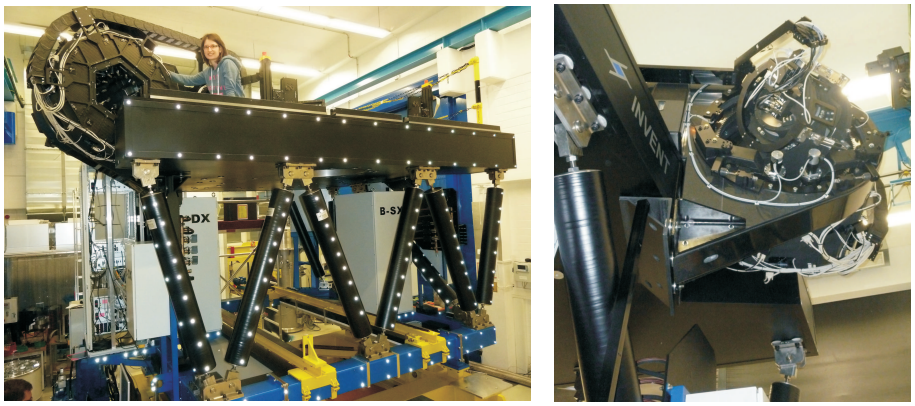

Figure 3.52: GWS mounted on the LN bench ready for the flexures test.

Afterwards the Fisba is removed and four F/15 sources mounted on a common plate are positioned at the entrance focal plane (see figure 3.53) by mechanical precision. The tilt of the F/15 beams is adjusted by shims.

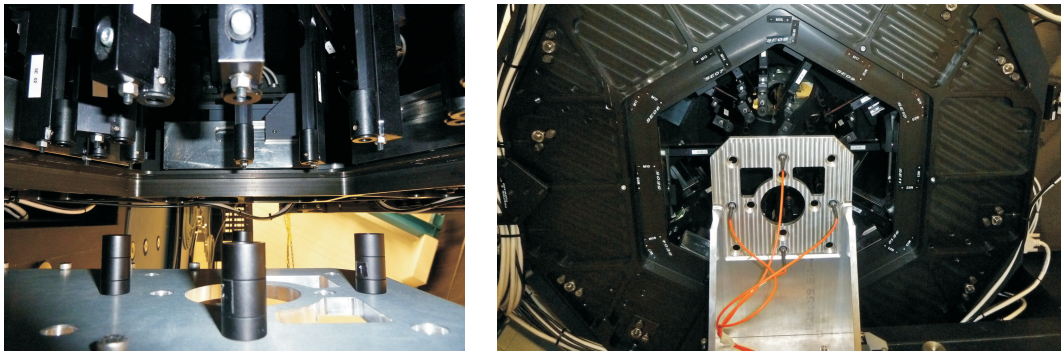

Figure 3.53: F/15 reference sources.

At this point the system is ready to perform all the measurements described in the following sections, repeated in a combination of bench tilt angles, bearing rotation angles and SEs radial positioning in the field, to try to disentangle possible flexures sources, reported in table 3.14.

We remind the quantities to be measured:

- Pupil image lateral shift
- SE lateral shift or wavefront tilt
- SE axial shift or wavefront defocus

	SEs	LN bench tilt	Bearing rotation	SEs radius in FoV
Test #1	All	0°, 15°, 30°, 45°, 60°	0°	79 mm (2.2')
Test #2	SE02, SE03, SE05, SE06, SE08, SE09, SE11, SE12	0°, 15°, 30°, 45°, 60°	-60°, -30°, 0°, 30°, 60°	79 mm (2.2')
Test #3	SE02, SE06, SE08, SE12	0°, 15°, 30°, 45°, 60°	0°	50 mm (1.4')
Test #4	SE04, SE06, SE10, SE12	0°, 15°, 30°, 45°, 60°	0°	79 mm (2.2') (repeatability test)

Table 3.14: Configurations for the Flexures Test.

Measurement of pupil image shift (a)

The pupil image position measurement is based on an edge fitting routine: the pupil edge is identified by a Sobel filter, then it is fit by a circle (pupil images through SE). The center of the circle (possibly averaged over four pupils if applicable) gives a measurement of the pupil position.
The pupil image lateral shift has been measured for each SE with the orientation of the GWS varying with respect to the gravity direction from 0° to 60°. At each step the tilt signal measured by the WFS is nulled and a set of images is acquired. Due to the fact that between two bench tilt positions the pupils shifted outside the CCD area, the result has been obtained combining the CCD50 motion necessary to keep the pupils inside the chip with the computed shift of the pupil in the images, obtained with the pupil edge fitting routine. The first measurement performed at 0° is taken as reference for the pupil image shifts of a given SE. In this way every common mode and each sources relative misalignment are removed (measured common motions are reported in figure 3.54).

The figures 3.56, 3.57, 3.58 and 3.59 show the shifts, on the pupil plane, of the barycenters of the four pupils re-imaged after passing through each SE during the tests listed in table 3.14. The pupils shift RMS values are reported on top of each figure, for the bench inclinations (0°, 15°, 30°, 45° and 60°).

Test #1a: Figure 3.55 shows the results obtained for the pupils shift due to flexures for each SE. There seems to be no obvious correlations between the measured shift and the SEs position (even vs. odd SEs, SEs "asterism",...) or the considered bench tilting run. The measured RMS shift of the pupils increases with the bench tilt angles (up to ≈46 μm for a 60° bench inclination), and this effect could be partially

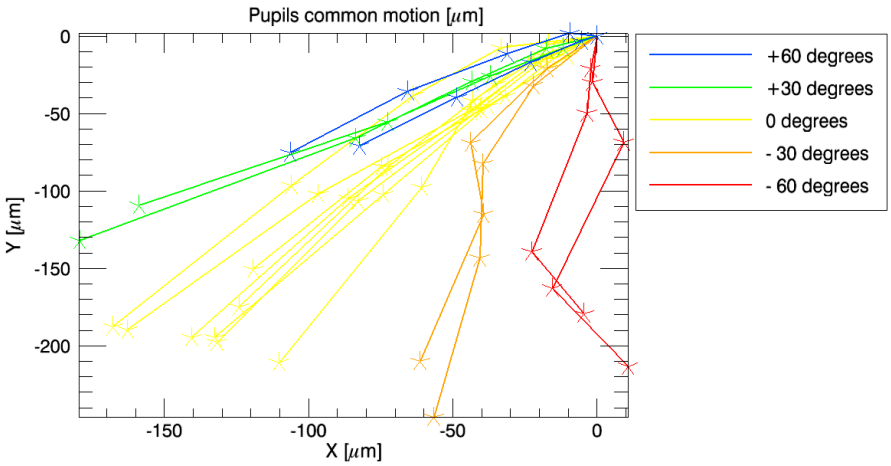

Figure 3.54: Pupils common motion in 16 different bench tilt runs. Different colors represent different bearing rotation angles.

due to a CCD50 shift along the optical axis. Such movement could be of the same order of magnitude of the CCD50 lateral shift.

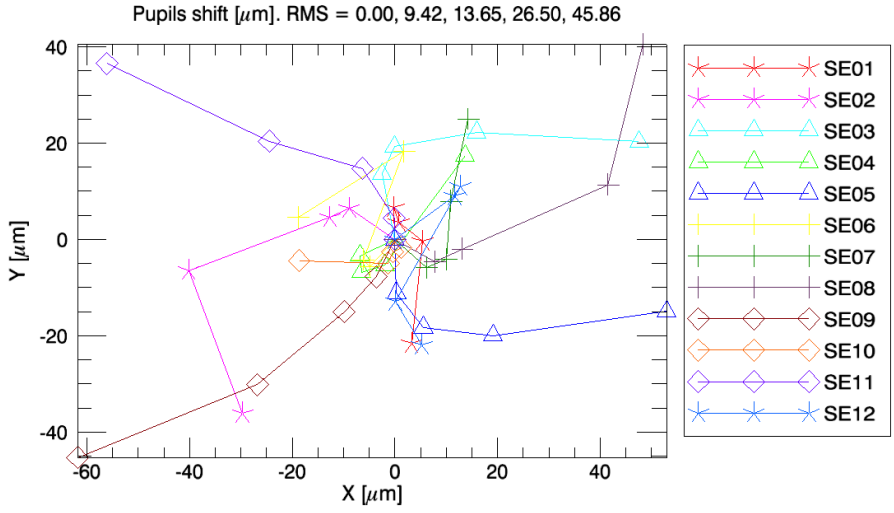

Figure 3.55: Pupils shift measured on the CCD50 for Test #1a. Different colors represent different SEs, while different symbols are used to group SEs tested in a common run. The pupils shift RMS are reported on top of the figure, for the bench tilt listed in table 3.14 (0°, 15°, 30°, 45° and 60°), indicated for each one by the points from the center toward the sides of the graph.

To try to remove a possible CCD50 axial shift effect from the data, an IDL

procedure has been realized. The pupils barycenters for each SE have iteratively been shifted on the pupil plane in the direction they would have shifted in case of a CCD defocus (this direction only depends on the source position) and of an amount proportional to the distance of the source from the center of the GWS field of view. The position of the "virtual" CCD which minimizes the RMS of the pupil shifts has been considered as "computed CCD50 defocus". Since, as will be clearer later, the flexures effect seems not to be very repeatable, this procedure has been separately repeated for each run. The obtained "corrected" pupils shift are reported in figure 3.56. While a clear evidence of correlation between the measured shift and the SEs position or the considered bench tilting run is still missing, the maximum RMS value decreased from ≈46μm to ≈29μm for a 60° bench inclination.

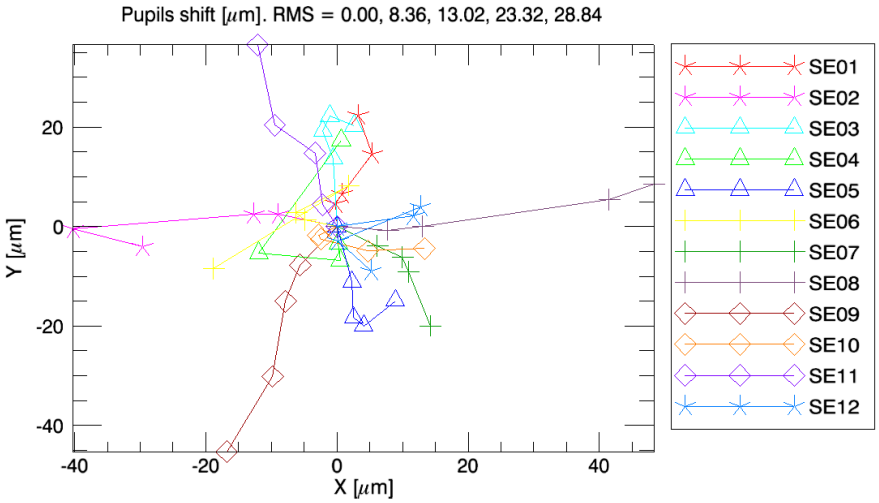

Figure 3.56: Pupils shift measured on the CCD50 and *a posteriori* corrected via software optimizing the CCD50 position along the optical axis for Test #1a. Different colors represent different SEs, while different symbols are used to group SEs tested in a common run. The pupils shift RMS are reported on top of the figure, for the bench tilt listed in table 3.14 (0°, 15°, 30°, 45° and 60°), indicated for each one by the points from the center toward the sides of the graph.

Test #2a: The obtained "corrected" pupils shifts (applying the CCD50 defocus optimization) are reported in figure 3.57, for 8 SEs in 5 different bearing rotation positions. The maximum RMS value decreased from ≈55μm to ≈23μm for a 60° bench inclination. Any evidence of correlation between the measured shift and the bearing position is missing.

Test #3a:: The obtained "corrected" pupils shift (applying the CCD50 defocus optimization) are reported in Figure 3.58, for 4 SEs placed at 3 different radial

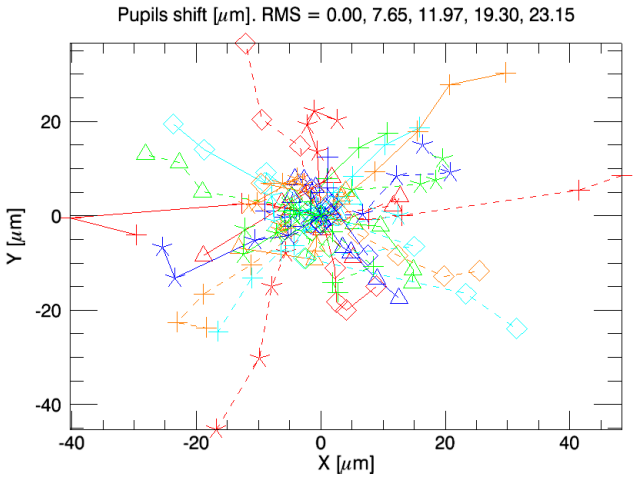

Figure 3.57: Pupils shift measured on the CCD50 and *a posteriori* corrected via software optimizing the CCD50 position along the optical axis for Test #2a. Different colors represent different bearing rotation angles. The pupils shift RMS are reported on top of the figure, for the bench tilt listed in table 3.14(0°, 15°, 30°, 45° and 60°), indicated for each one by the points from the center toward the sides of the graph.

positions inside the GWS field of view. The maximum RMS value decreased from ≈60μ to ≈30μm for a 60° bench inclination. Any evidence of correlation between the measured shift and the bearing position is missing.

Test #4a: The obtained "corrected" pupils shift (applying the CCD50 defocus optimization) are reported in Figure 3.59, for the repeatability test of pupils shift due to flexures for 4 SEs. The maximum RMS value decreased from ≈42μm to ≈19μm for a 60° bench inclination. Even with all the applied corrections, the measurement repeatability seems to be very low.

As discussed, a movement of the CCD50 along the optical axis can explain most (half) of the RMS shift of the pupils on the CCD, because of a defocus effect, and has been compensated by software, applying the values reported in table to obtain the RMS "corrected" values. Up to now, this term has been applied via software during the data analysis of the flexures test images, minimizing the overall pupil shifts RMS. Table 3.15 reports all the computed CCD50 axial shifts applied to obtain the RMS "correcte" values. Of course, being this the result of an optimization, it is possible to be compensating other effects. To check this, two further flexures test runs (run 1 and 2) have been performed. Figures 3.60 and 3.62 show the measured pupils shifts (red symbols) for run 1 and run 2, in which two different groups of four SEs have been selected. The optimization procedure, considering a full 60° bench tilt, gave a computed CCD50 shift along the optical axis of 131 μm and 154 μm for

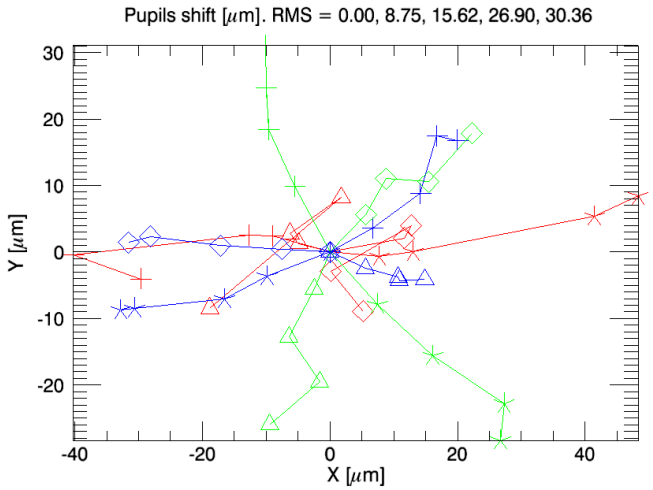

Figure 3.58: Pupils shift measured on the CCD50 and *a posteriori* corrected via software optimizing the CCD50 position along the optical axis for Test #3a. Different colors represent different radial positions. The pupils shift RMS are reported on top of the figure, for the bench tilt listed in table 3.14 (0°, 15°, 30°, 45° and 60°), indicated for each one by the points from the center toward the sides of the graph.

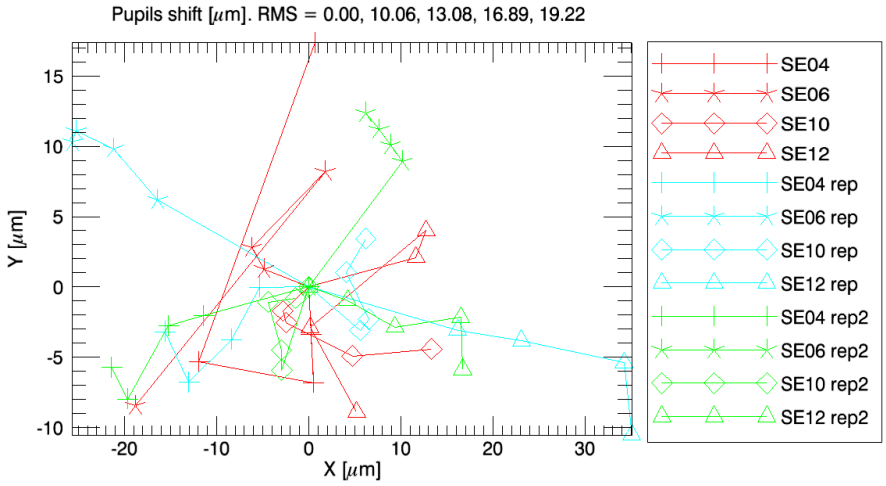

Figure 3.59: Pupils shift measured on the CCD50 and *a posteriori* corrected via software optimizing the CCD50 position along the optical axis for Test #4a. Different colors represent different runs, while symbols are related to the tested SEs. The pupils shift RMS are reported on top of the figure, for the bench tilt listed in table 3.14 (0°, 15°, 30°, 45° and 60°), indicated for each one by the points from the center toward the sides of the graph.

the two runs to obtain a minimum expected RMS value of ≈14 μm and ≈22 μm, respectively (green symbols). After this first measurement, for each run, the CCD50 has been shifted along the optical axis of the computed amount and the pupils' position have been measured again. Figures 3.61 and 3.63 show the result of this second measurement for the two runs. In both cases a small residual de-focus has been detected (this could due to the lack of a fine-tuning of the computing procedure calibration), but the actual RMS values have decreased from 48.3 μm and 55.5μm to 14.5 μm and 23.3 μm, in both cases very close to the expectations.

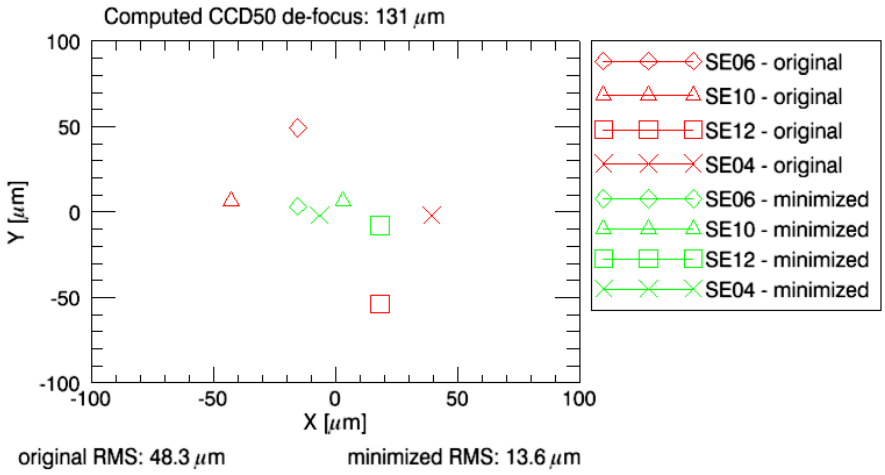

Figure 3.60: Result of run1, in which SE04, SE06, SE10 and SE12 and have been considered. Red symbols represent the actual pupil shift, while green symbols represent the expectation of the pupils positions for a 131 μm shift of the CCD50 to compensate for flexures for a ° bench tilt.

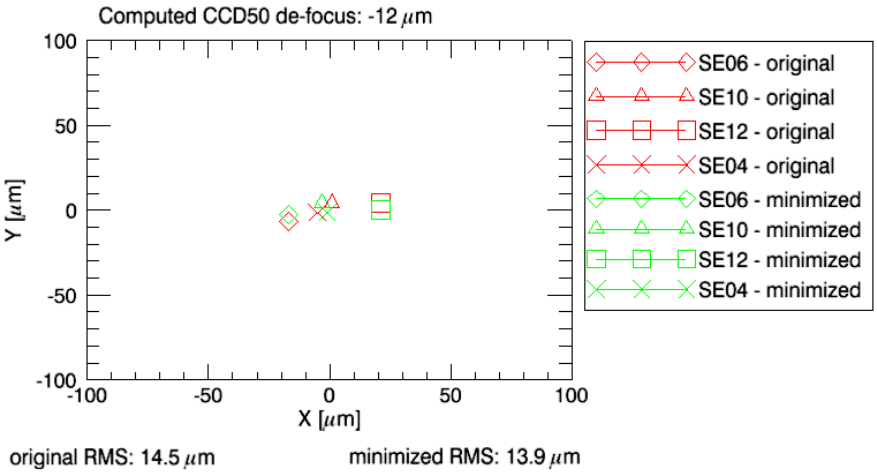

Figure 3.61: Result of run1, after the CCD50 re-adjustment. The measured pupils' positions are very close to the expectations.

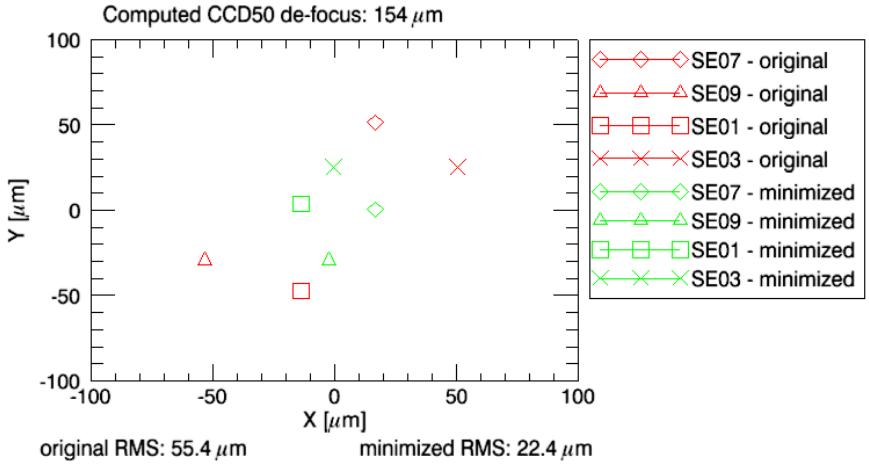

Figure 3.62: Result of run2, in which SE01, SE03, SE07 and SE09 have been considered. Red symbols represent the actual pupil shift, while green symbols represent the expectation of the pupils positions for a 154 μm shift of the CCD50 to compensate for flexures for a ° bench tilt.

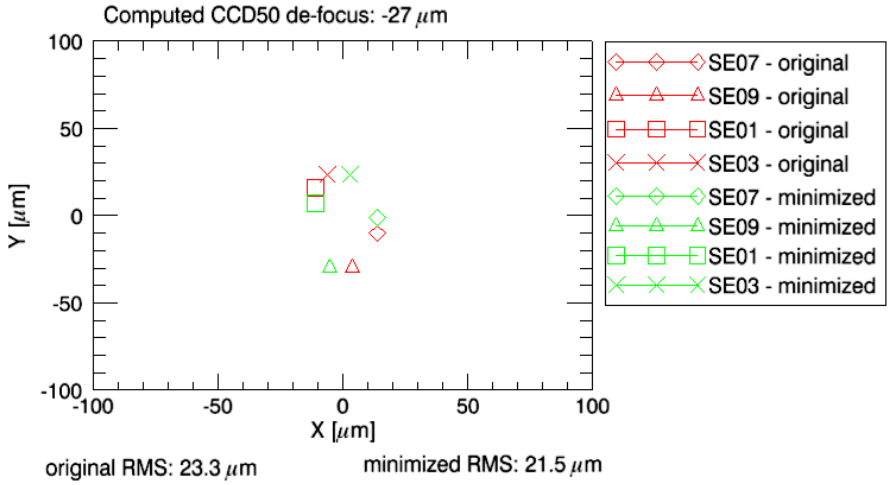

Figure 3.63: Result of run2, after the CCD50 re-adjustment. The measured pupils' positions are very close to the expectations.

	Bench tilt angle			
run	**15°**	**30°**	**45°**	**60°**
t1	-6	6	49	130
t2	-6	9	43	127
t3	-20	-20	29	33
t4	-12	-6	17	92
t5	-9	12	69	170
t6	-6	12	69	158
t7	6	29	147	193
t8	3	46	92	210
t9	-12	-9	23	81
t10	-32	-43	-43	-6
t11	-20	-29	14	109
t12	12	12	55	147
t13	9	49	144	190
t14	-17	-14	3	63
t15	-23	-35	-20	9
t16	17	55	98	225

Table 3.15: Computed CCD50 shifts (μm) for different runs and bench tilt angles. Colors represent different run characteristics: blue= -60 °; violet=-30 °; no color= 0 °; green= +30 °; yellow= +60 °; orange = in-out FoV.

Star Enlargers lateral shift (wavefront tilt) (b)

The measurement of the SE lateral shift is based on the calculation of the wavefront tilt slope detected by the pyramid wavefront sensor. The slope is given by the normalized difference of the integrated intensity of the four pupil images: if A, B, C, D denote the integrated intensity of the four pupils, the tilt slope (in arbitrary units) with respect to two orthogonal axes is given by (A+B-C-D)/(A+B+C+D) and (A+C-B-D)/(A+B+C+D). This tilt signal in arbitrary units is converted into an equivalent lateral shift of the SE with respect to the F/15 source according to the calibration defined in section 3.3.7. As a first step a given SE is centered on the F/15 source nulling the tilt signal measured by the pyramid wavefront sensor. Then a set of images is acquired. The SE lateral shift has been measured as the corresponding motor movement necessary to minimize the tip-tilt signature onto the four pupils for each SE when the orientation of the GWS with respect to the gravity direction and the previous step is repeated for several tilt angles (0° to 60°, with 15° steps) and all the configurations reported in table 3.14. The first measurement performed at 0° is taken as reference for the pupil image shifts of a given SE. In this way each source relative misalignment is removed.
Figures 3.64, 3.65, 3.66 and 3.65 show the shifts, on the entrance focal plane, of the SEs during one of the tests listed hereafter. The motion of each SE is translated and expressed as a movement in the SE01 reference frame.

Test #1b: All the measured shifts reported in Figure 3.64 are below 300 μm for a complete bench tilt (60°). No particular correlations between the measured shift and the selected SE position have been found.

Test #2b: All the measured shifts reported in Figure 3.65, in which the GWS rotation angle has been changed, are below 300 μm for a complete bench tilt (60°). No particular correlations between the measured shift and the selected rotation angle have been found.

Test #3b: All the measured shifts reported in figure 3.66, in which the SE radial position has been changed, are below 300 μm for a complete bench tilt (60°). No particular correlations between the measured shift and the SE position have been found.

Test #4b: All the measured shifts reported in Figure 3.67, concerning the repeatability test, are below 300 μm for complete bench tilt (60°). However the repeatability has not shown to be relevant.

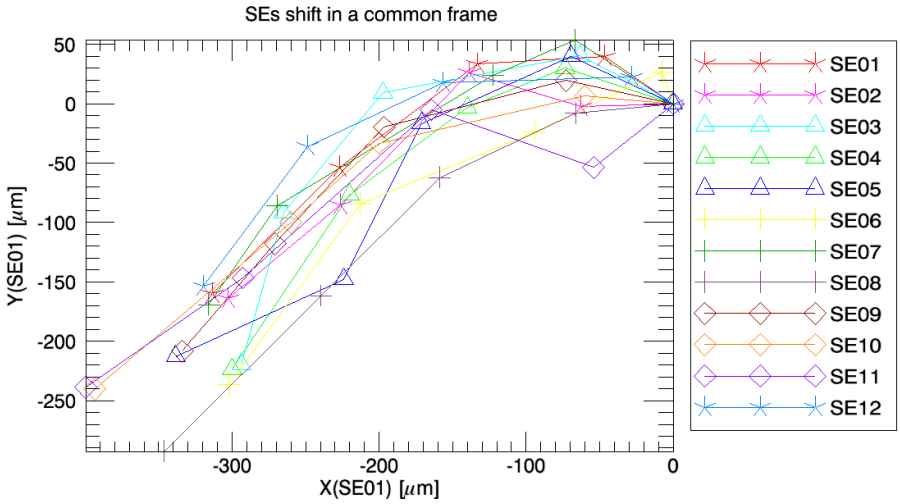

Figure 3.64: SEs shift measured as the motors movements necessary to minimize the tilt signal for Test #1b. Different colors represent different SEs, while different symbols are used to group SEs tested in a common run. Each point of each curve represents a bench tilt (left to right: 0°, 15°, 30°, 45° and 60°).

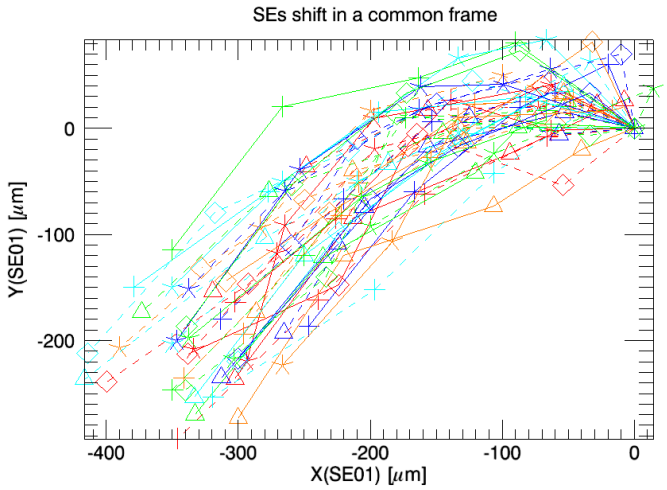

Figure 3.65: SEs shift measured as the motors movements necessary to minimize the tilt signal for Test #2b. Different colors represent different bearing rotation angles. Each point of each curve represents a bench tilt (left to right: 0°, 15°, 30°, 45° and 60°).

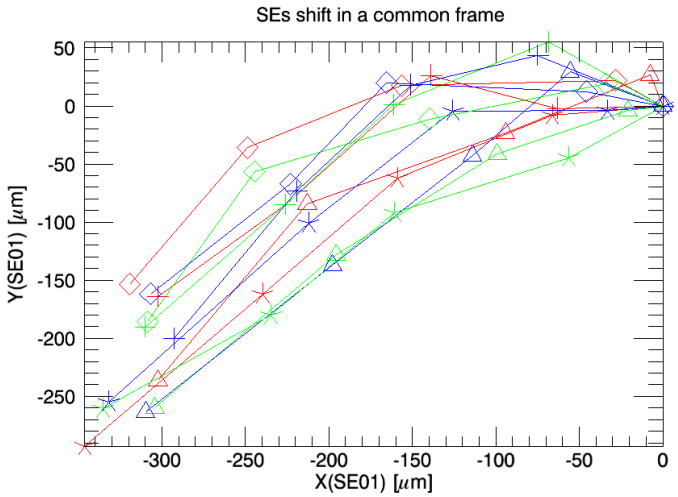

Figure 3.66: SEs shift measured as the motors movements necessary to minimize the tilt signal for Test #3b. Different colors represent different radial positions. Each point of each curve represents a bench tilt (left to right: 0°, 15°, 30°, 45° and 60°).

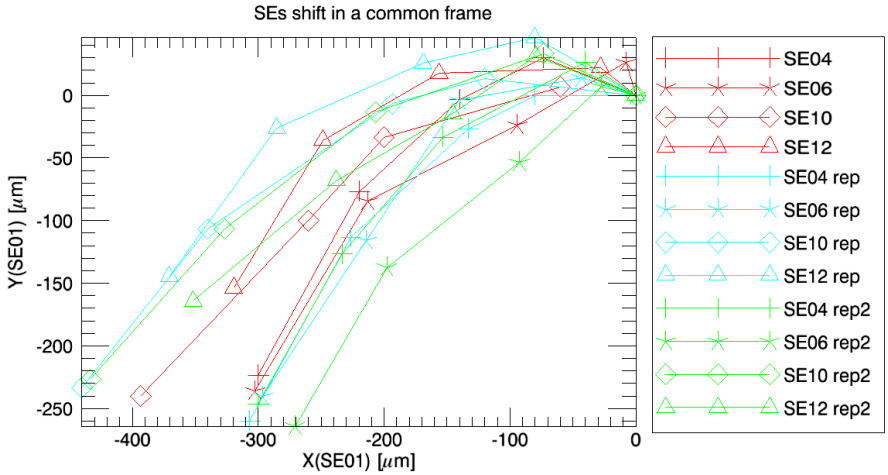

Figure 3.67: SEs shift measured as the motors movements necessary to minimize the tilt signal for Test #4b. Different colors represent different runs, while symbols are related to the tested SEs.Each point of each curve represents a bench tilt (left to right: 0°, 15°, 30°, 45° and 60°).

Star enlarger axial shift (wavefront defocus) (c)

The SE axial shift is measured in terms of wavefront defocus induced by this shift. A defocus measurement method is implemented, based on the fitting of the measured slopes by Zernike polynomials. In order to make the fitting as robust as possible, the data for the defocus measurements were taken after nulling the tip-tilt signal, measured by the PWFS, centering each star enlarger on the F/15 source image. Afterwards the defocus signal in arbitrary units is converted into an equivalent axial shift of the SE with respect to the F/15 source with the conversion obtained in section 3.3.7. A set of images is acquired and the SE axial shift is measured as the corresponding motor movement necessary to minimize the defocus signal onto the four pupils for each SE when the orientation of the GWS with respect to the gravity direction and the previous step is repeated for several tilt angles (0° to 60°, with 15° steps) and all the configurations reported in table 3.14. The first measurement performed at 0° is taken as reference for the axial shifts of a given SE. In this way each source relative misalignment is removed.

Figures 3.68, 3.69, 3.70 and 3.71 show the shifts, along the optical axis, of the SEs during one of the tests.

Test #1c: all the measured shifts reported in figure 3.68 for each SE are below 650μm for a complete bench tilt (60°). No particular correlations between the measured shift and the SE position have been found.

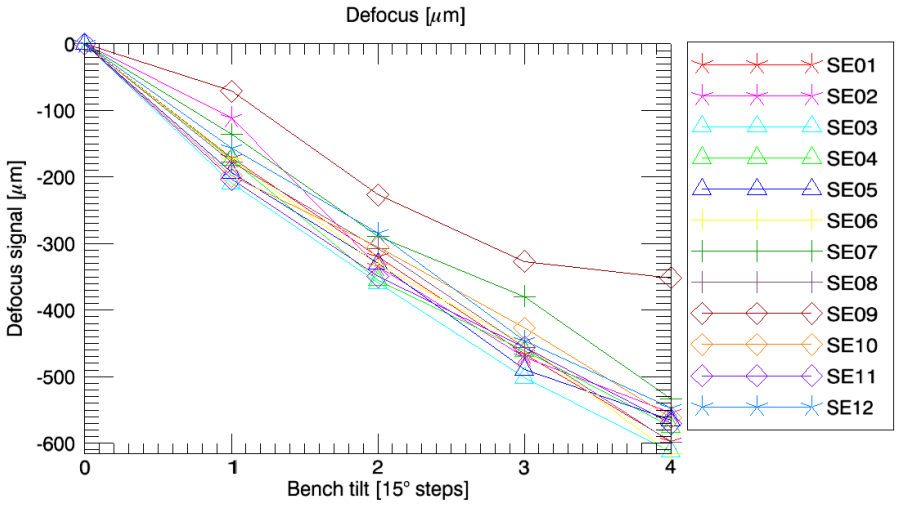

Figure 3.68: SEs axial shift measured as a defocus signature on the pupils for Test #1c. Different colors represent different SEs, while different symbols are used to group SEs tested in a common run.

Test #2c: all the measured shifts reported in figure 3.69 for each SE are below 650μm for a complete bench tilt (60°). No strong correlation between the measured shift and the bearing rotation position has been found.

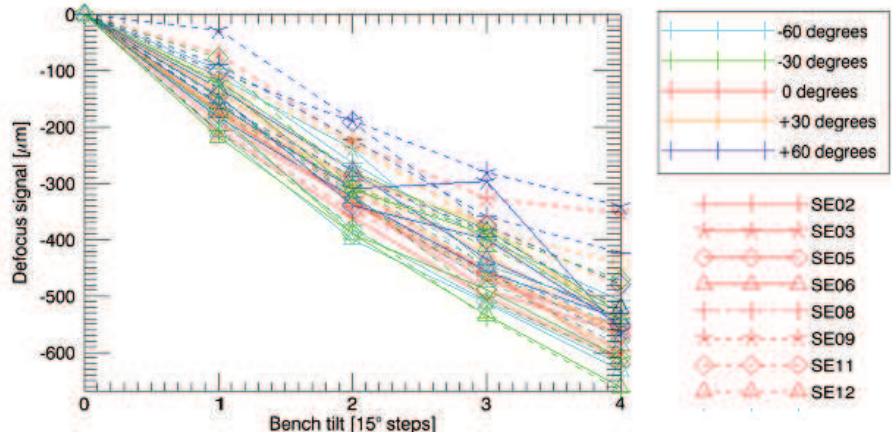

Figure 3.69: SEs axial shift measured as a defocus signature on the pupils for Test #2c. Different colors represent different radial positions.

Test #3c: all the measured shifts reported in 3.70 for each SE are below 650μm for a complete bench tilt (60°). No particular correlations between the measured shift and the SE position have been found.

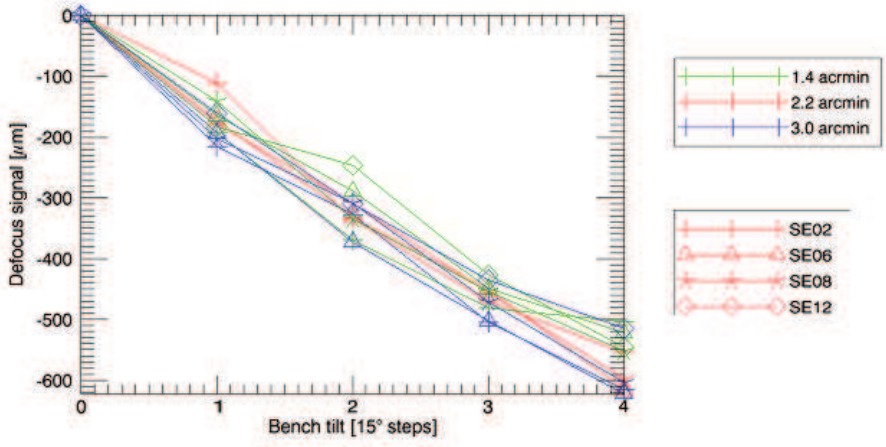

Figure 3.70: SEs axial shift measured as a defocus signature on the pupils for Test #3c. Different colors represent different radial positions.

Test #4c: all the measured shifts reported in 3.71 for each SE are below 650μm for a complete bench tilt (60°). As the previous ones, also this measurement seems not to be repeatable.

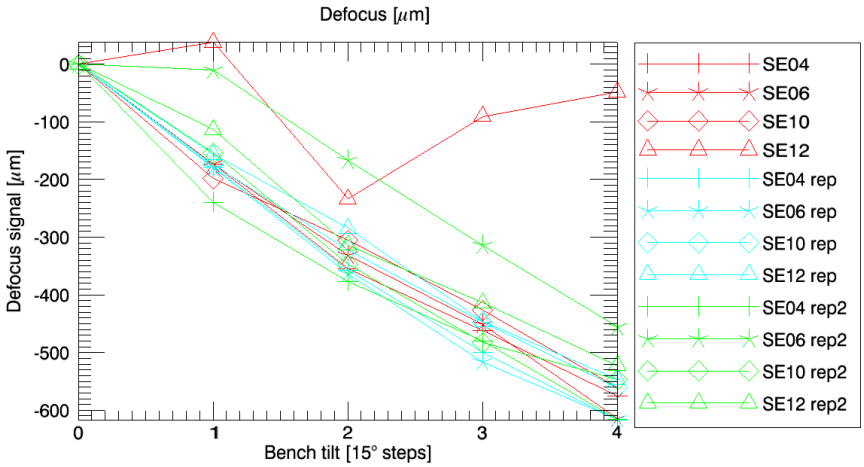

Figure 3.71: SEs axial shift measured as a defocus signature on the pupils for Test #4c. Different colors represent different runs, while symbols are related to the tested SEs.

Due to the fact that the flexures effects repeatability is negligible, instead of look-up tables to reduce the pupil blur and signal wavefront error, determining the implementation of software to correct for this errors during the exposure itself.

Results

After the GWS shipping to Heidelberg, flexures tests thoroughly described in this section were performed in order to quantify three main flexures effects:

- **SEs shift**, translating into a tip-tilt signal onto the WFS. The common part can be compensated re-centering the SEs during an exposure;
- **SEs tilt**, translating into a shift of the pupils on the detector peculiar for each SE, with a consequent pupil blur to be taken into account in the error budget. The common part can be compensated re-centering the CCD during an exposure;
- **SEs defocus**, translating into a defocus signal onto the WFS. The measures defocus does not seem to require any compensation during exposure.

The resulting RMS blur on the pupil for a 60° tilt have to be compared with the root sum square of the sources of error which affect the system during this test, which are listed in the following:

- GWS flexures;

- Bearing flexures;
- SE tilt due to support flexures (a fraction. Here considered 1/sqrt(2));
- SE tilt due to ring flexures (a fraction. Here considered 1/sqrt(2));
- SE tilt due to stage flexures (a fraction. Here considered 1/sqrt(2)).

Actually, this test more than a verification as the rotation one, has been used to quantify the "GWS flexures" term, having the other already estimated.

Figure 3.72 shows the results of the flexures test, considering all 12 SEs, even if for practical reasons (i.e. the flange) only 4 SEs could be tested in one single run.

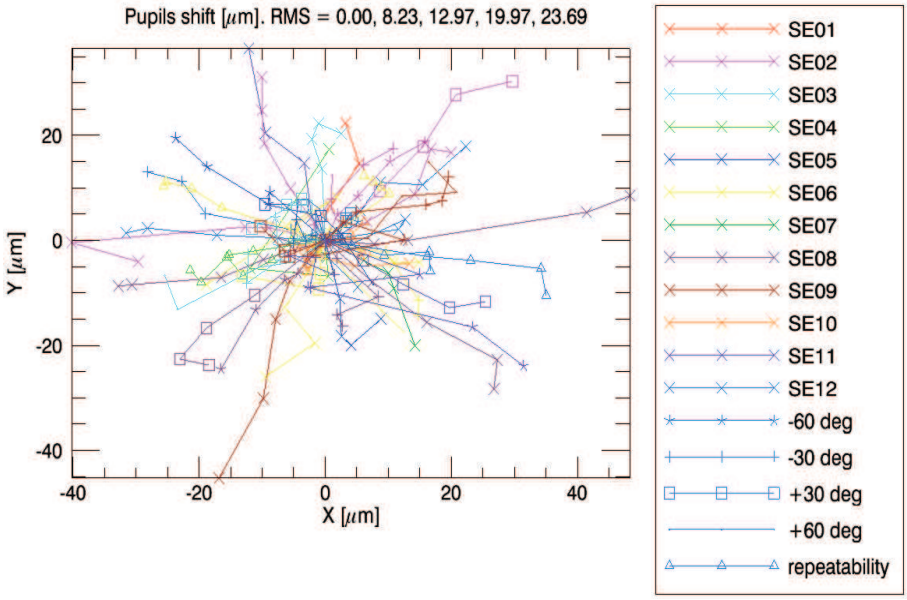

Figure 3.72: Pupils shift measured on the CCD50 and *a posteriori* corrected via software optimizing the CCD50 position along the optical axis. Different colors represent different SEs and different symbols represent different type of tests. The pupils shift RMS are reported on top of the figure, for the bench tilt (0°, 15°, 30°, 45° and 60°), indicated for each one by the points from the center toward the sides of the graph.

The estimated effect of GWS flexures, can be given for different bench tilt as reported in table 3.16 .

Bench tilt	0°	15°	30°	45°	60°
Pupil blur term	0 μm	8 μm	13 μm	20 μm	24 μm

Table 3.16: Estimated pupil blur term due to GWS flexures at different LN tilt angles.

Figure 3.73: A picture of the GWS mounted on the LN bench tilted by 60°.

3.4 Conclusions and next steps

In table 3.18 are summarized all items of the error budget discussed in section 3.3.2 and analyzed in a series of tests performed after the GWS integration and alignment to verify if our error budget pupils blur effect for different items were not underestimated:

- **rotation test (A)**: after the GWS system internal alignment, in which each

sub-system has been separately aligned and tested and the GWS has been completely assembled and internally aligned in a static configuration, some test on the system performance have been carried out to measure the different SEs pupils superposition stability during the bearing rotation. The details can be found in section 3.3.6. The root sum square of the listed items is 10.5 μm, which is compatible with the measured RMS blur of 9.4 μm.

- **pupil blur for SEs linear movements (B)**: this test is the measurement of the shift of each SE 4-pupil matrix on the detector. The shift has been measured illuminating the SEs with a monochromatic collimated beam, like the one used in the SEs alignment procedure, and computing the movement of the 4 spots re-imaged on the CCD during the movement of the SE along a pre-defined path. The root sum square of the considered items is 13.9 μm is compatible with most of the measured RMS blurs.

- **white light static pupil blur (C)**: this test aims to measure the pupil blur static. A calibrated USAF resolution test chart has been used as a reference for the measurement of the Modulation Transfer Function of the system. The root sum squared of the considered items is 9.2 μm, to be compared to the RMS radius of the actual static blur measured with the USAF target, which is $15.8/2 = 7.9\mu$m. The performance is then consistent with what claimed in the Error Budget.

- **flexure test (D)**: flexures test were performed in order to quantify three main flexures effects: SEs shift, tilt and defocus. The details can be found in section 3.3.7.

The error budget items verified or taken into account in these tests are indicated in table 3.18 respectively with the letter A,B,C or D or put into parenthesis if a contribution was considered, but has negligible value for the test.

The estimated effect of GWS flexures, retrieved from the successful flexures tests can be given for different bench tilt as reported in table 3.16 determining the SR values reported in table 3.17, where in the worst conditions (a tilt of 60 ° of the bench) the goal SR (0.60 in J-band and 0.85 in K-band) could anyhow be reached.

Bench tilt	15°	30°	45°	60°
SR (J)	0.76	0.73	0.65	0.60
SR (K)	0.92	0.90	0.87	0.85

Table 3.17: Estimated Strehl Ratio of the system for different LN bench tilt angles.

We can therefore declare successfully concluded the integration, alignment and verification of the first of the two GWS for LINC-NIRVANA which will be soon

Error source	Test ref.	blur [μm]	blur[sub-ap]	WFE [nm]
GWS Components				
SE diffraction	C	7	0.15	30
Linear stages wobble	B	5	0.10	22
Pyramid chromatism	C	6	0.13	26
Pyramid vertex angle	A	5	0.10	22
Pyramid face orthogonality	A	1	0.02	4
GWS internal alignment				
SE enlarging factor k		5	0.10	22
SE relative tilt	A	5	0.10	22
Pyramid orientation	A	5	0.10	22
PR optical quality	B (A) (C)	13	0.27	57
Thermal effects				
SE lens misalign. (thermal)		/	/	/
Linear stage wobble (thermal)		/	/	/
PR-I optical quality (thermal)		7	0.15	31
GWS misalignment wrt the bench				
Mismatch DM-WFS		5	0.10	22
GWS global defocus		N/A	N/A	N/A
GWS global tilt		N/A	N/A	N/A
GWS global de-center		N/A	N/A	N/A
Pupil matching on WFS		5	0.10	22
Bearing contribution				
Bearing wobble		1	0.02	4
Bearing runout		N/A	N/A	N/A
Bearing non-uniform rotation		N/A	N/A	N/A
Flexures				
GWS flexures	D	23	0.25	53
Bearing flexures	D	3.2	0.07	14
SE tilt due to support flex.	A(B)D	6	0.13	26
SE tilt due to ring flexures	A(B)D	4	0.08	17
SE tilt due to stage flexures	A(B)D	4	0.08	17
TOT WFE				**143**
				SR@J ≈0.60
				SR@K ≈0.85

Table 3.18: GWS pupil blur contributions Error Budget

shipped to LBT telescope. Due to its technical and programmatic complexity, in fact, LN's overall instrument commissioning has been subdivided into different individual implementation phases, of which the very first one aims for the "Demonstration of the Ground-layer Wavefront Sensor system (GWS)" and is defined as LN GWS Pathfinder experiment. Its main goal is to verify working interfaces and communication between the wavefront sensor system and its counterparts on the telescope side, comprising the adaptive secondary mirror as corrective element. The start of this campaign is scheduled for march 2013 and will be completed by a first on-sky verification of the system's end-to-end performance, while no science program is foreseen. The Pathfinder is mounted on a support structure and its main components (shown in figure 3.74) are: an annular mirror that picks of the 2-6' annular portion of the F/15 beam and send it toward the GWS where wavefront sensing is performed; a small flat mirror folding the central part of the LBT beam to the infrared test camera (IRTC) where the scientific object will be imaged; the electronics cabinet, containing motor controllers, CCD read-out electronics and a specialized unit for computing wavefront slopes (BCU).
At the time of this writing procedures to align the Pathfinder with respect to LBT are being devised.

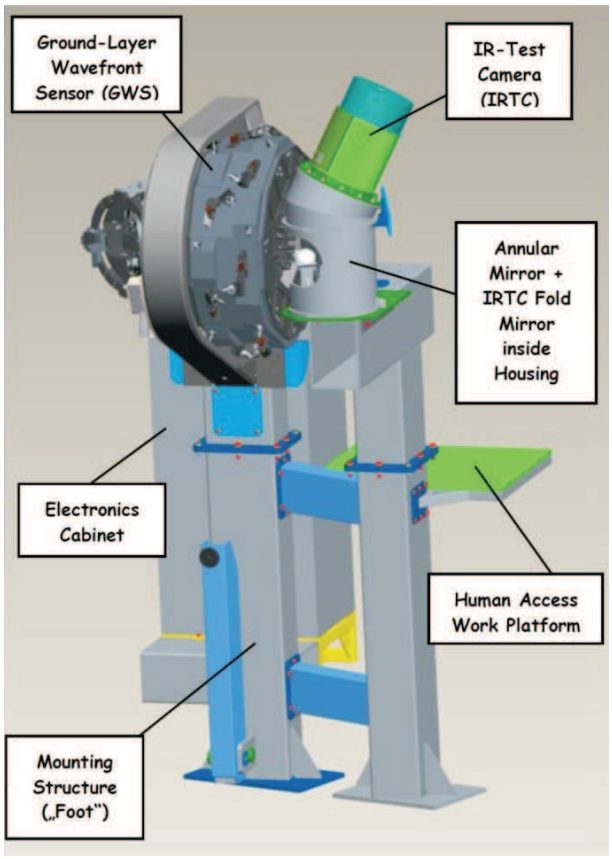

Figure 3.74: A CAD view of the Pathfinder experiment, where it main components are outlined.

Chapter 4

Very-Linear wavefront sensor for the E-ELT

In the framework of E-ELT, a 40-meter telescope, Adaptive Optics is mandatory to justify the huge costs and manpower to realize such a giant telescope and the complexity concerning everything around it (dome, structure, instruments...). To exploit the full potential of the telescope, in particular the resolving power of the telescope, Padova Adaptive Optics group has decided to push for a system based on very linear WFSs, working in open-loop MCAO looking at solely natural guide stars, in a FoV as large as allowed by the telescope.

At a time where cost reduction has the highest priority, AO concepts that do not rely, and could possibly co-exist, on expensive laser guide stars appear very attractive.

As stressed by Ragazzoni et al. (2012) it is highly important to remember that the step between a 10 meters class telescope and a 40 meters class telescope (i.e. E-ELT) is not only a matter of technological and complexity challenges. On the contrary a large number of parameters influencing the wavefront sensing and the correction need to be studied in more detail. This is part of the study which is being performed in a collaboration with ESO whose final goal is to define the feasibility of a system based on Global MCAO (GMCAO) concept correcting a 2 arcmin region, with the advantage to have a large FoV (up to 10 arcmin) to search for NGSs (though not excluding the possibility to use LGSs at the same time) and whose wavefront sensor does not trade sensitivity for linearity, exploiting to achieve the first one a PWFS and for the latter a YAW sensor.

In this chapter will be briefly explained the concept of Global MCAO and Virtual DMs (section 4.1), the very linear WFS concept and a possible opto-mechanical design (section 4.2) and will be described the aspects studied, focusing on how a PWFS behaves under imperfect illumination conditions (determined by the open-loop of the

system), both on literature and performing simplified numerical and analytical computations, with the purpose to understand the feasibility of the concept.

4.1 Global MCAO and virtual DMs

Global MCAO concept has been introduced by Ragazzoni et al. (2012) and is essentially an extension of MCAO wavefront sensing to a much larger FoV (of the order of 10') and a correction performed on a central restricted region of a few arcmin. The FoV is essentially limited by telescope optics or opto-mechanics as well as by the limit given by the meta-pupil coverage at the highest altitude of interest, which will be better explained in this section. Since MCAO technique has been demonstrated to work and to yield the expected advantages providing an homogenous correction for a few arcmin FoV, both in theory and experimentally on 8-meter class telescopes, as explained in section 1.5, a concept for a 40 meters telescope has started to be investigated. A telescope aperture increase from about 8 meters to about 40 meters has the consequence of allowing an overlap of its footprints for a larger angle of sight. Reminding that the geometrical distance at which pupils do not longer overlap defines a limit over which there is no gain in enlarging the FoV and considering as a "good" overlap the one achieved by MAD (for an 8 m telescope) for about 2' around 8 km height, we obtain a FoV of about 10' for an E-ELT telescope (see figure 4.1). This is the FoV in which it is possible to search for NGSs.

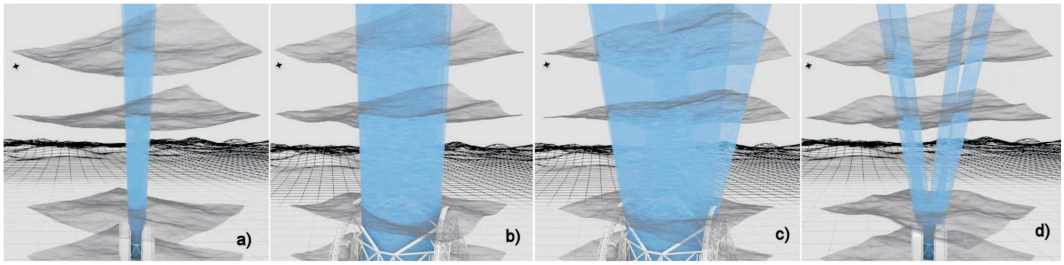

Figure 4.1: Different FoVs on different telescope apertures. a) An 8 m class telescope employing a 2' FoV in a MAD-like MCAO approach; b) the same 2' FoV for an ELT gives a much better and uniform sampling of the high altitude layers; c) in an ELT the same coverage as in MAD can be achieved with a larger Field of View (10'), linearly scaling with the ratio of the telescope diameters; d) an 8m class telescope employing a 10' FoV, on high layers pupils overlap is totally missing (Ragazzoni et al., 2012).

Reminding that in MCAO the correction achieved at a certain DM optically conjugated at a given height is effective not just at that height but also at adjacent ones and recalling the FoV vs. thickness rule (Ragazzoni et al., 2010), the enlargement of the FoV reduces the depth of focus of the correction of each DM, meaning that the sensor will be less sensitive to turbulent layers close to the DM. This translates into

a lower degree of correction and requires, in order to achieve similar performances the increase of DMs number. Given as fundamental a DM conjugated at the ground layer, from a rough linear estimation (based on Beckers (1988)), for an increase of the considered FoV by 5 times, 5 DMs instead of 1 DM would be required to achieve a similar correction. Adding the ground-layer DM we can consider a system made of 6 DMs.

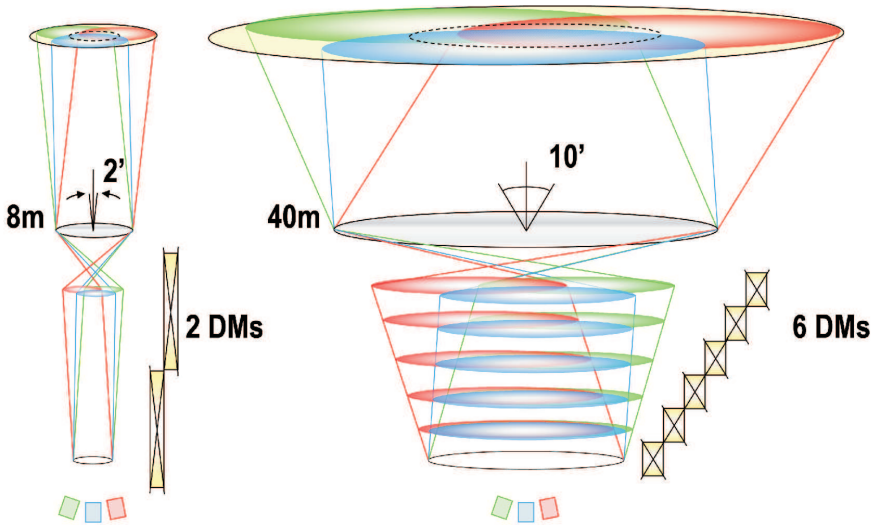

Figure 4.2: Enlarging the telescope entrance pupil allows to search for the same number of guide stars in a wider FoV to sense the same fraction of the metapupil at a given height (2' in a 8m-class telescope vs 10' in a 40m-class telescope). More DMs (real or virtual) are needed, because of the FoV vs thickness rule. This figure shows the comparison between a 2' FoV for a 8m-class telescope and a 10' FoV for a 40m-class telescope (Viotto et al., 2011).

The realization of such a system is, however, impractical, both for costs and technical reasons (i.e. complexity, DMs conjugation heights in a limited space and too many reflections causing loss of throughput).

In order to overcome this limitation a concept based on "virtual DMs" and on a "Very Linear WFS (VL-WFS)" has been introduced in Ragazzoni et al. (2010). The needed WFS has to be able to measure any incoming wavefront, within a wide range, rather than its deviation from zero, giving a perfect measurement of the wavefront itself. This is somehow in contrast with most of the existing wavefront sensors, as they usually operates around zero, in closed loop operation. A concept has been developed and is explained in section 4.2, however, for the moment let's assume it exists. Once the exact direction of the reference star is known, the effect of the actuators of the DMs on the WFS is predictable. Thus, knowing the actual movement of the DM surface one can directly compute with extremely high accuracy the signal coming out from the WFS. Given this degree of knowledge one can imagine to remove a DM and add its effects onto the WFS signal just on the stream of data

coming out from it. In this way the optical DM becomes a virtual one, a continuous region of memory where the actual displacement of the DM is stored and continuously updated. In this way the loop could be numerically closed with respect to a time evolving reference. Within this assumptions the information which should be given to the 6 DMs (the number of DMs is coming from the previous estimate) through a back-projection, to compensate the wavefront error, is given only to the 2 (or 3) real ones. Of course this information needs to contain both the one related to the DM located at the conjugated height and the one related to the other DMs, with a smoothing proportional to the footprint given by the corrected FoV angle and the separation between the actual DM and the virtual one. Obviously not all the turbulence spectrum will be fully covered but a strategy allowing for the most efficient way in terms of coverage of the spatial frequencies needs to be studied.
In principle, in this concept countless DMs could be employed, however, SNR issue has to be considered, because after a certain threshold the (small) gain due to an extra DM would vanish because of the extra SNR introduced by the mirror.
During a preliminary study a number of 7 DMs has been considered as the best compromise between a good correction (minimization of residuals) and a not so high noise in the extreme case of all reference sources positioned at the edge of the 10' FoV (instead of the 6 DMs total number roughly estimated). This is easy to be understood pictorially from the graph shown in figure 4.3. In the background is shown the so called h-f plane, where the strength of the expected turbulence at a certain height h above the observatory is mapped with respect to the spatial frequency f (based on Hubin et al. (2000) PARSCA flight 51 C_n^2 profile). In this preliminary approach the DM is assumed to correct perfectly all the spatial frequencies at the altitude at which it is conjugated, till the spatial sampling of the related DM (80 actuators on a 40 m diameter, meaning f= 2 m^{-1}) and only to a limited spatial frequencies defined by the footprint of the involved FoV with a plane conjugated to a certain height distance from the DM. These are represented by the hyperbolic surfaces in figure 4.3, while the red profile represents that would be removed by hypothetical perfect MAORI-like system working with the same DMs.

The FoV of 10 arcmin in which to search for NGSs has an area 25 times larger than the one of a MAD-like system (2' on a 8 m telescope), highly increasing the sky coverage, meant as the fraction of the sky in which proper references can be found, in order to achieve the required performance of the system. It is also worth to point out that the requirements in terms of FoV imposed to the telescope to achieve a larger FoV are not more stringent than the one to properly collect the LSGs rays that, because of the cone effect, need to arrive from a larger angle to correct the same FoV.

Another important thing to be noticed is the fact that, since we look at stars in a 10' FoV but we correct the central 2', and since we drive the real DMs present

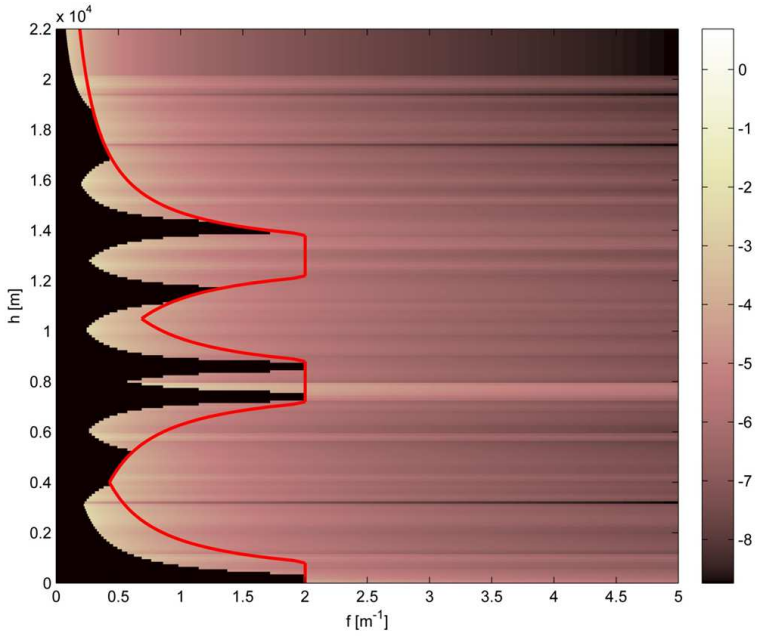

Figure 4.3: Example of correction performed by 7 DMs. The DM is assumed to correct perfectly all the spatial frequencies at the altitude at which it is conjugated, till the spatial sampling of the related DM (80 actuators on a 40 m diameter, meaning f= 2 m^{-1}) and only to a limited spatial frequencies defined by the footprint of the involved FoV with a plane conjugated to a certain height distance from the DM. the red profile represents the frequencies that would be removed by hypothetical perfect MAORI-like system working with the same DMs.To be noted is the fact that white represents strongest turbulence, which is concentrated in particular at the lowest f, so not just the total covered area needs to be observed, but the quality of its covering .

in the system also with the signal reconstructed at different heights with respect to the DMs conjugation altitudes, the WFS is essentially working in open loop and the correction implemented by the DMs cannot be monitored optically in the MCAO system. It is worthwhile to point out that this approach is not the first to work in open loop fashion, as MOAO system, described in section 1.8 works in a very similar way. It is possible, in fact, to visualize the proposed technique as an extension of the MOAO where the various corrected FoVs merge together into a single and larger one located in the center of the FoV.

The task of the on-going study is to perform a conceptual study of a solely NGS based MCAO system for the E-ELT, collecting information from literature, devising a design of a possible NGS GMCAO system. One of the main requirement to implement in reality this concept is the need of a WFS provided with a very high sensitivity and extreme linearity. In fact, this assumption allows to perform the

layer-oriented in a purely numerical fashion and not requiring to close any loop.

The main aspects to be analyzed are issues related to such the open loop configuration, as DMs hysteresis, noise sources in the system that will be unseen by the WFS and hence will unavoidably affect the quality of the resulting correction and the effects on the WFS. For the purpose of my thesis I will mostly concentrate on the related issues as the non-linearity of the WFS and its saturation.

4.2 Very-Linear WFS

The operations discussed in the previous section are not so easy to be performed with the usual standard WFS, like the Shack-Hartmann (S-H), the Curvature or the Pyramid one, since they have been conceived to perform in close loop and their linearity range is normally not high enough to provide open loop measurements. Of course, one could think to optimize the characteristic of any of the mentioned WFS to increase the linearity range (few lenses in the S-H case, small defocus in the Curvature case, modulation in the Pyramid case) but, in any case, being the WFS linearity inversely proportional to the sensitivity (see section 1.2.2), the sensor will of course decrease its capability to see the small details of the wavefront. Further to require extremely linearity, these WFS working in open loop will not benefit from the gain occurring when they work in closed loop. A simple way to make a WFS both linear and working with the gain proper of closed loop operations at the same time is to make it working in a local closed loop. This can be done replacing the WFS unit with a SCAO system with a DM (small and with high dynamic range) and a WFS closing the loop on each individual NGS.

The quality of the correction should be good enough to guarantee both a certain linearity regime of the WFS and a significant gain in the WFS quality operating in closed loop. Please note that the two points are somehow balancing each other. For example a perfectly closed loop will make the WFS looking basically zero, so from the latter no information would be retrieved, while all the information on the wavefront will be given by the actual shape of the DM. Since the problems of non-linearity of the DMs are known, a simple solution for retrieving the actual wavefront information is to illuminate the DM with a reference monochromatic light. and to sense the DM with a very linear WFS (technique also defined as referencing). The YAW (Gendron et al. (2010), described in section 1.8), has been selected as a candidate for such a device, being very linear and ideal to work with monochromatic light, and also having the conceptual advantage to give information in the same format as the Pyramid WFS (4 pupils). The Pyramid WFS is closing the loop through the DM and the residual are summed up with the measurement of the YAW monitoring of the actual shape of the DM. This WFS exploits the advantages of a closed loop Pyramid WFS, in particular

its sensitivity, but offers the linearity of the YAW too, basically only limited by the dynamic range of the DM. The corresponding extension of the dynamic range of the YAW could be made at the expense of a brighter reference source, that, assuming to split its light from the NGS one with a dichroic, would have no other drawback. It is worthwhile to highlight the fact that in the case of E-ELT a part of the turbulence will be reduced thanks to the adaptive M4 mirror, therefore even being an open-loop, the linearity requested range is lower.

Opto-mechanical design In Farinato et al. (2010) and Magrin et al. (2011) has been devised a possible opto-mechanical implementation for a group of WFSs able to derive a MCAO system in order to cover a FoV of the order of 1-2', but getting advantages from the starlight coming from a FoV as large as 10' in diameter. This involves a number of SCAO systems, conceived as movable arms, light-weighted and minimizing its obstruction in the focal plane. They can enter in the FoV, select and fold the light coming from a reference and analyze the wavefront giving an open-loop measurements of its aberrations.

This concept is shown in figure 4.4, in which the light picked-up from the star through a folding mirror and the monochromatic light injected through a fiber are sent to the DM (through a collimator), and the split through a dichroic is done after a re-focusing lens.

As already mentioned, even though the 2 sensors are completely different, they are both "pupil plane WFS" (the detector is on the pupil plane), and both of them are working with four images of the pupil; thus, choosing in a proper way the optical components of the two sensors, we can obtain identical sized pupils, meaning also identical detectors. In this way, the combination of the residual signal seen by the Pyramid WFS with the turbulent wavefront seen by the YAW can be done very easily (summing directly the signal obtained in the corresponding pupils of the two sensors).

In Farinato et al. (2010) are outlined some opto-mechanical details, including an overview of the required components, to show that the goal is attainable with today existing components, in particular the detectors considered in the design are E2V CCD 220, 240×240 pixels, and a suitable DM could be an ADAPTICA product having a diameter of 76 mm with 28×28 actuators. In alternative to the latter, commercial DMs from Boston Micromachines (such as the Kilo-DM, 9 mm, 32×32 actuators) could also be used. The optical layout is shown in figure 4.5.

A note has to be done on the number of arms which are required to ensure the maximum sky-coverage and, at the same time, a good overlap of the pupils at the level of the higher conjugation altitude. Previous studies (Viotto et al., 2011) have shown that, considering a 2' scientific FoV at a Galactic Latitude b = 90deg (conservative case), observed with a 40m-class telescope, if 3 suitable stars are found

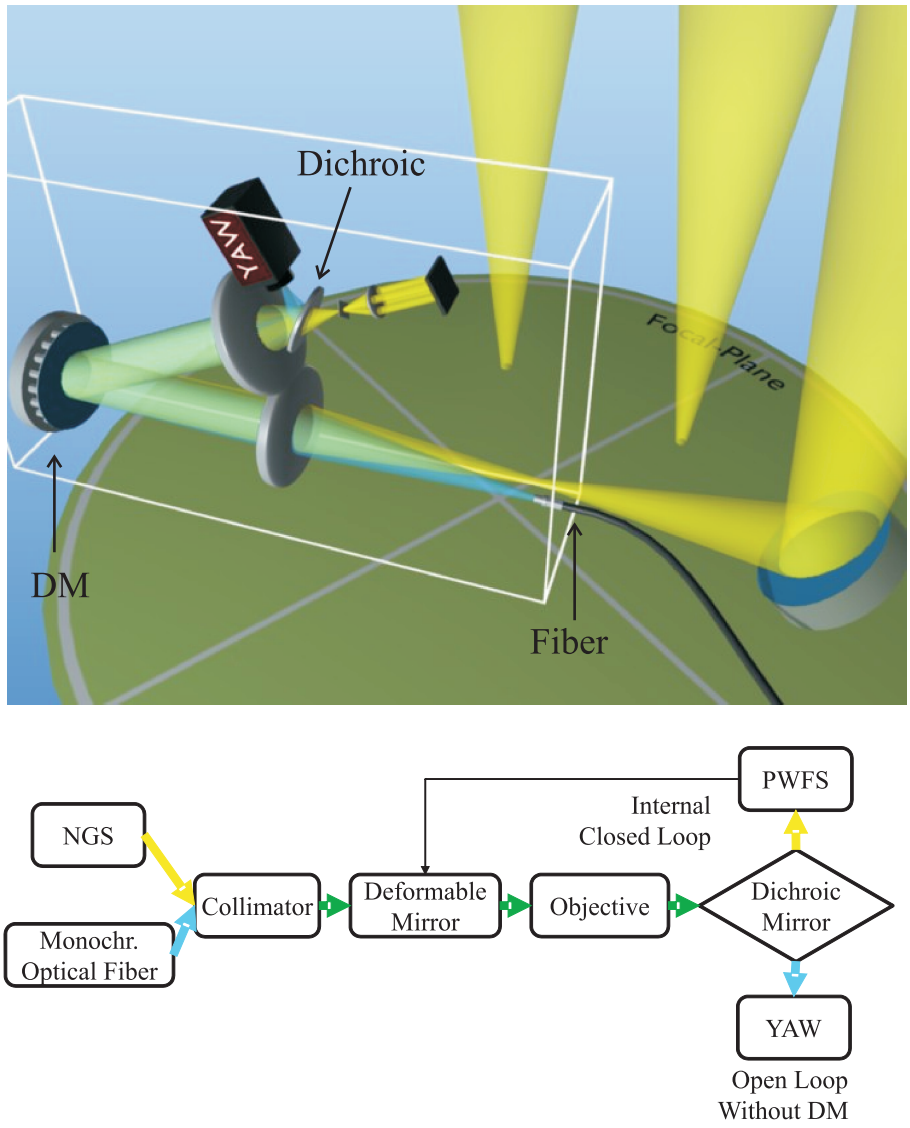

Figure 4.4: Each arm of the GMCAO is composed of 2 WFSs, the pyramid that works in closed loop fashion taking full advantage of its capabilities and the YAW working in open-loop. (Ragazzoni et al., 2012).

in the technical 10' FoV, the metapupil coverage at 10Km of altitude is always higher than 70%, so the probability to cover such a fraction of the metapupil only depends on the probability to find 3 stars in the technical FoV (which is 87%). If other cases, in which more references are considered, the probability to cover a high fraction of the metapupil decreases, since it always has to be weighted with the probability to find a higher number of suitable reference stars. Of course, for lower latitude fields, it becomes more likely to find a high number of suitable references, and observing at

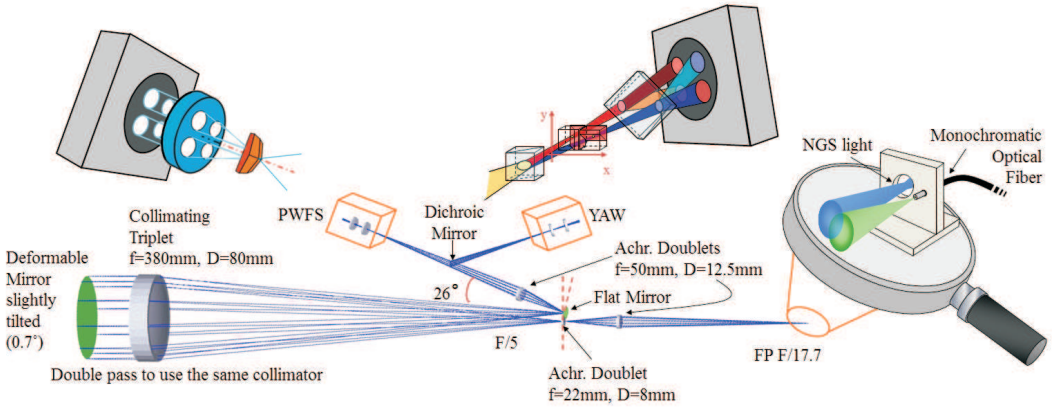

Figure 4.5: A possible optical layout of the VLWFS.

the galactic plane, even the probability to find 6 NGSs (which would allow to have a better coverage of the metapupil at high altitude turbulent layers) brighter than magnitude 15 is close to 1. Therefore, to maximize both the metapupil coverage at the highest altitude (10km in our study) and the probability to find a reasonable number of references, observing at the galactic pole most likely 3 references would be observed at the same time, while observing at the galactic plane a higher number of NGSs can be utilized.

It is to be noted that this approach is only mildly invasive of a current telescope design as basically requires to add a few Very Linear WFSs in the acquisition arm and to add reference fibers and small YAWs on the instrumentation side. The existence of one or more adaptive mirrors in the optical train before the WFSs not only can be easily handled in the correction scheme but it would greatly reduce the requirements in terms of dynamic range in the local DMs. First it eliminates in a single shot all the trouble deriving from the generation of the artificial stars (the laser and the launching system) and, second, it is much less invasive of the focal plane area than a LGS system based.

Of course, in case capacitive sensors DMs (i.e. the Adaptive Secondary Mirror of LBT by Microgate) become available with the needed inter-actuators spacing, the referencing through the YAW sensor could be removed, clearly simplifying the opto-mechanical implementation.

4.3 Ajar loop

As previously explained, the system that we propose is essentially working partially in open loop (what we call “ajar loop”); in fact, even if the DM shape can be monitored by some dedicated wavefront sensors, having in this way a feedback

on their shape (a locally close loop), the final output of the system (the corrected wavefront) is not seen by the WFS. This problem is essentially the same that has to be faced in MOAO techniques, as described in Section 1.8 where the correction is performed only in a certain direction in the sky, and thus the WFS cannot look at the references through the DMs and the system has to work in open loop and is the reason why several MOAO demonstrators are on-going in order to identify the most crucial aspects of this new generation of open loop systems. We concentrate here on the main cons of an open loop system which is that, due to the fact there is no feedback on the final result achieved, they are normally less accurate in the correction performed since they are unable to remove the disturbances occurring from external sources (but if these sources are differently monitored). In fact, the final correction totally depends on the accuracy and reliability of the corrector element (the DM in our case). Furthermore, even if the DM is perfectly applying the required correction, whatever disturbance might occur due to other error sources (i.e. local turbulence away from the DMs) may affect the system performance, in a very similar way to what happen in the non-common path of a typical close loop AO system. Thus, it becomes very important to identify every possible class of error source to make a comprehensive analysis of the Ajar Loop performance, showing which is the effect of each of them and ways to minimize their contribution. The list that we devise of the main error sources of an Ajar AO system is the following:

- The wavefront sensor
- The Deformable Mirror
- Static perturbation of the main optical train (misalignment, flexures, temperature change effects)
- Dynamic aberrations on the main optical train (local turbulence)

  Furthermore, it can also be considered that M4 of E-ELT will be an adaptive mirror conjugated to the ground-layer. Being all pupils super-imposed at the ground level, one can assume to correct the ground layer in closed-loop for the whole 10' FoV so that after a few iterations a partially corrected wavefront is given as input to the VL-WFS system, requiring a reduced dynamic range for the DM.

  For the purpose of my PhD work I have mainly focused into analyzing how a PWFS behaves in the case of a not-ideal illumination condition, in the case of partial wavefront correction, due to open loop, leading to a poor SR on the pin of the pyramid.

4.4 Pyramid WFSs in open loop: non-linearity and SR dependance issues

The pyramid WFS has been conceived initially as a practical means to arrange the light of a derivative measuring WFS, with the advantages described in section 1.2.2, and has been technologically demonstrated for the first time at the TNG telescope at Canary Islands (Ragazzoni et al., 2000b). After some theoretical discussion and prediction of its higher sensitivity with respect to the SH WFS (Ragazzoni and Farinato (1999), Vérinaud (2004)), validated by lab experiments (Peter et al., 2010), it recently succeeded to achieve outstanding performances at LBT with FLAO (Esposito et al., 2010). Said that, many characteristics of pyramid WFS still need to be better understood and verified, firstly theoretically, in particular to better understand pros and cons of its use in an AO system for a 40 m telescope. In the current envisaged approach the WFS to be used is a Pyramid WFS closing the loop on a local DM. Each arm is, in fact, observing one single NGS and the light is fed through a local DM, allowing the pyramid to work in close loop and take advantage especially on the gain in limiting magnitude it offers with respect to other WFSs. Because of several limitations, both from the practical point of view (limited bandwidth and number of actuators of the small local DM employed) and conceptual (noise due to the finite number of photo-electrons collected by the WFS), one should expect that the residual measured from the WFS would play a significant role in the GMCAO. In other words, the role of the closed local loop is the one to carry the WFS in the regime where the gain with respect to the SH is somehow secured to a certain extent, and the residual is left to the collection in real-time of the residual measured by the WFS, that has to be properly added, with the right scaling factor, to the measurement achieved on the DM, in a manner to be defined (both a DM able to feedback its actual position, for example by means of local capacitive sensors, or the optical measurement of it during the operations -referencing- can be envisaged). This raises the issue of establishing how much any non-linearity will affect such measurements, or in other words how linear the WFS has to be, determining, for example, the number of actuators needed for the small DM used to locally close the loop. Afterwards the PWFS performance dependance from the SR on the pin of the pyramid is verified, to be sure we can still exploit the higher sensitivity of this PWFS with respect to other ones even in open-loop conditions.

4.4.1 Linearity

In order to assess the effects of the non-linearity of the PWFS and determine the most suitable number of actuators for the DM, we began a simulation with Fourier wave-optics propagation of a perfect Pyramid Wavefront Sensor illuminating it with various kind of wavefront deformations (Zernike polynomials) with different

amplitudes and analyzed how the reconstructed wavefront differed from the original one.

A code to simulate a perfect PWFS, including diffraction effects, has been developed. First of all, a 128 pixels in diameter pupil ($Pupil(x, y)$) centered on a a 1024×1024 matrix (much larger than the pupil to reduce artifacts due to Fast Fourier Transforms (FFT)), is generated. We then generate a wavefront given by the product between one single Zernike polynomial (normalized so that its RMS value is equal to 1) and an amplitude a in the range 0.02-0.25 λ.

$$W_\lambda(x, y) = a \cdot {Z_j}^i(x, y)$$

Mapping this wavefront onto the previously defined pupil and by Fourier transforming it, the electric field intensity at the focal plane position is obtained.

$$EFP = FFT(Pupil(x, y) \cdot e^{-i2\pi W_\lambda(x,y)})$$

To have a feedback, PSF can be observed as the squared of the absolute value of the electric field.

$$PSF = (abs(EFP)^2)$$

In the (complex) electric field space we masked all but one quadrant of the matrix for each of the four quadrants of the Pyramid. By inverse Fourier transformation and again taking the squared modulus of the obtained electric field, the pupil illuminations on the four quadrants of the PWFS are obtained.

$$EFP_k = EFP \cdot PyrFace_k$$

with k=0,1,2,3

$$Pup_k = EFP_k \cdot_k Conj(EFP_k)$$

Combining these in the usual way for a 4 quadrant sensor, the estimate of the wavefront derivative is obtained.

$$S_x = \frac{(Pup_1 + Pup_2) - (Pup3 + Pup_4)}{Pup_1 + Pup_2 + Pup_3 + Pup_4} \qquad S_y = \frac{(Pup_1 + Pup_3) - (Pup_2 + Pup4)}{Pup_1 + Pup_2 + Pup_3 + Pup_4} \tag{4.1}$$

At this point the wavefront is reconstructed taking advantage of the Fourier Transforms properties as pointed out by Roddier and Roddier (1991)

$$Pyr_{WF} = FFT^{-1}(FFT(\frac{\delta}{\delta x}S_x + \frac{\delta}{\delta y}S_y) \cdot \frac{1}{f^2})$$

Finally, the retrieved wavefront is fitted with Zernike polynomials (considering for the fit Zernike polynomials up to 2 radial orders above the input one) and the residual value in terms of rms from the original wavefront is stored (res).

This process is exemplified in figure 4.6 for a coma aberration (${Z_{-1}}^3$) and is repeated for different aberrations (every time one single Zernike polynomial is inserted as input) and different amplitude of aberrations increasing with step 0.02 λ in the range $a = 0.002 : 0.25\lambda$.

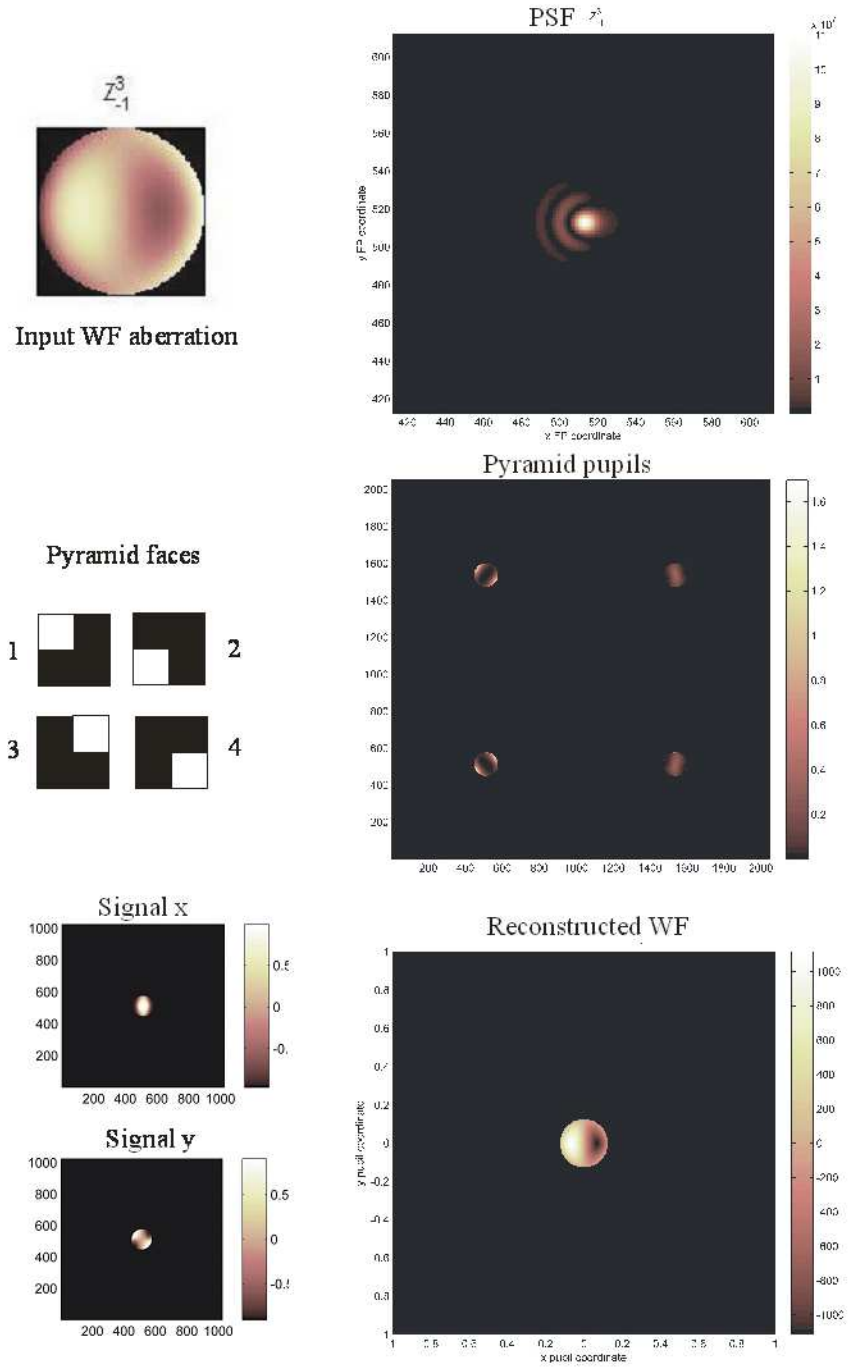

Figure 4.6: The main steps of our Fourier wave-optics propagation to reconstruct the wavefront after passing through perfect PWFS are shown. **Top-left**: the introduced aberration (coma). **Top-right**: aberrated PSF seen on the pin of the pyramid. **Centre-left**: simulated pyramid faces. **Centre-right**: pupils re-imaged after the pyramid. **Bottom-left**: computed signals.*Bottom-right*: reconstructed wavefront.

The PWFS working wavelength assumed is λ=0.8μm. For each radial order we consider a characteristic polynomial, plot the rms residual values (res) obtained at the different value and retrieve the linear fit on the first 5 points (meaning a up to 0.1 λ, where we assume the non-linearity issue to be negligible), we do not speculate on the option of numerical fitting the responsitivity of the WFS with more than a straight line pivoting around the origin. At this point we compute the residual in terms of rms wavefront for each amplitude, essentially what one should expect if perfect linearity in the case of perfect linearity. An example is shown in figure 4.7, for ${Z_{-1,+1}}^3$. We preliminary investigated the scatter of this non-linearity for various modes belonging to the same radial order class. It turns out that such scatter is small and decreases with radial order, as shown in figure 4.8. For each radial order we recorded the amplitude which would make the sensor exceed 10% of linearity (arbitrary chosen value) and the final retrieved values are plotted in figure 4.9 (blue full line), as well as the rms errors (blue dots).

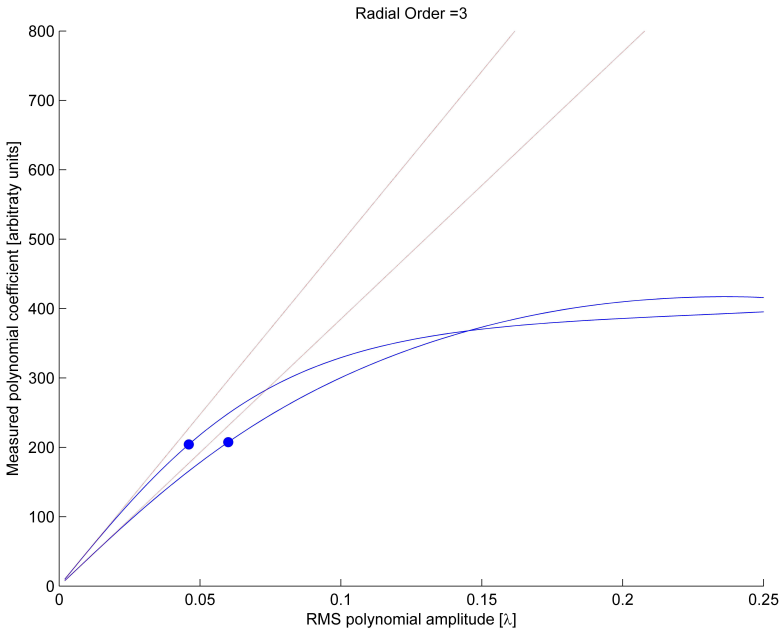

Figure 4.7: Best linear fit for ${Z_{-1}}^3 and {Z_{+1}}^3$. The blue lines correspond to the reconstructed polynomial coefficient as function of the RMS polynomial amplitude. The two blue circles correspond to a deviation from the linearity of 10%. The red lines correspond to the linear fit.

Further to the estimation of the non-linearity vs. radial order mode, a comparison with the expected variance of such specific modes has been performed. The expected variance has been computed by differentiation of the Noll's figures for the residual of

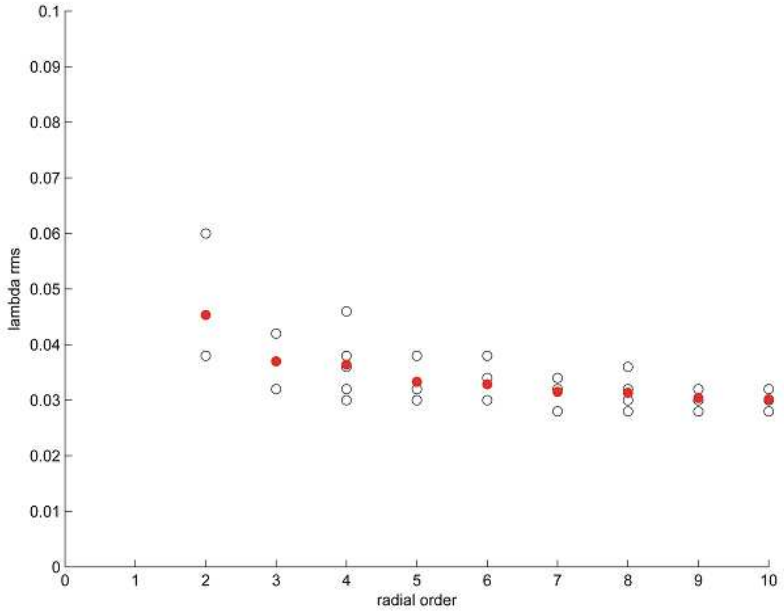

Figure 4.8: Scatter of rms residuals due to non-linearity for various modes belonging to the same radial order class. For each radial order we plot the measured polynomial coefficient corresponding to $Z_i{}^j$ vs the RMS polynomial amplitude of the introduced aberration $Z_i{}^j$. Such a scatter can be considered small and decreases with radial order.

the Kolmogorov turbulence for a given D/r_0, assuming a perfect correction perfectly up to a given Zernike polynomial (Noll, 1976), valid for N>10:

$$\sigma_N{}^2 = 0,2944 \cdot (N^{-\sqrt{3/2}} - (N+1)^{-\sqrt{3/2}} \cdot \left(\frac{D}{r_0}\right)^{-\frac{5}{3}} \left(\frac{\lambda}{2\pi}\right)^2$$

The comparison, assuming D=40 m and $r_0 = 20cm$ is shown in figure 4.9 where the red line represents the wavefront residual of the Kolmogorov turbulence for a single polynomial (only from the 10th radial order and upward) and the red dots the error due to the non-linearity of the pyramid.

At this point we have to consider that the number of polynomials increases as the radial order increase. Therefore the residual errors (blue dots) need to be weighted for that (multiplying each value by the number of modes of each mode, continuing on the assumption that a single radial order mode is representative of the whole set of that radial order), obtaining the purple line in figure 4.9, and at this point the expected residual errors due to non linearity vs. the maximum radial order corrected corrected on-board the VL-WFS are retrieved (magenta circles) .

We recall that the aim of this computation is to understand which degree of compensation is actually needed in the VL-WFS. It can be seen from the graph

that, for instance, truncating the actual compensation to a sampling of the pupil of 40 actuators over one pupil diameter, will allow for an error in the determination of the further modes (that will be used to compute the commands to the ELT DMs up to a sampling of 80x80) with an error due to non-linearity of the order of a few nm per mode. These will lead to an upper limit on the expected error because of a limited compensation in the locally closed loop in the VL-WFS.

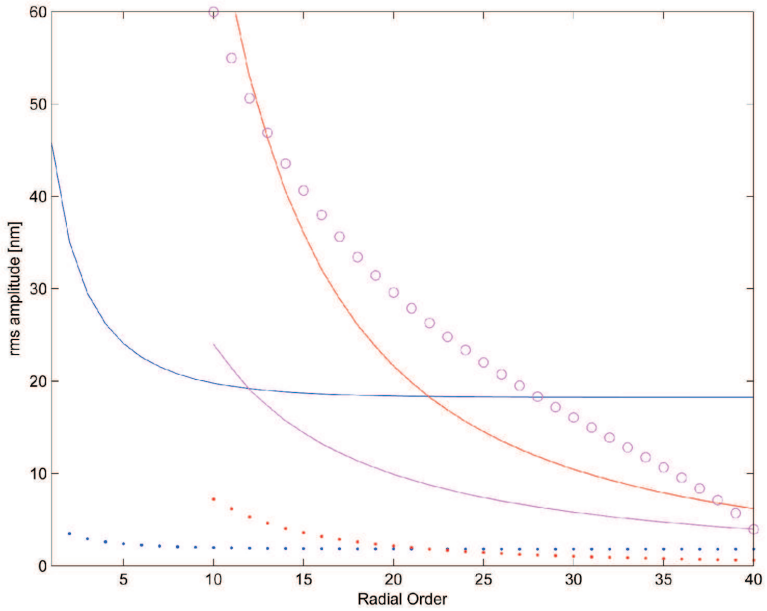

Figure 4.9: Estimation of the non-linearity versus radial order mode. The blue line is the RMS polynomial amplitude at which the error due to non-linearity is 10% represented by the blue dots. The red line is the wavefront residual of the Kolmogorov turbulence (D=40 m, λ=500 nm, r_0=20 cm) for a single polynomial of the corresponding radial order. The red dots represent the error on the measurement of a single polynomial of the corresponding radial order due to non-linearity of the pyramid. The magenta line is the RMS sum of these errors considering the number of polynomials of the corresponding radial order. The magenta circles are the cumulative RMS sum of the magenta line and represent residual errors due to non-linearity versus the maximum radial order corrected.

4.4.2 Pyramid vs Shack-Hartmann magnitude gain for different Strehl ratios

Using the work of Ragazzoni and Farinato (1999) as a starting-point, the magnitude gain of the Pyramid WFS with respect to the SH WFS has been further investigated, through an essentially analytical method. Considering a 40-meter telescope, we aimed at finding the magnitude gain dependence from the SR on the pyramid pin.
The same assumptions of Ragazzoni & Farinato (1999) have been considered and are hereafter recalled:

- the same reconstructor is applied for both PWFS and SH, assuming they are measuring the first derivative of the wavefront, as in geometrical approximation;
- the lenslet size of the SH lenslet array and the sampling of the pupils in the PWFS are equal to each other and equal to r_0;
- $N^2 = (D/r_0)^2$ is the number of sub-apertures (with D the telescope diameter);
- the pyramid is not modulated;
- we are in closed loop conditions, therefore the spot on the pin of the pyramid has an angular size λ/D (with λ the working level of the WFS) and λ/r_0 is the angular size of each SH spot;
- n^* is the number of photons collected by the detector in a single sub-aperture for a single integration time;
- each SH spot is characterized by a centering error due to photon shot noise given, in angular units, by $\sigma^2 = (\frac{\lambda}{r_0})^2 \cdot \frac{1}{n^*}$, therefore the N^2 independent estimate will produce a final error on the tilt estimation given by $\sigma^2_{SH-tilt} = (\frac{\lambda}{Nr_0})^2 \frac{1}{n^*} = (\frac{\lambda}{D})^2 \frac{1}{n^*}$
- the noise propagation coefficients for the SH WFS are described by the following equation (Rigaut and Gendron, 1992):

$$\sigma^2{}_{SH} = \sigma^2{}_{ph} \sum_{q=1}^{Q} \left[0.590 \ (q+1)^{-2.05} + 0.174(q-1)(q+1)^{-2} \right] \qquad (4.2)$$

where $\sigma^2{}_{ph}$ is the photonic noise error proportional to the square root of the photons number, q the Zernike radial order and Q=D/r_0 is the maximum radial order.

- in the PWFS case the behavior is almost identical to the one of a quadrant sensor located on the focal plane, collecting the whole light of the telescope in a single diffraction limited spot as $\sigma^2_{PWFS-tilt} = (\frac{\lambda}{ND})^2 \frac{1}{n^*} = \sigma^2_{SH-tilt}(\frac{r_0}{D})^2$.
- the PWFS for a Zernike polynomial of the q-th Zernike radial order is estimated as $\sigma^2_{PWFS-q} = \sigma^2_{SH-q}(\frac{qr_0}{D})^2$, meaning that the sensitivity of the sensor is inversely proportional to the second power of the focal spot linear dimension. This is reasonably estimated recalling that the diffraction limit is a direct consequence of the Heisenberg uncertainty principle, being the uncertainty of the measurement of the momentum of the photon along the focal plane directly linked to the uncertainty on its entrance pupil position. This leads to the fact that any measurement aiming to identify the location on the pupil of a photon approaching the focal plane in such a situation will destroy the λ/D resolving power capability. In the case of a full diffraction limit the four pupils look, in fact, homogenous, while in the case of an increase of the spot size on the pyramid pin there is a direct relationship with the size of the zone of the incoming pupil where the aberration measurement is taking place. So the variable D in the $\sigma^2_{PWFS-tilt}$ equation can be replaced by D/q (being q=1 for the tilt we obtain D).

  To obtain the pyramid coefficients Eq. 4.2 is multiplied by a factor $(q/Q)^2$,

$$\sigma^2{}_{PYR} = \sigma^2{}_{ph}\left(\frac{q}{Q}\right)^2 \sum_{q=1}^{Q}\left[0.590\ (q+1)^{-2.05} + 0.174(q-1)(q+1)^{-2}\right] \quad (4.3)$$

The last equation has been confirmed experimentally by Peter et al. (2010) up to Q=7 in the framework of PYRAMIR (fig.8 of the cited paper, reported in figure 4.10). We contacted the author to better understand the conditions under which the results were obtained and we were informed that their data were retrieved in laboratory and that the SR on the pin of the pyramid was of the order of 90−95%.

The estimate of the magnitude gain at different maximum radial orders obtained by Ragazzoni and Farinato (1999) for an infinite SR, through the relationship $g = -2.5log\frac{\sigma^2{}_{SH}}{\sigma^2{}_{PYR}}$, is shown in figure 4.11.
To extend the concept, as a first thing the noise propagation errors have been computed for the case D=40 m and r_0=20 cm, representing the case of R-band (0.8 μm), where the WFS will likely be working, therefore the maximum radial order is Q=200. The obtained result is shown in figure 4.12.
Using Noll's (1976) formula to compute the residual WFE (σ^2), assuming that the AO system corrects perfectly up to a specific number of Zernike modes the deformed wavefront (therefore no other noise contribution is considered) and assuming a Kolmogorov turbulence:

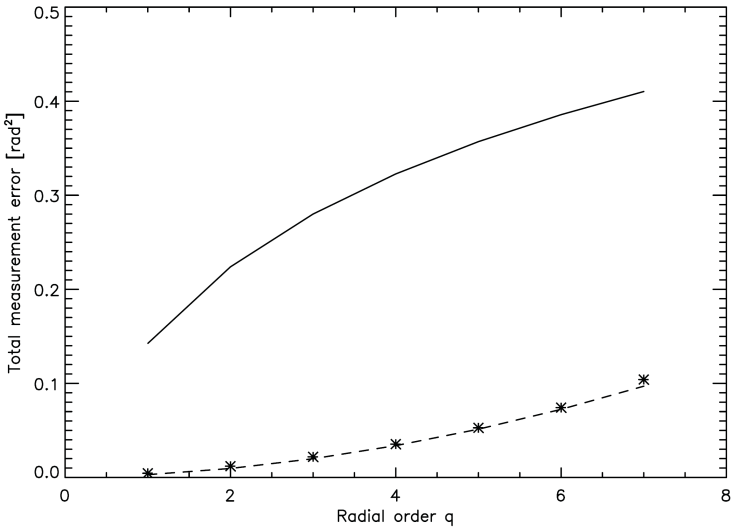

Figure 4.10: Measurement error coefficient for a correction of radial order with maximum radial order Q = 7. Solid line marks the theoretical error of a SHS under the same conditions, dashed line denotes the predictions by Ragazzoni and Farinato (1999), asterisks show Peter et al. (2010) measurements. Note that the error bars vanish within the asterisks.Peter et al. (2010).

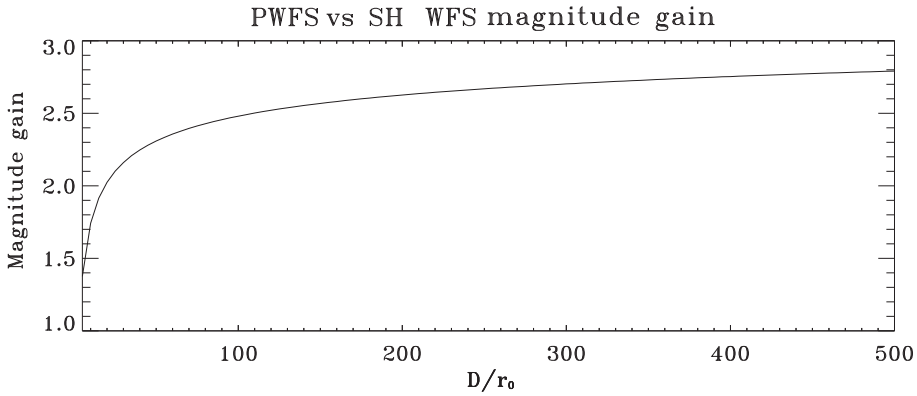

Figure 4.11: PWFS vs SH magnitude gain for infinite SR for different maximum radial orders (depending on D and r_0)(Ragazzoni and Farinato, 1999).

$$\sigma^2 = \frac{0,2944 N_{\text{Zern}}^{-\sqrt{3/2}} \left(\frac{D}{r_0}\right)^{-\frac{5}{3}}}{(2\pi)^2}$$

and applying to the WFE the Marechal approximation

$$SR = e^{-(2\pi\ \sigma)^2}$$

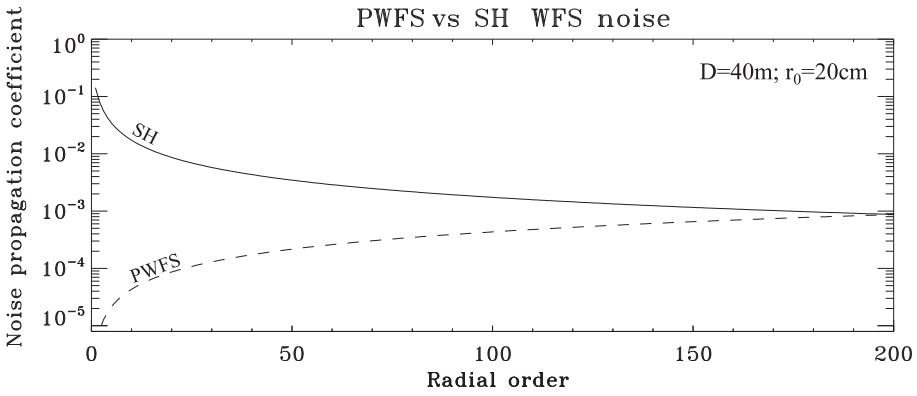

Figure 4.12: Noise propagation coefficients for PWFS (dashed line) and SH WFS (full line) for the case D=40 m and r_0=20 cm (R-band).

we obtained the dependence of the SR from the maximum corrected radial order, which is shown in figure 4.13 (bottom), both for the R-band case (r_0=20 cm, where the WFS will work) and for the K-band (r_0=1 m, where the scientific camera will work). It is possible to see how the same maximum corrected radial order leads to a poor SR in R and to a high SR in K.

At this point, to obtain the dependance of the magnitude gain from the SR, we will consider the noise propagation error for the PWFS to be equal to $\sigma^2{}_{PYR}$ up to the corrected radial order, and equal to $\sigma^2{}_{SH}$ at higher radial orders. This last one is an assumption to be able to compare the total gain magnitude, not considering any improvement of the PWFS with respect to the SH one after the value corresponding to the maximum corrected radial order.

In figure 4.13 (top) are shown with a green line the noise propagation errors for the PWFS for a SR of about 0.3 on the pin of the pyramid, corresponding to a number of "perfectly" corrected radial orders of 100.

Varying the value of maximum corrected radial order is therefore possible to retrieve the relationship between SR and magnitude gain of the PWFS vs the SH WFS, shown in figure 4.14. The curve in figure 4.14 saturates at the magnitude gain value given in figure 4.11 (about 2.6) considering a D/r_0=200 as maximum radial order, meaning a 40 meter telescope. Therefore, it can be inferred that for a 40 m telescope, even with a SR of 0.3 on the pin of the pyramid, obtained correcting 100 radial orders for the considered case (r_0=20 cm), is present a gain of more than 2 magnitudes of the PWFS with respect to the SH WFS (see Figure 11).

Modulation by small amounts (i.e. a few λ/D) would essentially solve the linearity problem described in section 4.4.1. But the question which immediately arises is "How much a modulation will degrade the performances in terms of expected gain?" The answer to this question can be found in the literature. In Vérinaud (2004) is shown the plot of the gain with respect to the SH spot size (see fig.8 of the cited work

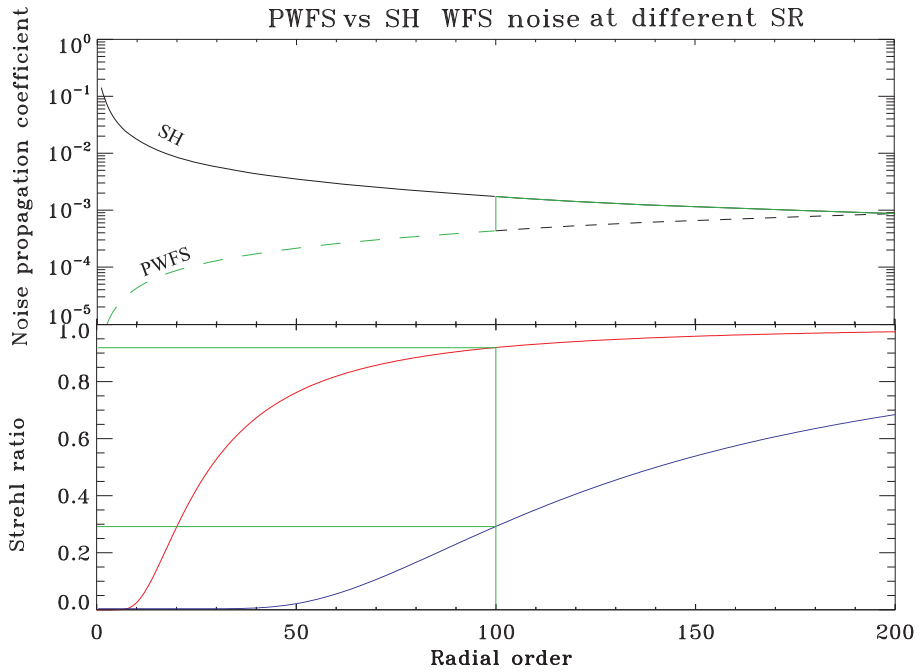

Figure 4.13: Bottom: relationship between SR and maximum corrected radial order. The green lines show the SR corresponding to a number of corrected radia order=100, which is about 0.3 for R-band (blue curve) and above 0.9 for K-band (red curve). **Top**: the noise propagation errors for the PWFS are considered to be equal to σ^2_{PYR} up to the corrected radial order, and equal to σ^2_{SH} for higher orders. The figure is the same as figure 4.12 but the "new" coefficients (indicated by the green dashed line) for a pyramid not working in closed loop are considered to compute the graph plotted in figure 4.14 .

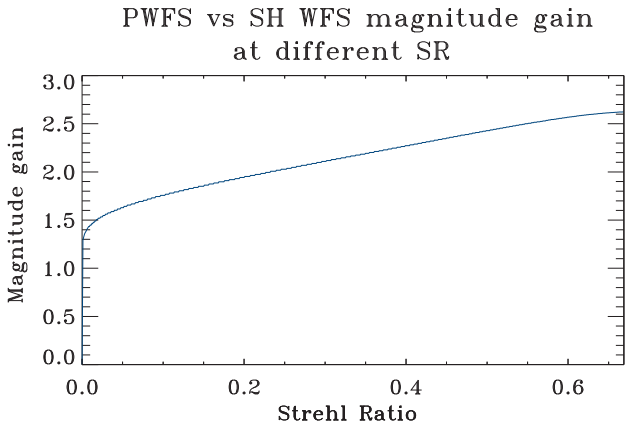

Figure 4.14: Magnitude gain of the SH with respect to the PWFS at different SR for the case D=40 m and r_0=20 cm.

that is reported in figure 4.15). Assuming that the SH has a choice of the lenslets of

different D/r_0, this means that 100% correspond to N=D/r_0 λ/D. From the graph is possible to infer that for a modulation of a few λ/D the gain in magnitude is approximately the same, while it decreases linearly after about 20% of equivalent spot modulation. It is worth to point out that in the paper the slight (about 0.5) magnitude smaller gain computed here is mainly due, as the author points out, to the comparison with the spatially filtered SH as high order spatial frequency are optically cut-out before being injected into the wavefront sensing devices.

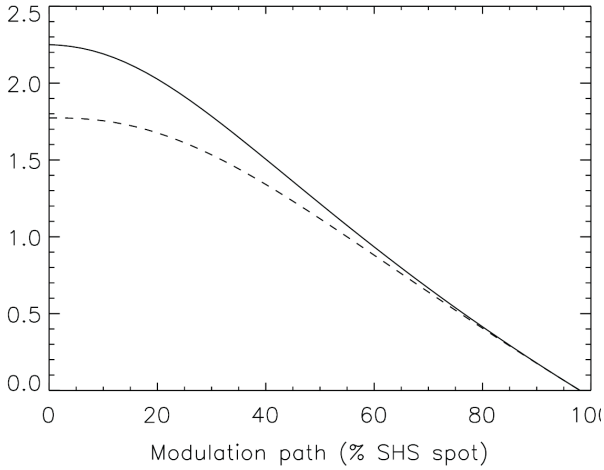

Figure 4.15: Gain in magnitude of the PWFS with respect to the SHS versus beam modulation amplitude for a 100 m (solid line) and a 10 m (dashed line) telescope. Sub-aperture size 25 cm.

4.5 Conclusions

The concept of GMCAO has solid basis, both because of the used WFSs, in particular concerning the PWFS, giving great results in the past years, and the MCAO concept, proven on sky with MAD and achieving scientific results almost in every night of operation, even being just a demonstrator. Of course there are many new concepts involved and a diameter of the telescope which cannot make us believe to just scale ideas greatly working on 8 m class telescopes. A large FoV of 10 arcmin defined by telescope optics can be used, increasing by 25 times with respect to an 8 meter telescope the area in which to search for NGSs, highly increasing the sky coverage. For this reason, the system has been designed in a small SCAO systems able to enter in the FoV to look at up to 6-7 NGSs, without interfering with LGSs, proposing itself as a back-up solution or a co-existent one in case of economic or practical problems connected with availability LGSs in the first years of telescope operations. This system aims to the correction of the central 2' FoV, therefore it is working in a partial open-loop, similarly to what happens with MOAO. This is certainly the most critical issue and for this reason a number of theoretical studies to understand the behavior of different components inside the system is going on in a contract with ESO. In my PhD thesis I focus mainly on the study (performed through simplified simulations) of the behavior of the PWFS under imperfect illumination conditions, in particular verifying the possible effects on the WFE of non-linearity and to verify the gain of the PWFS vs the SHWFS at different SR, other that the known gain achieved when the loop is closed. So far all results have been encouraging, but of course simulations could be improved to take into account further aspects and an overall definition of doability, costs and achievable results is still ongoing.

Conclusions

In this PhD work three different systems, marked by the presence of one or more Pyramid Wavefront Sensors, have been studied. They are difficult to be compared (even though they are based on the same optical concepts) because they range from applications to the human eye (6 mm, WATERFALL), to instrumentation for the 40-meter E-ELT (VL-WFS), passing through a very complex system featuring more than 100 degrees of freedom to be mounted on 8.4 m $\times$ 2 LBT telescope (GWS for LINC-NIRVANA).

Each project includes various phases, which, depending on the challenges, can last many years. I had the opportunity to participate at several phases of these projects with some commonalities and many differences:

- WATERFALL, concerned the study and realization of a prototype for opthalmologic application;
- GWS for NIRVANA, the alignment, verification and integration phase with the related work of writing documentation, which has almost reached its commissioning phase;
- the VL-WFS is in its very early phase, concepts and new ideas (mostly coming from our group) have to be organized in order to make a real proposal of a Global MCAO instrument for the E-ELT.

WATERFALL project aims to the realization of a prototype for commercial application of the Intra-Ocular Lenses properties, meaning therefore a pupil size of about 8 mm. It needs to be compact, limited in costs and it is designed in order to be adjustable and allow the analysis of IOL's with different focal lengths. Being illuminated by a static source, high pupil sampling is not very relevant since only low order Zernike polynomials need to be analyzed, whereas linearity needs to be large since, depending on the IOL's focal length, the spot imaged on the pin of the pyramid would largely vary in size. Moreover, it has the advantage that the time needed to analyze the data can be of the order of tenths of seconds, to be compared

with much larger bandwidths needed for an astronomical AO system, where the turbulence is distorting the wavefront.
I worked on the design, implementation and characterization of the prototype of a pyramid WFS to analyze the quality of several IOLs and to determine their dioptric power with a precision of $\pm$ 0.125 D.
The final results of the testing phase have been successfull and encouraging for a future possible commercialization of a user-friendly, compact system performing within the requirements.
I was actively involved in the alignment, integration and verification phase of one of the two Ground-layer Wavefront Sensors for LINC-NIRVANA. In the complete LINC-NIRVANA system, there will be two GWSs, one for each LBT arm that would work together interferometrically with two high layer WFS to correct turbulence in a 30" FoV, in a Multiple Field of View Multi-Conjugated Adaptive Optics system.

GWS is a very complex multi-pyramid system, that can look for up to 12 NGSs on an annular FoV of 2-6' (making it the largest FoV WFS realized), which will be optically co-added on a detector to increase the SNR and therefore it allows using also fainter stars. Even if the concept behind this system has been already proved in the Multi-conjugated Adaptive optics demonstrator (MAD), and in the GWS the tomographic part can be considered easy, being all pupils superimposed, its main difficulties consist in the tight tolerances defined for its alignment, which had to be carefully studied through an error budget which needed to be often updated to make a realistic estimate of the final system performances. Each PWFS has a low linearity range, trying to improve at most the sensitivity of the sensor, and assuming that the atmosphere itself will be a sort of modulator, at least in the transition between open and closed-loop.
The first GWS, after being assembled and tested in Padova laboratories and further on at MPIA institute in Heidelberg, is almost ready to be shipped to LBT, to perform the so called Pathfinder experiment, with the aim to correct ground-layer turbulence, thanks to LBT Adaptive Secondary mirror of 672 actuators to which it is optically conjugated.

Finally, I have participated to the study to assess the feasibility of a Very-Linear WFS for E-ELT using solely natural guide stars, to be able exploit the resolution of this telescope not depending on LGSs availability. In fact, the FoV usable to find NGSs (to correct a 2' central FoV) is 10', a great increase in the sky coverage when compared to the 2' FoV usable in an 8 meter class telescope. It has to be remembered, in fact, that the 6' FoV of the GWS can be used to sense only the lower heights of turbulence. This study is based on several innovative concepts developed in the last years, among which the PWFS that has a key role to increase the sensitivity

and, as a consequence, the final achievable sky coverage. I participated to the study phase of this new WFS, especially trying to better understand PWFS characteristics of linearity, sensitivity, gain magnitude with respect to other wavefront sensors in conditions of imperfect illumination. Because of the ajar loop in which the system is operating, is very important to identify the latter to then minimize the noise contribution.

In figure 4.16 I tried to summarize pictorially the commonalities and differences of the projects involved in my PhD work. The three projects ranging from different applications, but based on the same optical concepts, are compared for what concerns their PWFS linearity and the overall complexity (which of course depends on the considered items to define it), focusing mainly of technical challenges, both in realization and in reaching the required specifications. The project status is also represented.

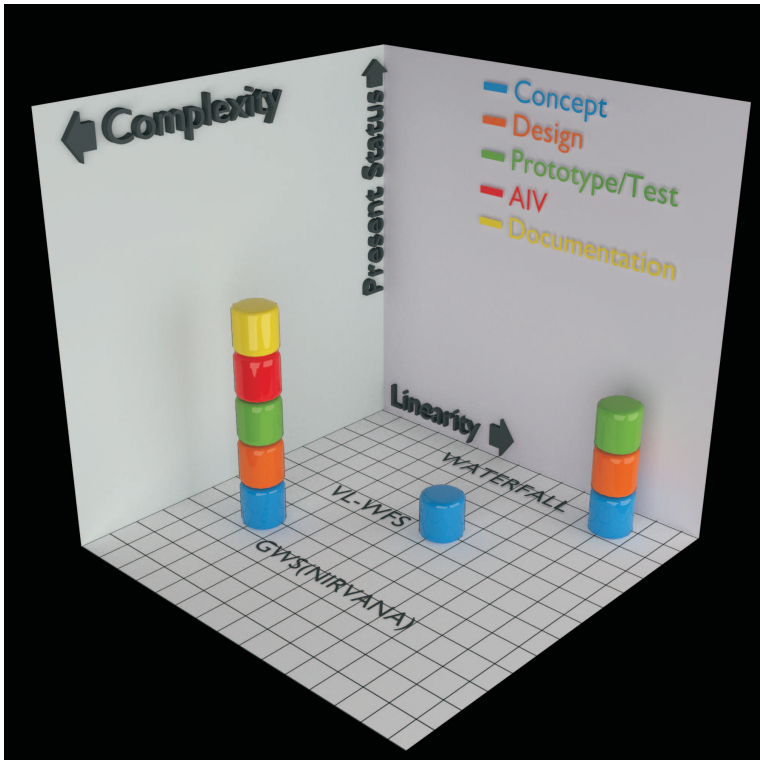

Figure 4.16: This figure aims to compare graphically the three projects described in my PhD work, in terms of PWFS linearity and overall complexity, showing also the reached status for each project.

Appendix A

Acronyms

AIV: Assembly, Integration and Verification
AO: Adaptive Optics
CA:Clear Aperture
CCD: Charge Coupled Device
CS: Curvature wave-front Sensor DM: Deformable Mirror
ELT: Extremely Large Telescope
FEA: Finite Element Analysis
FL:Focal Lenght
FoV: Field of View
FWHM: Full Width Half Maximum
GLAO:Ground-layer Adaptive Optics
GMCAO: GLOBSL Multi-Conjugate Adaptive Optics
GS: Guide Star
GWS: Ground-layer Wavefront Sensor
IOL: Intra-Ocular Lens
IR: Infrared
LBC: Large Binocular Camera
LBT: Large Binocular Telescope
LINC-NIRVANA: The LBT INterferometric Camera and Near-InfraRed/Visible Adaptive iNterferometer for Astronomy
LGS: Laser Guide Star
LO: Layer-Oriented
MAD: Multi-Conjugate Adaptive Optics Demonstrator
MCAO: Multi-Conjugate Adaptive Optics
MFoV: Multiple Field of View
MHWS: Medium High Wavefront Sensor
NGS: Natural Guide Star
OAP: Off-Axis Parabola

OPD: Optical Path Difference
PR-I: Pupil Re-Imager
PSF: Point Spread Function
PWFS: Pyramid wave-front Sensor
SCIDAR: SCIntillation Detection And Ranging
SE: Star Enlarger
SH: Shack-Hartmann
SNR: Signal-to-Noise Ratio
SO: Star-Oriented
SR: Strehl Ratio
VLT: Very Large Telescope
WFE: WaveFront Error
WFS: WaveFront Sensor

Bibliography

D. R. Andersen, J. Stoesz, S. Morris, M. Lloyd-Hart, D. Crampton, T. Butterley, B. Ellerbroek, L. Jolissaint, N. M. Milton, R. Myers, K. Szeto, A. Tokovinin, J.-P. Véran, & R. Wilson. *Performance Modeling of a Wide-Field Ground-Layer Adaptive Optics System*. PASP, **118**, 1574–1590, 2006.

L.C. Andrews. *Field Guide to Atmospheric Optics*. Spie Field Guides. SPIE Press, 2004. ISBN 9780819453181.

C. Arcidiacono. *MAD Layer Oriented Technical Nights Report*. 2007.

C. Arcidiacono, E. Diolaiti, R. Ragazzoni, J. Farinato, & E. Vernet-Viard. *Sky coverage for layer-oriented MCAO: a detailed analytical and numerical study*. Proc. SPIE, **5490**, 563–573, 2004.

H. W. Babcock. *The Possibility of Compensating Astronomical Seeing*. PASP, **65**, 229, 1953.

A. Basden, N. A. Bharmal, T. Butterley, N. Dipper, T. Morris, R. Myers, & A. Reeves. *A study of MOAO behind GLAO for EAGLE*. Proc. SPIE, **8447**, July 2012.

J. M. Beckers. *Increasing the Size of the Isoplanatic Patch with Multiconjugate Adaptive Optics*. M.-H. Ulrich, editore, European Southern Observatory Conference and Workshop Proceedings, **30**, 693, 1988.

J. M. Beckers. *Detailed compensation of atmospheric seeing using multiconjugate adaptive optics*. Proc. SPIE, **1114**, 215–0, 1989.

J. M. Beckers. *Adaptive optics for astronomy: principles, performance and applications*. ARA&A, **31**, 13–62, 1993.

P. Bizenberger, E. Diolaiti, S. Egner, T. M. Herbst, R. Ragazzoni, D. Reymann, & W. Xu. *LINC-NIRVANA: optical design of an interferometric imaging camera*. Proc. SPIE, **6269**, 2006.

M. Chun, R. Wilson, R. Avila, T. Butterley, J.-L. Aviles, D. Wier, & S. Benigni. *Mauna Kea ground-layer characterization campaign*. MNRAS, **394**, 1121–1130, 2009.

J. B. Costa, R. Ragazzoni, A. Ghedina, M. Carbillet, C. Vérinaud, M. Feldt, S. Esposito, E. Puga, & J. Farinato. *Is there need of any modulation in the pyramid wavefront sensor?*. Proc. SPIE, **4839**, 288–298, 2003.

J.-G. Cuby, S. Morris, T. Fusco, M. Lehnert, P. Parr-Burman, G. Rousset, J.-P. Amans, S. Beard, I. Bryson, M. Cohen, N. Dipper, C. Evans, M. Ferrari, E. Gendron, J.-L. Gimenez, D. Gratadour, P. Hastings, Z. Hubert, E. Hugot, P. Jagourel, P. Laporte, V. Lebrun, D. Le Mignant, F. Madec, R. Myers, B. Neichel, T. Morris, C. Robert, H. Schnetler, M. Swinbank, G. Talbot, W. Taylor, F. Vidal, S. Vivès, P. Vola, N. Welikala, & M. Wells. *EAGLE: a MOAO fed multi-IFU NIR workhorse for E-ELT*. Proc. SPIE, **7735**, July 2010.

E. Diolaiti, L. Schreiber, I. Foppiani, & M. Lombini. *Dual-channel multiple natural guide star wavefront sensor for the E-ELT multiconjugate adaptive optics module*. Proc. SPIE, **8447**, July 2012.

S. E. Egner, W. Gaessler, T. M. Herbst, & R. Ragazzoni. *A Closed Loop Layer-oriented Adaptive Optics Test Bed: Applications to Ground-Layer Adaptive Optics*. PASP, **119**, 1114–1125, 2007.

S. Esposito & A. Riccardi. *Pyramid Wavefront Sensor behavior in partial correction Adaptive Optic systems*. Astron. Astrophys., **369**, L9, 2001.

S. Esposito, A. Riccardi, L. Fini, A. T. Puglisi, E. Pinna, M. Xompero, R. Briguglio, F. Quirós-Pacheco, P. Stefanini, J. C. Guerra, L. Busoni, A. Tozzi, F. Pieralli, G. Agapito, G. Brusa-Zappellini, R. Demers, J. Brynnel, C. Arcidiacono, & P. Salinari. *First light AO (FLAO) system for LBT: final integration, acceptance test in Europe, and preliminary on-sky commissioning results*. Proc. SPIE, **7736**, July 2010.

J. Farinato, R. Ragazzoni, C. Arcidiacono, A. Brunelli, M. Dima, G. Gentile, V. Viotto, E. Diolaiti, I. Foppiani, M. Lombini, L. Schreiber, P. Bizenberger, F. De Bonis, S. Egner, W. Gässler, T. Herbst, M. Kürster, L. Mohr, & R.-R. Rohloff. *The Multiple Field of View Layer Oriented wavefront sensing system of LINC-NIRVANA: two arcminutes of corrected field using solely Natural Guide Stars*. Proc. SPIE, **7015**, July 2008.

J. Farinato, V. Viotto, R. Ragazzoni, C. Arcidiacono, A. Baruffolo, M. Dima, G. Gentile, D. Magrin, & P. Rossettini. *A compact design of a WFS for a natural guide star-based ELT adaptive optics system*. Proc. SPIE, **7736**, July 2010.

R. Foy & A. Labeyrie. *Feasibility of adaptive telescope with laser probe*. A&A, **152**, L29–L31, 1985.

D. L. Fried. *Optical Resolution Through a Randomly Inhomogeneous Medium for Very Long and Very Short Exposures*. JOSA, **56**, 1372, 1966.

D. L. Fried. *Focus anisoplanatism in the limit of infinitely many artificial-guide-star reference spots.*. Journal of the Optical Society of America A, **12**, 939–949, 1995.

E. Gendron, M. Brangier, G. Chenegros, F. Vidal, Z. Hubert, G. Rousset, & F. Pouplard. *A new sensor for laser tomography on ELTs*. Adaptative Optics for Extremely Large Telescopes, 2010.

E. Gendron, F. Vidal, M. Brangier, T. Morris, Z. Hubert, A. Basden, G. Rousset, R. Myers, F. Chemla, A. Longmore, T. Butterley, N. Dipper, C. Dunlop, D. Geng, D. Gratadour, D. Henry, P. Laporte, N. Looker, D. Perret, A. Sevin, G. Talbot, & E. Younger. *MOAO first on-sky demonstration with CANARY*. A&A, **529**, L2, 2011.

F. Hammer, F. Sayède, E. Gendron, T. Fusco, D. Burgarella, V. Cayatte, J.-M. Conan, F. Courbin, H. Flores, I. Guinouard, L. Jocou, A. Lançon, G. Monnet, M. Mouhcine, F. Rigaud, D. Rouan, G. Rousset, V. Buat, & F. Zamkotsian. *The FALCON Concept: Multi-Object Spectroscopy Combined with MCAO in Near-IR*. J. Bergeron & G. Monnet, editori, Scientific Drivers for ESO Future VLT/VLTI Instrumentation, 139, 2002.

J.W. Hardy. *Adaptive optics for astronomical telescopes*. Oxford University Press, 1990.

T. Herbst, R. Ragazzoni, D. Andersen, H. Boehnhardt, P. Bizenberger, A. Eckart, W. Gaessler, H.-W. Rix, R.-R. Rohloff, P. Salinari, R. Soci, C. Straubmeier, & W. Xu. *LINC-NIRVANA: a Fizeau beam combiner for the large binocular telescope*. Proc. SPIE, **4838**, 456–465, 2003.

T. M. Herbst, P. Bizenberger, M. Ollivier, H.-W. Rix, & R.-R. Rohloff. *Fizeau Interferometry ON THE Large Binocular Telescope*. Science with the Large Binocular Telescope, 193, 2001.

T. M. Herbst & P. M. Hinz. *Interferometry on the Large Binocular Telescope*. Proc. SPIE, **5491**, 383, 2004.

J. M. Hill & P. Salinari. *Large Binocular Telescope project*. Proc. SPIE, **4837**, 140–153, 2003.

N. Hubin, R. Arsenault, R. Conzelmann, B. Delabre, M. Le Louarn, S. Stroebele, & R. Stuik. *Ground Layer Adaptive Optics*. Comptes Rendus Physique, **6**, 1099–1109, 2005.

N. N. Hubin, M. Le Louarn, M. S. Sarazin, A. A. Tokovinin, & E. Viard. *New challenges for adaptive optics: the OWL 100-m telescope*. P. L. Wizinowich, editore, Proc. SPIE, **4007**, 1100–1107, July 2000.

A. Kolmogorov. *The Local Structure of Turbulence in Incompressible Viscous Fluid for Very Large Reynolds' Numbers*. Akademiia Nauk SSSR Doklady, **30**, 301–305, 1941.

M. Le Louarn & N. Hubin. *Improving the seeing with wide-field adaptive optics in the near-infrared*. MNRAS, **365**, 1324–1332, 2006.

J. Liang, B. Grimm, S. Goelz, & J. F. Bille. *Objective measurement of wave aberrations of the human eye with the use of a Hartmann-Shack wave-front sensor*. Journal of the Optical Society of America A, **11**, 1949–1957, 1994.

D. Magrin, R. Ragazzoni, M. Bergomi, A. Brunelli, M. Dima, , & V. Farinato, J.and Viotto. *Pyramid based locally closed loop wavefront sensor: an optomechanical study*. Adaptative Optics for Extremely Large Telescopes, 2011.

E. Marchetti, R. Brast, B. Delabre, R. Donaldson, E. Fedrigo, C. Frank, N. Hubin, J. Kolb, J.-L. Lizon, M. Marchesi, S. Oberti, R. Reiss, J. Santos, C. Soenke, S. Tordo, A. Baruffolo, P. Bagnara, & The CAMCAO Consortium. *On-sky Testing of the Multi-Conjugate Adaptive Optics Demonstrator*. The Messenger, **129**, 8–13, 2007.

P. J. McCarthy. *Scientific potential of ground layer adaptive optics on large telescopes*. Proc. SPIE, **7736**, July 2010.

R. M. Myers. *Recent progress and perspectives for GLAO and MOAO*. Proc. SPIE, **7736**, July 2010.

R. J. Noll. *Zernike polynomials and atmospheric turbulence*. JOSA, **66**, 207–211, 1976.

D. Peter, M. Feldt, T. Henning, S. Hippler, J. Aceituno, L. Montoya, J. Costa, & B. Dorner. *PYRAMIR: Exploring the On-Sky Performance of the World's First Near-Infrared Pyramid Wavefront Sensor*. PASP, **122**, 63–70, 2010.

T. Pfrommer, P. Hickson, & C.-Y. She. *A large-aperture sodium fluorescence lidar with very high resolution for mesopause dynamics and adaptive optics studies*. Grl, **36**, 15831, August 2009.

R. Ragazzoni. *Propagation delay of a laser beacon as a tool to retrieve absolute tilt measurement*. Astrophys. J., **465**, L73–L75, 1996a.

R. Ragazzoni. *Pupil plane wavefront sensing with an oscillating prism*. JModOpt, **43**, 289–293, 1996b.

R. Ragazzoni. *No Laser Guide Stars for adaptive optics in giant telescopes?*. A&A, **136**, 205–209, 1999.

R. Ragazzoni, C. Arcidiacono, M. Dima, P. Dri, J. Farinato, G. Gentile, D. Magrin, & V. Viotto. *How to break the FoV versus thickness rule in MCAO*. Adaptative Optics for Extremely Large Telescopes, 2010.

R. Ragazzoni, M. Bergomi, A. Brunelli, M. Dima, J. Farinato, D. Magrin, L. Marafatto, & V. Viotto. *Global wavefront sensing for extremely large telescopes*. Proc. SPIE, **8447**, July 2012.

R. Ragazzoni, E. Diolaiti, J. Farinato, E. Fedrigo, E. Marchetti, M. Tordi, & D. Kirkman. *Multiple field of view layer-oriented adaptive optics. Nearly whole sky coverage on 8 m class telescopes and beyond*. A&A, **396**, 731–744, 2002.

R. Ragazzoni, E. Diolaiti, E. Vernet, J. Farinato, E. Marchetti, & C. Arcidiacono. *Arbitrarily Small Pupils in Layer-Oriented Multi-Conjugate Adaptive Optics*. PASP, **117**, 860–869, August 2005.

R. Ragazzoni & J. Farinato. *Sensitivity of a pyramidic Wave Front sensor in closed loop Adaptive Optics*. A&A, **350**, L23–L26, 1999.

R. Ragazzoni, J. Farinato, & E. Marchetti. *Adaptive optics for 100-m-class telescopes: new challenges require new solutions*. Proc. SPIE, **4007**, 1076–1087, 2000a.

R. Ragazzoni, A. Ghedina, A. Baruffolo, E. Marchetti, J. Farinato, T. Niero, G. Crimi, & M. Ghigo. *Testing the pyramid wavefront sensor on the sky*. P. L. Wizinowich, editore, Proc. SPIE, **4007**, 423–430, July 2000b.

R. Ragazzoni, T. M. Herbst, W. Gaessler, D. Andersen, C. Arcidiacono, A. Baruffolo, H. Baumeister, P. Bizenberger, E. Diolaiti, S. Esposito, J. Farinato, H. W. Rix, R.-R. Rohloff, A. Riccardi, P. Salinari, R. Soci, E. Vernet-Viard, & W. Xu. *A visible MCAO channel for NIRVANA at the LBT*. Proc. SPIE, **4839**, 536–543, 2003.

R. Ragazzoni, E. Marchetti, & F. Rigaut. *Modal tomography for adaptive optics*. A&A, **342**, L53–L56, 1999.

R. Ragazzoni, E. Marchetti, & G. Valente. *Adaptive-optics corrections available for the whole sky*. Nature, **403**, 54–56, 2000c.

A. Riccardi. *Analisi e sviluppo di un nuovo sensore di fronte d'onda per sistemi ottici adattivi basato sul "test" di Foucault*. Universitï¿½ degli Studi di Firenze, 1996.

F. Rigaut. *Ground Conjugate Wide Field Adaptive Optics for the ELTs*. ESO Astrophysics Symposia, **58**, 11, 2002.

F. Rigaut & E. Gendron. *Laser guide star in adaptive optics - The tilt determination problem*. A&A, **261**, 677–684, August 1992.

F. Roddier. *The effects of atmospheric turbulence in optical astronomy*. Prog. Optics, **19**, 281–376, 1981.

F. Roddier & C. Roddier. *Wavefront reconstruction using iterative Fourier transforms*. Applied Optics, **30**, 1325–1327, 1991.

G. Rousset, T. Fusco, F. Assemat, E. Gendron, T. Morris, C. Robert, R. Myers, M. Cohen, N. Dipper, C. Evans, D. Gratadour, P. Jagourel, P. Laporte, D. Le Mignant, M. Puech, H. Schnetler, W. Taylor, F. Vidal, J.-G. Cuby, M. Lehnert, S. Morris, & P. Parr-Burman. *EAGLE MOAO system conceptual design and related technologies*. Proc. SPIE, **7736**, July 2010.

W. H. Southwell. *Wave-front estimation from wave-front slope measurements*. JOSA, **70**, 998–1006, 1980.

M. Tallon & R. Foy. *Adaptive telescope with laser probe - Isoplanatism and cone effect*. A&A, **235**, 549–557, 1990.

V. L. Tatarski. *Wave propagation in a turbulent medium*. Dover Publications, 1961.

T. Travouillon, J. S. Lawrence, & L. Jolissaint. *Ground-layer adaptive optics performance in Antarctica*. Proc. SPIE, **5490**, 934–942, 2004.

C. Vérinaud. *On the nature of the measurements provided by a pyramid wave-front sensor*. Optics Communications, **233**, 27–38, 2004.

V. Viotto, R. Ragazzoni, C. Arcidiacono, M. Bergomi, A. Brunelli, M. Dima, D. Magrin, & J. Farinato. *Sky coverages on ELTs with a reference area much larger than the compensated one*. Adaptative Optics for Extremely Large Telescopes, 2011.